


1-1-2016

Static And Dynamic Behavior Of Carbon Fiber Reinforced Aluminum (carall) Laminates

Gurpinder Singh Dhaliwal
Wayne State University,

Follow this and additional works at: https://digitalcommons.wayne.edu/oa_dissertations

 Part of the [Materials Science and Engineering Commons](#), and the [Other Mechanical Engineering Commons](#)

Recommended Citation

Dhaliwal, Gurpinder Singh, "Static And Dynamic Behavior Of Carbon Fiber Reinforced Aluminum (carall) Laminates" (2016). *Wayne State University Dissertations*. 1525.
https://digitalcommons.wayne.edu/oa_dissertations/1525

This Open Access Dissertation is brought to you for free and open access by DigitalCommons@WayneState. It has been accepted for inclusion in Wayne State University Dissertations by an authorized administrator of DigitalCommons@WayneState.

**STATIC AND DYNAMIC BEHAVIOR OF CARBON FIBER
REINFORCED ALUMINUM (CARALL) LAMINATES**

by

GURPINDER SINGH DHALIWAL

DISSERTATION

Submitted to the Graduate School

of Wayne State University,

Detroit, Michigan

in partial fulfillment of the requirements

for the degree of

DOCTOR OF PHILOSOPHY

2016

MAJOR: MECHANICAL ENGINEERING

Approved By:

Advisor

Date

© COPYRIGHT BY

GURPINDER SINGH DHALIWAL

2016

All Rights Reserved

DEDICATION

To my parents, beloved wife & son, Rannfateh Singh and friends for always
supporting, helping, and standing by me.

ACKNOWLEDGEMENTS

I would like to offer my sincerest gratitude to my advisor, Professor Golam Newaz for supporting and providing suggestions to me throughout my research work. I would like to thank him for providing me the opportunity to work with him in Advanced Composite Research Lab. The level of my Ph.D. degree is an attribute of his encouragement and support for me. I would like to thank Dr. Emmanuel Ayorinde, Dr. Leela Mohana Reddy Arava and Dr. Christopher Eamon for serving as my committee members.

I am very grateful to Dr. Matt Zaluzec from Ford Motor Company for providing the material support for this research work through university research program (URP). I would also like to thank all of my friends and lab mates who helped and encouraged me during my research. Finally, I would like to thank Mr. Bassam Kas-Mikha, machine shop technician, for helping me in manufacturing parts and developing test fixtures used in this research work. I would like to thank my family finally for all of the sacrifices they have made for me. Words cannot express my sincere gratitude to my mother, father, mother-in-law and father-in-law for their continuous support and encouragement to strive towards my goal. In the end, I would like to thank my beloved wife Baldeep Kaur for being always present and her constant support.

.

TABLE OF CONTENTS

Dedication	ii
Acknowledgments	iii
Nomenclature	viii
List of Tables	x
List of Figures	xii
CHAPTER 1: INTRODUCTION	1
1.1: Fiber Metal Laminate Composite	1
1.1.1: Aramid Fiber Reinforced Aluminum Laminates (ARALL)	2
1.1.2: Glass Fiber Reinforced Aluminum Laminates (GLARE)	4
1.1.3: Carbon Fiber Reinforced Aluminum Laminates (CARALL)	6
1.2: Fiber Metal Laminates (FMLs) Processing	8
1.3: Applications	10
1.4: Low-Velocity Impact and Compression after Impact Tests	13
1.5: Rationale	15
CHAPTER 2: LITERATURE REVIEW AND OBJECTIVES	17
2.1: Glass Fiber Reinforced Aluminum Laminates (GLARE)	17
2.1.1: Static, Thermal Residual Stress Behavior and Modeling of GLARE	17
2.1.2: Impact Behavior and Impact Event Modeling of GLARE FMLs	22
2.2: Aramid Fiber Reinforced Aluminum Laminates (ARALL)	27
2.2.1: Static, Thermal Residual Stress Behavior and Modeling of ARALL	27
2.2.2: Impact Behavior and Impact Event Modeling of ARALL FMLs	29
2.3: Carbon Fiber Reinforced Aluminum Laminates (CARALL)	30

2.3.1: Static, Thermal Residual Stress Behavior and Modeling of CARALL	30
2.3.2: Impact Behavior and Impact Event Modeling of CARALL FMLs	33
2.4: Research Objectives	36
CHAPTER 3: FIBER METAL LAMINATE MATERIALS & CONSTRUCTION	38
3.1: Material Description	38
3.2: Fiber Metal Laminate Construction	41
3.3: Preliminary Tests	44
3.3.1: Double Notch Shear Strength Test	44
3.3.2: Static T-Peel Test	47
3.3.3: Polyester Synthetic Surfacing Veil Cloth Tensile Test	49
3.3.4: Scanning Electron Microscope (SEM) Cross-section Imaging	52
3.4: Specimen Details	52
3.5 Weight Savings with CARALL FMLs	54
3.5.1: Rule of Mixture Equations	54
3.5.2: Sample Weight Measurement	55
CHAPTER 4: THERMAL RESIDUAL STRESSES	56
4.1: Analytical Method	56
4.2: Thermal Residual Stresses Finite Element Analysis	58
CHAPTER 5: STATIC TENSILE TEST AND DATA ANALYSIS	62
5.1: Tensile Test Experimental Aspects	62
5.1.1 Effect of Polyester Veil Cloth Layers on Tensile Behavior of CARALL FMLs	63
5.2: Tensile Test Finite Element Analysis	66
5.2.1: Discretization of Tensile Fiber Metal Laminate Specimen	66

5.2.2: Composite (CFRP) Layers Material Model	67
5.2.3: Aluminum Material Model	68
5.2.4: Delamination Failure Model	70
5.2.5: Predicted Thermal Residual Stress Initialization	74
5.3: Tensile Test Experimental and Finite Element Analysis Results Comparison	76
CHAPTER 6: THREE POINT FLEXURAL TEST AND DATA ANALYSIS	82
6.1: Three point Flexural Test Experimental Aspects	82
6.1.1: Effect of Polyester Veil Cloth Layers on Flexural Behavior of CARALL FMLs	85
6.2: Flexural Test Finite Element Analysis	86
6.2.1: Discretization of Flexural Test Fiber Metal Laminate Specimen	87
6.2.2: Loading Pin and Support Rods Modeling	87
6.3: Flexure Test Experimental and Finite Element Analysis Results Comparison	88
CHAPTER 7: LOW VELOCITY IMPACT TEST AND DATA ANALYSIS	95
7.1: Low-Velocity Impact Test Experimental Aspects	95
7.1.1: Effect of Polyester Veil Cloth Layers on Impact Behavior of CARALL FMLs	96
7.2: Low-Velocity Impact Test Finite Element Analysis	101
7.2.1: Discretization of Impact Test Fiber Metal Laminate Specimen	101
7.2.2: Delamination Failure Model	103
7.2.2.1: Cohesive Zone Model	103
7.2.2.2: Mixed-Mode Cohesive Zone Model Derivation	105
7.3: Impact Test Experimental and Finite Element Analysis Results Comparison	109
7.3.1: Force-Displacement Characteristics	109
7.3.2: Damage Morphologies	112

7.3.3: C-scan and Finite Element Analysis Results Comparison	119
7.3.4: Carbon Fiber/Epoxy Layers Tensile Failures Numerical Predictions	123
7.3.5: Absorbed Energy and Energy Restitution Coefficient	126
7.4: CARALL-A and CARALL-B FMLs Impact Behavior Comparison	128
CHAPTER 8: COMPRESSION AFTER IMPACT (CAI) TEST AND DATA ANALYSIS	130
8.1: CAI Test Experimental Aspects	130
8.1.1: Effect of Polyester Veil Cloth Layers on CAI Behavior of CARALL FMLs	132
8.1.2: CARALL-A and CARALL-B FMLs CAI Behavior Comparison	138
8.2: CAI Numerical Simulation Aspects	142
8.2.1: CAI Test Numerical Predictions	144
CHAPTER 9: CONCLUSIONS AND RECOMMENDATIONS	152
9.1: Conclusions	152
9.2: Recommendations	156
References	157
Abstract	171
Autobiographical Statement	174

NOMENCLATURE

FML	fiber metal laminate
ARALL	aramid fiber composite aluminum laminate
CARALL	carbon fiber composite aluminum laminate
GLARE	glass fiber composite aluminum laminates
VARTM	vacuum assisted resin transfer molding
CFRP	carbon fiber reinforced plastics
AL	aluminum
MPa	megapascal
GPA	gigapascal
ASTM	American Society for Testing and Materials
MTS	Mechanical testing systems
Psi	pound-force per square inch
MIN	minute
CRF	carbon fiber
cm	centimeter
MVF	metal volume fraction
CVF	cloth volume fraction
cc	cubic centimeter
KN	Kilo Newton
mm	millimeter
FE	Finite Element
FEA	Finite Element Analysis
NFLS	normal failure stress
SFLS	shear failure stress
v	poison ratio
W	Watt
m	meter
K	Kelvin
°C	degree Celsius

ρ	density
g	gram
J	joule
τ	shear stress
ϵ	strain
σ	stress
E	modulus of rigidity
α	thermal coefficient of expansion
T, ΔT	temperature, change in temperature
G	shear modulus
X, Y, Z	co-ordinate system directions
S	shear strength
t	Thickness

Subscripts

FML	Fiber metal laminate
c'	composite
m	matrix
AL, al	aluminum
f	fiber
1, 2, 3	orthotropic material co-ordinate system
x, y, xy	stress directions
f'	flexural
t	tensile
c	compressive
n	normal
T	Tensile
y	yield
eff	effective

LIST OF TABLES

Table 1.1: Commercially available ARALL FMLs	4
Table 1.2: Commercially available GLARE grades	6
Table 3.1: Chemical composition of aluminum 5052-H32 alloy	38
Table 3.2: Mechanical properties of aluminum 5052-H32	39
Table 3.3: Twill weave carbon fiber/epoxy properties	40
Table 3.4: Aluminum-carbon fiber/epoxy bond shear strength results	45
Table 3.5: Aluminum-carbon fiber/epoxy bond normal strength results	49
Table 3.6: Properties of epoxy matrix and E-glass fiber used in turner's equation	51
Table 3.7: Tensile and thermal expansion properties of the polyester veil cloth	51
Table 3.8: Specimen notations and layup sequence for CARALL fiber metal laminates	54
Table 3.9: Weight savings with CARALL laminates obtained with rule of mixture equations	55
Table 3.10: Weight savings with CARALL FMLs obtained by measuring weight of samples	55
Table 4.1: Thermal residual stress predictions in flexural samples	60
Table 5.1: Parametric control card for dynamic relaxation in LS-Dyna	75
Table 5.2: Results of experimental tensile tests	81
Table 6.1: Results of experimental flexural tests	94
Table 7.1: Ultimate central deflection & crack lengths in outer layers of CARALL-A FMLs	100
Table 7.2: Ultimate central deflection & crack lengths in outer layers of CARALL-B FMLs	100
Table 7.3: Cohesive zone delamination model input data	107
Table 7.4: Steel impactor properties	108
Table 7.5: Peak load levels of different CARALL FMLs	112
Table 8.1: Failure mode codes as per ASTM D7137	132

Table 8.2: Compression after Impact (CAI) test results for CARALL specimens	137
Table 8.3: Comparison between experimental and FEA predictions for residual strength of CARALL-A specimens	147
Table 8.4: Comparison between all FMLs regarding peak load	149
Table 8.5: Comparison between experimental and FEA predictions for residual strength of CARALL-B specimens	150

LIST OF FIGURES

Figure 1.1: Fiber metal laminate schematic.	1
Figure 1.2: Classification of fiber metal laminates.	2
Figure 1.3: Schematic representation of ARALL fiber metal laminate	3
Figure 1.4: Crack bridging mechanism of ARALL laminates	3
Figure 1.5: Schematic illustration of GLARE laminate	5
Figure 1.6: Schematic diagram of a 2/1 CARALL laminate	7
Figure 1.7: Different woven fibers weave patterns	7
Figure 1.8: Schematic of typical solvent prepregging process	8
Figure 1.9: Automated tape layer machine	9
Figure 1.10: Large autoclave for curing completely assembled A380 Glare panels	10
Figure 1.11: First ARALL cargo door installed on the C-17 aircraft	11
Figure 1.12: GLARE stiffeners in cargo bay area in F28 aircraft	12
Figure 1.13: The application of GLARE as the upper fuselage panel for A380	13
Figure 1.14: Candidate areas for aerospace ARALL and GLARE	13
Figure 1.15: Typical damage cases of composite laminates structures	14
Figure 3.1: Aluminum 5052-H32 sheet used in making fiber metal laminates	38
Figure 3.2: Individual carbon toes in unidirectional and fabric style prepreg systems	39
Figure 3.3: Woven carbon fiber/epoxy prepreg before curing	40
Figure 3.4: Polyester synthetic surface veil cloth	41
Figure 3.5: Mechanical interlocking induced due to crevices produced by abrasion	42
Figure 3.6: Autoclave vacuum press machine used for curing the laminates	43
Figure 3.7: Vacuum press curing cycle at 0.35 MPa pressure	44
Figure 3.8: Schematic of double notch test specimen	45
Figure 3.9: (a) Double notch shear test coupon (b) coupon secured in MTS testing machine (c) damaged test coupon	46

Figure 3.10: Typical force-displacement curve obtained from double notch shear test	46
Figure 3.11: Schematic of T-peel specimen along with dimensions	47
Figure 3.12: T-Peel test being conducted	48
Figure 3.13: Typical load-disp. curve obtained from T-peel tests of CFC-AL bond	49
Figure 3.14: Polyester veil coupon during test and damaged specimen after test	50
Figure 3.15: Typical stress-strain response of polyester surfacing veil/epoxy laminate	50
Figure 3.16: SEM image of CARALL FML Cross section	52
Figure 3.17: Carbon fiber/epoxy –AL laminates nomenclature and stacking sequence	53
Figure 4.1: Effect of ply thickness on residual thermal stresses	57
Figure 4.2: Thermal residual FE model schematics of CARALL-A & B flexure FMLs	59
Figure 4.3: X stress plots for residual thermal stresses; (a) CARALL-A, (b) CARALL-A with veil cloth layers	61
Figure 4.4: X stress plots for residual thermal stresses; (a) CARALL-B, (b) CARALL-B with veil cloth layers	61
Figure 5.1: Nominal dimensions of tensile test samples	62
Figure 5.2: Tensile test setup with MTS machine	63
Figure 5.3: Tensile behavior of CARALL FMLs without veil cloth layers	64
Figure 5.4: Tensile behavior of CARALL FMLs having polyester veil cloth layers	65
Figure 5.5: Static tensile simulation FE model	67
Figure 5.6: Effective stress-effective plastic strain curve used as input to material model	70
Figure 5.7: Bilinear traction-separation law for mode I crack in tension	71
Figure 5.8: Iso-lines of internal parameter α	72
Figure 5.9: Parameters in softening model	73
Figure 5.10: FEA & experimental stress-strain plots for CARALL-A specimens	76
Figure 5.11: FEA and experimental failed Specimen of CARALL-A with no veil cloth	76

Figure 5.12: FEA & experimental stress-strain plots for CARALL-B specimens	77
Figure 5.13: FEA and experimental failed specimen of CARALL-B with no veil cloth	78
Figure 5.14: FEA & experimental stress-strain plots of CARALL-A specimens having polyester surface veil cloth layers	78
Figure 5.15: FEA and experimental failed specimen of CARALL-A having veil cloth layers	79
Figure 5.16: FEA & experimental stress-strain plots for CARALL-B specimens having polyester surface veil cloth layers	79
Figure 5.17: FEA and experimental failed specimen of CARALL-B having veil cloth layers	80
Figure 6.1: Three-point flexural test setup	83
Figure 6.2: MTS compression testing machine with three-point flexural fixture	84
Figure 6.3: Typical flexural behavior plots for CARALL FMLs	85
Figure 6.4: Three-point flexural finite element model	87
Figure 6.5: Experimental and FEA flexural stress-strain behavior of CARALL-A and CARALL-A with polyester veil cloth layers	89
Figure 6.6: Flexural failure modes of CARALL-A fiber metal laminates	90
Figure 6.7: Flexural failure modes of CARALL-A FMLs having cloth layers	90
Figure 6.8: Experimental and FEA flexural stress-strain behavior of CARALL-B FMLs	91
Figure 6.9: Flexural failure modes of CARALL-B fiber metal laminates	92
Figure 6.10: Flexural failure modes of CARALL-B FMLs having cloth layers	93
Figure 7.1: Impact support fixture and test tower	95
Figure 7.2: Force-displacement plots for CARALL-A FMLs made with and without veil cloth	97
Figure 7.3: Force-displacement plots for CARALL-B FMLs made with and without veil cloth	97
Figure 7.4: Damage morphology of CARALL-A specimens cured with and without cloth layers on impacted and non-impacted sides	98

Figure 7.5: Damage morphology of CARALL-B specimens cured with and without cloth layers on impacted and non-impacted sides	99
Figure 7.6: Ultimate central deflection schematic	100
Figure 7.7: Details of FE model for impact simulation as in actual experiments	102
Figure 7.8: Different regions of a crack	104
Figure 7.9: Cohesive zone stress distribution	104
Figure 7.10: Mixed-mode traction-separation law	106
Figure 7.11: Experimental and FEA force-displacement plots for CARALL-A FMLs made with veil cloth	109
Figure 7.12: Experimental and FEA force-displacement plots for CARALL-A FMLs cured without using veil cloth layers	110
Figure 7.13: Experimental and FEA force-displacement plots for CARALL-B FMLs made with veil cloth layers	111
Figure 7.14: Experimental and FEA force-displacement curves for CARALL-B FMLs made without using veil cloth layers	111
Figure 7.15: Damage morphologies of CARALL-A specimen made without cloth layers	112
Figure 7.16: Damage morphologies of CARALL-A specimen made with veil cloth layers	113
Figure 7.17: Cross-section images of CARALL-A specimens made without using polyester synthetic surfacing veil cloth layers under different impact energies	114
Figure 7.18: Cross-section pictures of CARALL-A specimens made with polyester surfacing veil cloth layers under different impact energies	115
Figure 7.19: Damage morphologies of CARALL-B specimen made without cloth layers	116
Figure 7.20: Damage morphologies of CARALL-B specimen made with veil cloth layers	116
Figure 7.21: Cross-section images of CARALL-B specimens made without using polyester synthetic surfacing veil cloth layers under different impact energies	117
Figure 7.22: Cross-section images of CARALL-B specimens made with polyester synthetic surfacing veil cloth layers under different impact energies	118

Figure 7.23: Ultrasonic C-scan method schematic illustration	119
Figure 7.24: FFT frequency setup	120
Figure 7.25: A-scan frequency setting	120
Figure 7.26: Comparison between C-scan and FEA predictions for delamination in CARALL-A specimens under different impact energies	121
Figure 7.27: Comparison between C-scan and FEA predictions for delamination in CARALL-B specimens under different impact energies	122
Figure 7.28: Delamination area results for CARALL-A specimens at different impact energies	123
Figure 7.29: Delamination area results for CARALL-B specimens at different impact energies	123
Figure 7.30: Numerical prediction of tensile failures of CFRP layers in CARALL-A FMLs made without using polyester synthetic surfacing veil cloth layers	124
Figure 7.31: Numerical prediction of tensile failures of CFRP layers in CARALL-A FMLs made with polyester synthetic surfacing veil cloth layers	124
Figure 7.32: Numerical prediction of tensile failures of CFRP layers in CARALL-B FMLs made without using polyester synthetic surfacing veil cloth layers	125
Figure 7.33: Numerical prediction of tensile failures of CFRP layers in CARALL-B FMLs made with polyester synthetic surfacing veil cloth layers	125
Figure 7.34: Energy consumed by CARALL-A FMLs during an impact event	126
Figure 7.35: Energy Restitution Coefficient results for CARALL-A FMLs	127
Figure 7.36: Energy absorbed by CARALL-B FMLs during an impact event	127
Figure 7.37: Energy Restitution Coefficient results for CARALL-B FMLs	127
Figure 7.38: Force-displacement plot for CARALL-A & -B FMLs having veil cloth layers	128
Figure 7.39: Force-displacement plot for CARALL-A & -B FMLs cured without using polyester synthetic surfacing veil cloth layers	129
Figure 8.1: Compression After Impact along with damaged FML sample	130
Figure 8.2: Acceptable failure modes as per ASTM standard	131

Figure 8.3: Compression After Impact (CAI) load-displacement curves for CARALL-A cured with polyester cloth layers impacted at different impact energies	133
Figure 8.4: Compression After Impact (CAI) load-displacement curves for CARALL-A cured without using polyester cloth layers impacted at different impact energies	133
Figure 8.5: Residual strength versus impact energy for CARALL-A FMLs	134
Figure 8.6: Compression After Impact (CAI) load-displacement curves for CARALL-B cured with polyester cloth layers	135
Figure 8.7: Compression After Impact (CAI) load-displacement curves for CARALL-A cured without using polyester cloth layers	135
Figure 8.8: Residual strength versus impact energy for CARALL-B FMLs	136
Figure 8.9: Failure mode of CARALL-A specimens	137
Figure 8.10: Failure mode of CARALL-B specimens	138
Figure 8.11: CAI load-displacement curves for CARALL-A and CARALL-B cured with polyester cloth layers impacted at 14J and 31J impact energies	138
Figure 8.12: CAI load-displacement curves for CARALL-A and CARALL-B cured without using polyester cloth layers impacted at 14J and 31J impact energies	139
Figure 8.13: Residual strength versus impact energy for CARALL-A and CARALL-B FMLs cured with polyester surfacing veil cloth layers	140
Figure 8.14: Residual strength versus impact energy for CARALL-A and CARALL-B FMLs cured without polyester surfacing veil cloth layers	140
Figure 8.15: Delaminated area versus residual strength of CARALL specimens cured with polyester surfacing cloth layers	143
Figure 8.16: Delaminated area versus residual strength of CARALL specimens cured without using polyester surfacing cloth layers	141
Figure 8.17: CAI test setup adopted in numerical simulation	144
Figure 8.18: Numerical Predictions of CAI test load displacement curves of CARALL-A cured with polyester cloth layers	145
Figure 8.19: Numerical Predictions of CAI test load displacement curves of CARALL-A cured without polyester cloth layers	146

Figure 8.20: Comparison between residual strength experimental results and FEA predictions for CARALL-A FMLs	146
Figure 8.21: Numerical failure mode predictions of CARALL-A specimens	147
Figure 8.22: FEA predictions for delamination in CARALL-A specimens under compressive loading	148
Figure 8.23: Numerical Predictions of CAI test load displacement curves of CARALL-B cured with polyester cloth layers	148
Figure 8.24: Numerical Predictions of CAI test load displacement curves of CARALL-B cured without using polyester cloth layers	149
Figure 8.25: Comparison between residual strength experimental results and FEA predictions for CARALL-B FMLs	150
Figure 8.26: Numerical failure mode predictions of CARALL-B specimens	151
Figure 8.27: FEA predictions for delamination in CARALL-B specimens under compressive loading	151

CHAPTER 1 INTRODUCTION

1.1 Fiber Metal Laminate Composite

Fiber-reinforced-matrix laminated composite could be adhesively bonded with metal layers to form a structural material. The story of the development of Fiber Metal Laminates can be traced back to Delft University, Netherlands around 1980 [1, 2]. Fiber Metal Laminates (FML) are ultra-lightweight structural materials developed with the combination of alternating thin, high strength metallic sheets and fiber reinforced adhesive layers as seen in figure 1.1. As FMLs are made with thin aluminum sheets, they have same mechanical, forming and machining properties as that of aluminum alloys but with reduced density.

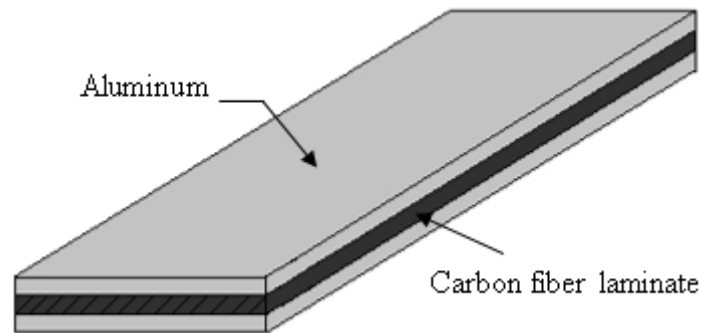


Figure 1.1: Fiber metal laminate schematic (Typical layer thickness, AL=0.5 mm, CFC=0.2 mm)

Besides, Fiber metal laminates have superior fatigue characteristics as compared to fiber reinforced composites. This hindrance to fatigue crack propagation is due to crack bridging effect of inner fiber layers that provide inherent resistance to crack propagation. FMLs are not susceptible to large internal damage when subjected to impact loading, unlike traditional composite materials. Individual FMLs configurations also possess better corrosion resistance and fire resistance properties as compared to metallic and composite materials. Hybrid FMLs systems can be created by utilizing different materials with many diverse combinations. Figure 1.2 gives the classification of various fiber metal laminates based on metal plies.

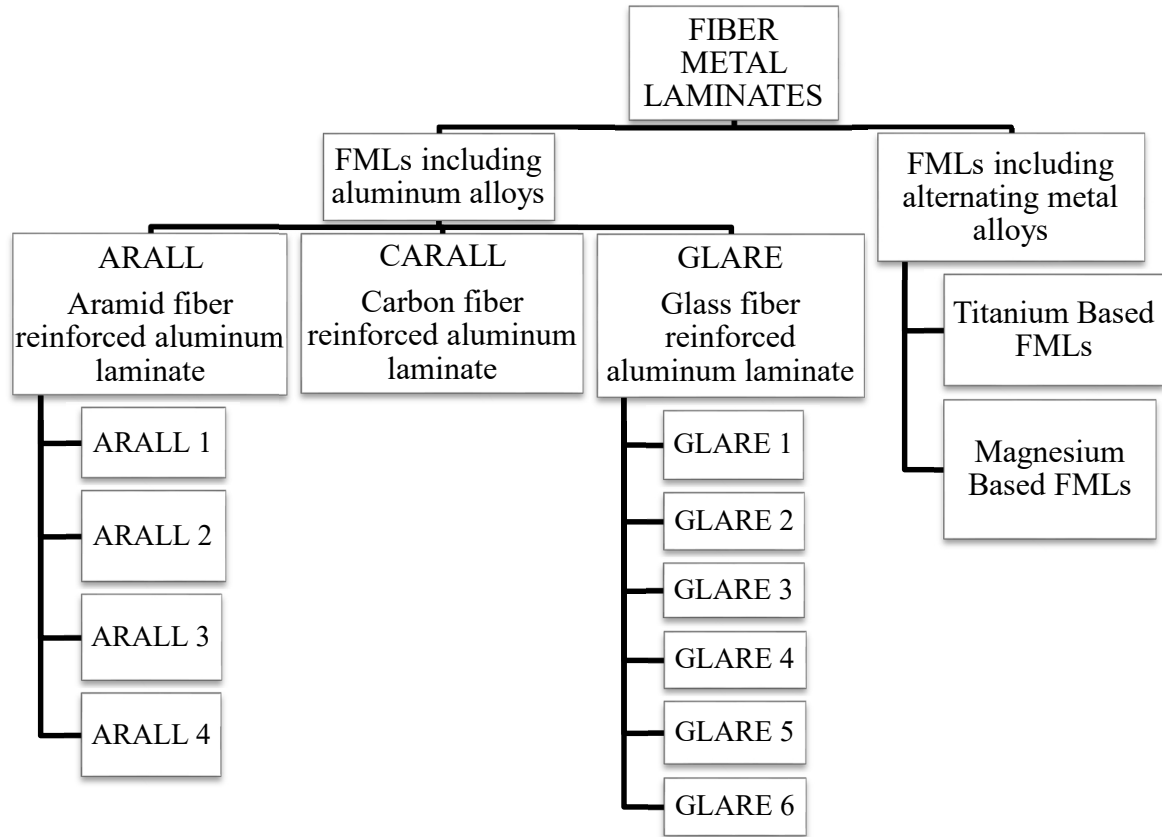


Figure 1.2: Classification of fiber metal laminates [3]

Given below is the brief discussion of different types of fiber metal laminates.

1.1.1 Aramid Fiber Reinforced Aluminum Laminates (ARALL)

L.B. Vogelsang [4] and colleagues in 1978 at Delft University made the first advancement in fiber metal laminate technology by developing first fiber metal laminate called ARALL. It was a structural material suitable for aerospace applications because of high strength, fatigue insensitive and low weight characteristics. Figure 1.3 schematically illustrates ARALL laminate with alternating thin aluminum alloy layers and uniaxial or biaxial aramid fiber prepreg.

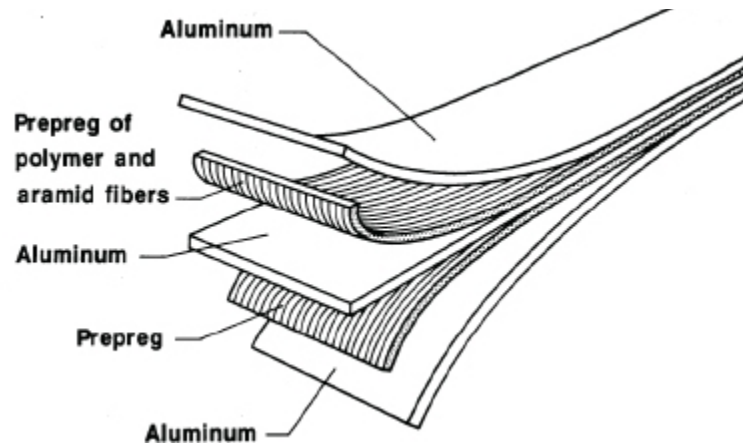


Figure 1.3: Schematic representation of ARALL fiber metal laminate.[5]

ARALL laminates are developed with the utilization of high strength aramid fibers encapsulated in a structural epoxy adhesive intervened between many layers of thin aluminum alloy sheets. ARALL has built in characteristic of high strength-to-weight ratio because of its constituents materials. As a result, the major effort of ARALL was to provide optimal damage tolerance by retarding fatigue crack growth[6]. Figure 1.4 shows the crack bridging mechanism of ARALL laminates.

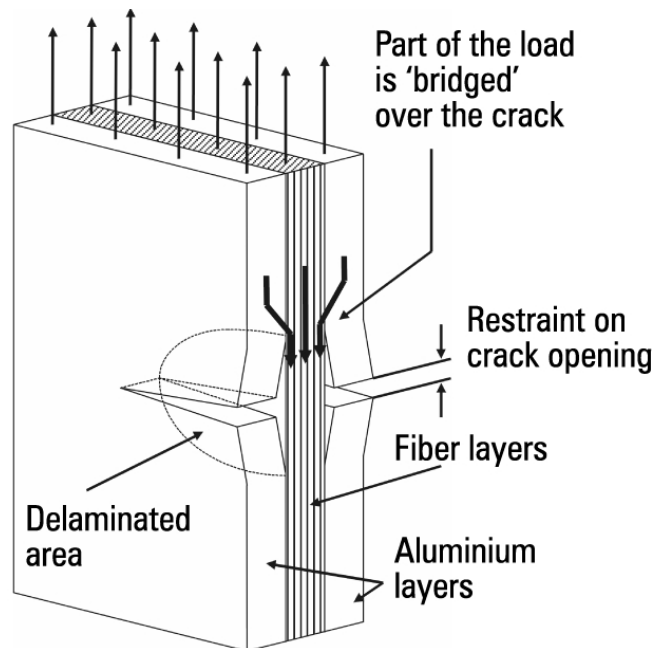


Figure 1.4: Crack bridging mechanism of ARALL laminates [7]

By using various types of aluminum alloys, four different types of ARALL were produced. With the acceptance of two international patents in the year 1984, Alcoa Company started a pilot production of four different types of standardized ARALL materials as sufficient confidence in this material had been gained [8]. A list of commercially produced ARALL laminates is given in Table 1.1. ARALL was originally selected by US Air Force to be used as a material for the highly fatigue rear cargo door of the C-17 cargo aircraft to reduce overall weight.

Table 1.1: Commercially available ARALL FMLs [9]

	Metal type	Metal thickness (mm)	Fiber layer (mm)	Fiber Direction (°)	Characteristics
ARALL 1	7075-T6	0.3	0.22	0/0	Fatigue, strength
ARALL 2	2024-T3	0.3	0.22	0/0	Fatigue, formability
ARALL 3	7475-T76	0.3	0.22	0/0	Fatigue, strength, exfoliation
ARALL 4	2024-T8	0.3	0.22	0/0	Fatigue, elevated temperature

1.1.2 Glass Fiber Reinforced Aluminum Laminates (GLARE)

GLARE, the next generation of fiber metal laminates was initially developed at Delft university for aeronautical applications with an aim to improve the ARALL fiber metal laminates by using advanced glass fibers in 1990. Later in 1991, a large-scale manufacturer of fibers and chemicals known as AKZO in partnership with Aluminum Company of America (ALCOA) and Delft produced four types of commercial GLARE FMLs using advanced glass fibers instead of aramid fibers. There is better adhesion between the glass fibers in GLARE as compared to ARALL fiber metal laminates. A schematic representation of GLARE fiber metal laminate having 3/2 configuration is shown in Figure 1.5.

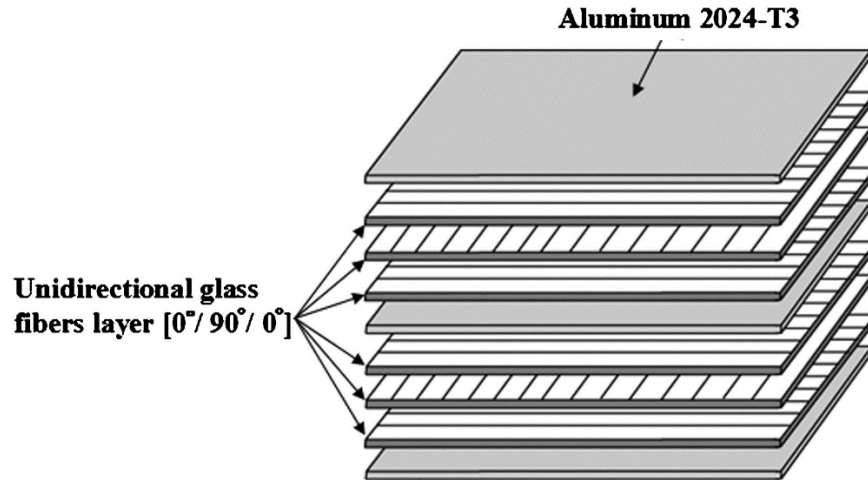


Figure 1.5: Schematic illustration of GLARE laminate.[10]

GLARE has much more loading flexibility than ARALL because of enhanced compressive properties of glass fibers over aramid fibers. Due to which glass fiber failure in GLARE under fatigue loading occurs very rarely. Glare has higher tensile and compressive strength, better impact behavior, and higher residual strength as compared to ARALL fiber metal laminates. Crossply fibers build up is possible in GLARE laminates due to better adhesion between the glass fiber and resin. As a result, GLARE laminates are much more suitable for biaxial stress conditions. These properties seem to make GLARE has a wider range of potential applications.[8] GLARE laminates now-a-days are produced in six different standard grades as shown in Table 1.2. Unidirectional S2 glass fibers embedded in the epoxy adhesive are used in all six standard grades of GLARE materials. GLARE material prepregs are commercialized with a nominal fiber volume fraction of 60 % in all six standard classes. Currently, GLARE is being utilized in the main fuselage skin and the leading edges of the horizontal and vertical tail planes of Airbus A380 aircraft.[3]

Table 1.2: Commercially available GLARE grades.[3]

GRADE	SUB	Metal Type	Metal Thickness (mm)	Fiber Layer (mm)	Fiber Direction (°)	Characteristics	
GLARE	1	-	7475-T761	0.3-0.4	0.266	0/0	Fatigue, strength, yield stress
	2	GLARE 2A	2024-T3	0.2-0.5	0.266	0/0	Fatigue, strength
		GLARE 2B	2024-T3	0.2-0.5	0.266	90/90	Fatigue, strength
	3	-	2024-T3	0.2-0.5	0.266	0/90	Fatigue, impact
	4	GLARE 4A	2024-T3	0.2-0.5	0.266	0/90/0	Fatigue, strength in 0 direction
		GLARE 4B	2024-T3	0.2-0.5	0.266	90/0/90	Fatigue, strength in 90 direction
	5	-	2024-T3	0.2-0.5	0.266	0/90/90/0	Impact
	6	GLARE 6A	2024-T3	0.2-0.5	0.266	+45/-45	Shear, off-axis properties
		GLARE 6B	2024-T3	0.2-0.5	0.266	-45/+45	Shear, off-axis properties

1.1.3 Carbon Fiber Reinforced Aluminum Laminates (CARALL)

The poor compressive strength of ARALL laminates led to the development of carbon reinforced aluminum laminates to improve this limitation. Carbon fiber/epoxy prepregs layers are utilized in CARALL Laminates instead of aramid/epoxy prepregs. Carbon fiber/epoxy composites have higher specific modulus but lower specific strength, failure strain and impact resistance as compared to aramid fiber/epoxy composites. Under the fatigue loading, aramid fiber composites showed better low cycle fatigue performance but worse high cycle fatigue performance as compared to carbon fiber composites. The crack bridging effect is very efficient in CARALL laminates due to the high stiffness of carbon fibers. As a result, of which there are very low crack growth rates in these laminates. The production process of CARALL laminates is similar to ARALL and GLARE laminates. Surfaces of aluminum sheets are chemically

pretreated for good adhesion between aluminum alloys and carbon fiber/epoxy layers before the curing process. After, the lamination process, the whole laminated system is cured under temperature and pressurized conditions in an autoclave. Figure 1.6 provides a representation of carbon reinforced aluminum laminate.

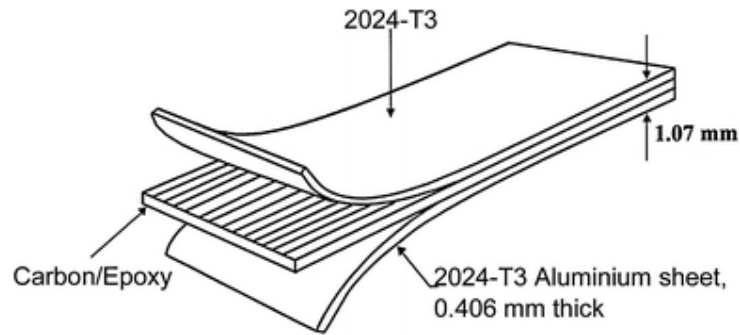


Figure 1.6: Schematic illustration of a 2/1 CARALL laminate.[11]

CARALL laminates are most suitable for space applications because of their high stiffness and good impact properties. Other requests for this laminate is impact-absorbers for helicopter struts and aircraft seats.[12] Now-a-days woven carbon fiber/epoxy prepregs are becoming more dominant over the unidirectional prepreg layers in CARALL laminates due to their bi-directional balance properties in fabric plane.[13] Different carbon fiber weave patterns used in CARALL laminates are shown in figure 1.7.

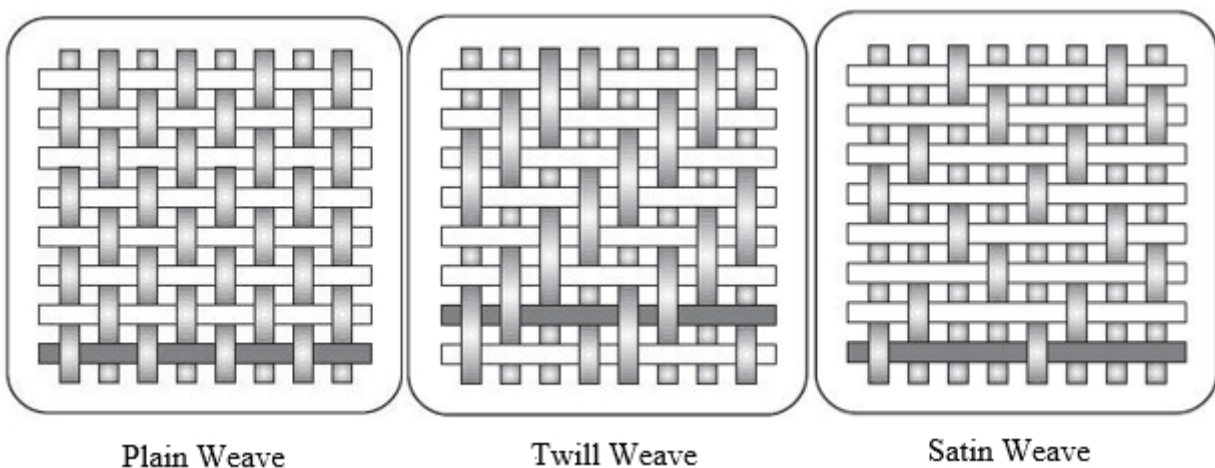


Figure 1.7: Different woven fibers weave patterns.[14]

1.2 Fiber Metal Laminates (FMLs) Processing

Fibrous prepreg layers used in fiber metal laminates are manufactured with the help of prepreg machines. Hot melt process and the solvent dip process are the commonly used methods to produce composite preregs. Hot melt process can be utilized by produce both fabric and unidirectional preregs whereas solvent dip method applies to manufacture only fabric preregs. There are two stages of the hot metal process. A thin film of the heated resin is coated on a paper substrate in the first stage. In the second stage, the resin is impregnated into the fiber resulting in the final prepreg on the application of pressure and heat in the prepreg machine, which is ultimately wound on a core. The solvent dip method involves dissolving the resin in a solvent bath and immersing the reinforcing fabric in the resin solution. The solvent is then separated from the prepreg using a drying oven. An illustration of typical solvent based prepreg manufacturing process is shown in Fig 1.8.

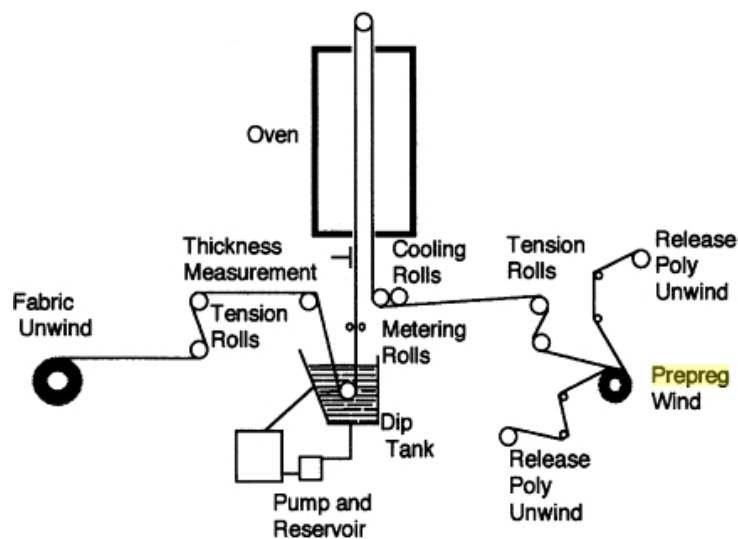


Figure 1.8: Schematic of typical solvent prepregging process.[15]

Metal sheets are cut into shape, stretched and tempered to improve their crystal arrangement during the fiber metal laminates manufacturing process. Later, the metal surfaces are

pretreated with etching agents to enhance the adhesion to the prepreg before bonding lay-up. Next step in fiber metal laminates manufacturing is assembling parts before bonding. During layering process, the metal parts and fiber layers are stacked on top of each other with the proper adhesive film between them. The major difficulty in practice is getting the desired level of precision in a sufficiently clean environment. Therefore, hand lay-up or automated layup through automatic tape layer machines can be used depending upon production volume. Jigs are used to place the parts to be bonded in the right position in hand lay method. Different layers are positioned correctly with the help of pins. Lasers are used for layering relatively large flat surfaces. Good shapes and positions are projected by laser on material in green light. Adhesive during lay-up is just a film from which foil has to be removed before layup. An automatic tape lay-up machine being used to place fiber reinforced adhesive layer over metal sheet is shown in Figure 1.9.



Figure 1.9: Automated tape layer machine [16]

Fiber metal laminates can be developed through several manufacturing techniques like vacuum assisted resin transfer molding (VARTM), autoclave molding, bond assisted single step assembly, etc. In autoclave molding, after positioning the neatly layered parts into the vacuum

chamber, pressure and temperature are applied. The temperature and pressure are applied to prepared parts for a significant amount of time depending upon the time required for resin cross-linking. The cured parts are then cooled down by reducing the temperature gradually to room temperature. An autoclave machine used for curing large fiber metal laminates panel is shown in figure 1.10.



Figure 1.10: Large autoclave for curing completely assembled A380 Glare panels[17]

1.3 Applications

Fiber metal laminated composites are mainly used in the aerospace industry specifically due to their increased stiffness and strength in comparison to aluminum. ARALL was originally selected by US Air force to be used as a material for the highly fatigued rear cargo door of the C-17 cargo aircraft to reduce overall weight [18] shown in Figure 1.11. ARALL 3 fiber metal laminates were used to build wing panels by Fokker for F-27 aircraft to achieve 25 % weight reduction as compared to aluminum material [19]. ARALL fiber metal laminates find its usage in secondary structures, mainly impact susceptible areas as lower flap skins (C-130, DHC DASH-

8), etc. in early test applications. ARALL fiber metal laminates are used to manufacture dorsal covers of United States Air force's T38 military aircraft [20].

A special variant of ARALL was used as armor plating in the year 1986. This ARALL type consists of ceramic tiles on the outside to break up a bullet that would hit the material while the ARALL backing layer would absorb the remaining kinetic energy and would stop the bullet in this way. The tubes made of ARALL fiber metal laminates can be used in applications for chemical and nuclear industry because they remain leak proof even if damaged [19]. Fokker also used ARALL as material to develop crack stoppers for early F-100 aircraft. ARALL was also used as material to manufacture missile load platform by Sandia in a US government military project.



Figure 1.11: First ARALL cargo door installed on the C-17, February 27, 1991.[21]

GLARE laminates are not susceptible to the low-frequency fiber failure like ARALL which makes it well suited to fuselage applications. The application of GLARE panels in the upper fuselage of the Airbus A380 commercial aircraft as shown in figure 1.13 represents the first use of FMLs within a large scale commercial aircraft and is an indication of the future

applications of GLARE within modern airplanes [22]. GLARE FMLs are used for various structural applications including a full-scale rear pressure bulkhead and fuselage barrel tests by several aircraft manufacturer like Cessna, Bombardier Aerospace, and Deutsche Aerospace. GLARE was used for the maintenance of the corroded aluminum stiffeners in the cargo bay area of an airplane used to transport seafood by replacing them with the GLARE stiffeners, see Fig 1.12. The prepreg layer works as the corrosion barrier, and the corrosion of the stiffeners stopped after the outer aluminum layer was corroded.

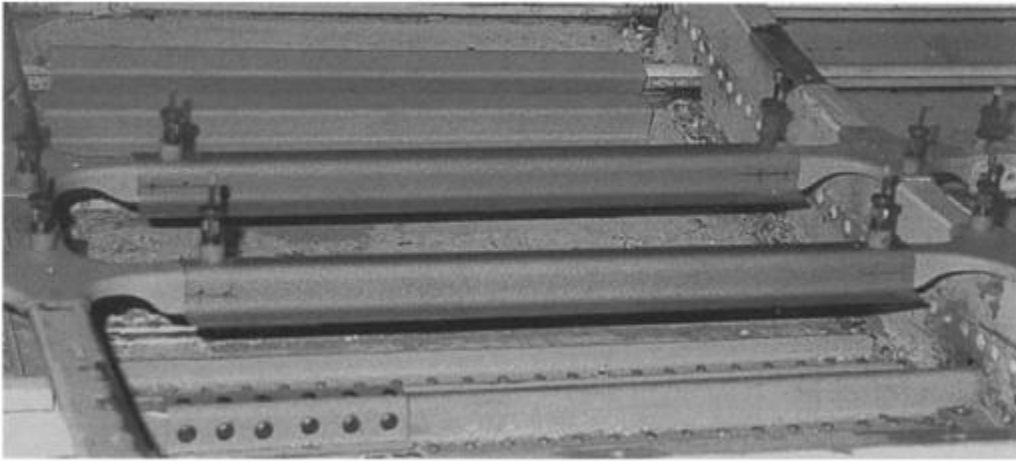


Figure 1.12: GLARE stiffeners in cargo bay area in F28.[19]

GLARE is used in the production of forward radar bulkhead for the Learjet LEAR 45 business aircraft because of its combination of high stiffness and excellent bird-strike impact resistance. GLARE laminates also find their application in the production of A330/A340 cockpit crown, explosion hardened Id3 containers, aircraft electronics cabinets and bulk cargo bay floors on Boeing 777 jet liners. The area of aircraft which is most susceptible to impacts is Bulk cargo floors. GLARE laminates are used as a floor material because of their superior impact resistance for Airbus's A320/A321, A330/A340 families of aircraft as well as on MD-11 retrofits. The ideal areas for application of fiber metal laminates on aircraft are summarized in Figure 1.14.

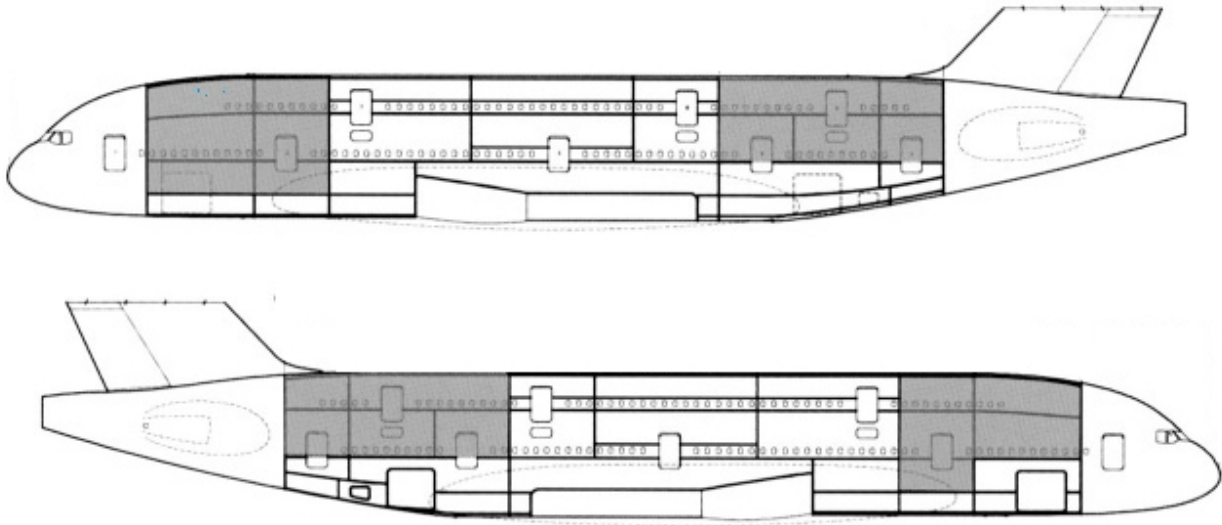


Figure 1.13: The application of GLARE as the upper fuselage panel for A380 [21]

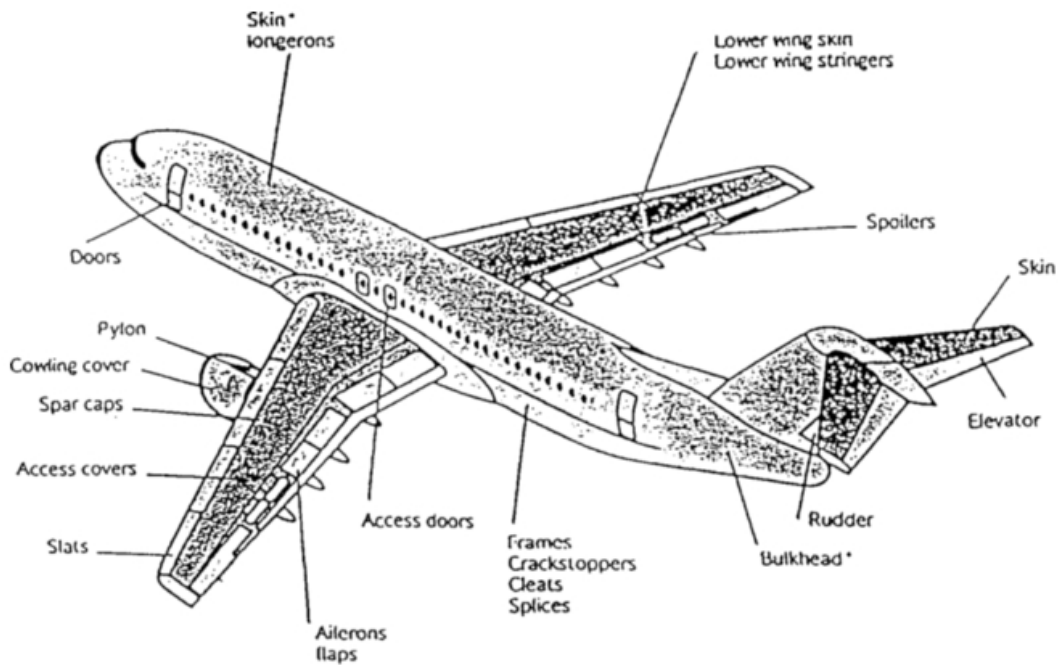


Figure 1.14: Candidate areas for aerospace ARALL and GLARE [23]

1.4 Low-Velocity Impact and Compression After Impact Tests

Impact incidents are the most important source of damage to fiber reinforced composites laminates. Impact event can be expected to occur such as tool drop on the fiber metal laminate structure. Impact event can result in significantly different damage patterns for a given composite

configuration due to the magnitude of the velocity of the foreign object. A good example of high-velocity impact even is ballistic penetration. The elastic and plastic deformations of metallic material dissipates the impact energy and still the structure keeps a good margin of structural integrity. The damage is usually more severe in reality than that seen on the surface of the fiber reinforced composite materials. Some of the typical damage cases for fiber reinforced composite structures are shown in Figure 1.15.

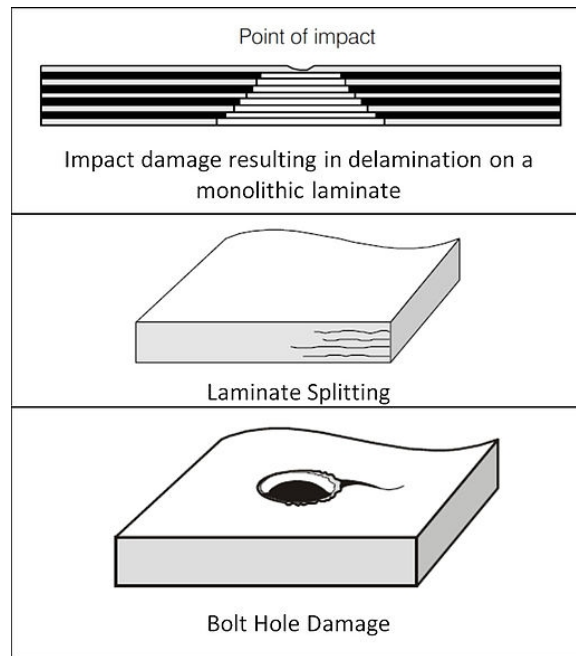


Figure 1.15: Typical damage cases of composite laminates structures [24]

The damaged caused by the low-velocity impact event can extend to a much greater extent than the barely visible evidence on the surface of fiber metal laminates due to which the strength of the material may significantly reduce and finally the material may lead to failure without any warning. Therefore, it is very crucial to conduct a test for the measurement of the residual strength of the fiber metal laminate structure through post impact experimental testing. Low-velocity impact tests utilizing a manual drop tower were used to evaluate the impact response of fiber metal laminate composite specimens. The carbon fiber reinforced aluminum

laminated samples were impacted at the center with different energy levels. The residual strength of specimens was evaluated by performing compression after impact (CAI) test with MTS machine. The impact event damage size was characterized by utilizing C-scan equipment as well as destructive techniques. A finite element analysis per LS-DYNA was utilized to predict detailed, and accurate stress distribution results of the fiber metal laminate composite under dynamic loading.

1.5 Rationale

Research work on flexural & tensile properties of carbon fiber reinforced aluminum fiber metal laminates composites are done by several researchers such as Sherman Dov et al. (1995), Lin C.T. et al. (1994), Lawcock G. et al. (1997), Xia Y. et al. (2007) & Rajkumar G. et al. (2014). The work was primarily focused on the experimental determination of the properties of these fiber metal laminates. C.T Lin investigated the thermal residual strains in various carbon fiber reinforced aluminum laminates (CARALL) by using the deflection of an asymmetric laminate and the yield point shift of the aluminum alloy in the laminate as experimental methods and classical lamination theory as a tool to perform the theoretical calculation of residual strains. Lawcock G. et al. studied the effect of adhesion between aluminum sheets and fiber composite prepreg on the tensile and interlaminar shear strength properties of carbon-fiber-reinforced metal laminates by using two different aluminum surface treatments. Xia Y. et al. investigated the effect of strain rate on the carbon fiber reinforced aluminum laminates. The prediction of the thermal residual stress and progressive damage failure of carbon fiber reinforced aluminum laminates through finite element analysis is not found in the literature. The cost, curing process are vital factors along with weight savings and high strength for the application in automotive industry. Fewer steps, easy preparation, and faster curing cycle are the main requirements of

curing process in the automotive industry. The work on carbon fiber reinforced aluminum laminate by using no acid etching, or anodization treatment of aluminum layers and no external adhesive is not studied in literature with a focus on the automotive industry.

The impact response of glass fiber reinforced aluminum laminates have been studied by the majority of researchers. However, only few research articles have been found in literature studying the impact response of CARALL fiber metal laminates. Song S.H. et al. (2010) studied the impact performance of CARALL laminates with the drop weight impact tests and dynamic non-linear transient simulations. Bienias J. et al. (2012) investigated the resistance to low-velocity impact of aluminum alloys and a carbon/ epoxy composite laminates. Yu, G.C., et al. (2015) Studied the effect of the properties of aluminum alloy on the low-velocity impact response of CARALL. The effect of the addition of resin rich polyester veil cloth between the interfaces of carbon fiber/epoxy and aluminum layers is not studied in these research articles. The main reason for using such layers is to provide a buffer layer between AL and CFC layer to ensure no corrosion effect. In the previous numerical simulations performed in these articles, the initialization of predicted thermal residual stress is taken into consideration as considered in my numerical simulation. As a result, of which I was able to accurately capture the failure modes of CARALL laminates under tensile, flexure and low-velocity impact tests. Modeling each lamina of carbon fiber layers with shell elements having two through-thickness integration points makes a notable difference in the modeling approach followed in this research and numerical impact simulations performed in previous literature articles.

CHAPTER 2 LITERATURE REVIEW AND OBJECTIVES

2.1 Glass Fiber Reinforced Aluminum Laminates (GLARE)

2.1.1 Static, Thermal Residual Stress Behavior and Modeling of GLARE

Abouhamzeh M. et al.[25]conducted a research study to predict the cure process related shape deviations as a result of residual thermal stresses in fiber metal laminates using finite element modeling and experiments. They reported that acceptable agreement between FE model and experiment was found in predicting the geometric shape of cured GLARE panels. They found an out of plane deformation of approximately 11 mm using digital image correlation in non-symmetric GLARE laminates and approximately 18 mm in symmetric glare laminates using linear variable differential transformer curvature measurement method.

Guo Yajun et al. [26] measured the residual stresses in glass fiber reinforced aluminum laminates (GLARE) using several experimental testing methods. They measured 16 MPa residual thermal stress in aluminum layers and -12 MPa in glass fiber layers of GLARE panels having 2/1 layup configuration with X-ray diffraction method. Residual stresses in aluminum layers were measured as 44 MPa and -116 MPa in fibrous layers of GLARE panels using the etching technique. Per Hofslagare [27] made a comparison between X-ray diffraction, neutron diffraction and strain measurement throughout destructive layer removal residual thermal stress measurement methods on fatigue-damaged glass fiber reinforced metal laminates, particularly in for a fatigue-induced metal crack in the laminate. They found a good agreement between different methods. Per Hofslagare et al. [28] studied the effect of thermal residual stresses and bonding strength on delamination crack growth behavior of glass fiber reinforced aluminum laminates (GLARE). They performed optical crack growth measurements for surface cracks

combined with in situ ultrasonic measurements to determine the delamination size and shape to improve the understanding of the mechanisms of crack growth in GLARE fiber metal laminates.

Kawai et al. [29] studied the off-axis inelastic behavior and strength of GLARE 2 under static loading conditions by applying the classical lamination plate theory. Three methods; (i) no-ply fracture method, (ii) complete-ply fracture method and (iii) incomplete ply fracture method was adopted by the author to investigate the influence of degradation methods on modeling of the GFRP failure. The no ply fracture method predicted higher tangent moduli and strengths than experimental results after yielding of aluminum layers in the stress-strain diagrams drawn till the ultimate failure of the laminate. Overestimated stiffness reduction and less strength were reported by the complete-ply fracture method. The stiffness in fiber direction was retained by the incomplete-ply fracture method after GFRP layers have satisfied the Tsai–Hill criterion gives acceptable agreement when compared with experimental results.

Cepeda-Jiménez C.M et al. [30] studied the damage tolerance of glass fiber reinforced composite by flexural and shear tests. They reported that GLARE laminate shows a maximum bending stress of 689 MPa whereas the Al 2024 alloy presents a high bending strength 750 MPa but the ductility is limited as compared to glare in flexure test. Khalili et al. [31] investigated the mechanical properties of steel/aluminum/GFRP laminate. Their results indicated that energy absorption, stiffness, and displacement were significantly increased due to the presence of steel layers in FML sample with respect to other FML samples. They reported that an increase of 16 times was observed in the stiffness of the composite with steel layers for some configurations in bending and an increase of nearly 4 times as compared to the corresponding GFRP sample was found in the displacement under the point of loading

Park S. Y et al. [32] studied the effect of surface pre-treatment and void content on the interfacial characteristics of GLARE laminate. They reported that bonding strength of GLARE laminates was effectively enhanced by the changes in surface roughness and surface energy. An indication of interfacial bonding enhancement to a certain extent with the low void content of GLARE FML by autoclave pressure is given by their Experimental results. Soltani P. et al. [33] studied the nonlinear elastic behavior of GLARE Fiber Metal Laminates under in-plane loading conditions by using finite element modeling approach to predict the stress–strain response and deformation behavior of GLARE laminates. They have reported an acceptable agreement between the FE model stress–strain predictions and experimental results available in the literature. They also investigated the tensile properties of different grades of GLARE having 3/2 layup with aluminum alloy 2024-T3 as metal layers subjected to same axial tensile load and found considerable differences in the slope of the second part of bilinear stress–strain curves of different GLARE grades because of various orientations of the fibers in prepreg layers.

Hagenbeek M. et al. [34] studied the static properties of fiber metal laminates. An effective analytical method for calculation of uniaxial stress-strain curves valid for all types of GLARE laminates is proposed. Metal Volume Fraction approach in combination with the Norris failure model is used to predict allowable blunt notch strength. Shear yield strength of fiber metal laminates is predicted by using the volume fraction approach. Predicted results of these models were compared with the experimental results available in literature and a good agreement between those was found by them. Asha M.V. [35] studied three types of FMLs such as 2/1 GLARE, 3/2 GLARE, and 5/4 GLARE laminates to determine the tensile, flexural properties and failure mode of the GLARE laminates and plain aluminum sheets with the same thickness. The authors reported that tensile and flexural strength of glass-fiber-reinforced aluminum (GLARE)

laminates is purely dependent on the volume percentage of fiber, and it exhibits improvement over the properties of aluminum sheets.

Baumert B. K. [36] studied mechanical characteristics of glass fiber reinforced epoxy and 2024-T3 aluminum alloy fiber metal laminates made by the vacuum assisted resin transfer molding process. They have reported the tensile and fatigue test results of these FMLs having two different thicknesses, with and without holes in the aluminum alloy sheets and compared to mechanical property predictions as well as to GLARE 3 data. Wu et al. [37] evaluated nonlinear tensile response and fracture behavior of FMLs, GLARE 4 and GLARE 5 subjected to in-plane loading through analytical modeling and numerical simulation. The fracture is expected to happen in glass/epoxy layer when the strain in it reaches the ultimate failure strain, as aluminum has a much higher ductility than the fiber/epoxy composite layer and it is predicted by using maximum strain failure criterion in this study. Both a numerical simulation based on finite element modeling and modified classical lamination theory based an analytical constitutive model, which incorporate the elastoplastic behavior of the aluminum alloy described by the flow theory of von-Misses type are used to predict the stress-strain response and deformation behavior of GLARE laminates. They have also discussed the Fracture modes of these laminates. At high-stress levels, the analytical model predictions deviate from experimental results. The author opined that further studies are necessary to predict the progressive failure. The author also opined that damage progression and degradation should be focused on the future models

Iaccarino et al. [38] developed a simplified model to predict the tensile and shear stress – strain behavior of fiberglass/ aluminum laminates. Experimental tests were carried out to find the tensile stress-tensile strain curve of an aluminum/fiberglass hybrid laminate, consisting of 0/90 S2 glass/epoxy lamina and Al 2024 T3 sheets. The laminate response was predicted theoretically

by using modified Classical Lamination Theory, which accounts for the inelastic behavior of the aluminum through a simple constitutive law. Maximum strain criterion and Tsai-Hill criterion are used as failure criteria for aluminum and fiberglass respectively. Experimental results are compared with theoretical predictions. Complex failure mechanisms leading to final failure were cited as main reason for the deviations between predictions and experimental results. For accurate predictions of the final failure strength and to model the damage development, the requirement of more sophisticated models than proposed in this work is highlighted by the author.

Sadeghi M. et al. [39] investigated the tensile, bending and impact properties of GLARE material and the effect of fiber orientation on them. Their test results show that zero orientation of glass fiber sheet in laminate considerably improves the mechanical properties. Esfandiar H. et al. [40] studied analytically the nonlinear tensile behavior of GLARE fiber metal laminates under in-plane loading. The modified classical laminated plate and orthotropic plasticity theories were used to predict the stress-strain response of GLARE laminates. They have reported that the GLARE behavior is almost bilinear under tensile loading and in the longitudinal direction the tensile strength of unidirectional GLARE laminates are substantially stronger than aluminum alloys.

M. Abouhamzeh [41] presented Classical Lamination Theory (CLT) and an additional term depending on the cure shrinkage based analytical model to predict the warpage and residual stresses developed during curing of Fiber Metal Laminates (FMLs) for both free and constrained (molded) cure of composite laminates. They found that the residual stresses developed in the fiber layers are considerable but the ones in the aluminum layer are much less. The curvature and the deflection of the panel after cure, before cool-down, is smaller compared to the ones

developed during cool-down. M. Abouhamzeh [42] investigated the influence of cure-induced effects on the geometry of non-symmetric GLARE panels. The distortions and residual stresses were obtained by reheating the un-symmetric laminate combined with strain measurement until the thermal forces are balanced in the layers. He observed that FMLs have considerable residual stresses which represent some curvature after completion of cure and before cool-down (if released from the mold). The curvature vanishes during cool-down and then changes direction. Thermoelastic model based on CLT showed that considering the real bending-strain-free temperature (as a way of considering the curing effects) improves the results compared to the experimental values. Botelho, Edson Cocchieri, et al. [43] compared the tensile, compressive, shear strength, damping behavior of CARALL, GLARE fiber metal laminates with those to carbon and glass fiber reinforced laminates. The environmental effect on the fiber metal laminates was also studied in this investigation. They reported that, even under the relatively harsh conditions, the moisture absorption in FML composites is slower than polymer composites due to the barrier of the aluminum outer layers.

2.1.2 Impact Behavior and Impact Event Modeling of GLARE Fiber Metal Laminates

Caprino G. et al. [44] studied the low-velocity impact performance of fiberglass–aluminum composites made of 2024 T3 sheets and S2-glass/epoxy prepreg layers. The speed and mass of impactor along with energy were varied to study the effect of these parameters on the material behavior. They reported that the overall force–displacement curve only depends on the impact energy, rather than on the mass and speed separately. Penetration energy for monolithic aluminum is higher than for the fiberglass–aluminum. Their results show that glare seems to offer better performance in terms of penetration energy and damage resistance than carbon fiber

and glass fiber-reinforced laminates. They also reported that the energy required for the first failure is very low and is similar to the energy inducing first cracking in the 2024 T3 sheets.

Ardakani M.A. et al. [45] investigated the influence of interfacial adhesive bonding on impact behavior of several glass-fiber reinforced aluminum (GLARE) laminates with various level of bonding adhesion. They reported that laminates with poor interfacial adhesion have greater damage size as compared to that of laminates with robust adhesion between aluminum and glass layers. They also reported that laminates with strong bonding have 30% lower maximum central deflections than that of FMLs with poor adhesion. Contact forces of FMLs with good adhesion bonding are about 25% higher than specimens having a weak bonding. Liu Y.X. et al. [46] studied the impact damage performance of different types of GLARE fiber-metal laminates using indenters with various shapes and sizes. The test results showed that GLARE 3 FML's with cross-ply orientation offer higher impact resistance than unidirectional GLARE 2. They also reported that more severe local damages occurred with smaller indenters whereas larger global deflection appeared when larger size indenters were used. The energy dissipated mainly through delamination and cracks in fiber-metal laminates impacted by smaller size indenters whereas more energy may be absorbed due to large global deformation for laminates impacted by larger size indenters.

Ardakani M.A. et al. [47] investigated the impact resistance and damage characteristics of GLARE4/3, GLARE3/2 and GLAREWB3/2 laminates under low-velocity impact loading with different energies. They have reported that layout sequence and interfacial adhesive bonding have a significant effect on the impact behavior of GLARE laminates. They also investigated the influence of repeated impacts on the response of laminates. Experimental test results showed that the impact behavior of GLARE laminates is very dependent on their

thickness. A damaged area in thin GLARE 3/2 was 3 to 5 times larger than thick GLARE 4/3. GLARE laminate's impact resistance is more sensitive to its thickness in repeated impact loading. Liu Y.X. et al. [48] investigated the low-velocity impact responses and damage of GLARE and ARALL fiber-metal laminates. They reported that major failure mechanisms that are mostly seen in low-velocity impact event include delamination between the aluminum and fiber-epoxy layers, visible shear crack in the outer aluminum layer on the non-impact face, Through-thickness cracks in the aluminum sheets and critical damage in the fibrous layers including delamination between adjacent fiber-epoxy laminae. They also reported that the ARALL offered poorer impact resistance than GLARE. GLARE laminates with of cross-ply orientation provided better impact resistance than GLARE with unidirectional plies.

Rajkumar G.R et al. [49] experimentally investigated the effect of repeated low-velocity impacts on the tensile strength of glass fiber-reinforced aluminum fiber metal laminates using drop weight impact tester. Their test results indicated that ultimate tensile strength, failure strain, and ductility of all specimens initially decrease with an increase in a number of impacts and then remain constant. Tsartsaris N. et al. [50] studied the low-velocity impact response of a fiber metal laminate (FML) panels consisting of aluminum alloy 7475 T761 and unidirectional S2 glass/epoxy oriented in a cross-ply configuration through testing and finite element simulations. The tests showed that FML laminates absorb the impact energy through localized plastic deformation and through failure at the interface between the layers. Numerical simulations of low-velocity impact performed with the LS-DYNA3D finite element code to predict the complex damage patterns and post impact deformed shapes showed fairly close agreement with experimental results.

Seo H. et al. [10] studied the impact response of FML with finite element modeling. Two and three-dimensional failure criteria in ABAQUS are used to model stiffness degradation of the glass-fiber-reinforced composite layers and the load time history, maximum deflection, and damage progression was examined using an explicit finite element model. The FE simulation results showed good agreement with experimental results. Jeremy F. Laliberté et al. [51] investigated the low-velocity impact behavior of GLARE fiber metal laminates to study the damage modes and mechanisms through which the panels absorb the energy of impact. They reported that the primary damage modes change and the relative amount of absorbed energy also change with the increase the level of impact energy. Having more fibers in one direction leads to a more predictable and gradual onset of panel penetration

Jeremy F. Laliberté et al. [52] developed a continuum damage mechanics based material model using a user-defined material subroutine to predict the impact response GLARE panels. He reported that the model with the tiebreak-interface delamination model showed some sensitivity to the mesh density giving over-prediction of the delamination damage for lower mesh densities and under- prediction of the dent depth. Guocai Wu et al. [53] investigated the impact properties and damage tolerance of glass fiber reinforced aluminum laminates with cross-ply glass prepreg layers. They showed that both GLARE 4 and GLARE 5 laminates have better impact properties than those of 2024-T3 monolithic aluminum alloy.

Taheri-Behrooz, F. et al. [54] studied the effect of stacking sequence on the impact behavior of fiberglass–aluminum fiber metal laminates under the drop weight impact test. They reported that $[Al-(\pm 45)_8-Al]$ layups has higher load-bearing capacity before failure of the outer aluminum layer than the specimens having $[Al-(0/90)_8-Al]$, $[Al-(0/90)_4-(\pm 45)_4-Al]$ and $[Al-(\pm 45)_4-(0/90)_4-Al]$ layups. Patryk Jakubczak et al. [55] investigated the influence of low-velocity

impact on the residual strength of GLARE fiber metal laminates by carrying out compression after impact (CAI) tests as per ASTM norms. He found out that the critical stress and damage of specimen occur in the areas located far from the impact damage during sample compression in the case of fiber metal laminates. He also reported that occurrence of damage during compression test does not depend on the presence of the impact damage, which makes it impossible to assess strength reduction caused by compression of thin fiber metal laminated panels after impact.

Starikov, Roman [56] conducted series of low-velocity impact tests on standard GLARE which is based on thin Al 2024-T3 & FM94 composite prepreg and HSS (High static strength) GLARE which consists of thin Al 7475-T761 and FM906 prepreg. He found that HSS GLARE laminates were more resistant to denting than the standard GLARE specimens based on the measured dent depth versus applied impact energy test results. He also reported that more energy was absorbed by composite fracture related mechanisms including delamination in HSS GLARE because less applied impact energy was dissipated by plastic deformation of the 7475-T761 aluminum layers. Furthermore, the measured delamination was larger in the case of HSS GLARE. G. Caprino et al. [57] conducted the low-velocity impact tests on glass fiber/aluminum laminates consisting of 2024 T3 sheets and S2-glass/epoxy prepreg layers using an instrumented drop weight machine by keeping the mass of impactor constant and varying the energy by adjusting the drop height. They found out that the material response was unaffected by the actual speed adopted and the resulting load–displacement curves were highly non-linear, with the stiffness of specimen rapidly increasing with increasing the displacement. They developed an analytical model based on simple second-order polynomials and additional hypotheses supported by the results generated, to represent the load variation as a function of displacement during both

the loading and the rebound phase. They also reported that the fundamental impact features, such as the overall force–time curve, dissipated energy, and contact duration, were effectively calculated from the model.

F.D. Morinière [58] developed an analytical quasi-static method to evaluate the flexural behavior of GLARE during low-velocity impact by combining the impact variables in a single platform based on the First-order Shear Deformation Theory (FSDT), the Classical Laminate Theory (CLT), the law of conservation of energy, and the Newton’s laws of motion. They reported that the model predicted with a precision of 5% contact time, impact force, maximum displacement, perforation energy, and impact velocity in comparison to test results and provides information on the role of 2024-T3 aluminum and S2-glass/FM94-epoxy prepreg, with respect to energy absorption, plate bending, and damage propagation.

2.2 Aramid Fiber Reinforced Aluminum Laminates (ARALL)

2.2.1 Static, Thermal Residual Stress Behavior and Modeling of ARALL

Bala Singh et al. [59] measured the residual stress in aluminum alloy sheets in ARALL fiber metal laminates formed by using alternate layers of aluminum alloy sheets and unidirectional aramid fibers-epoxy composite both by x-ray diffraction and layer removal methods. They found that the residual stress in the longitudinal direction in AL-alloy sheet are tensile and vary between 33 Mpa and 18 MPa. The stresses vary between 23 to 2 MPa in the transverse direction and are compressive in nature. Wu et al. [60] made statistical analysis, stress analysis and failure characteristics analysis of two types of tension specimens (ARALL). The effect of specimen geometries on mechanical properties was studied by considering straight sided and dog bone specimens. It was concluded that the tensile properties are not dependent on specimen type. Both experimental and analytical studies results are compared.

Hai Yan et al. [61] studied the failure behavior of ARALL (Aramid Aluminum Laminate) under tensile loading using of acoustic emission (AE), optical metallography (OM) and scanning electronic micro- scope (SEM), and analyzes the fracture surfaces of ARALL and its fracture characteristics. The damage models of ARALL are discussed in this paper. The results showed that under tensile loading, ARALL will yield and its strength will decrease with the increase in the content of resin. During fracture process, AE amplitude distribution curves showed three obvious peaks corresponding to the debonding between fibers and resin, regional delamination damage and breakage of a some fibers, and delamination damage of large region and final fracture of large numbers of fibers.

WU H.F. [62] studied the effect of elevated and cryogenic temperatures on the Aramid fiber metal laminates subjected to tensile loading at temperatures ranging from -300°F - 400°F and at room temperature exposure. Their results showed that no reduction in ultimate tensile strengths, tensile yield strengths and moduli obtained for the longitudinal or transverse directions of ARALL 1–4 laminates at cryogenic temperatures. However, these properties showed a tendency to decrease with increasing temperature when determined at the elevated temperatures after 1, 10 and 100 h of exposure. Chen, J.L et al. [63] modeled the elastic-plastic behavior of an ARALL laminate by a macro-mechanical orthotropic plasticity theory and by classical laminated plate theory. A three-parameter plastic potential function is used in the orthotropic plasticity model. The aluminum layers were assumed to orthotropic elastic-plastic and the Kevlar composite layers are assumed to be linearly elastic in the laminated plate theory They found that the orthotropic plasticity model gives accurate results of total strain with 1·2% error and stress-strain curves up to a failure can be described with the laminated plate theory.

Kanakalatha P. [64] characterized the aluminum alloy sheet aramid fiber metal laminates using two different aluminum alloys DTD 687 and aluminum- lithium alloy. The results of tensile, compressive and interlaminar shear strength tests showed that these laminates have a higher tensile strength, lower density, and slightly lower young's modulus as compared with monolithic aluminum alloy sheets.

2.2.2 Impact Behavior and Impact Event Modeling of ARALL Fiber Metal Laminates

C.T Sun et al. [65] studies the low-velocity impact characteristics of ARALL fiber metal laminates to find the failure modes due to impact. Their results show that the strength reduction in ARALL laminates resulting from impact depends on the fiber orientation. Transverse direction strength remains insensitive to impact damage, while the fiber direction strength, decreases as impact velocity increases beyond a certain range. Volt A. [66] investigated the Low-velocity impact response of monolithic aluminum alloys, ARALL laminates, and thermoplastic composites. The results of this research show that the damage resistance of aramid ARALL is comparable with that of the composite materials but it is poor as compared to aluminum alloys. They also reported that the residual strength after impact damage of ARALL is also similar to that of the thermoplastic composites.

Vlot A. [67] conducted the impact tests on the monolithic aluminum and ARALL specimens under tensile loading. He reported that the effect of initial tensile loading on the damage size and the residual strength of the ARALL is small for the normal operating stresses ($\sigma < 200\text{MPa}$). William P. Hoogsteden, [68] studied the impact and compression after impact behavior of ARALL fiber metal laminates. He reported that compressive buckling was the mode of failure during the compression after impact test of ARALL laminate due to a very small thickness of laminates. He also found that the increasing the impact energy decreased the

buckling load of the specimens and no growth of the interior damage was revealed by C-scan done after compression after impact testing. B.M. Liaw et al. [69] studied the impact-induced damage mechanisms in Glare and ARALL fiber-metal laminates subject to drop-weight impacts at various energies and temperatures. They found out that quasi-isotropic lay-up configuration provides the best impact resistance whereas unidirectional laminate offers the worst and the minimum impact energy required to cause cracking is approximately proportional parabolically to thickness. They also observed that temperature does play a significant role in impact resistance, unlike aluminum/acrylic sandwich.

Vlot [70] studied the low & high-velocity impact tests and static indentation behavior of monolithic AL 2024-T3, 7075-T6, various grades of GLARE & ARALL fiber metal laminates, and R-glass fiber & T 800H carbon fiber reinforced composite laminate specimens with a circular clamped test area. He reported that the aramid and carbon reinforced fiber metal laminates require little energy to create the first fiber failure in the material. GLARE FMLs have first cracking energies which are close to or even better than the monolithic alloys. He also observed that the damaged zone after impact is for fiber metal laminates is smaller than for fiber reinforced composite materials having permanent dent depth is approximately equal to the monolithic alloy.

2.3 Carbon Fiber Reinforced Aluminum Laminates (CARALL)

2.3.1 Static, Thermal Residual Stress Behavior and Modeling of CARALL FMLs

Sherman Dov et al. [71] studied the mechanical behavior of a laminate consisting of monolithic thin alumina plates alternating with unidirectional carbon/epoxy prepreg tapes. Multiple fracture mechanisms led the FML to exhibit pseudo-ductile behavior and enhanced strain energy dissipation. A minimal volume fraction of the reinforcing layers is required to

exhibit this behavior. They also investigated the influence of a number of layers and volume fraction on transverse properties. A simple shear lag theory was used to estimate the loss of stiffness with increase in the applied strain.

Lin C.T. et al. [72] investigated the thermal residual strains in various carbon fiber reinforced aluminum laminates (CARALL) by both experimental methods and theoretical analysis. They used the deflection of an asymmetric laminate and the yield point shift of the aluminum alloy in the CARALL laminate as experimental methods to measure thermal strains. Classical lamination theory was used to perform the theoretical calculation of residual strains. A good agreement was observed in residual strains determined by each experimental method and by theoretical calculation. The thermal residual stress in the aluminum layer was found to be roughly proportional to the volume fraction of the carbon/epoxy layer for CARALL laminate reinforced with unidirectional carbon fibers.

Lawcock G et al. [73] studied the effect of adhesion between aluminum sheets and fiber/epoxy layers on the mechanical properties of carbon-fiber-reinforced metal laminates by using two different ways of aluminum surface treatments methods. They used standard P2-Etch and modified FPL-Etch procedures as surface treatment methods with the application of a silane coupling agent. Double cantilever beam experiment conducted by author showed a six times increase in interfacial fracture toughness by using the latter surface treatment method. 10 % reduction in interlaminar shear strength was observed for a laminate with poor interfacial adhesion (P2-Etch method) in flexural tests. They found no clear difference in the tensile properties of laminates associated with both surface treatment methods.

The effect of adhesion between fiber and matrix on the residual strength behavior of carbon-fiber-reinforced metal laminates was studied by using treated and untreated carbon fibers

in an epoxy resin system by Lawcock G et al. [74]. Interfacial failure was observed the untreated fiber composites while matrix failure was showed by the treated fiber composites. A reduction of 7.5% was observed in the interlaminar shear strength value for the untreated fiber laminates by both three-point and five point bend tests. An excellent increase in strength for the untreated fiber specimens over the treated ones was found in residual strength and blunt notch tests.

Y.B. Hu et al. [75] studied the flexural and interlaminar shear strength (ILSS) of carbon fiber reinforced titanium laminates. He found out that micro-roughness structures were formed on the titanium surface after anodization which improved the interlaminar bond strength between titanium and polyimide. He also reported that these FMLs possess excellent flexural and interlaminar properties at both room temperature and elevated temperature and found no delamination between the titanium layer and the fiber-reinforced polyimide layer after 1000 times thermal shock through thermostability tests. E.C. Botelho et al. [76] evaluated and compared the adhesion of different families of fiber-epoxy composite/metal laminates using carbon fiber and glass fiber fabrics as reinforcements for the hybrid laminates. They reported that chromic acid anodization (CAA) resulted in better wetting properties. They found out that, for both carbon fiber-epoxy/metal and glass fiber-epoxy metal laminates, the interlaminar shear strength results were close to the interlaminar shear strength results found in the literature (approx. 40.0 MPa)

Junqing Zhao et al. [77] used ultrasonic C-scan and A-scan approach to evaluate the damage of the asymmetric CFRP-Al (carbon fiber reinforced aluminum alloy) laminates. They reported on the basis of comparison results and pulse echo analysis that when the specimen is subjected to repeat tensile test with 70% elastic limit strain load of the CFRP laminates, the interface separation between CFRP and Al will not occur but the delamination within CFRP

laminates becomes the major damage of the asymmetric CFRP-Al laminates. E.C. Botelho et al. [78] studied the influence of moisture on shear properties of carbon fiber/epoxy composites and CARALL by using interlaminar shear (ILSS) and Iosipescu tests. They observed that hygrothermal conditioning degraded the Iosipescu shear strength of CF/E and CARALL composites due to the higher moisture absorption in these materials. They have reported a decrease in the shear results by nearly 12 and 6%, respectively.

G.R. Rajkumar et al. [79] studied the effect of strain rate and layup configuration on the tensile and flexural behavior of GLARE and CARALL FMLs having 3/2 stacking sequence. They observed that tensile strength increased with increasing the strain rate while flexural strength decreased with increasing the strain rate. They also reported that carbon fiber based FMLs have maximum tensile and flexural strength whereas glass fiber based FMLs showed minimum strengths and hybrid structure strengths lies between them. Jung Goo Kim et al. [80] studied the tensile behaviors of CARALL FMLs with different stacking sequences for carbon fiber/epoxy layers at strain rates between 0.001/s and 100/s and compared the properties of these FMLs to the results of aluminum and carbon fiber reinforced polymer composites tested under the same conditions. They reported that tensile strength of the AL alloy specimen was decreased by 5% as the strain rate increased. However the tensile strength and the failure strain increased as the strain rate increased for the CARALL FMLs, and the increase in tensile strength varied depending on the stacking sequence of the CFRP layer.

2.3.2 Impact Behavior and Impact Event Modeling of CARALL Fiber Metal Laminates

Bieniaś J. et al. [81] investigated the resistance to low velocity impact of aluminum alloys and a carbon/epoxy composite laminates. Their results show that the ply orientation in unidirectional carbon/epoxy and aluminum laminates has particular importance for their impact

resistance. They have reported that the fiber metal laminate system with 0/90 and (± 45) ply sequences in the carbon fiber reinforced composite have the best behavior followed by the (0) configuration.

Song S.H. et al. [82] studied the impact performance of CARALL laminates with the drop weight impact tests and dynamic non-linear transient simulations. The experimental results of this study verify that the specimen impacted by 2.35 J shows no critical damage but there were significant fiber and matrix failures in CFRP layers and a shear crack on the aluminum surface of specimen impacted by 9.40 J. The similar tendency was observed with the numerical analysis also. They reported that the specimen impacted by 2.35 J absorbed 64% and specimen impacted by 9.40 J absorbed 83% of the impact energy. Lawcock G. [83] investigated the effect of fiber/matrix adhesion on the impact properties of carbon fiber reinforced metal laminates. Their results show that the laminates with the weaker fiber/matrix adhesion associated with the untreated carbon fibers exhibit larger damage zones and in slightly higher energies for the first failure, although the rear face crack length and ultimate indentation after impact are smaller for a given impact energy. They also reported that the laminates with untreated fibers have the higher residual tensile strength after impact due to increased fiber/matrix splitting in the composite layer. Kim H.S. [84] studied the low-velocity impact damage characteristics of aluminum/composite hybrid drive shaft whose composite layer was placed interior to the aluminum layer of the shaft. They have reported that when the thickness of the aluminum tube was larger than the 3 mm, the damaged area of the composite layer decreased significantly. Their results also showed that when the glass fabric composite was employed as an insulating layer, the damaged mode changes from the delamination failure between the aluminum tube and the

glass fabric composite to the delamination failure between the plies of the carbon epoxy composite layer.

Yu, Guo-Cai, et al. [85] investigated the low-velocity impact behavior of the carbon fiber aluminum laminates (CARALL) to study the effect of the properties of aluminum alloy on the low-velocity impact response of CARALL. He performed numerical simulation using user-defined materials subroutine (VUMAT) with Hashin's 3D damage constitutive model. He reported that impact resistance property of CARALL is better than Glare due to the enormous strength and stiffness of carbon fiber reinforced composite (CFRP). He also showed that the impact resistance of CARALL is improved by increasing the yield strength of the aluminum alloy. G.R. Rajkumar et al. [86] investigated the repeated low-velocity impact behavior of glass fiber reinforced aluminum laminates and carbon fiber reinforced aluminum laminates at the same location using drop weight tester. They observed that monolithic aluminum plates, GLARE, and CARALL FMLs show different behavior for load carrying capacity and damage behavior. The maximum load carrying capacity is higher in the case of monolithic aluminum due to the superior energy-absorbing behavior of Al alloy. The damage is localized only at impact area in the case of GLARE and CARALL FMLs, hence lower energy-absorbing capacity. They also reported that GLARE offer a better energy absorption than CARALL due to carbon-based FML allows the progression of cracks within the laminate.

Bienias Jaroslaw [87] conducted a comparative study on the low-velocity impact resistance of aluminum/carbon and glass fiber metal laminates investigating the influence of fiber orientations on the load-time response, damage size and damage depth in relation to various energy levels. They observed that carbon fiber laminates showed a higher tendency to a perforation in comparison to laminates containing glass fibers. They also reported that GLARE

FMLs absorbed energy mainly through plastic deformation as well as through delamination initiation and propagation, whereas CARALL fiber metal laminates absorb energy through penetration and perforation. J. Bieniaś et al. [88] investigated the impact behavior and damage mechanisms of carbon fiber reinforced aluminum hybrid laminates in comparison to classic carbon fiber reinforced polymer (CFRP) at low-velocity impact event. They reported that the absorbed impact energy is mainly connected with elastic response and damage of the laminate in the case of carbon fiber reinforced composites whereas in case of fiber metal laminates it is also associated with plastic deformation of the laminate, occurring especially in the metal layers. They also reported that delamination propagation and impactor penetration may be prevented by metallic aluminum layers due to high impact resistance of fiber metal laminates. The CARALL systems developed in some of the above mentioned research studies [81] had adhesive layer between metal and composite layers, whereas in others no information about the use of adhesive film was mentioned. So it was assumed that these FMLs are cured with the adhesive film layers as well.

2.4 Research Objectives

Carbon fiber reinforced aluminum laminates are developed primarily by using the adhesive films along with the etching or anodization of aluminum layers in the literature articles reviewed. Therefore, the processing of these laminate involves an additional step i.e acid treatment of aluminum layers impacting both cost and time. One of the objectives of this research work was to process the carbon fiber reinforced aluminum laminates without using any adhesive film and acid treatment of aluminum layers with the vision to investigate opportunities of using these light-weight fiber metal laminates made up of woven carbon fiber/epoxy sheets

and aluminum layers for automotive applications by making manufacturing process of FMLs faster and more cost effective.

It is considered that enough integrity can be maintained without the use of adhesives and acid etching or anodization of aluminum layers. There is a possibility of a galvanic cell formation leading to corrosion when carbon fiber/epoxy and aluminum are directly brought into contact in the presence of electrolytic media due to the high potential difference. To address this issue, in the second division of this research; the CARALL laminates were processed by inserting an epoxy resin rich polyester veil cloth in between the carbon fiber and aluminum layers. The major other objectives of this research work can be summarized as:

- Experimental characterization of damage mechanisms and behavior of these fiber metal laminates under tensile, flexural and impact loading
- Measurement of the residual strength of the fiber metal laminate structure through post impact experimental testing i.e. CAI test.
- Analytical prediction of thermal residual stresses developed during the curing of these fiber metal laminate under the effect of temperature and pressure through finite element analysis
- Investigation of the effect of resin rich layer (polyester veil cloth) on flexural, tensile, low-velocity impact & compression after impact characteristics of carbon fiber reinforced aluminum laminates.
- Numerical prediction of three-point flexural, tensile and low-velocity impact behavior of the CARALL FMLs using LS-DYNA finite element analysis.
- Calculation of weight savings with carbon reinforced fiber metal laminates in reference to monolithic aluminum of similar geometrical parameters.

CHAPTER 3 FIBER METAL LAMINATE MATERIALS & CONSTRUCTION

3.1 Material Description

Aluminum 5052-H32 material was used for the Aluminum layers in the fiber metal laminate configurations. As 5052-H32 aluminum has excellent finishing qualities, it is often referred to as "Anodize Quality Aluminum". In order to cause substantial lowering of the melting point without producing brittleness, magnesium is the major alloying element in 5052. A schematic illustration of aluminum 5052-H32 sheet is shown in Figure 3.1. 5052 series is far stronger than the 1100 or 3000 series aluminum and have good forming qualities. 5052-H32 has good resistance to corrosion, especially in salt water or marine atmospheres. Weldability is also very good for aluminum 5052 series. The chemical composition of aluminum 5052-H32 is given in Table 3.1. The mechanical properties of the 5052-H32 aluminum alloy are given in Table 3.2.

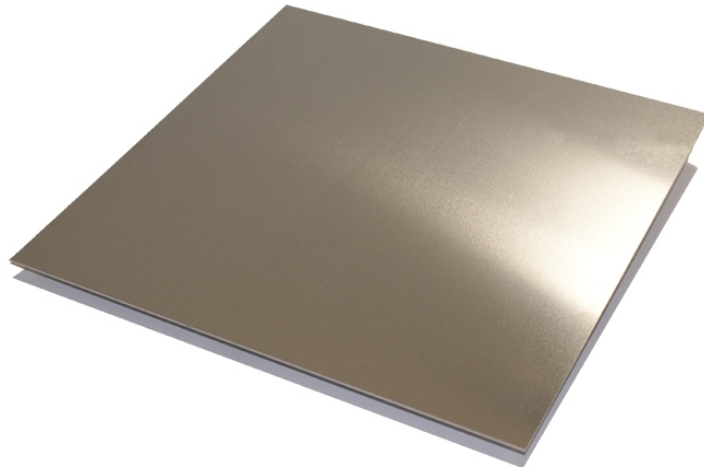


Figure 3.1: Aluminum 5052-H32 sheet used in making fiber metal laminates.[89]

Table 3.1: Chemical composition of aluminum 5052-H32 alloy [90]

Manganese (Mn) Max	Silicon (Si) Max	Chromium (Cr)	Copper (Cu) Max	Iron (Fe) Max	Zinc (Zn) Max	Magnesium (Mg)
0.1	0.25	0.15-0.35	0.1	0.4	0.1	2.2-2.8

Table 3.2: Mechanical properties of aluminum 5052-H32.

Properties	ρ (g/cc)	E (GPa)	UTS (Mpa)	σ_y (Mpa)	ϵ_{eff} plastic	ν	α , /°C	G (GPa)	Shear Strength (Mpa)
	2.68	70.3	228	150	0.09	0.33	25.7×10^{-6}	26.4	138

Woven carbon fiber/epoxy prepreg known as VTM264/CF302 manufactured by CYCTEC was used as a material for the fibrous layers in the fiber metal laminate construction. This prepreg system has 2 x 2 twill weave fabric style with 3K FT300B40B fibers. Twill weave fabric style is constructed with interlocking of reinforcement carbon tows upon themselves with over/under placement during the weaving process. Here the size of carbon tow is represented by 3K. Bundle of continuous carbon fibers having size generally 5-10 microns is known as carbon tow. A number of filaments in tow describes the size of the tow. Multiplication by 1000 is indicated by the letter K to the filament number. Therefore, 3000 carbon filaments are contained by 3K size carbon tow. 2 x 2 designation stands for that there are two tows per inch in each direction. Figure 3.2 describes the individual carbon tows in unidirectional and woven fabric prepreg systems.

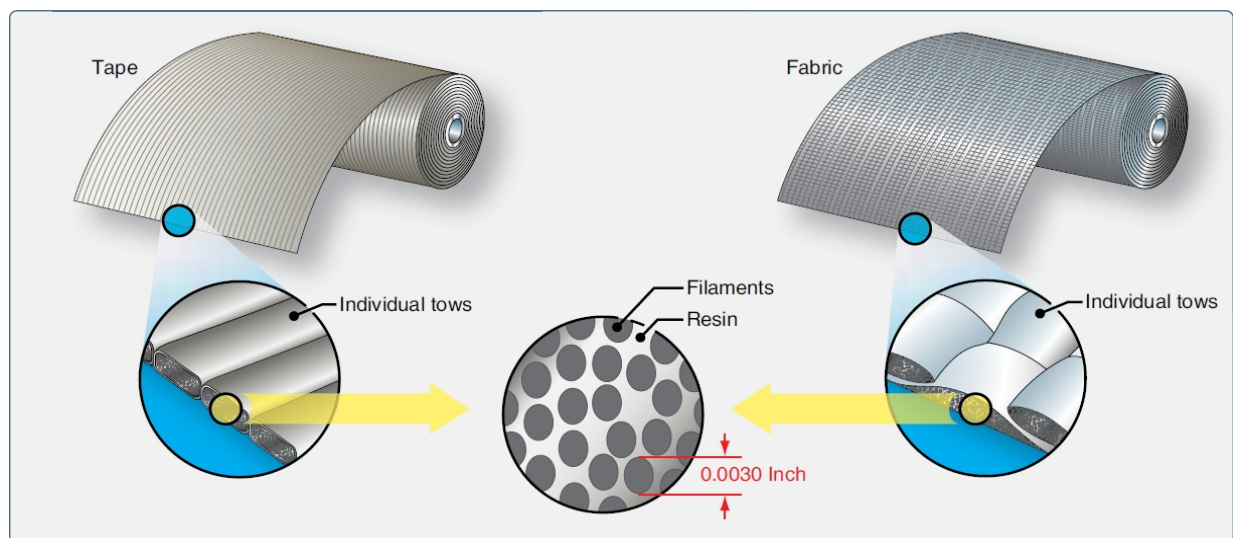


Figure 3.2: Individual carbon tows in unidirectional and fabric style prepreg systems [91]

Twill weave offers greater conformability and delivers a slightly more strength as compared to plain weave counterparts. It is highly desirable for modern composites parts in auto, marine and sporting goods industries because of its signature appearance. The schematic diagram of fibers with twill weave construction style is described in figure 1.7. The in-plane mechanical properties of the woven carbon fiber/epoxy prepreg are given in Table 3.3. A viewgraph of woven carbon fiber/epoxy prepreg before curing used in the FML manufacturing is shown in Figure 3.3.

Table 3.3: Twill weaves carbon fiber/epoxy properties

Material	ρ (kg/m ³)	E_{11} (GPa)	E_{22} (GPa)	ν_{21}	G_{12} (GPa)	G_{23} (GPa)	X_c	Y_c	X_t	Y_t	S_c	$\alpha \cdot 10^{-6}$, /°C
							(MPa)					
Carbon fiber	1600	60	60.5	0.05	3.90	2.30	540	560	700	745	95	2.8



Figure 3.3: Woven carbon fiber/epoxy prepreg before curing.

The synthetic surface veil used in this research is a non-woven fabric manufactured from Dacron®106 homopolymer and it is commercially known as Nexus®. It. This polyester fiber has an aperture design that provides the necessary flexibility for the fabrication. Nexus® polyester fiber surfacing fabrics are formed by a unique binder-free process of hydraulic fiber entanglement that results in a web with both vertical and horizontal fiber orientation. This ability to orient fiber vertically as well as horizontally improves the interlaminar bond strength of surface layers reinforced with Nexus. The relatively high fiber elongation of Nexus® fabrics makes them particularly compatible with corrosion resistant laminating resins. These fabrics can be applied to both interior and exterior surfaces of products offering excellent impact, corrosion, weather, and UV-resistance. The thickness of polyester surfacing veil cloth is approximately close to 8 mils. A viewgraph of polyester surfacing veil is shown in figure 3.4.

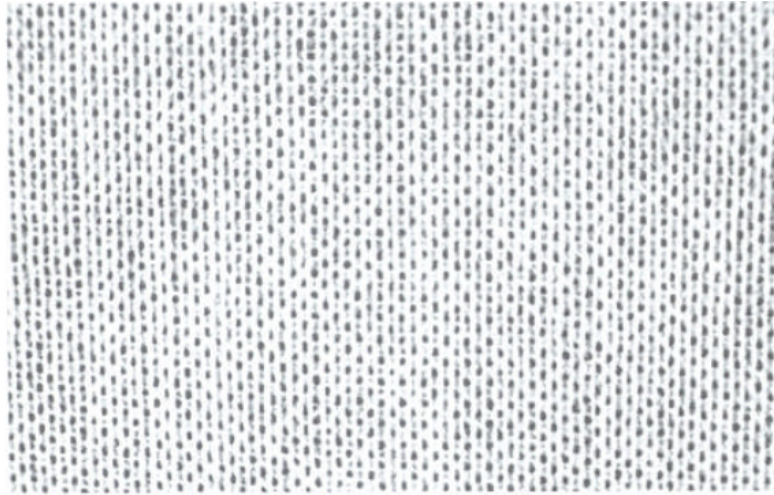


Figure 3.4: Polyester synthetic surface veil.

3.2 Fiber Metal Laminate Construction

Fiber metal laminates specimens were cured by using flat steel mold plates of 12" x 12". Release agent was applied to mold plates in order to facilitate the removal of specimens after curing. Grit paper was used to make the surface of aluminum sheet slightly rough so as to

increase the interlocking b/w the carbon fiber and aluminum layers. A schematic of mechanical interlocking produced by abrasion in cured laminate is shown in figure 3.5.

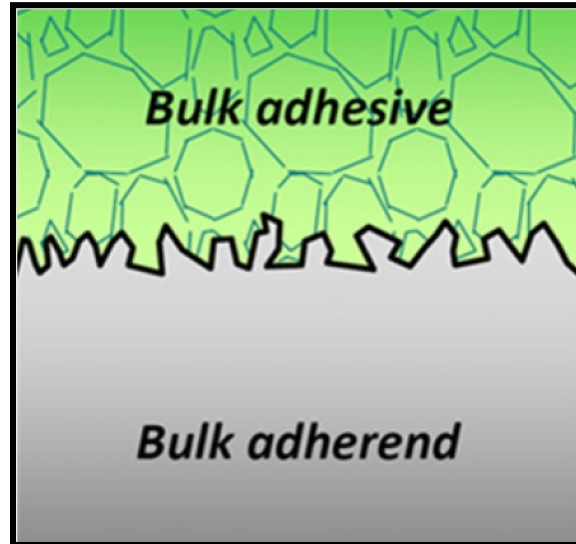


Figure 3.5: Mechanical interlocking induced due to crevices produced by abrasion. [32]

Aluminum sheets were not treated with any other surface pretreatment like phosphoric acid etching or chromic acid anodization etc. in order to make the laminate curing process fast as is desired in the automotive sector. The aluminum sheets were then cleaned with a solution of acetone in order to ensure that no grease or any other dirt remained on it. Later these sheets were cut into desired profile with the help of water jet cutting machine. Carbon fiber/epoxy prepreg layers were then cut accordingly with hand cutter. Prepreg plies were hand laid on the shaped aluminum sheets and no external adhesive was used at the carbon fiber/epoxy and aluminum interface. The uncured specimens were then placed between the mold plates which were prepared earlier by applying mold release agent. The whole system including mold plates and uncured specimens was placed in the vacuum press shown in figure 3.6 to cure the fiber metal laminate specimens. During the curing process, the layered prepreg and aluminum system was kept in vacuum and 0.35 MPa pressure was applied on the layered system at 135°C for 60 minutes. The carbon fiber/epoxy & aluminum layered system was then cooled by passing mist

and water over the platten for 15 minutes each. The completely cured laminate was removed from the mold plate after the completion of the curing cycle. The complete curing cycle used for making the fiber metal laminates in vacuum press is shown in figure 3.7. Cured FML specimens were cleaned with the help of Dremel tool to remove the extra resin that came outside the samples.

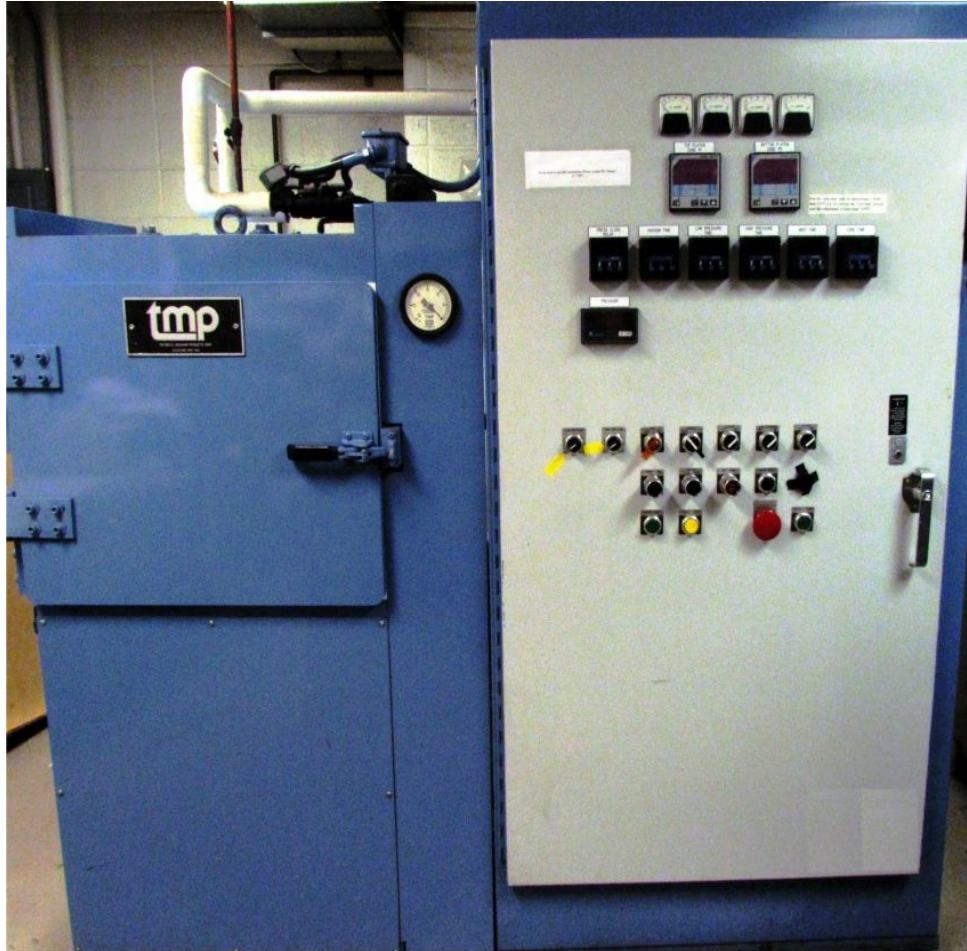


Figure 3.6: Autoclave vacuum press machine used for curing the laminates

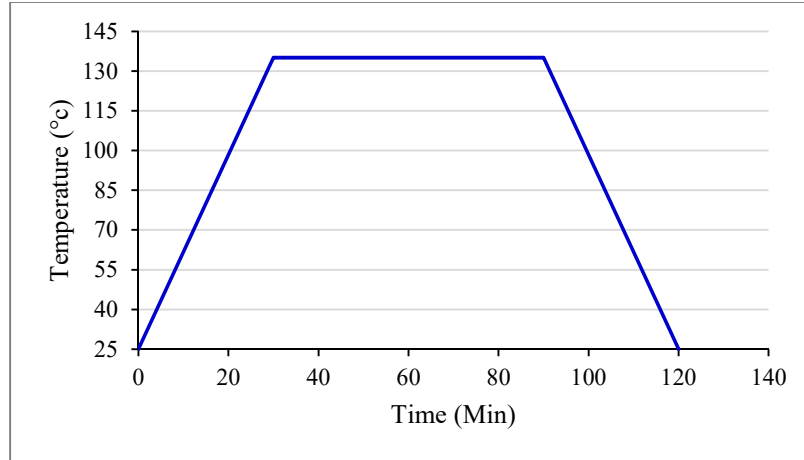


Figure 3.7: Vacuum press curing cycle at 0.35 MPa pressure.

3.3 Preliminary Tests

Several mechanical properties of fiber metal laminates constituents are needed for finite element analysis of these FMLs. Basic properties of carbon fiber/epoxy prepreg and aluminum were provided by the material suppliers. To model the interaction between aluminum and carbon fiber/epoxy layers accurately in finite element analysis, normal strength and shear strength of aluminum-carbon fiber/epoxy bond was required. Therefore, T-peel and double notch shear strength test was conducted to evaluate the shear strength of aluminum-carbon fiber/epoxy bond.

3.3.1 Double Notch Shear Strength Test

Double notch shear tests on carbon fiber/epoxy and aluminum symmetric hybrid samples were done as per ASTM D3846 [92] test method. Hybrid fiber metal laminate samples of 152.4 mm x 12.7mm containing 6 plies of woven carbon fiber/epoxy prepreg on each side of the aluminum sheet having 1mm thickness were cured for double notch shear tests. The groove was cut into the carbon fiber and aluminum layers and with the help of Dremel tool to define a joint zone of 12.5 mm. To avoid direct pressure on the laminate in the gripping area, Grit paper is used on the laminate. The schematic of hybrid FML test sample is shown in figure 3.8.

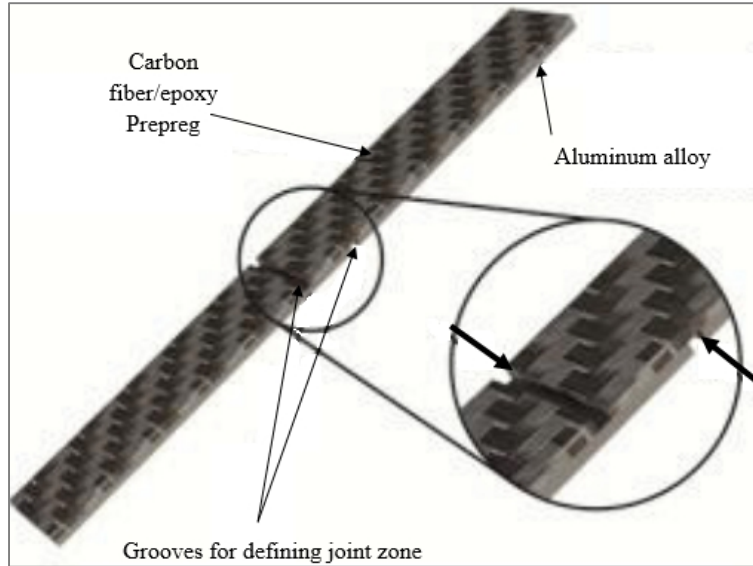


Figure 3.8: Schematic of double notch test specimen.[93]

Double notch shear tests were performed by using MTS machine at a strain rate of 0.5 mm/sec. The load carried by carbon fiber/aluminum bond length was converted to stress data by using force-stress relationship formula to get the shear strength of bond b/w carbon fiber and aluminum layers. Double notch test coupon secured in MTS testing machine and damaged test coupon is shown in figure 3.9. Force-displacement plots obtained from the double notch shear test are shown in figure 3.10. Shear strength calculations for the strength of the bond is shown in Table 3.4. This shear strength value obtained for carbon fiber/epoxy and aluminum bond is utilized as an input parameter for the numerical modeling in LS-DYNA.

Table 3.4: Aluminum-carbon fiber/epoxy bond shear strength results

S.no	Test Type	Load, P (N)	Shear Stress (MPa)
1	Double Notch Shear Test	4555.53	13.54
2		4061.63	13.45
3		4960.47	14.81
4		3187.34	13.60
		Average	13.85

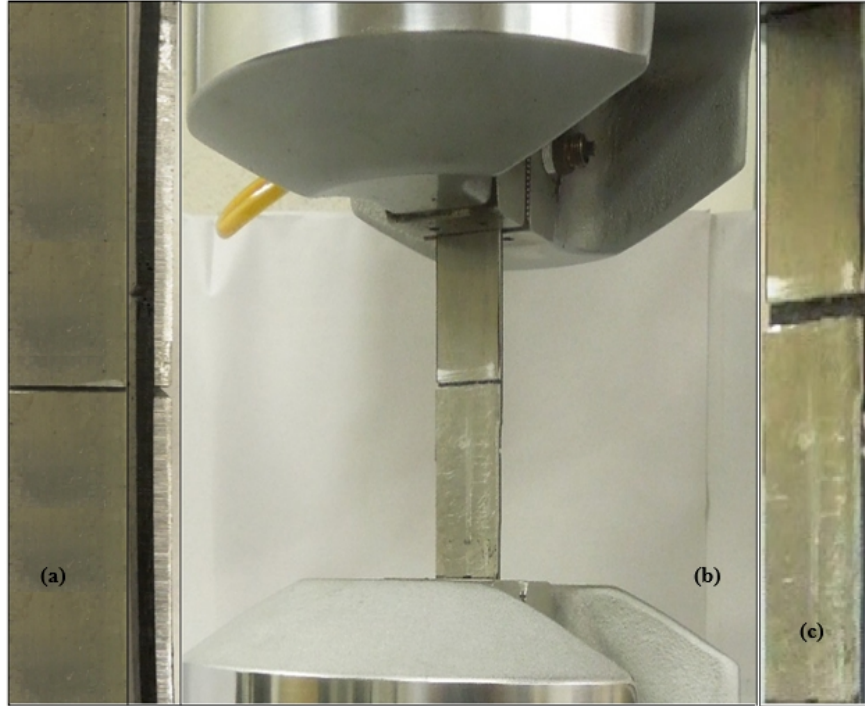


Figure 3.9: a) Double notch shear test coupon (b) coupon secured in MTS testing machine (c) damaged test coupon.

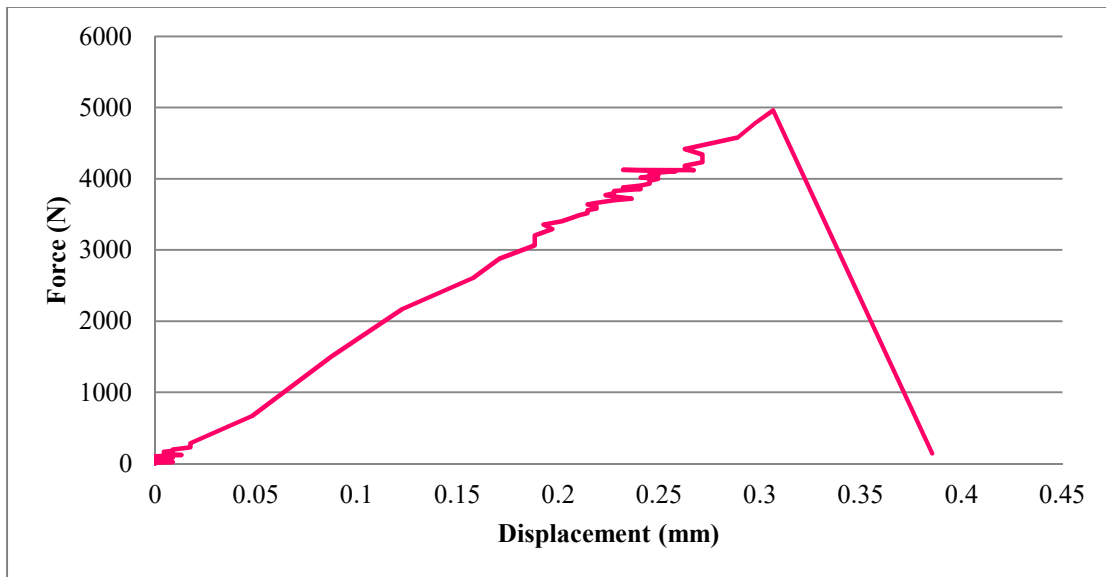


Figure 3.10: Typical force-displacement curve obtained from double notch shear test.

3.3.2 Static T-Peel Test

The peel resistance of carbon fiber/epoxy-aluminum bond was determined by conducting a T-peel test by referring ASTM D1876 [94] and ISO 11339 [95] standards. Relative peel resistance of adhesive joints manufactured from flexible metallic adherend (e.g. thin steel or aluminum alloy sheet) is most widely determined by the T-(or 180°) peel test. The adherend is said to be flexible if it bends through 90° without breaking or cracking. Peel resistance being defined as the average force per unit test specimen width, measured along the bond line that is required to separate progressively two adherend members of a bonded joint [95].

Hybrid FML specimens having 200 mm x 25.4mm geometrical dimensions containing 50.4 mm initial crack provided by placing Teflon sheet in between woven carbon fiber/epoxy prepreg and aluminum sheet each having 1 mm thickness were cured for T-peel tests. Prior to bonding, the surface roughness of aluminum adherend was increased with grit paper of size 60 and then degreased with acetone. The hinges were glued to specimens in the region having the initial crack with the help of the epoxy resin by keeping it at room temperature for curing by itself for 24 hrs. The purpose of using the hinges was to not fix the angle between the bond line and the direction of applied force during the test. The specimen schematic with dimensions is shown in Figure 3.11.

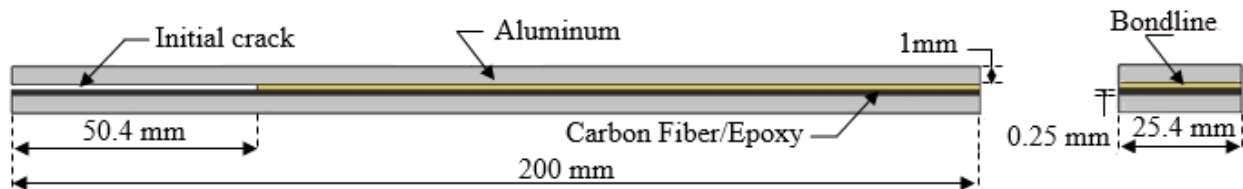


Figure 3.11: Schematic of T-peel specimen along with dimensions (mm).

T-peel static strength can be detrimentally influenced by specimen misalignment, although the effect is very small for the bond line thickness (i.e. 0.1 mm) used in the test. This

effect becomes more apparent with increasing bond line thickness. Testing was very simple because it doesn't require any special fixture. Tensile tests were conducted with displacement rate of 0.5mm/sec on specimens under standard laboratory conditions (23°C/50% relative humidity) according to ASTM specifications. The specimens were held by a pair of well-aligned servo-hydraulic operated wedge action grips with a lateral pressure of 0.7 MPa. Instron MTS machine software was used to control the test machine and to collect the test data. Five specimens per conditions were tested. Figure 3.12 illustrate the specimen during the T-peel test.



Figure 3.12: T-Peel test being conducted.

Peel strength is defined as the force per unit width required to start failure and maintain a specified rate of failure using of a stress applied in a peeling mode [95]. Static strength (peak load/force to initiate failure) and average peeling force (Figure 3.13) were the two type of loads recorded for each test. The static strength data along with the average peeling force is shown in Table 3.5 for carbon fiber/epoxy-aluminum specimens. Static normal strength was considered on the basis of average peeling force rather than peak load to neglect the effect accumulated resin at the crack tip of initial crack during bonding of hinges to the specimen.

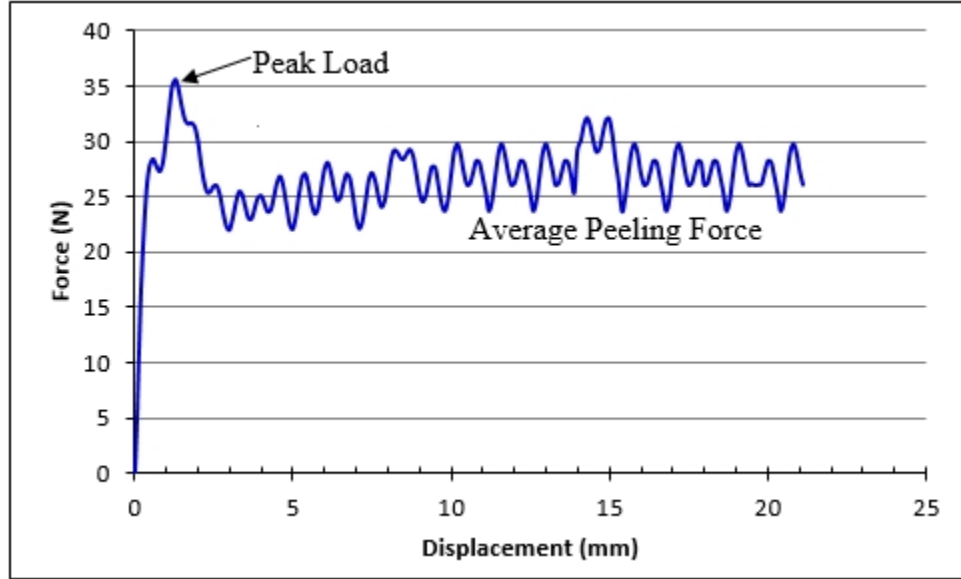


Figure 3.13: Typical load-displacement plot achieved from T-peel tests of CFC-aluminum bond.

Table 3.5: Aluminum-carbon fiber/epoxy bond normal strength results.

S.no	Average Peeling Load (N)	Static Strength	Test Type
1	23	37	T-Peel Test
2	28	44	
3	18	55	
4	15	25	
5	20	35	
Average	20.8	39.2	

3.3.3 Polyester Synthetic Veil Tensile Test

Tensile tested were carried to determine the properties of polyester synthetic veil/epoxy layers so that parameters can be used as input to the finite element analysis. A panel consisting of eight layers of polyester surfacing veil/epoxy having 200 x 200 dimensions was prepared by employing hand layup method and cured with autoclave vacuum press using the same curing cycle as of carbon fiber/epoxy. The cured panel was cut into test coupons having dimensions of 200 mm x 25.4 x 1.35 mm with the help of band saw. The cross section samples were maintained as rectangular to avoid failure near the grip. To avoid direct pressure on the specimen in the grip

area, grit paper was used on the laminate in the gripping. An extensometer was used during the test to obtain strain data from the coupon. The specimen during the tensile and damaged coupon after the test is shown in figure 3.14.

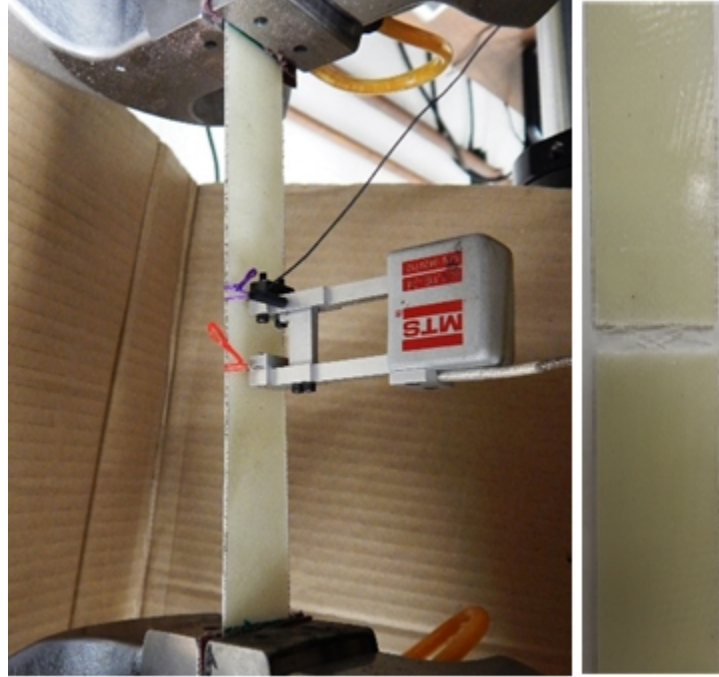


Figure 3.14: Polyester surfacing veil coupon during the test and damaged specimen after the test.

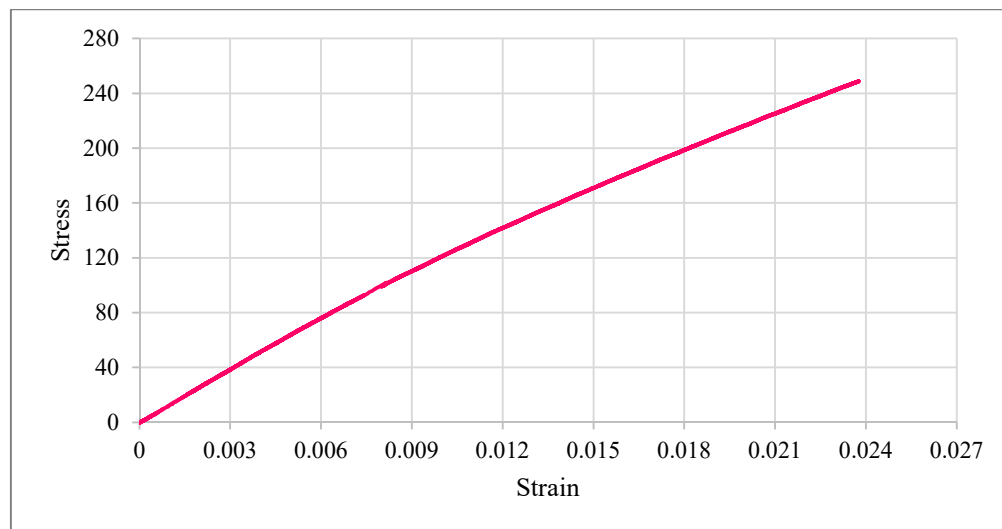


Figure 3.15: Typical stress- strain response of polyester synthetic surfacing veil/epoxy laminate

The load-displacement data of machine was converted to the stress-strain curve considering specimen geometrical dimensions. The typical stress- strain response of polyester synthetic surfacing veil/epoxy laminate is shown in figure 3.15. Elastic modulus, ultimate tensile strength, and the strain were obtained from the results. The thermal expansion coefficient data for polyester synthetic surfacing veil was not available in the literature. So its thermal expansion coefficient was assumed close to E-glass fabric surfacing veil and calculated by considering Turner's equation which takes into account the modulus of both matrix and fibers. The subscripts m and f in the turner's equation represents the epoxy matrix and E-glass fiber. The properties of E-glass fiber and epoxy matrix used to calculate the thermal expansion coefficient of surfacing veil cloth is given by Table 3.6. Tensile and thermal expansion coefficient properties for the polyester veil cloth is summarized in Table 3.7.

$$\alpha_v = \frac{\alpha_m k_m v_m + \alpha_f k_f v_f}{k_m v_m + k_f v_f} \quad (1)$$

Table 3.6: Properties of epoxy matrix and E-glass fiber used in turner's equation

Properties	CTE, α (C^{-1})	Modulus, k (GPa)	Volume fraction, v
Eglass Fiber	$10 \cdot 10^{-6}$	72	0.3
Epoxy matrix	$45.6 \cdot 10^{-6}$	3.7	0.7

Table 3.7: Tensile and thermal expansion properties for the polyester veil cloth.

Material	ρ (kg/m ³)	E (GPa)	Failure stress (MPa)	v	CTE, α (C^{-1})
Cloth	1471	14.5	240	0.34	$0.381 \cdot 10^{-6}$

3.3.4 Scanning Electron Microscope (SEM) Cross-section Imaging

The presence of epoxy resin layer between CFRP and aluminum layers in specimens cured by without any external adhesive film was observed by using SEM imaging technique. This epoxy resin layer will act as a barrier between CFRP and aluminum layers and help to hinder the occurrence of galvanic corrosion on aluminum layers. The cross section of CARALL fiber metal laminate sample was carefully cut from multiple locations by using a diamond cutter and polished by using sand paper # 1200. The presence of epoxy resin layer having 4 μm average thickness between adjacent CRFP and aluminum layer is shown in figure 3.16:

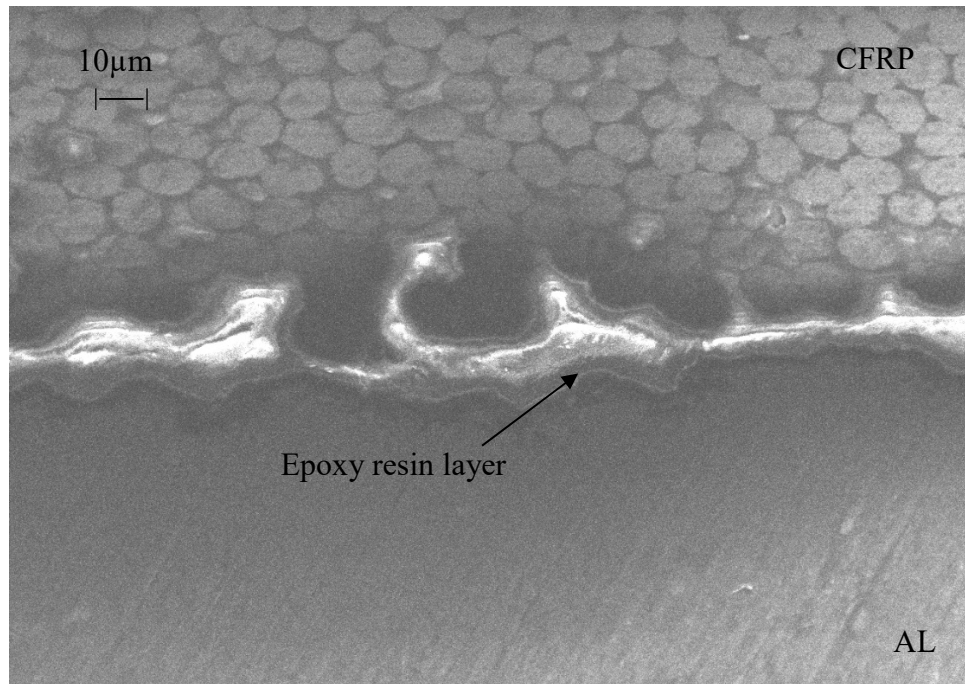


Figure 3.16: SEM image of CARALL's Cross section.

3.4 SPECIMEN DETAILS

Carbon fiber reinforced aluminum laminates having two different stacking sequence were studied in this research. The effect of inserting epoxy resin dipped veil cloth between the aluminum and carbon fiber/epoxy layers on the both type of laminates. The layup sequence of all

the samples studied in this research work along with the nomenclature adopted for naming the samples is schematically described in figure 3.17 (a) & (b).

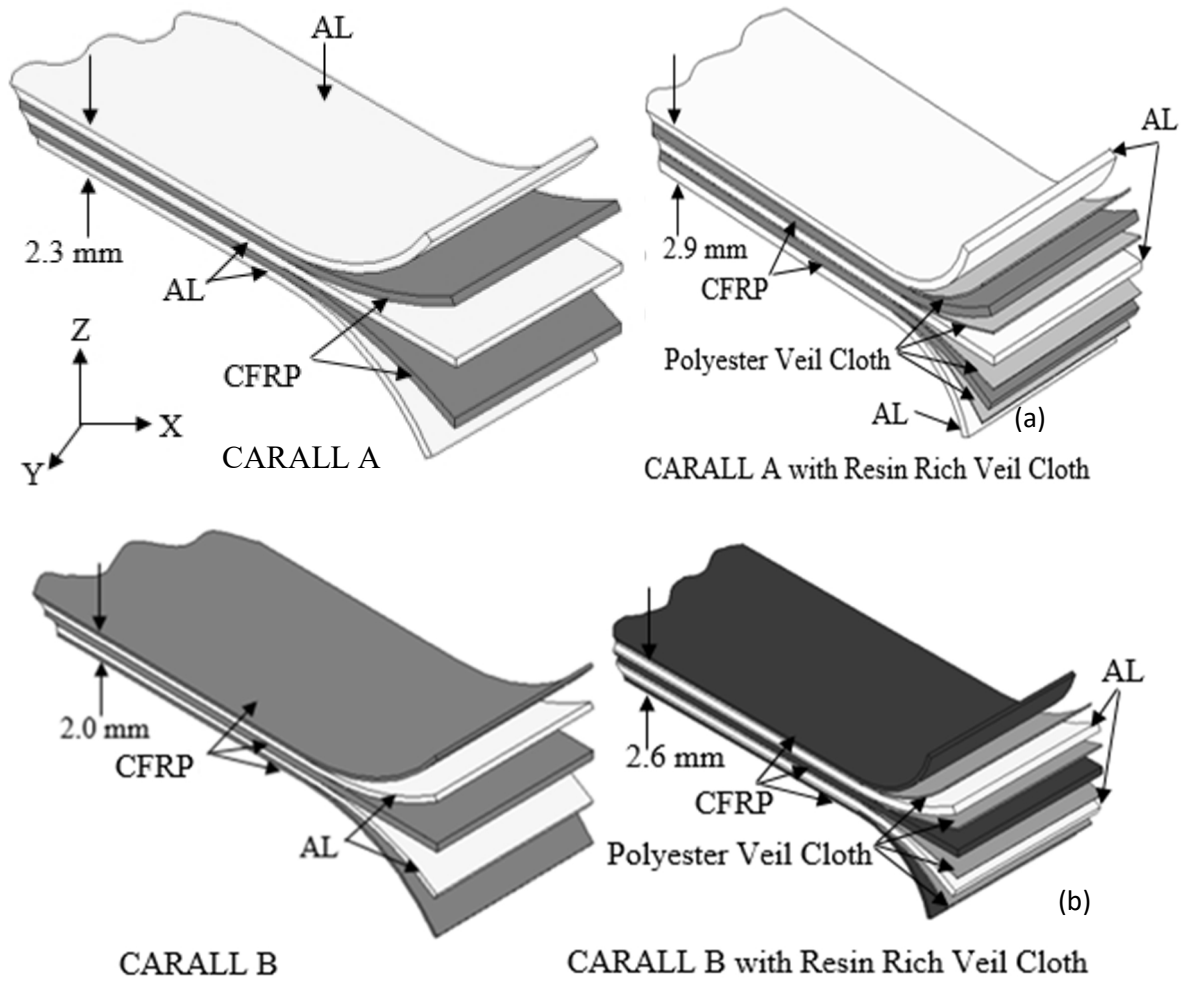


Figure 3.17: Carbon fiber/epoxy –aluminum laminates nomenclature and stacking sequence.

The samples of both configurations were accurately weighed and their geometrical dimensions were measured using slide caliper before undergoing the test procedure. The calculation of weight savings was done by comparing the calculated weight of samples through metal volume fraction formulation to the weight of monolithic pure Aluminum 5052-H32 samples. The total laminate thickness, specimen type, metal volume fraction of all type of samples is provided in Table 3.8.

Table 3.8: Specimen notations and layup sequence for CARALL fiber metal laminates

Specimen Designation	Layup Sequence	Metal Volume Fraction (%)	Laminate Thickness (mm)
CARALL A	AL-CFRP-AL-CFRP-AL	65	2.3±0.08
CARALL A with Cloth Layers	AL-Cloth-CFRP-Cloth-AL-Cloth-CFRP-Cloth-AL	49.2	2.9±0.1
CARALL B	CFRP-AL-CFRP-AL-CFRP	50	2.0±0.03
CARALL B with Cloth Layers	CFRP-Cloth-AL-Cloth-CFRP-Cloth-AL-Cloth-CFRP	35	2.6±0.12

3.5 Weight Saving with CARALL FMLs

Rule of mixture equations was employed to calculate the weight savings by using carbon fiber reinforced aluminum laminate as described in the following section. The reduction in weight results obtained from the rule of mixtures analytical equations was compared to those obtained by measuring the weight of the samples. Rule of mixture equations showed excellent agreement with the weight reduction results obtained from specimen weight measurement. Table 3.9 and 3.10 provides the results obtained from the rule of mixture equations and specimen weight measurement, respectively.

3.5.1 Rule of mixture

Density of carbon fiber, $\rho_f = 1.8 \text{ g/cc}$

Epoxy matrix density, $\rho_m = 1.3 \text{ g/cc}$

Fiber volume fraction, $V_f = 0.52$

Carbon fiber/epoxy laminate density, $\rho_{C'} = \rho_f V_f + \rho_m (1 - V_f) = 1.56 \text{ g/cc}$

Metal Volume Fraction (MVF) = Total thickness of aluminum layers/ Total FML thickness

FML Density (ρ_{FML}) = $MVF * \rho_{AL} + (1 - MVF) * \rho_{C'}$ (2)

Veil cloth Density, $\rho_{vc} = 1.47 \text{ g/cc}$

Veil cloth volume fraction (CVF) = Total thickness of veil cloth layers/ Total FML thickness

$$\text{FML Density with cloth } (\rho_{\text{FMLwith cloth}}) = \text{MVF} * \rho_{\text{AL}} + \text{CVF} * \rho_{\text{vc}} + (1 - (\text{MVF} + \text{CVF})) * \rho_{\text{C}} \quad (3)$$

Table 3.9: Weight savings with CARALL laminates obtained with rule of mixture equations

Sample	Monolithic AL Thickness (cm)	Monolithic AL Weight (g)	FML Thickness (cm)	MVF	$\rho_{\text{FML}}^{\text{g/cc}}$	FML Volume (cm ³)	FML Weight (g)	Weight savings %
CARALL A	0.3	31.12	0.23	0.65	2.29	8.903	20.38	34.5
CARALL A with cloth Layers			0.29	0.51	2.08	11.22	23.33	25.0
CARALL B	0.254	26.35	0.2	0.492	2.11	7.858	16.58	37.0
CARALL B with cloth Layers			0.26	0.38	1.93	10.06	19.42	26.2

The carbon fiber reinforced laminate specimens with different constituents and layup sequence offer different weight savings results. As expected the addition of resin dipped veil cloth effect the weight saving results by decreasing it approximately by 8-9 % due to increase in the thickness of the laminate. Although there is a decrease in weight savings, there is a possibility of savings approximately around 25 % of using CARALL laminates.

3.5.2 Sample Weight Measurement

Table 3.10: Weight savings with CARALL laminates obtained by measuring the weight of samples.

sample	Monolithic AL Weight (g)	FML Weight (g)	Weight savings %
CARALL A	31	20	35.4
CARALL A with cloth Layers		22	29.1
CARALL B	26	16	38.4
CARALL B with cloth Layers		19	26.9

CHAPTER 4 THERMAL RESIDUAL STRESSES

Fiber metal laminates are lightweight materials, consisting of very thin layers of metallic sheets interspersed with layers of fiber reinforced adhesives. The engineering aim behind the design of fiber metal laminates is to have combined best properties of metals and fiber-reinforced composites. Different materials can be used to create such hybrid material systems. However, in reality, any arbitrary combinations of materials would result in poor structural quality due to the existence of difficulties such as very high residual thermal stresses during the fabrication process, galvanic corrosion, etc. during the manufacturing of these mixed materials. Residual stresses are developed in fiber metal laminates (FML) during autoclave curing process due to a mismatch between coefficients of thermal expansion of fiber layers and metal layers.

Several others parameters such as thermal contraction which arises during the post-fabrication cooling process, laminate layup, volumetric shrinkage of resin, the morphology of fibers, mold material, thermal gradient during cooling, etc. contribute to the development of these residual stresses. The undesirable effects of residual stresses are distortions of finished components when cooled and removed from molds (dimensional stability), failure in the manufactured products (e.g. matrix cracking, interfacial failure, ply failure) etc. Such stresses can subsequently reduce the design life and durability of Fiber metal laminates. Therefore, prediction and measurement of residual stresses are important in relation to achieve the durable performance of fiber metal laminates. Therefore, the prediction of these residual stresses was done in the above stated two FML configurations before predicting their mechanical behavior.

4.1 Analytical Method

An analytical model was developed to estimate and validate the FEA results for residual thermal stresses. The sum of residual stresses developed during the cooling process has to be

zero when the FML is in an unloaded state. In other words, it means that the forces of the layers need to be balanced. Therefore, the following equations can be developed for estimating the residual thermal stress in FML configuration considering properties of layers.

$$\sigma_{al} = \frac{(\alpha_c - \alpha_{al}) * \Delta T}{\frac{1 - \nu_{al}}{E_{al}} + \frac{2(1 - \nu_c)t_{al}}{E_c t_c}} \quad (4)$$

$$\sigma_c = \frac{(\alpha_{al} - \alpha_c) * \Delta T}{\frac{(1 - \nu_{al}) * t_c}{2E_{al}t_{al}} + \frac{(1 - \nu_c)}{E_c}} \quad (5)$$

In the above equations, the subscripts "al" and "c" stand for aluminum and woven composite, respectively. The symbol t_{al} is the notation for the thickness of an aluminum layer and t_c is the total thickness of the carbon fiber/epoxy layers. The temperature change ΔT is considered with negative sign since it is cooling down the process.

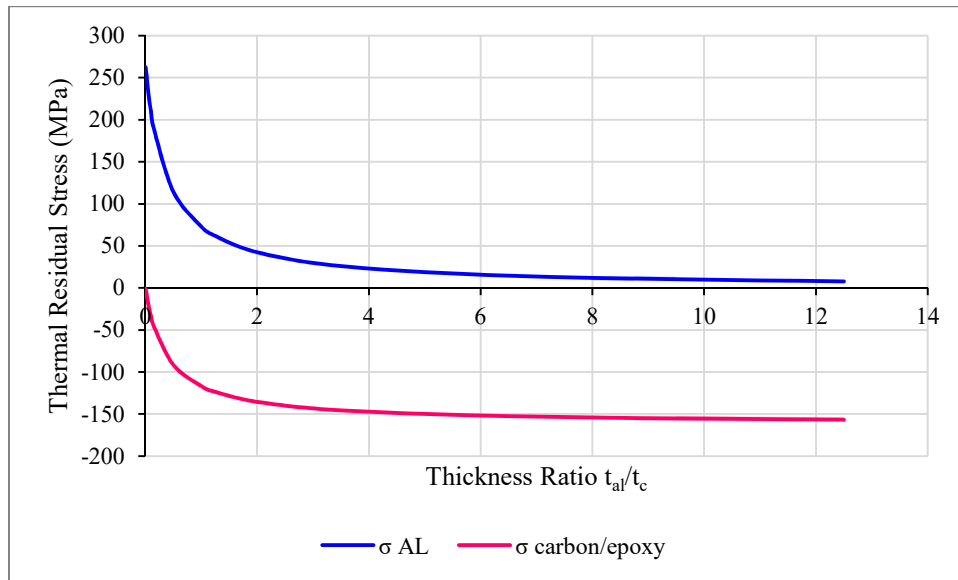


Figure 4.1: Effect of ply thickness on thermal residual stresses.

The effect of thickness of fiber metal laminates constituents layers on the thermal residual stress can be described on by plotting the variation of residual thermal stress as a function of thickness ratio. Figure 4.1 describes the thermal stress variation with thickness ratio

for CARALL-A configuration. It can be seen that ply thickness plays an important role in the magnitude of the residual stresses. As expected, the results show tensile stresses in metallic layers and compressive stresses in Carbon fiber/epoxy composite layers.

4.2 Thermal Residual Stresses Finite Element Analysis

A three-dimensional (3D) finite element (FE) model was developed to predict cure-induced residual stresses for tensile, flexural and low-velocity impact specimens. The three-dimensional FE package, LS-Dyna was used for the prediction of geometrical changes of the woven carbon/epoxy composite reinforced aluminum alloys specimens. Layered solid elements with perfect bonding between the layers are used. The element formulation ELFORM 16 with full integration has been used for both aluminum and carbon fiber/epoxy layers. Since the cool-down part is dominant in the development of distortions, this part of cure cycle is used as a primary modeling in static simulation of residual stresses. Ls-Dyna FE package calculates the thermal residual stresses considering a linear relationship between thermal strain and change in temperature at every increment in simulation time. Thermal stress is calculated by using strain values at each integration point as

$$\sigma = E \cdot \epsilon = E \cdot \alpha \cdot t \quad (6)$$

The thermal load is ΔT , the temperature difference between ambient temperature and cure temperature. The thermal load was applied through *Thermal Load Curve keyword on the FE model. The aluminum layers were modeled using Piecewise Linear Plasticity model. Enhanced Composite Damage material model and Plastic Kinematic model was employed for modeling the carbon fiber/epoxy and synthetic surfacing veil layers. Thermal Expansion coefficient was added to both materials through Add Thermal Expansion material card. The contact between adjacent layers was applied using, Tied Surface To Surface contact algorithm. Material properties are assumed to be independent of temperature during analysis and in the final (after cool down) phase. The material

properties of carbon fiber/epoxy and aluminum layers used in the residual thermal stress modeling are given in Tables 3.2, 3.3 and 3.7. Finite element models developed for thermal residual stress prediction for flexural specimens are shown in Figure 4.2.

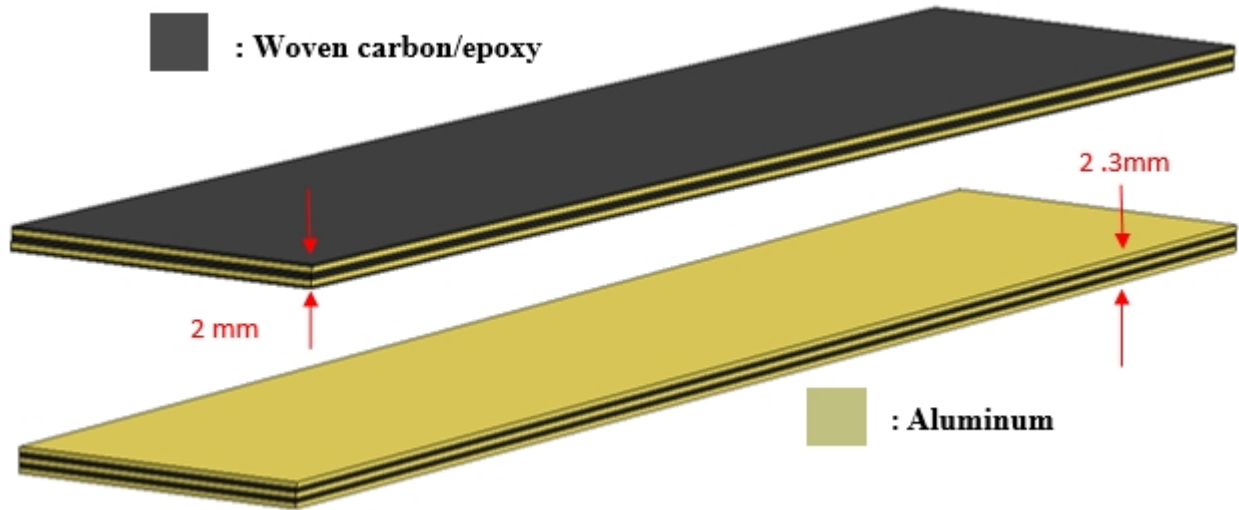


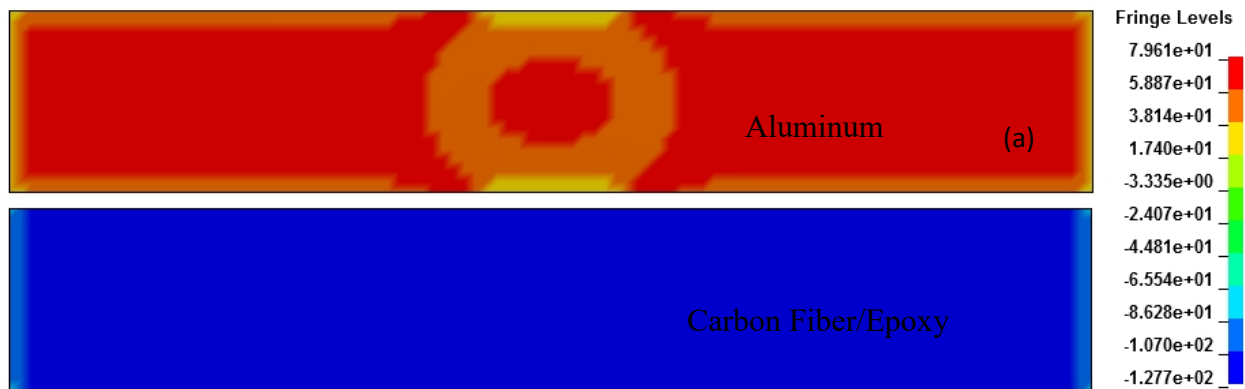
Figure 4.2: Thermal residual stress FE model schematics of CARALL-A & B flexure specimens

Thermal residual stresses were predicted for all specimens studied in this research. Force equilibrium based thermal residual stress theoretical model does not take shape effect into consideration, as a result it generated identical results for all specimens. Moreover, it is not applicable to specimens made by inserting synthetic veil cloth layers because it is only valid for laminates made up of two constituents. A comparison between analytical model and finite element model results is made in Table 4.1 for CARALL-A & B flexural specimen's only as the analytical model is not shaped dependent. Finite element thermal residual stress predictions for CARALL-A & B flexural specimens made by inserting synthetic surfacing veil cloth is also mentioned in Table 4.1.

Table 4.1: Thermal residual stress predictions in flexural samples.

		CARALL-A		CARALL-A with veil	CARALL-B		CARALL-B with veil
		FEA	Theory		FEA	Theory	
Aluminum Layers (Mpa)	σ_x	79.61	86.75	90.2	106.9	100.2	133.2
	σ_y	85.14	86.75	90.3	107.2	100.2	132.4
	τ_{xy}	≈ 0	0	≈ 0	≈ 0		≈ 0
Carbon Fiber/epoxy Layers (Mpa)	σ_x	-127.7	108.4	-119.4	-109	-100.3	-80.3
	σ_y	-126.2	108.4	-120.6	-109	-100.3	-80.0
	τ_{xy}	≈ 0	0	≈ 0	≈ 0		≈ 0
Polyester Veil Cloth Layers (Mpa)	σ_x			-12.2			5.23
	σ_y			-10.6			2.96
	τ_{xy}			≈ 0			≈ 0

A close agreement has been found between the thermal residual stress results produced by FEA results and analytical model results. Thermal residual stress also shows the effect of the addition of synthetic surfacing veil cloth layers. Residual stresses are reduced in aluminum layers whereas they get increased in carbon fiber/epoxy layers with the addition of polyester veil layers. Figure 4.3 & 4.4 exemplifies the FEA X stress predictions contours of CARALL-A & CARALL-A with veil layers specimens and CARALL-B & CARALL-B with veil layers specimens, respectively



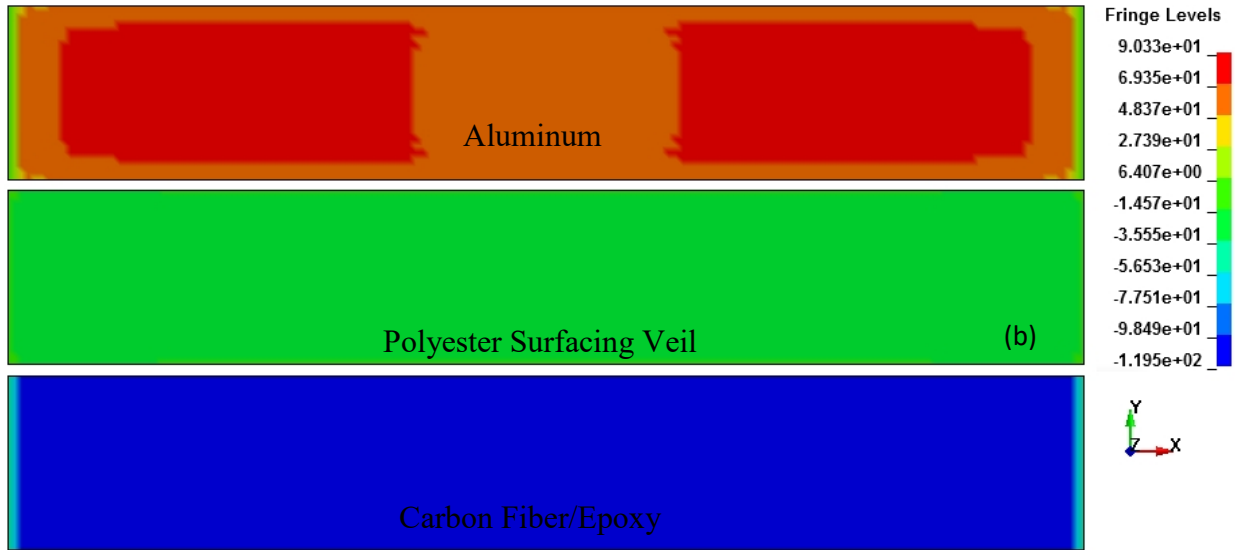


Figure 4.3: X stress plots for residual stresses; (a) CARALL-A, (b) CARALL-A with veil layers

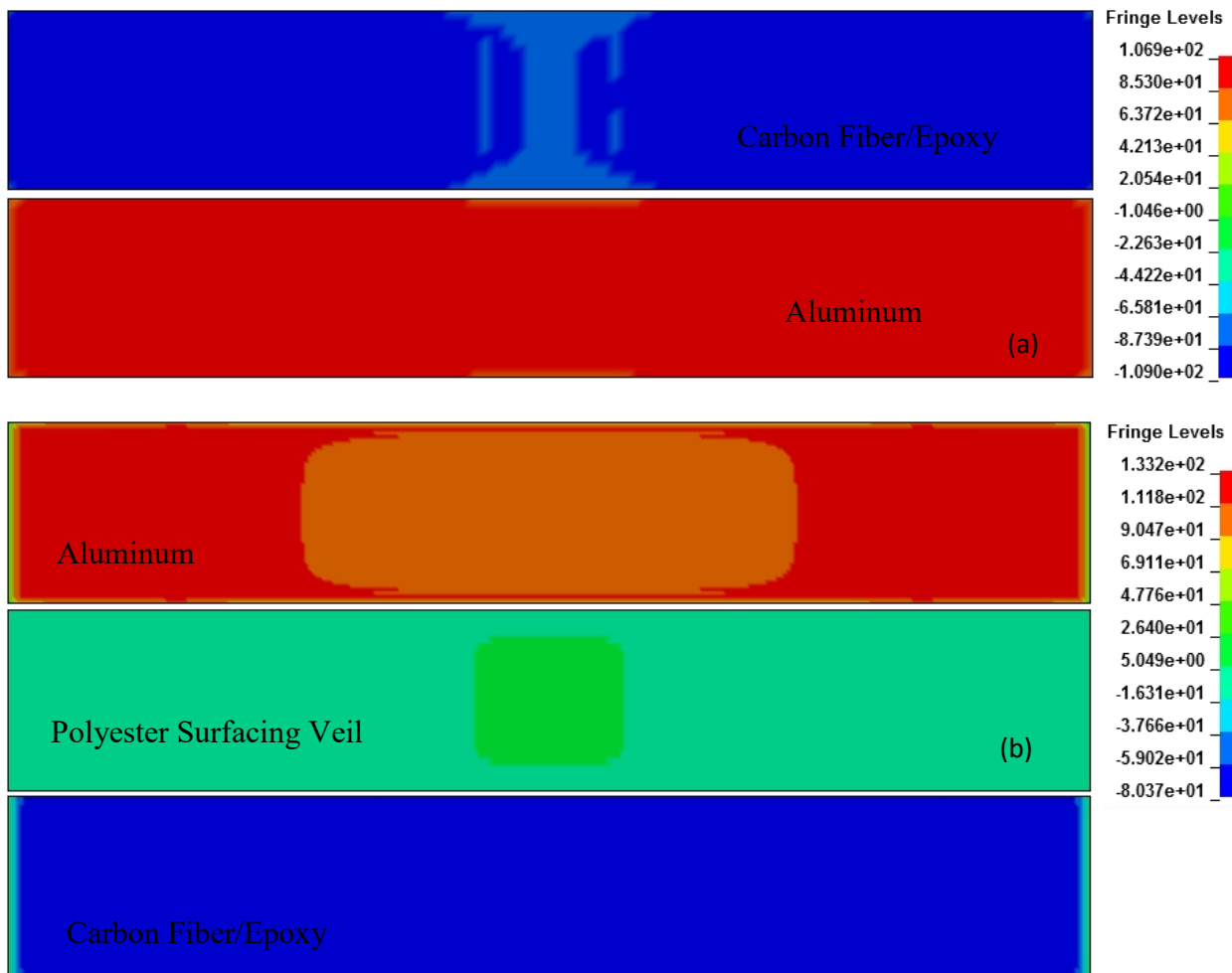


Figure 4.4: X stress plots for residual stresses; (a) CARALL-B, (b) CARALL-B with veil layers

CHAPTER 5 STATIC TENSILE TEST & DATA ANALYSIS

5.1 Tensile Test Experimental Aspects

Tensile tests were conducted on CARALL fiber metal laminate samples according to ASTM D 3039 standard to obtain Young's modulus, the tensile strength, the strain to failure, as well as the failure modes of each system. Tensile tests were conducted at room temperature (25°C) on the standard specimens and the results were compared together in order to study the mechanical behavior of both fiber metal laminate configurations and compare the results with plain monolithic aluminum 5052-h32 samples. The nominal dimensions of samples are shown in figure 5.1.

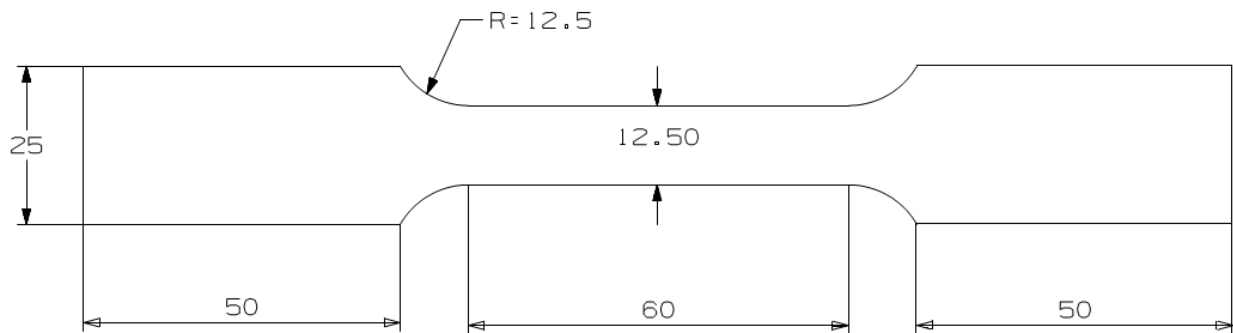


Figure 5.1: Nominal dimensions of tensile test samples

Tensile tests were carried out at a constant displacement rate of 0.05 mm/s using MTS Instron machine equipped with the hydraulic wedge grips with 200KN force capacity. Clip-on extensometer with a gauge length of 20 mm was used to measure the modulus of elasticity of each sample. The load transducer which is located on the top record the load taken by the beam. Load taken by fiber metal laminated beams, machine displacement and time duration of the test were written down at 0.1s intervals with the help of the computerized controlled compression testing machine. The entire duration of three point tensile tests was monitored with the help of pictures and videos, which were later analyzed for critical failure mode and correlated with the

time data obtained from the computerized controlled data acquisition system. The complete test setup including MTS Instron testing machine and the FML specimen during the tensile test is shown in figure 5.2.



Figure 5.2: Tensile test setup with MTS machine.

5.1.1 Effect of Polyester Synthetic Surfacing Veil Cloth Layers on Tensile Behavior

FML's tensile properties are greatly influenced by their individual components. Composite and metal layers are loaded elastically in a first linear part of the stress-strain curve. So, FML configurations exhibit well-defined elastic response from the composite layers and aluminum up to 0.2% strain in tensile stress- strain curves. The stress-strain-curve gets into a transition area, once the metal starts yielding, where it is no longer linear. Since the tensile behavior of carbon fiber composite is linear elastic until fracture, the stress-strain relation becomes linear again as the carbon fiber layers are still reinforcing the laminate. It is well known that in the tensile mode, the Al yields but does not fail until the composite layers have failed.

Fiber metal laminate configurations have a combination of high stiffness and strength from the composite layer and good impact properties from the aluminum layer. The load–displacement curves were converted to the tensile stress–strain diagrams for specimens of each category. Typical stress-strain plots characterizing the tensile response of CARALL-A & CARALL-B without the veil cloth is shown in figures 5.3, whereas the tensile response of both FMLs having polyester veil cloth layers is shown in figure 5.4.

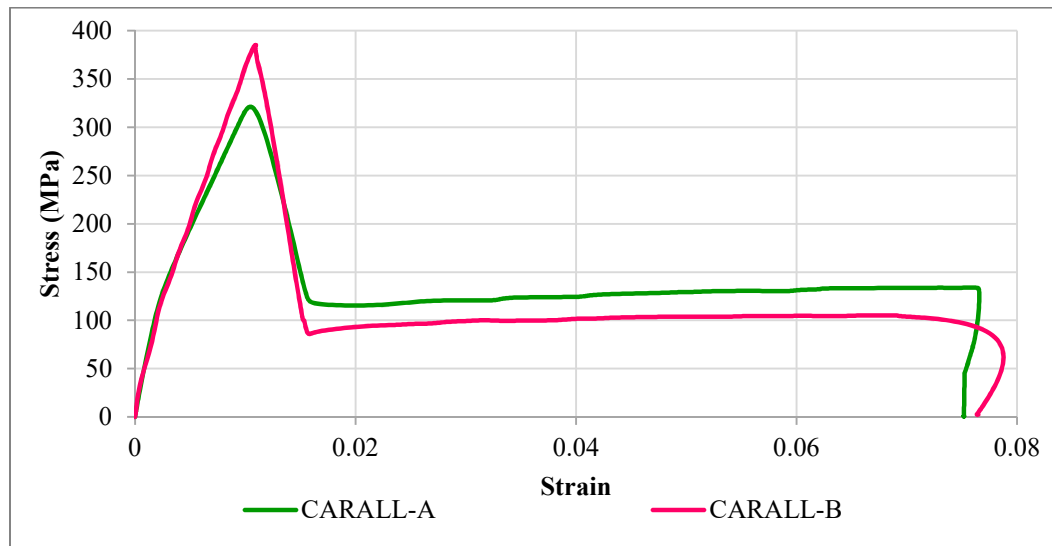


Figure 5.3: Tensile behavior of CARALL FMLs without veil cloth layers.

It can be observed from figure 5.3 that the tensile strength of CARALL-B is more than CARALL-A FML. Carbon fiber/epoxy and aluminum layers fail at different strain values in both FMLs as the interface bond are not strong enough to transfer the stresses to aluminum layers after the failure of carbon fiber/epoxy layers. Carbon fiber/epoxy and aluminum layers failed at strain value of 0.011 and 0.078 respectively in both configurations. The difference in the strength values of aluminum layers after the failure of carbon fiber/epoxy layers at a tensile strain level of 0.011 in both FMLs is due to the volume fraction of aluminum layers. The strength of aluminum layers is reduced to about 125 MPa in CARALL-A FMLs whereas in CARALL-B it is reduced to 100 MPa due to less volume fraction of aluminum in CARALL-B.

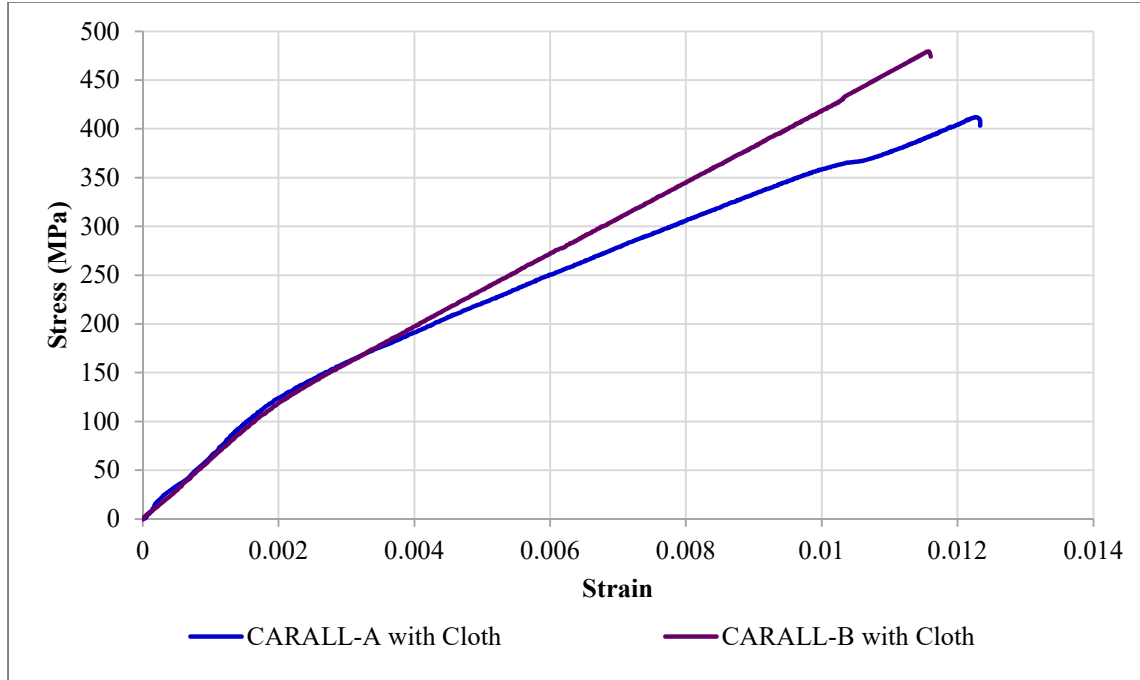


Figure 5.4: Tensile behavior of CARALL FMLs having polyester veil cloth layers.

The interface bond between the carbon fiber/epoxy lamina and the aluminum plays an important role in the transfer of stresses in FML composites as fiber matrix interface bond plays in the carbon fiber reinforced laminate composites. The addition of polyester surfacing veil cloth makes the interface bond much stronger. As a result, of this, the tensile stresses are transferred to aluminum layers in specimens made with polyester surfacing veil cloth. The carbon fiber/epoxy and aluminum layers failed approximately at same strain value i.e. 0.012 (figure 5.4) due to the transfer of stresses. In addition to making the interface bond stronger, the addition of polyester veil cloth also increases the ultimate tensile strength of both CARALL FML specimens which can be inferred by comparing Figures 5.3 and 5.4.

5.2 Tensile Test Finite Element Analysis

The tensile behavior of FMLs was modeled by commercially available LS-DYNA FEM software. Static analysis was performed by using explicit time integration scheme. The development of FE model for tensile test numerical simulations in LS-DYNA includes discretization of geometry into finite elements, modeling of a composite material including intralaminar failure and delamination failure, modeling of aluminum material with strain-based failure criteria, initialization of predicted thermal residual stresses and applying appropriate boundary conditions.

5.2.1 Discretization of Tensile FML Specimen

Hypermesh, a preprocessor for finite element mesh generation is used to build the tensile FE model for CARALL FML configurations. Both the aluminum layers and carbon fiber/epoxy layers in FE model were modeled with 8-node solid elements (ELFORM 2). Element length of 1.5 mm was maintained in the gauge length region and 2 mm in the grip area of tensile FE models for both FMLs. In the normal solution phase, the appropriate boundary conditions were employed to perform the tensile simulation of CARALL FML specimens. The specimens were constrained from one end in all three translation degrees of freedom and pulled from another end at a loading of 0.05mm/s. Since the delamination failure between carbon fiber/epoxy and aluminum layers is only observed in gauge length region of tensile FML specimens in experimental work, therefore carbon fiber/epoxy layers were connected to aluminum layers by Contact Automatic One Way Surface to Surface Tiebreak Contact in gauge length region and Tied Automatic Surface to Surface contact was used to connect the carbon fiber/epoxy & aluminum layers in grip area. The load-displacement data were collected using LS-PrePost and

Microsoft Excel software. Figure 5.5 describes the finite element mesh and boundary conditions adopted for tensile simulation of CARALL FML specimens.

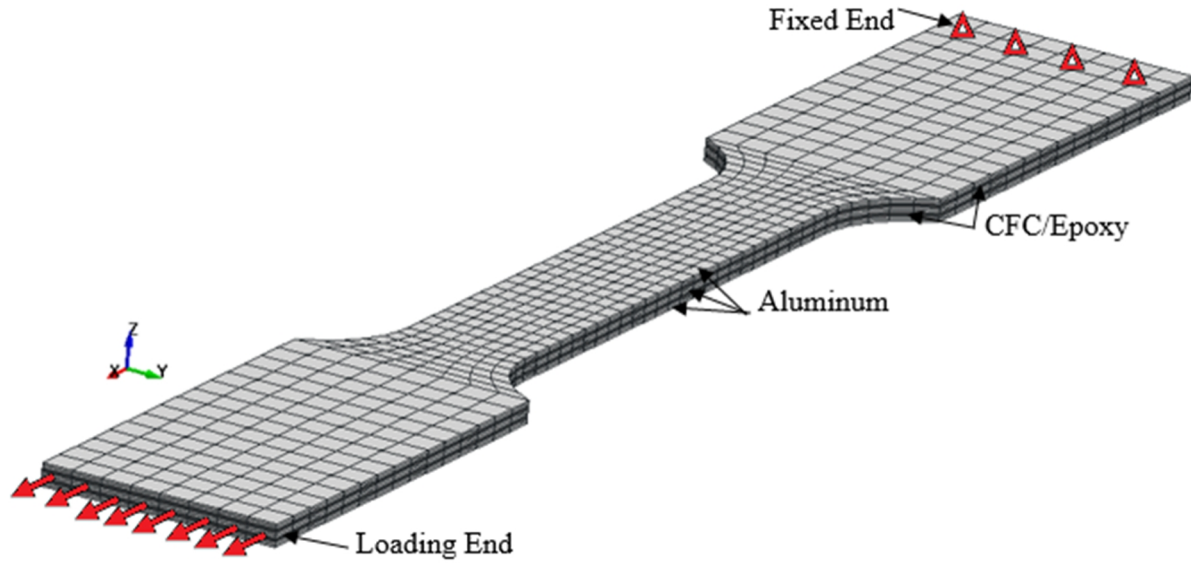


Figure 5.5: Static tensile simulation FE model

5.2.2 Composite (CFRP) Material Model

The tensile behavior of the woven carbon fiber/epoxy layers was modeled using Chang-Chang [96] damage initiation criteria inbuilt in Enhanced Composite Damage (Mat_054) material model of LS-DYNA. According to this failure criterion, damage in composite laminate occurs when one of the following failure equations is equal to or greater than zero. Fiber tension, fiber compression, matrix tension, and matrix compression are the four failure modes considered in Chang-Chang failure criteria [96]. The failure equations are represented separately as follows:

$$\text{Tensile failure, fiber direction: } e_{f,T}^2 = \left[\frac{\sigma_1}{X_T} \right]^2 + \Psi \left[\frac{\tau_{12}}{S} \right] - 1 \begin{cases} \geq 0 & \text{failure} \\ < 0 & \text{elastic} \end{cases} \quad (7)$$

$$\text{Compressive failure, fiber direction: } e_{f,C}^2 = \left[\frac{\sigma_1}{X_C} \right]^2 - 1 \begin{cases} \geq 0 & \text{failure} \\ < 0 & \text{elastic} \end{cases} \quad (8)$$

$$\text{Tensile failure, matrix direction: } e_{m,T}^2 = \left[\frac{\sigma_2}{Y_T} \right]^2 + \left[\frac{\tau_{12}}{S} \right]^2 - 1 \begin{cases} \geq 0 & \text{failure} \\ < 0 & \text{elastic} \end{cases} \quad (9)$$

$$\text{Compressive failure, matrix dir: } e_{m,C}^2 = \frac{\sigma_1^2}{2S^2} + \frac{\sigma_2^2}{Y_C^2} - 1 + \frac{\tau_{12}^2}{S^2} - 1 \begin{cases} 0 & \text{failure} \\ < 0 & \text{elastic} \end{cases} \quad (10)$$

Where ; σ_1 is the nominal stress in the lamina in the fiber direction, σ_2 is the nominal stress in the lamina in the matrix direction, τ_{12} is the nominal shear stress in the plane of lamina, X_T is the tensile strength of the fibers, X_C is the compressive strength of the fibers, Y_T is the tensile strength in the transverse direction of the fibers, Y_C is the compressive strength in the transverse direction of the fibers, S is the shear strength, Ψ is the shear stress correction parameter in the tensile failure mode. The value of Ψ equal to zero was considered in the finite element analysis performed in this research study. Failure strains can also be applied in addition to these stress-based failure criteria's. If strain-based failure criteria are utilized, the stress values are kept at the same level after meeting the Chang-Chang criteria until the failure strains are reached. The element is removed from the calculation when the stress based chang-chang failure criteria are met or failure strain reaches its maximum value. In this study failure strains for CFRP layers were not used.

5.2.3 Aluminum Material Model

The piecewise linear plasticity material model (Mat_024) was utilized to model the elastoplastic behavior of aluminum layers by defining effective stress-effective plastic strain curve obtained from experimental data. The failure of aluminum layers was modeled in this study by defining a plastic failure strain in the constitutive model card of LS-DYNA. The effective stress-effective plastic strain curve used as input to piecewise linear plasticity material model is shown in figure 5.6. The material properties parameters of aluminum and carbon fiber/epoxy used for predicting the flexural and tensile behavior of FMLs are presented in Table 3.2 and 3.3. The mechanical properties of 5052-H32 aluminum alloy shown in Table 3.2 were

evaluated experimentally with the tensile test performed in the lab and cross-checked with the values given in reference [97]. In this material model the plasticity treatment includes strain rate and yield function is defined as

$$= \frac{1}{2} S_{ij} S_{ij} - \frac{\sigma_y^2}{3} \quad 0 \quad (11)$$

Where

$$\sigma_y = \beta[\sigma_0 + f_h \varepsilon_{eff}^p] \quad (12)$$

In this material model, the hardening function $f_h(\varepsilon_{eff}^p)$ can be defined in tabular form or specified in linear form as $f_h \varepsilon_{eff}^p = E_p \varepsilon_{eff}^p$. The effective plastic strain is defined as $\varepsilon_{eff}^p = \int_0^t \frac{2}{3} \dot{\varepsilon}_{ij}^p \varepsilon_{ij}^p dt$ and σ_0 denotes the initial yield strength. The plastic strain rate $\dot{\varepsilon}_{ij}^p$ is the difference between the total and elastic strain rates. The strain rate effects can be added in this model by using the Cowper-Symonds model. The yield stress is scaled in this model with the factor $\beta = 1 + \frac{\dot{\varepsilon}}{C}^{1/p}$ where C and p are the user defined input constants. The complete mathematical equations for piecewise linear plasticity material model can be found in LS-DYNA theory manual [98]. However, we have not used any strain rate and hardening effects in our analysis. The implementation of the piecewise linear plasticity model is done in LS-DYNA by updating the deviatoric stresses elastically, checking the yield function and the deviatoric stresses are accepted if the yield function is satisfied. The incremental plastic strain is computed if the yield function is not satisfied.

$$\varepsilon_{eff}^p = \frac{(1.5 S_{ij}^* S_{ij}^*)^{0.5} - \sigma_y}{3G + E_p} \quad (13)$$

Where G and E_p are the shear modulus and actual plastic hardening modulus respectively. The trial deviatoric stress S_{ij}^* state is then scaled back as

$$S_{ij}^{n+1} = \frac{\sigma_y}{(1.5S_{ij}^*S_{ij}^*)^{0.5}} S_{ij}^* \quad (14)$$

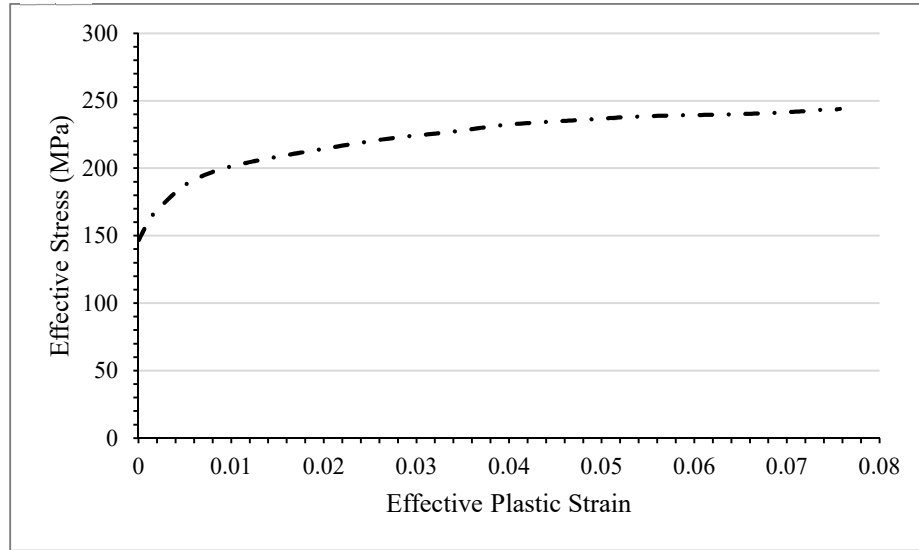


Figure 5.6: Effective stress-effective plastic strain curve used as input to the constitutive material model.

5.2.4 Delamination Failure Model

Interlaminar delamination between the carbon fiber/epoxy (CFRP) and aluminum interfaces was modeled by employing cohesive tiebreak algorithms available in LS-DYNA[99]. The transmission of both compressive and tensile forces is allowed in these penalty-based contact algorithms which are used to model connection between surfaces. The tie-break contact algorithms prevent the separation of the slave node from the master segment before failure of a connection and after the failure, the contact behaves like surface to surface contact with thickness offsets due to the removal of tensile coupling. Depending upon the nature of the connection, an optional failure criterion can be defined in all tie-break contacts. In this study, to simulate interlaminar debonding the *CONTACT AUTOMATIC SURFACE TO SURFACE TIEBREAK - DYCOSS Option 7 was chosen [100-102]. The cohesive contact criteria in this tiebreak contact algorithm are based on the bilinear constitutive traction-separation law. The linear elastic/linear softening model for mode 1 crack opening is shown in figure 5.7.

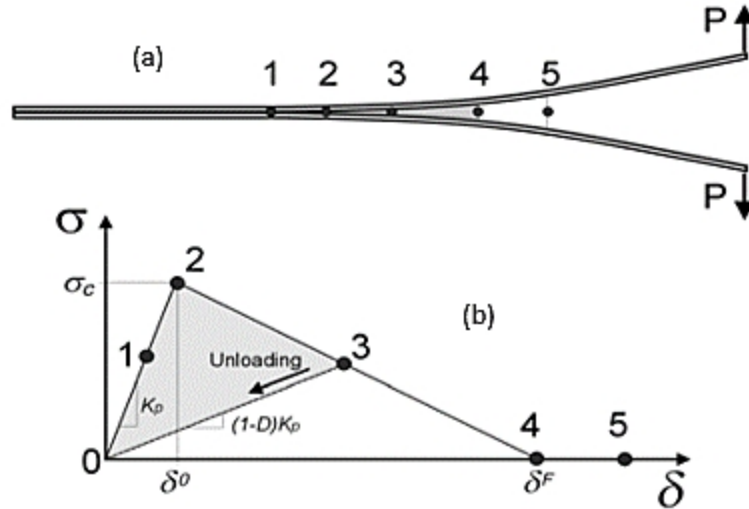


Figure 5.7: Bilinear traction-separation law for mode I crack in tension [103].

The stress-strain assumption with key points and the corresponding points with delamination progression are shown in figure 5.7 (b) and (a). As point 1 is in elastic part of the material response, no material damage had occurred at this point and the unloading would follow the elastic line. The onset of damage is represented by point 2 and material softening (damage growth) starts at the point. When the loading had progressed to point 3, the material has suffered some damage but the plies have not separated yet (damage parameter (α) is greater than zero but less than 1). The unloading is assumed to follow start line from point 3 to 0 if occurs at point 3. Non-recoverable energy dissipated to partial damage of bonding is represented by the shaded area in figure 5.7(b). The plies have separated permanently at point 4 as the damage parameter (α) had reached unity. Fracture energy (G) required to delaminate two plies is represented by the total area of the triangle (0-2-4). It is input parameter in LS-DYNA having energy/area as units.

In DYCOSS discrete crack model, the interface forces in the uncracked state (point 1) are calculated from the relative displacements assuming linear elastic behavior.

$$= \begin{matrix} i_I \\ i_{II} \end{matrix} = \begin{matrix} k_I & 0 \\ 0 & k_{II} \end{matrix} \begin{matrix} i_I \\ i_{II} \end{matrix} = K \quad (15)$$

Where σ_I and σ_{II} are the stresses in mode I and mode II, k_I and k_{II} are secant stiffness terms for mode I and mode II and δ_I and δ_{II} are the displacements for mode I and mode II. The allowable shear stresses may increase under increasing normal stress for heavy woven fabrics laminate. The relation for the crack initiation, in this case, is developed by extending Hashin criterion with a friction angle (ϕ) given as

$$f = \frac{\max(\sigma_I, 0)^2}{NFLS} + \frac{\sigma_{II}}{SFLS - \sin(\phi) \min(0, \sigma_I)}^2 = 1 \quad (16)$$

Where NFLS is normal failure stress, SFLS is the shear failure stress and ϕ is the friction angle in degrees. When the loading beyond the crack initiation point, the degradation of material is described by considering two damage variables D_I and D_{II} .

$$\begin{matrix} \sigma_I \\ \sigma_{II} \end{matrix} = \begin{matrix} 1 - D_I & 0 & k_I & 0 \\ 0 & 1 - D_{II} & 0 & k_{II} \end{matrix} \begin{matrix} \delta_I \\ \delta_{II} \end{matrix} \quad (17)$$

Where $1-D$ is stress reduction factor. The value of D ranges from 0 to 1. Damage evolution in mode I depend on displacement δ_I only. The concept of friction angle is extended in damage growth process for compressive normal displacements resulting in iso-lines α in $\delta_I - \delta_{II}$ planes are shown in figure 5.8.

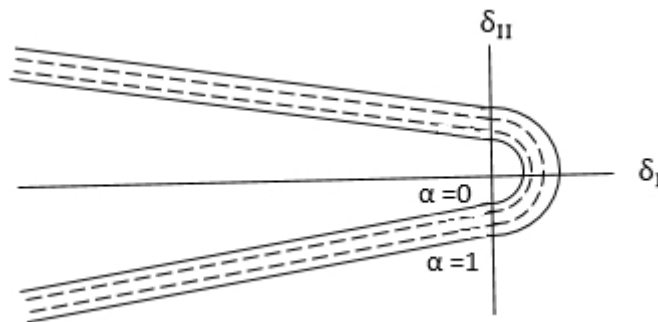


Figure 5.8: Iso-lines of internal parameter α [104].

The relation for crack propagation in terms of internal parameter α is given as

$$f = \frac{\max(\sigma_I, 0)^2}{NFLS(\alpha)} + \frac{\sigma_{II}^2}{SFLS(\alpha) - \sin(\alpha) \min(0, \sigma_I)} = 1 \quad (18)$$

The interface stresses are expressed in terms of interface displacements as:

$$\sigma_I = k_I(\alpha) \delta_I ; \quad \sigma_{II} = k_{II}(\alpha) \delta_{II} \quad (19)$$

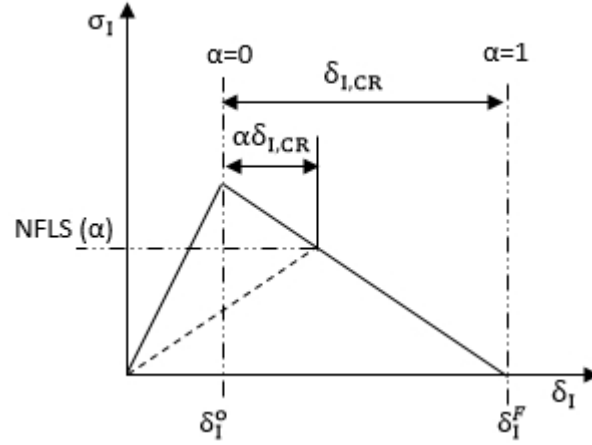


Figure 5.9: Parameters in softening model [104].

From figure 5.9;

$$NFLS(\alpha) = k_I(\alpha) (\alpha \delta_{I,CR} + \delta_I^0) ; SFLS(\alpha) = k_{II}(\alpha) (\delta_{II,CR} + \delta_{II}^0) \quad (20)$$

$$\delta_{I,CR} = \frac{F_I}{k_I} - \delta_I^0 ; \quad \delta_{II,CR} = \frac{F_{II}}{k_{II}} - \delta_{II}^0 \quad (21)$$

The initial and final displacement for mode I and mode II are given as

$$\delta_I^0 = \frac{NFLS}{k_I(0)} ; \quad \delta_I^F = \frac{2G_I A}{NFLS} ; \quad \delta_{II}^0 = \frac{SFLS}{k_{II}(0)} ; \quad \delta_{II}^F = \frac{2G_{II} A}{SFLS} \quad (22)$$

Substituting equation 19 and 20 into 18; we get

$$\frac{\max(0, \sigma_I)^2}{k_I(\alpha) (\alpha \delta_{I,CR} + \delta_I^0)^2} + \frac{\sigma_{II}^2}{k_{II}(\alpha) (\delta_{II,CR} + \delta_{II}^0)^2 (1 - \sin(\alpha))} = 1 \quad (23)$$

The above equation is a nonlinear equation between α and known interface displacements.

Linearizing it with respect to α gives;

$$d = \frac{1}{2 \frac{(\max(0, \sigma_I))^2 \delta_{I,CR}}{k_I(\alpha) (\alpha \delta_{I,CR} + \delta_I^0)^3} + 2 \frac{(\delta_{II})^2 \delta_{II,CR}}{k_{II}(\alpha) (\delta_{II,CR} + \delta_{II}^0)^3}} \quad (24)$$

After α is calculated, the secant terms are obtained as

$$k_I = \frac{(1 - \alpha) \delta_I^0}{\delta_{I,CR} + \delta_I^0} k_{I,ini} ; k_{II} = \frac{(1 - \alpha) \delta_{II}^0}{\delta_{II,CR} + \delta_{II}^0} k_{II,ini} \quad (25)$$

The damage matrix is given as;

$$D = \begin{matrix} D_I() & 0 \\ 0 & D_{II}() \end{matrix} = \begin{bmatrix} \frac{\alpha_{I,CR} + \sigma_I^0}{\tau_{I,CR} + \tau_I^0} & 0 \\ 0 & \frac{\alpha_{II,CR} + \sigma_{II}^0}{\tau_{II,CR} + \tau_{II}^0} \end{bmatrix} \quad (26)$$

The interface stresses for the crack development state are given by;

$$\begin{matrix} \sigma_I \\ \sigma_{II} \end{matrix} = \begin{matrix} 1 - D_I() & 0 \\ 0 & 1 - D_{II}() \end{matrix} \begin{matrix} k_I & 0 \\ 0 & k_{II} \end{matrix} \begin{matrix} \sigma_I \\ \sigma_{II} \end{matrix} = (1 - D)K \quad (27)$$

The complete mathematical equations for DYCOSS discrete crack model can be found in Lemmen and Meijer technical paper [104]. In this study, mode II failure condition was considered dominant for modeling interlaminar delamination crack growth in an area located locally underneath the loading pin. Therefore only shear failure strength (SFLS) =15 MPa and shear energy release rate (ERATES) = 0.23 MPa*mm was used as input to delamination model. Due to the lack of available data, mode II energy release rate value was assumed.

5.2.5 Predicted Thermal Residual Stresses Initialization

The thermal Residual stress (discussed in the previous chapter) which comes into picture during the curing process of laminates was initialized to FE model with the help of dynamic relaxation option in LS-Dyna. Dynamic relaxation is carried out before the explicit analysis in LS-Dyna i.e. in pseudo time before the actual simulation time. The simulation time resets to zero after the initialization state is achieved and the normal stage of the solution automatically begins from the initialized state. Dynamic relaxation allows LS-Dyna to approximate solutions to linear and nonlinear static or quasi-static processes. Control dynamic relaxation control card parameters are described in Table 5.1

Table 5.1: Parametric control card for dynamic relaxation in LS-Dyna [105]

Card	1	2	3	4	5	6	7	8
Variable	NRCYCK	DRTOL	DRFCTC	DRTERM	TSSFDR	IRELAL	EDTTL	IDRFLG
Type	I	F	F	F	F	I	F	I
Default	250	0.001	0.995	infinity	TSSFAC	0	0.04	0

IDRFLG parameter in dynamic relaxation control card controls the manner in which the preloaded state is computed. If IDRFLG is set to 1 or -1, a transient “dynamic relaxation” analysis is started, in which an explicit analysis is performed and DRFCTR factor is used to damped by means of scaling nodal velocities in each time step. When the ratio of current distortional kinetic energy to peak distortional kinetic energy (the convergence factor) falls below the convergence tolerance (DRTOL) or when the time reaches DRTERM, the dynamic relaxation analysis stops and the current state becomes the initial state of the subsequent normal analysis. Distortional kinetic energy is defined as total kinetic energy less the kinetic energy due to rigid body motion. Distortional kinetic energy history computed during the dynamic relaxation phase is automatically written to a file called “relax”. This file can be read as an ASCII file by LS-PrePost and its data plotted. The relax file also includes a history of the convergence factor. Dynamic relaxation was invoked by setting SIDR parameter to 1 in the define curve commands. Curves so tagged are applicable to the dynamic relaxation analysis phase. Curves with SIDR set to 0 or 2 are applicable to the normal phase of the solution. At the completion of the dynamic relaxation stage and before the start of the normal solution stage, a binary dump file (d3dump01) and a “prescribed geometry” file (drdisp.sif) were written by LS-Dyna. Either of these files can be used in a subsequent analysis to quickly initialize to the preloaded state without having to repeat the dynamic relaxation run.

5.3 Tensile Experimental Test and FEA Results Comparison

The correlation between experiment and finite element analysis is made by plotting stress-strain curves in the same scatter plot. FEA and experimental stress-strain curves for CARALL-A & B specimens made by not using polyester veil cloth layers are shown in Figure 5.10 & 5.11. Similarly, figure 5.14 & 5.16 depicts the correlation between FEA and experimental results for CARALL-A & B specimens made by using polyester synthetic surfacing veil cloth layers.

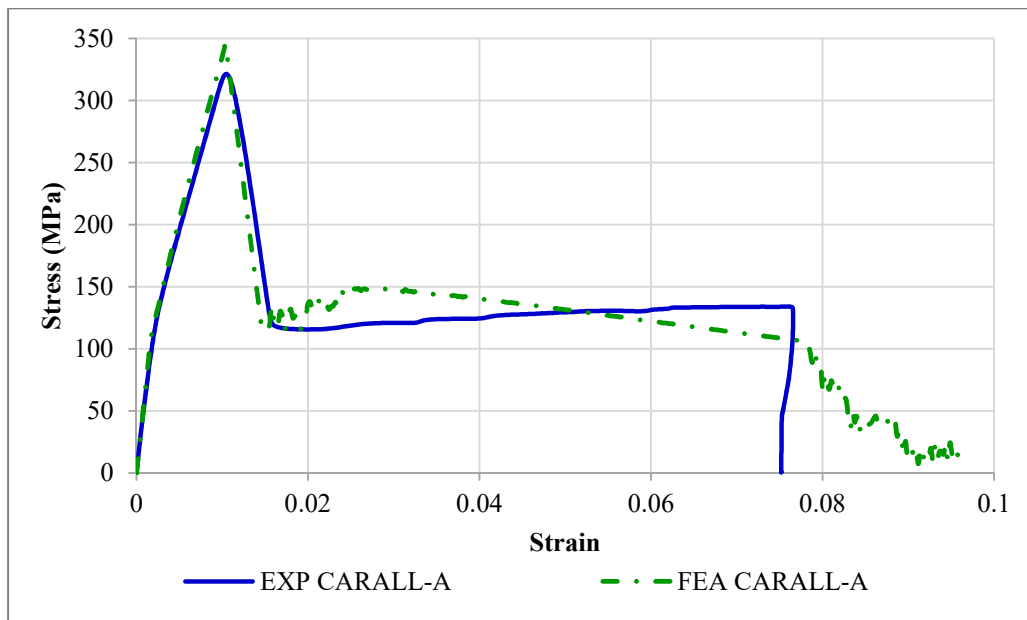


Figure 5.10: FEA & experimental stress-strain plots for CARALL-A specimens

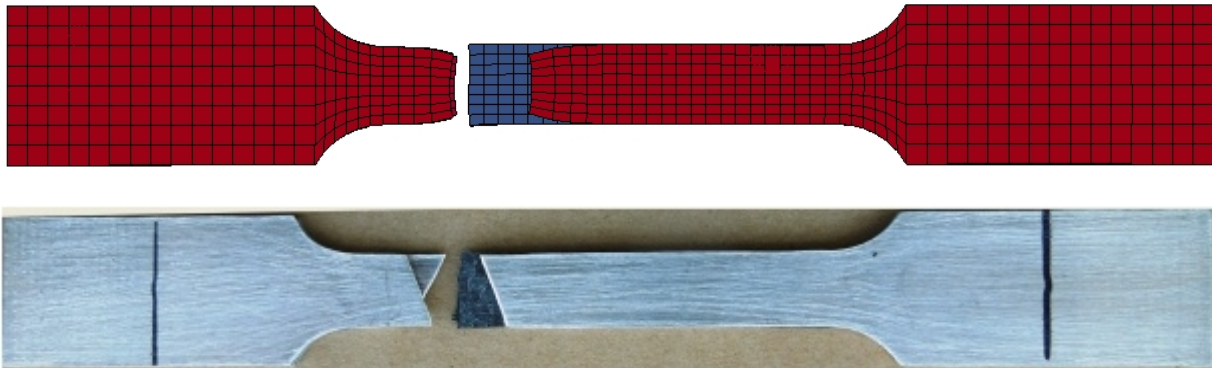


Figure 5.11: FEA and experimental failed Specimen of CARALL-A with no veil cloth.

The CARALL specimens made without using polyester veil cloth layers shows the linear elastic response up to strain level of 0.1 % whereas specimens made with cloth layers shows elastic response up to 0.2 %. The load carrying capacity of all specimens in the linear region is around 30% of the maximum load. In the linear region both FRP and aluminum is assumed to act as a single component. The response observed from 0.1 or 0.2 % strain to their peak strength is a result of uneven load sharing between aluminum and carbon fiber layers due to their different poisson ratios. Less ductile carbon fiber/epoxy layers bear more load as compared to high ductile aluminum layers.

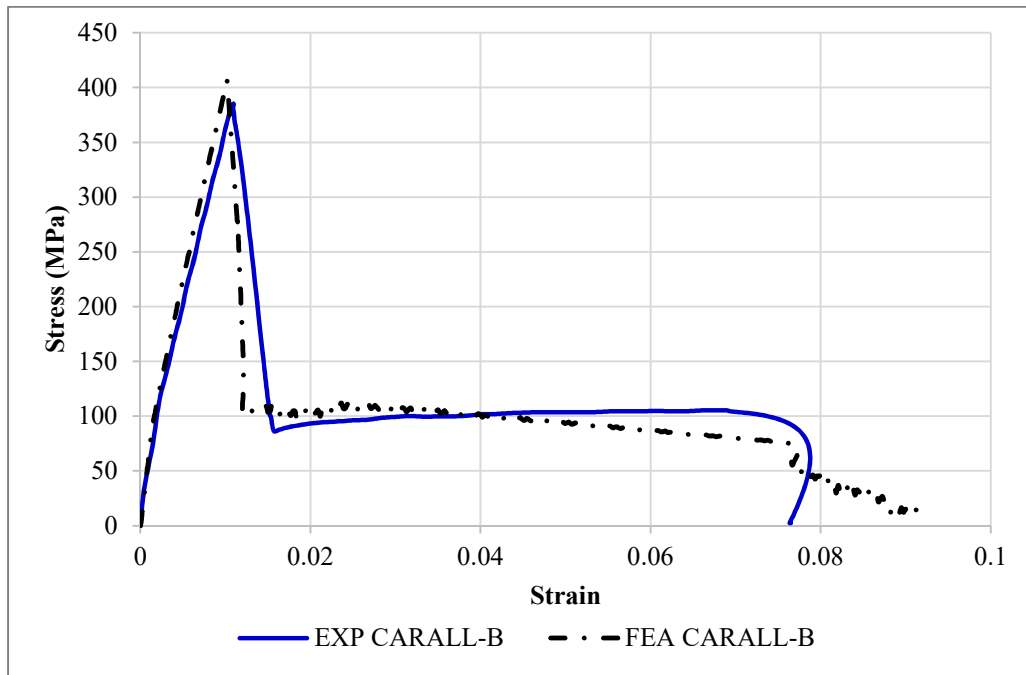


Figure 5.12: FEA & experimental stress-strain plots for CARALL-B specimens

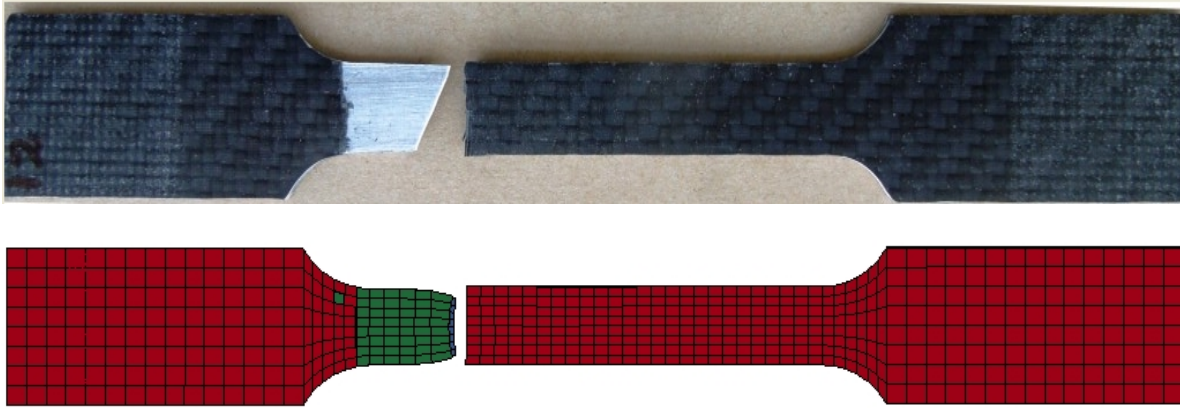


Figure 5.13: FEA and experimental failed specimen of CARALL-B with no veil cloth.

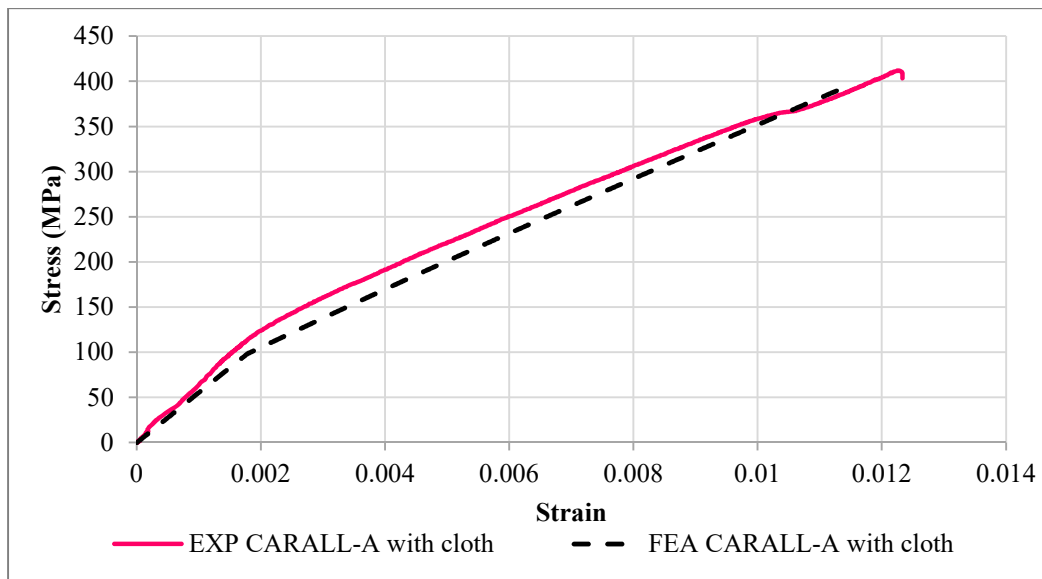


Figure 5.14: FEA & experimental stress-strain plots for CARALL-A specimens having veil cloth

The maximum strength attained by CARALL-A specimens made without using cloth layers and with veil cloth layers are 325 MPa and 410 MPa, respectively. Similarly, the maximum strength attained by CARALL-B specimens made without using cloth layers and with veil cloth layers are 400 MPa and 475 MPa, respectively. After attaining the peak, the aluminum layers does not fail immediately in specimens made without using polyester veil cloth layers whereas it fails immediately in specimens made with veil cloth layers. The FEM model results showed good correlation with experimental results for all different types of CARALL specimens.

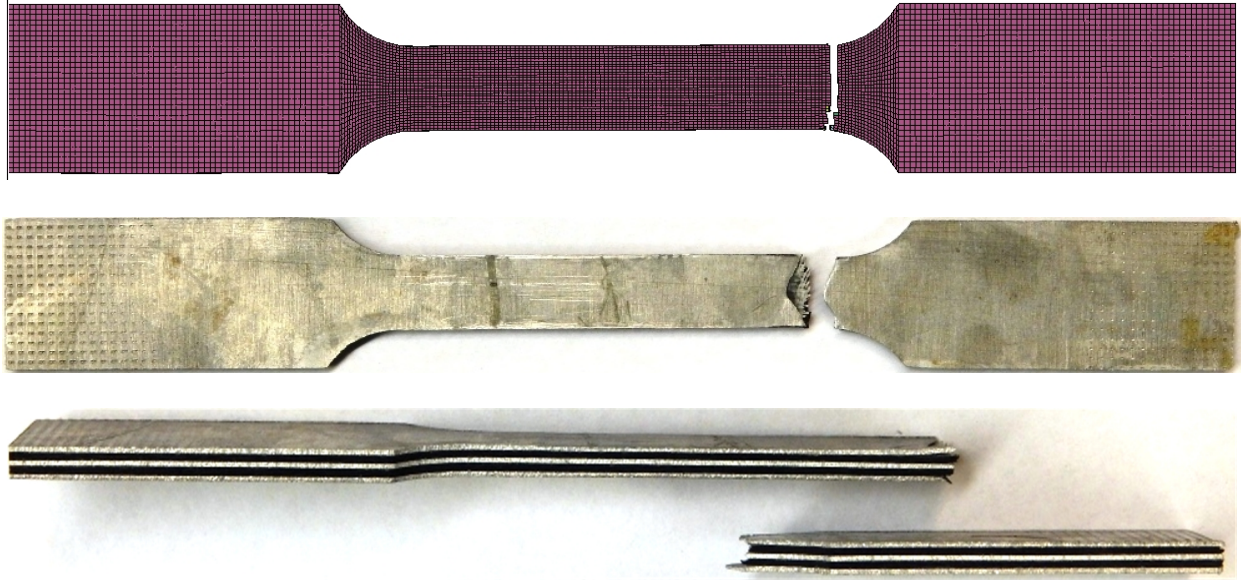


Figure 5.15: FEA and experimental failed specimen of CARALL-A having veil cloth layers

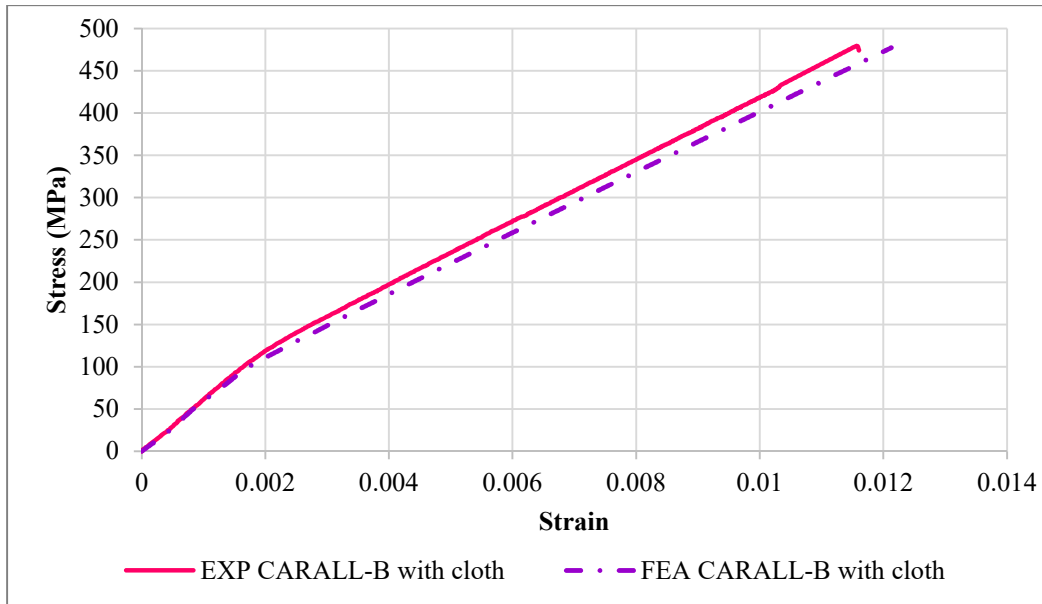


Figure 5.16: FEA & experimental stress-strain plots for CARALL-B specimens having veil cloth



Figure 5.17: FEA and experimental failed specimen of CARALL-B having veil cloth layers

It can be clearly inferred from the fracture surfaces of experimental failed specimens that aluminum layers in FMLs of all combinations were fractured at an angle approximately equal to 65 degrees to the loading direction due to the direction of dislocation-related slip plane and slip direction of the metal crystal [106]. The carbon fiber layers fractured almost at angle 90 degrees to the loading direction showing good bonding strength between carbon fiber and epoxy matrix. Finite element models also captured the fractured surfaces of aluminum and fibrous layers of all FMLs combinations depicting necking induced fracture surface for aluminum layers and 90 degrees fractured surface for carbon fiber layers. A comparison between tensile properties of both FML types and monolithic 5052-H32 aluminum alloy are tabulated in Table 5.2. It can be observed from the tabulated results that there is a significant increase in the tensile strength in comparison to aluminum 5052-H32 strength for both type of FMLs whereas the modulus of FMLs and monolithic aluminum is comparatively similar.

Table 5.2: Results of tensile experimental tests

Property/Sample	Monolithic Aluminum 5052-H32	CARALL-A	CARALL-B	CARALL A with cloth layers	CARALL B with cloth layers
Maximum tensile strength (MPa)	240	330	385	373	425
Strain at CFC layers breaking point ϵ_{\max} (%)	0.086	0.0105	0.0104	0.0123	0.0114
Young's Modulus, E (GPa)	69.7	70.3	69.8	72.8	73.3
Density ρ (g/cm ³)	2.68	2.29	2.11	2.08	1.93
Specific Tensile strength (MPa/(g/cm ³))	79.48	144.1	182.46	179.3	220.2
Tensile strength increase as compared to AL (%)	---	37.5	60.4	55.4	77.2

CHAPTER 6 THREE-POINT FLEXURAL TEST & DATA ANALYSIS

6.1 Three-point Flexural Test Experimental Aspects

ASTM standard test procedures are referred for conducting the flexural test. ASTM C 393 and ASTM D 790 are standard test procedures which deal with flexure on composite materials. ASTM C 393 is a standard test method for evaluating flexural performance of sandwich constructions whereas ASTM D790 standard test procedure is commonly used to determine flexural properties of unreinforced and reinforced plastics

Three-point bend fixtures were utilized for performing flexural tests on hybrid fiber metal laminated beams. The flexural fixture was placed on the lower platen of MTS compression testing machine having 200 KN load capacity. Lower supports and loading pin are two parts of the test fixture. Lower supports contains two cylindrical pins of diameter 12.7 mm secured on supports with the help of the springs. The distance between the two supports commonly known as span length can be adjusted to a maximum value of 254mm. The loading pin with the same diameter as that of support pins was rigidly secured to the top platten of the machine. The bottom part of the flexural fixture i.e. is lower supports was adjusted so that the loading pin is exactly over the mid-span of the hybrid fiber metal laminated beam.

Considering 40:1 as the ratio between support span to a thickness of the laminate as recommended by ASTM test procedure, the span length of 101.6 mm was kept. Large support span-to- thickness ratio was chosen so that the failure in the specimens occurs only due to the bending moment. Specimen total length was maintained at 152.4 mm so that an overhanging length of 25.4 mm can be allowed beyond the lower support pins on each side. The three-point

flexural fixture is shown in figure 6.1 and complete test setup including compression testing machine is shown in figure 6.2.

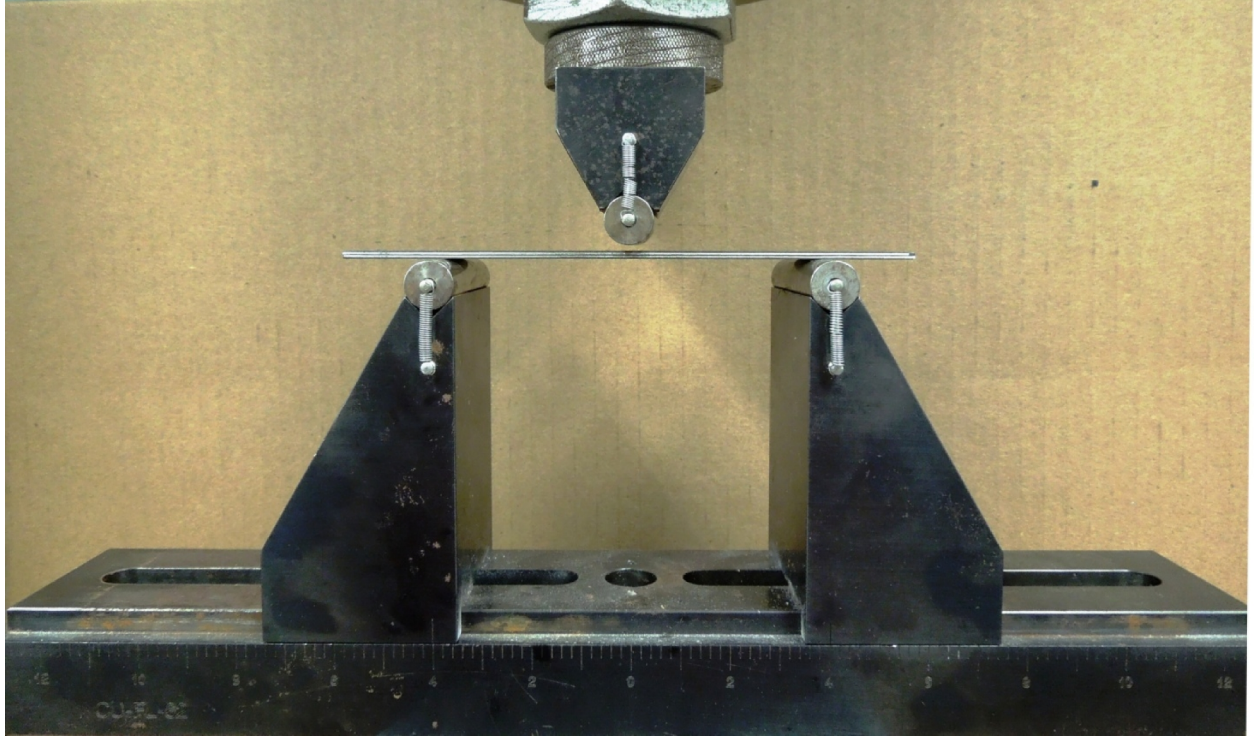


Figure 6.1: Three-point flexural test setup

Three Point Flexural test were conducted in displacement control mode by moving the lower supports against the hybrid fiber metal laminated beam at a rate 0.05 mm/s. The load transducer which is located on the top record the load taken by the beam. The load carried by fiber metal laminated beam, Machine displacement and time duration of the test were recorded at 0.5s intervals with the help of the computerized controlled compression testing machine. The load, displacement data were converted to stress-strain by using equations (28) and (29) provide in the ASTM standard test procedure D 790.

$$\text{Flexural Stress } \sigma_f = \frac{3 P L}{2 b d^2} \quad (28)$$

$$\text{Flexural Strain } \epsilon_f = \frac{6 D d}{L^2} \quad (29)$$

Where; P is load taken by beam in N

L is the support span length (mm)

d is the thickness of the laminated beam

b is the width of the laminated beam

D is the deflection of the middle of the support span.

The entire duration of the three-point flexural test was documented with the help of pictures and videos, which were later analyzed for critical failure mode and correlated with the time data obtained from the computerized controlled data acquisition system. All the laminates were scanned with the C-scan equipment prior to testing to check the presence of any interface bonding defects between CFRP and aluminum layers. The results were excellent showing good bonding at all interfaces.

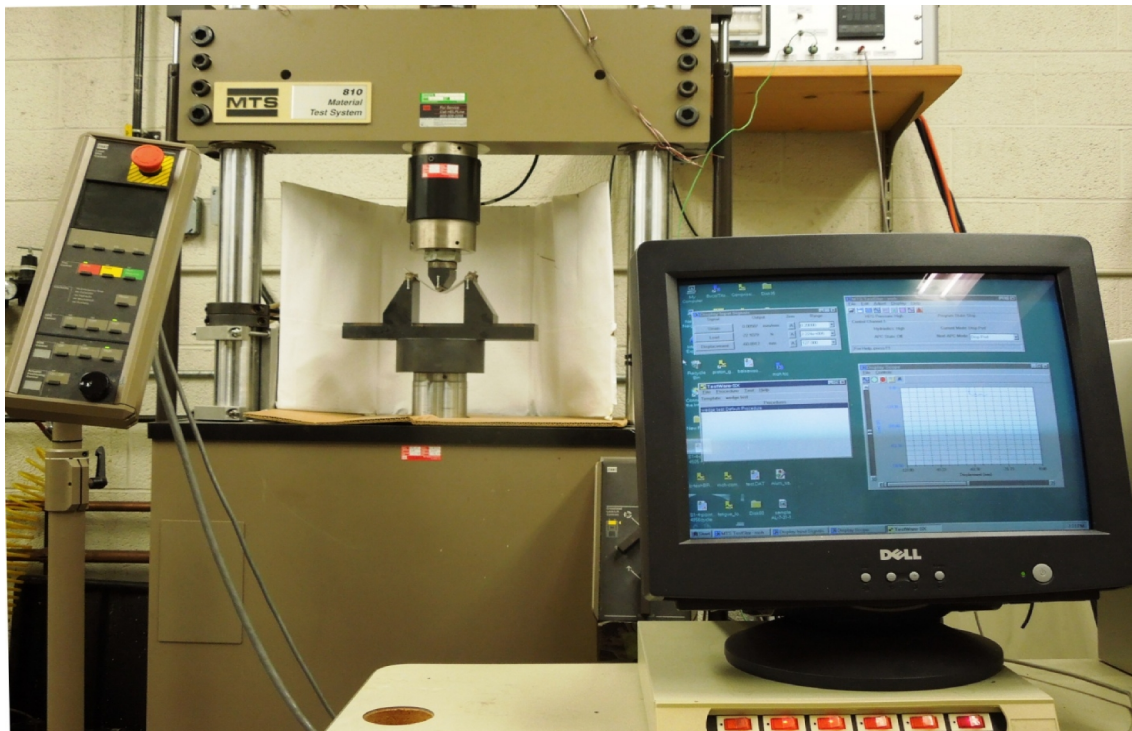


Figure 6.2: MTS compression testing machine with three-point flexural fixture

6.1.1 Effect of Polyester Synthetic Surfacing Veil Cloth on Flexural Behavior

The three-point flexural tests were conducted on MTS Instron machine and flexural behavior of both fiber metal laminate configurations is compared to each other in figure 6.3. As expected the fiber metal laminate configuration CARALL-B behaves stiffer than CARALL-A after the aluminum yielding region. This behavior can be justified by the fact the metal volume fraction of CARALL-A is more than CARALL-B fiber metal laminate configuration. Due to which CARALL-A laminate is showing more ductile behavior after the aluminum has yielded. The strength of both configurations is comparatively same. There is the difference in strain level at which the failure of carbon fiber layers takes place in both laminates. In CARALL-B FML, it failed at approximately 0.015 strain whereas in CARALL-A FML at 0.027

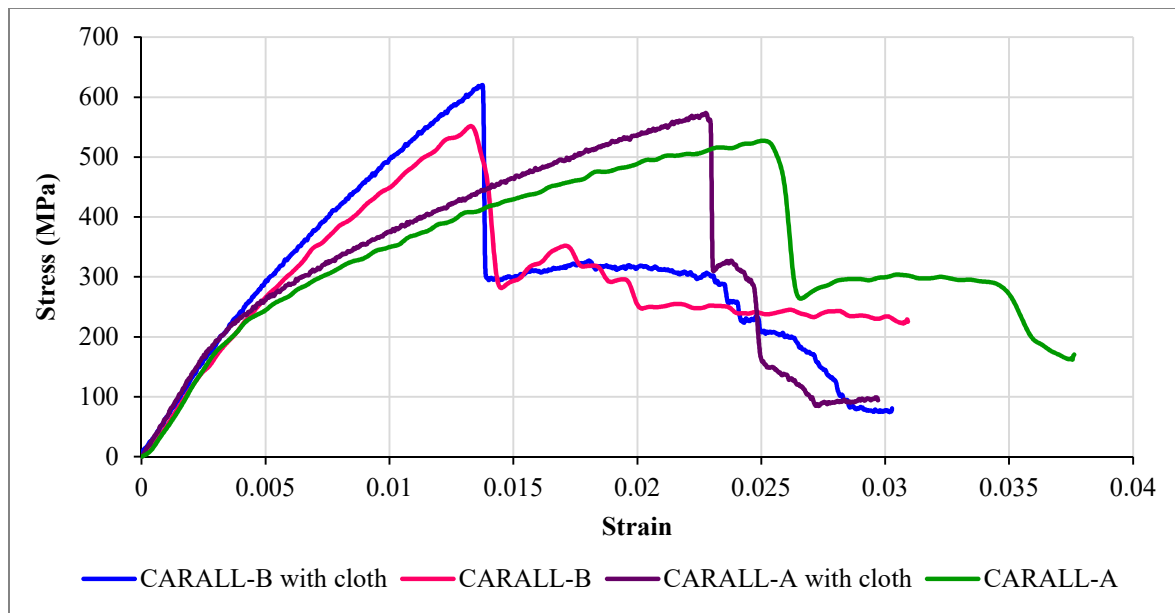


Figure 6.3: Typical flexural behavior plots for CARALL FMLs

The addition of polyester synthetic surfacing veil cloth affects the flexural behavior of both CARALL laminates by increasing the flexural strength (figure 6.3) before failure of specimens. This increase in strength is due to improvement in interlaminar bond strength and reduced delaminated area. Polyester surfacing veil cloth layers reduced the failure strain in

CARALL-A FMLs to 0.023 from 0.027, which is the failure strain of specimens with no veil cloth layers. The addition of polyester surfacing veil cloth does not show any effect on the failure strain of CARALL-B FMLs. A major difference observed in CARALL-A FMLs due to the addition of veil cloth was the simultaneous failure of carbon fiber/epoxy and aluminum layers under tension after reaching the ultimate flexural strength. The carbon fiber/epoxy and aluminum layers fail separately at difference strain values in CARALL-A specimens having no polyester surfacing veil cloth layers.

6.2 Flexure Test Finite Element Analysis

Finite element analysis technique has emerged as one of the most important and helpful tools available to engineer for use in design analysis with the advent of computers. The composite design and analysis problems are complex as they require several input parameters. Therefore, it is very crucial to have a profound understanding of all aspects of fiber metal laminate composite behavior before selecting and applying a material model to computational model. LS-Dyna, a nonlinear finite element analysis code have large no of material models for composite materials along with the failure modes.

FML flexure specimens that were experimentally investigated are computationally analyzed with the help of LS-Dyna finite element analysis package to have a further understanding of failure mechanisms. Three-point bending finite element simulation model involves a difference in the discretization of elements and boundary conditions as compared to tensile test simulation. Thermal stress prediction and initialization were performed in the similar fashion as done in the tensile analysis using dynamic relaxation. The material models for carbon fiber/epoxy & aluminum layers and delamination model were kept same as tensile test simulation. The input parameters to the delamination model, material properties of carbon

fiber/epoxy and aluminum material were kept identical to the tensile simulations. The details aspects of finite element model related to these things can be found in chapter 5.

6.2.1 Discretization of Flexural Fiber Metal Laminate Specimen

The aluminum layers of the specimen are modeled as two layers of 3D hexahedral selective reduced (S/R) integrated continuum linear solid elements with eight nodes (ELFORM 2). The Layers of CFRP are modeled with one layer of 3D hexahedral solid elements having same element formulation as that of aluminum layers. The total number elements in FE model for each aluminum and CFRP layer are 3400 and 1700 respectively. Finite element mesh was generated with an element size of 1.5 mm for both aluminum and CFRP layers having 152.4 mm x 25.4 mm geometric dimensions. The finite element model of CARALL FML with a detailed view of tiebreak interface contacts between adjacent layers is shown in figure 6.4.

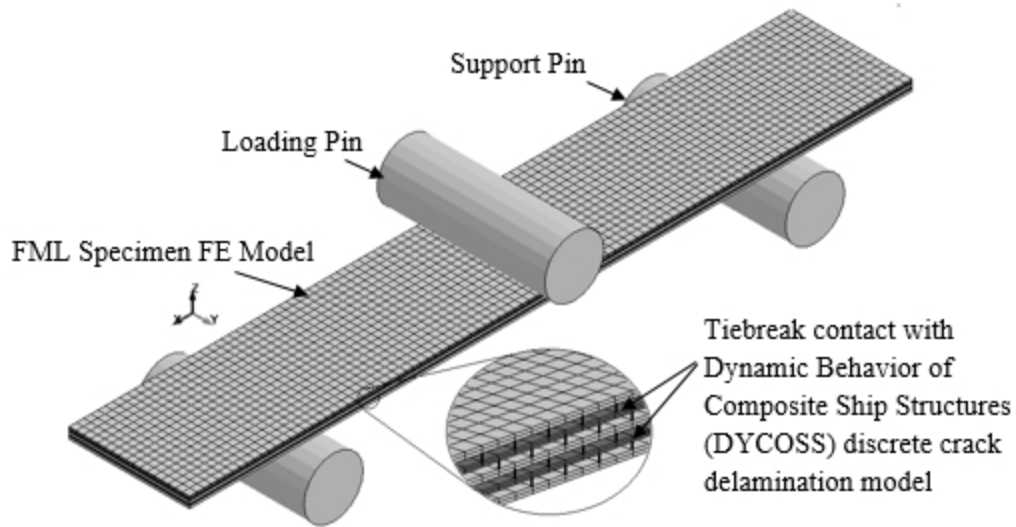


Figure 6.4: Three-point flexural finite element model

6.2.2 Loading Pin & Support Rods Modeling

The loading pin and support rods are modeled with a rigid material. Surface to surface contact having a friction coefficient $\mu=1.0$ was assumed for the interaction between supporting rod and specimen allowing finite sliding. The interaction between loading pin and the specimen

was assumed to have an automatic surface to surface contact with friction coefficient equal to one. Appropriate displacement boundary conditions were assigned to two nodes of the specimen to prevent rigid body motion. The loading pin moves statically 0.05 mm downward in a second. The supports rods were constrained in all degree of freedoms.

6.3 Flexural Experimental Test and FEA Results Comparison

The experimental and FEA predictions for the flexural behavior of all FMLs are presented in the form of a stress-strain curve in Figure 6.5 and 6.8. The predictions made through FEM analysis are shown in dashed lines and the experimental results are plotted in solid lines in these figures. The progressive damage behavior of CARALL fiber metal laminate specimens is characterized and explicated with the stress-strain curves. Experimental and FEA failure modes of CARALL-A FMLs at a specific location of the stress-strain curves can be referred in figures 6.6 and 6.7, whereas for CARALL-B FMLs can be found in figures 6.9 and 6.10.

In the flexural stress-strain curve of CARALL-A FML shown in figure 6.5, initially, a linear region of deformation is found where the load carrying capacity of the samples increases with deformation. This corresponds to global bending of the laminated specimen. After the linear deformation region, the flexural behavior of fiber metal laminate specimen shows the plasticity region due to the metal layers plastic deformation (up to point 1). When the tensile stress in the tension side carbon-epoxy layer reaches failure stress, it initiates a crack in fibers and matrix. As the carbon-epoxy layer fails a sudden drop in load is noted; (region 1-2 in fig 6.5). The load corresponding to region 2-3 of the curve in fig. 6.5 is carried by compression side located above the neutral axis and aluminum layer on tension side.

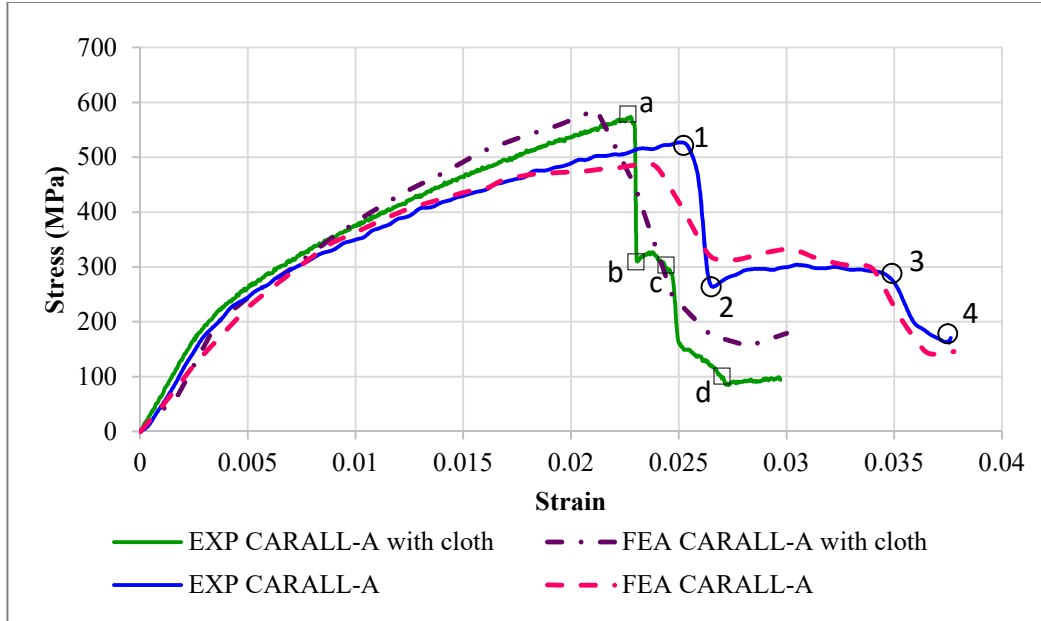


Figure 6.5: Experimental and FEA flexural stress-strain behavior of CARALL-A and CARALL-A with polyester veil cloth layers.

Later, the greater amount of load is transferred to an aluminum layer which is on the tension side after the tensile failure of CRF layer. As a result, a crack grows in this layer in the vicinity of point 3 of the flexural stress-strain curve. Due to which there is a further decrease in load carrying capacity of the beam as described by region 3-4 of figure 6.5.

The addition of polyester synthetic surfacing veil cloth layers affects the failure modes of specimens after the failure of carbon epoxy layer due to tensile loading described by region a-b in figure 6.5. The failure of aluminum layer which is on the tension side occurs earlier after the tensile failure of CRF layer in this case as compared to CARALL-A FML without cloth layers due to reduced delamination resulting from improved AL-CFRP bond strength. The region c-d describes the reduction in load due to the failure of the aluminum layer due to tensile stresses developed. Finite element analysis also captures the failures in layers through element deletion with an adequate accuracy and at right strain level for both CARALL-A and CARALL-A with veil cloth layers FMLs.


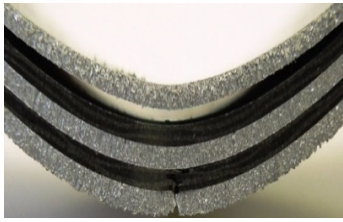

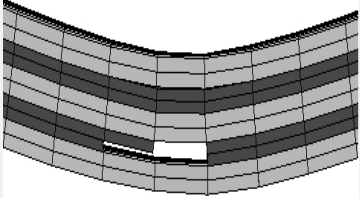
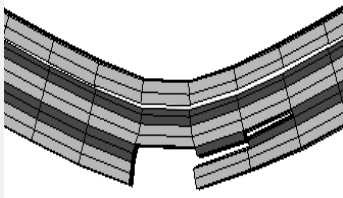
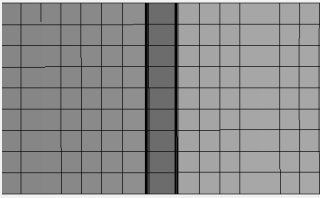
Sample Type	Carbon fiber (CFRP) layer breakage	Delamination b/w upper aluminum & CFRP layer	Crack in lower aluminum layer viewed from bottom
	Location on stress-strain curve Pt (1)	Location on stress-strain curve Pt (3)	Location on stress-strain curve Pt (3)
CARALL-A Experiment Failure Mode			
CARALL-A FEA Failure Mode			

Figure 6.6: Flexural failure modes of CARALL-A fiber metal laminates



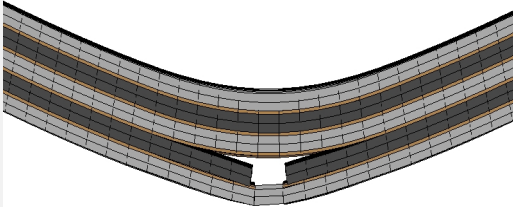
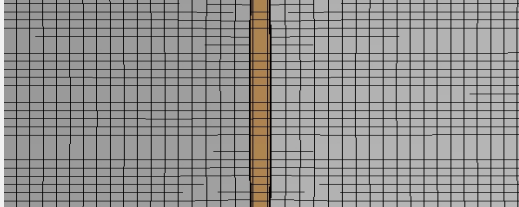
Sample Type	Carbon fiber (CFRP) layer breakage	Crack in lower aluminum layer viewed from bottom
	Location on stress-strain curve Pt (a)	Location on stress-strain curve Pt (c)
CARALL-A with Polyester Surfacing Veil		
CARALL-A with Polyester Surfacing Veil		

Figure 6.7: Flexural failure modes of CARALL-A FMLs having cloth layers.

The contribution of plastic deformation of aluminum layers is less than the CARALL-A to the flexural stress-strain curve of CARALL-B FML. It showed mainly a linear relationship between load and deformation before the tensile failure of CRF layer as shown by region up to point (1) in figure 6.8. A tensile rupture failure of CRF layer was observed after reaching the

maximum tensile strength of CRF layer shown by region (1)-(2) of figure 6.8 resulting in a sudden decrease in loading carrying capacity of the laminated composite beam. After the tensile rupture failure of CRF layer, the transferred load to remaining CRF and aluminum layer were sustained by them up to point (3) of flexural stress-strain curve [region (2)-(3)]. When the compressive stress in the top CRF layer reaches failure stress (at point 3 of flexural stress-strain curve), it initiates a crack in fibers and matrix, resulting in a further decrease in strength of FML beam described by region (3)-(4) of figure 6.8. The load transferred to aluminum layers after CFRP top layer failure results in plastic deformation of aluminum layers. This portion of the flexural test procedure is described in the region (4)-(5) in the stress- strain curve.

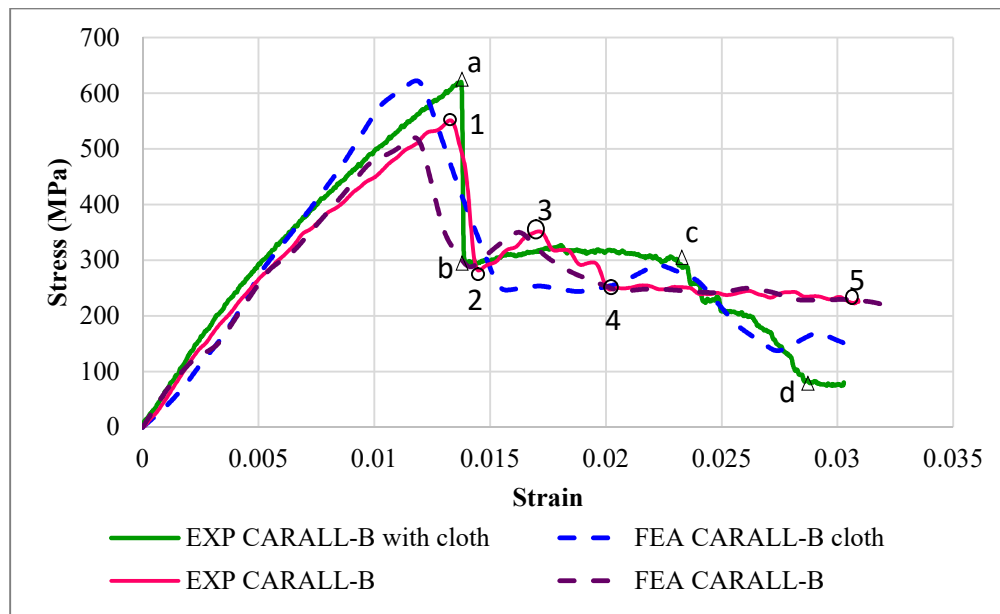


Figure 6.8: Experimental and FEA flexural stress-strain behavior of CARALL-B FMLs

The flexural response and the failure modes of CARALL-B are also affected by the polyester veil cloth layers like the CARALL-A FML. In the global bending region of the stress-strain curve, the CARALL-B laminate behaves slightly stiffer reaching up to a higher maximum failure stress (point-a in figure 6.8). The loss of stiffness due to the tensile failure of outer carbon fiber/epoxy and polyester veil cloth layers is described by region a-b of stress-strain curve shown

in figure 6.8. The region b-c in the stress-strain response of CARALL-B FML having polyester veil cloth layers represents the load carried by the FML beam after the failure of outer CFRP and cloth layers. A difference of no compressive failure of the top CFRP layer underneath the loading point can be noted in this region as compared to the same region 2-3 of CARALL-B stress-strain response. The compressive failure of top CFRP layer underneath the loading point, tensile failure of middle CFRP and aluminum layers occurs after point c in region c-d of the stress-strain curve.

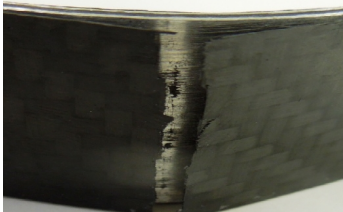
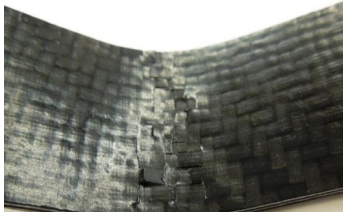

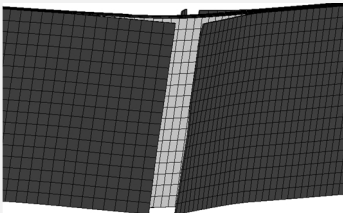
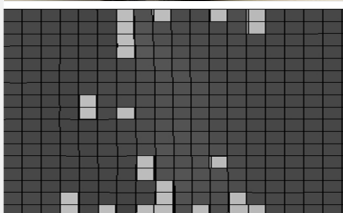
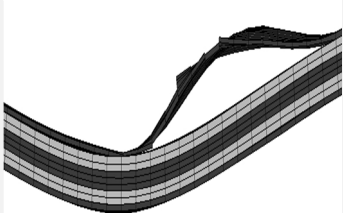
Sample Type	Failure of lower CFRP layer viewed from bottom	Fibers pull out underneath the loading nose	Delamination b/w upper CFRP and aluminum layer
	Location on stress-strain curve Pt (a)	Location on stress-strain curve Pt (b)	Location on stress-strain curve Pt (c)
CARALL-B Experiment Failure Mode			
CARALL-B FEA Failure Mode			

Figure 6.9: Flexural failure modes of CARALL-B fiber metal laminates




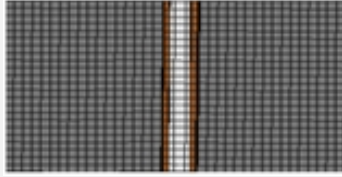
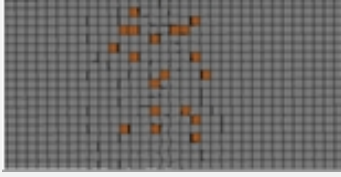
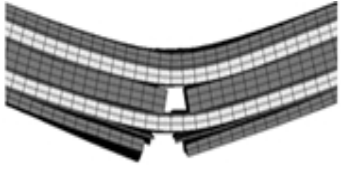
Sample Type	Failure of lower CFRP layer viewed from bottom	Fibers pull out underneath the loading nose	Delamination b/w upper CFRP and aluminum layer
	Location on stress-strain curve Pt (a)	Location on stress-strain curve Pt (a)	Location on stress-strain curve Pt (a)
CARALL-B with Polyester Surfacing Veil			
CARALL-B with Polyester Surfacing Veil			

Figure 6.10: Flexural failure modes of CARALL-B FMLs having cloth layers

The elongation in the region b-c is due to reduced delamination between successive layers as a result of increased interlaminar strength of FML beam because of the presence of polyester synthetic surfacing veil cloth layers. Adhesive delamination was found to be reduced in both CARALL-A & CARALL-B FMLs due to the addition of surfacing veil cloth layers. The predominant failure patterns found in CARALL-A FMLs were a crack in bottom aluminum layer and carbon fiber (CFRP) layer breakage due to tensile stresses developed during flexure loading, whereas failure of lower CFRP layer due to tensile stresses was greatly dominant over other failure modes in influencing the flexural behavior of CARALL-B FMLs. A good agreement is observed in experimental results of progressive damage characterization and FEM predictions for both types of FMLs. A comparison between flexural properties of both FML types and monolithic 5052-H32 aluminum alloy are tabulated in Table 6.1. It can be observed from the tabulated results that there is a significant increase in the specific bending strength in comparison to aluminum 5052-H32 strength for both type of FMLs whereas the modulus of FMLs and monolithic aluminum are comparatively similar.

Table 6.1: Results of flexural experimental tests

Property/Sample	Monolithic Aluminum 5052-H32	CARALL-A	CARALL-B	CARALL A with cloth layers	CARALL B with cloth layers
Maximum bending strength (MPa)	340	515	546	560	620
Maximum strain at breaking point ϵ_{max} (%)	0.032	0.027	0.015	0.022	0.013
Bending stiffness, E (GPa)	69.2	68.3	70.1	71.5	72.3
Density ρ (g/cm ³)	2.68	2.29	2.11	2.08	1.93
Specific bending strength (MPa/(g/cm ³))	126.8	222.7	289.1	269.2	321.2
Specific bending stiffness (GPa/(g/cm ³))	25.8	29.82	33.23	34.37	37.46
Specific bending strength increase (%)	---	79.1	127.9	112.3	153.3

CHAPTER 7 LOW-VELOCITY IMPACT TEST & DATA ANALYSIS

7.1 Low-Velocity Impact Test Experimental Aspects

ASTM standard D7136 [107] was referred to investigate the low-velocity impact behavior of FMLs. A drop weight impact test on CARALL FMLs was performed using a hemispherical striker having a weight of 1.819 kg and a tip diameter of 28.39 mm. A rectangular specimens with a dimensions of 152.4 x 101.6 mm were clamped to a 20 mm thick aluminum plate having a 125mm x 75 mm cutout located at the center with the help of four toggle clamps having a minimum holding capacity of 1100 N. The tips of the clamps were made of neoprene rubber with a durometer of 70-80 Shore A. Guide pins were used to position the specimen centrally over the cutout.

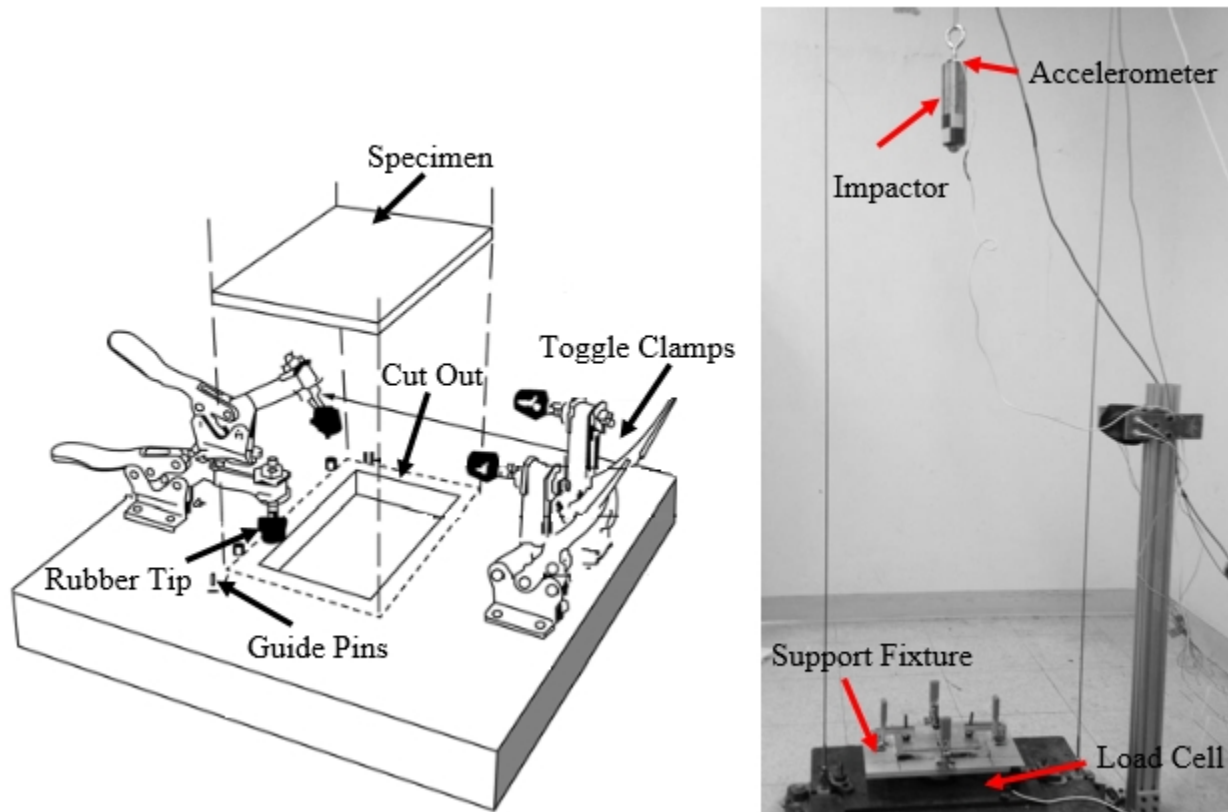


Figure 7.1: Impact Support Fixture and Test Tower [107]

The fixture was aligned to a rigid base using bolts. A representative base design is shown in Fig 7.1a. The designated impact energy was obtained by adjusting the height of the hemispherical impactor. The velocity of the impactor nose was measured with the help of accelerometer located on the top of the striker. The contact force between the striker and the specimen was measured by utilizing load cell located underneath the rigid support fixture. The acceleration-time signal measured by the acquisition system was integrated twice to obtain the displacement. The impact acceleration-time and force-time relation were obtained for each impact event. The CARALL FMLs were experimentally tested at impact energies of 14J, 21J, and 31J by utilized the drop weight impact tower shown in Fig 7.1b. An assumption of no energy loss was made in the calculations for the contact between the striker tip and sample during the impact event. Some specimens were carefully sliced through the center to observe the damage behavior through the laminate thickness with the help of cross-sectional microscopy. All the laminates were scanned with the C-scan equipment prior to testing to check the presence of any interface bonding defects between CFRP and aluminum layers. The results were excellent showing good bonding at all interfaces.

7.1.1 Effect of Polyester Surfacing Veil Cloth Layers on Low-Velocity Impact Behavior

The typical force-displacement (F-D) response of CARALL-A specimens manufactured with and without polyester surfacing veil cloth is compared with each other at different impact energies in figure 7.2. Similarly, the force-displacement response comparison of CARALL-B specimens made with and without veil cloth layers is shown in Figure 7.3. The force-displacement response of CARALL specimens made without using veil cloth layers are in dashed lines and the response of CARALL specimens made with veil cloth layers are plotted in solid lines. A gaussian data smoothing technique was used over the experimental data to remove

the noise captured by acquisition system during the impact test. Each F-D curve has an ascending portion of loading known as bending stiffness due to the resistance of the composite to impact loading, the peak load value and descending section of unloading.

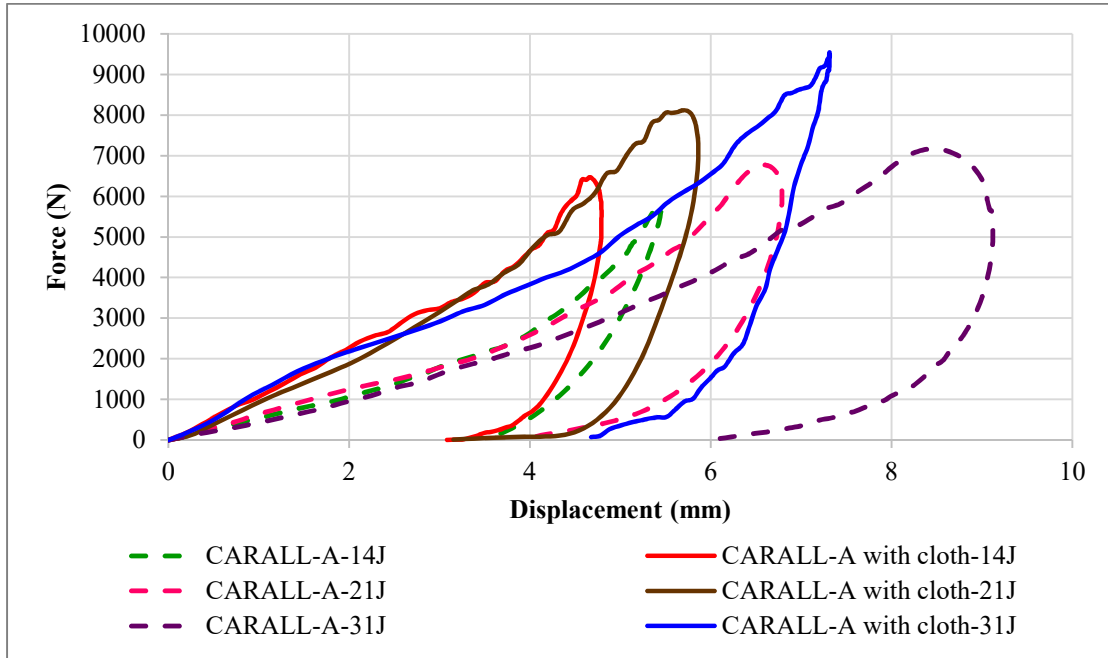


Figure 7.2: Force-displacement plots for CARALL-A FMLs made with and without veil cloth

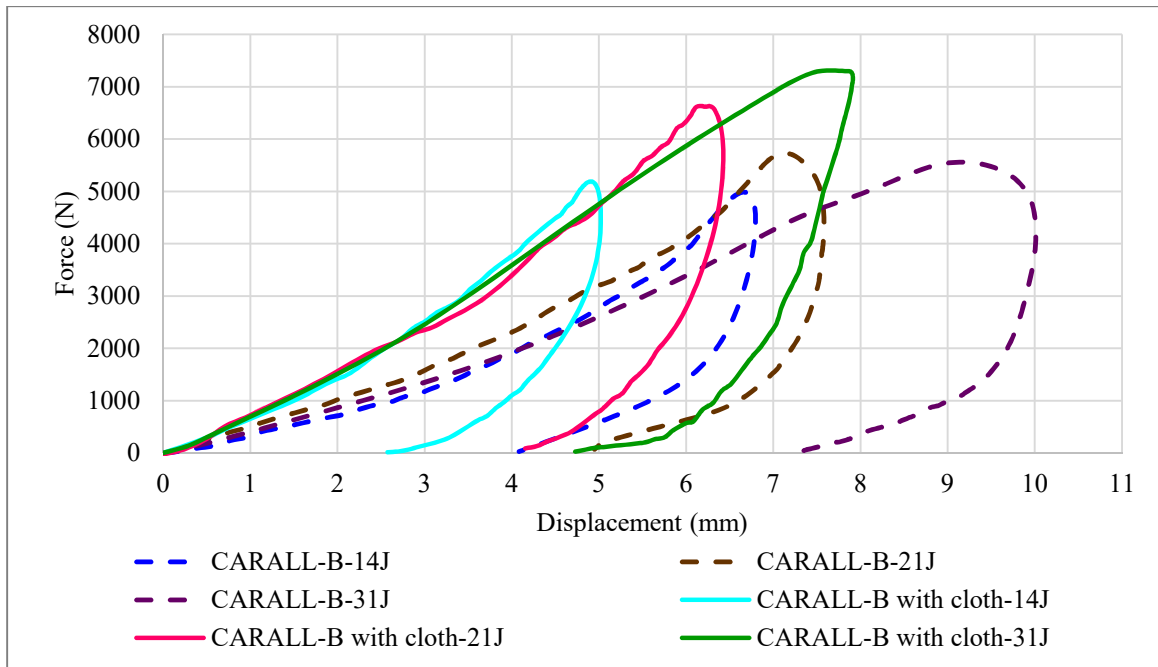


Figure 7.3: Force-displacement plots for CARALL-B FMLs made with and without veil cloth

It can be observed from figures 7.2 and 7.3 that the both CARALL-A & B specimens made with the addition of polyester veil cloth layers showed higher peak forces and smaller permanent central deflections as compared to specimens made without veil cloth layers at all impact energies. The increase in peak forces is due to improve the interlaminar bond strength of the FMLs due to the presence of polyester veil cloth layers with act as resin carrier while curing of laminates. With the increase in impact energy, more delamination, fiber and matrix damage was observed in specimens made without using veil cloth layers resulting in larger permanent central deflection as compared to specimens made with veil cloth layers at all impact energies in both types of CARALL FMLs. The damage morphologies for both types of CARALL specimens made with and without cloth layers are evaluated at impacted and non-impacted side at all the impact energies as shown in figures 7.4 and 7.5.

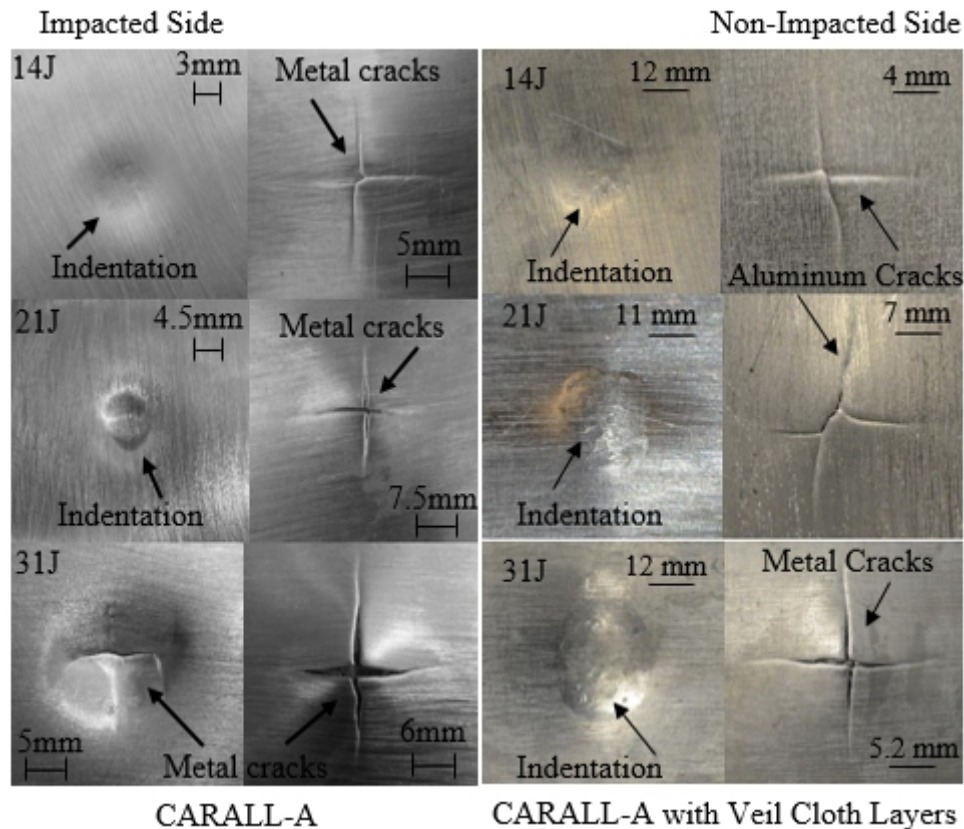


Figure 7.4: Damage morphology of CARALL-A specimens on impacted and non-impacted sides

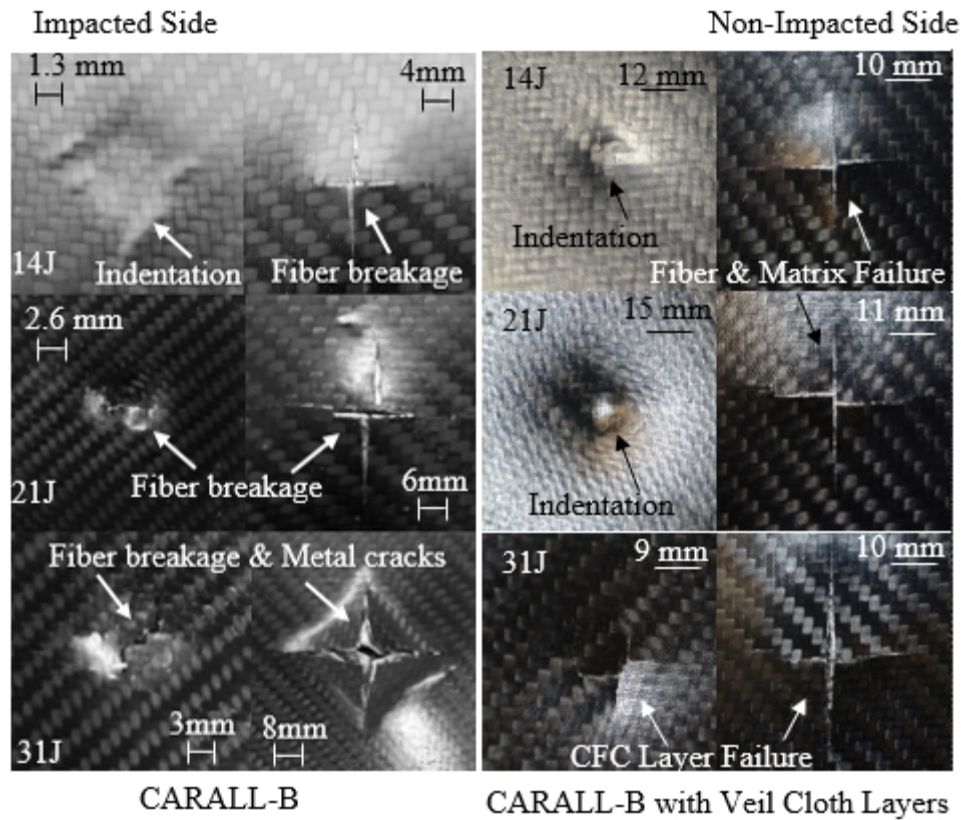


Figure 7.5: Damage morphology of CARALL-B specimens on impacted and non-impacted sides

The polyester veil cloth layers tend to make the laminate behaves as single material by improving the interlaminar bond strength and thus reducing the cracks in the non-impacted sides of aluminum and carbon fiber/epoxy layers in CARALL-A & B FMLs made with veil cloth layers. The major difference made in the damage morphologies with the addition of polyester veil cloth layers in both types of FMLs can be seen at the 31J impact energy. CARALL-A specimens made without veil cloth layers showed an indentation-induced crack in an aluminum layer on the impacted side at 31J impact energy shown in figure 7.4 whereas the CARALL-A specimens having veil cloth layers does not show this type of crack on the impacted aluminum layer. Apart from reducing the damage size of impacted carbon fiber/epoxy layer in CARALL-B specimens, the addition of veil cloth layers also hinders the failure of internal metallic layers as can be seen in figure 7.5 at 31J impact energy. Table 7.1 and 7.2 provides a comparison of the

impact induced crack lengths measured on the impacted and the non-impacted sides respectively, along with the ultimate central deflection in CARALL FMLs specimens made with and without using polyester veil cloth layers at various impact energies. A schematic describing the method adopted to measure the central deflection of CARALL FMLs is shown in Figure 7.6.

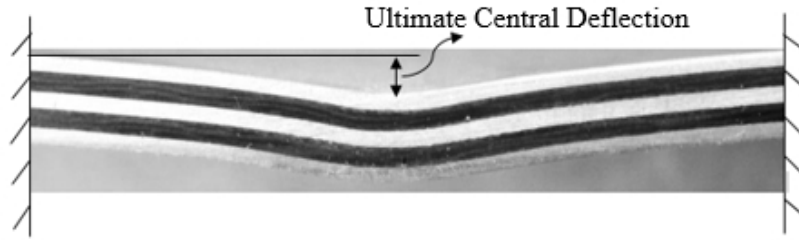


Figure 7.6: Ultimate Central Deflection Schematic

Table 7.1: Ultimate central deflection and crack lengths in outer layers of CARALL-A FMLs

Impact energy (J)	CARALL-A			CARALL-A with Polyester Veil Cloth Layers		
	Crack Lengths (mm)		Ultimate Central Deflection (mm)	Crack Lengths (mm)		Ultimate Central Deflection (mm)
	Impacted Side	Non-Impacted Side		Impacted Side	Non-Impacted Side	
14	0	20	5.45	0	16.17	4.74
21	0	24	6.78	0	21.40	5.89
31	18	31	9.11	0	29.06	7.31

Table 7.2: Ultimate central deflection and crack lengths in outer layers of CARALL-B FMLs

Impact energy (J)	CARALL-B			CARALL-B with Polyester Veil Cloth Layers		
	Crack Lengths (mm)		Ultimate Central Deflection (mm)	Crack Lengths (mm)		Ultimate Central Deflection (mm)
	Impacted Side	Non-Impacted Side		Impacted Side	Non-Impacted Side	
14	5	30	6.79	0	29.2	5.02
21	12	46	7.58	0	39.5	6.4
31	20	55	10.01	13.2	45.72	7.9

7.2 Low-Velocity Impact Finite Element Analysis

The low-velocity impact response of CARALL FMLs was modeled with the help of commercially available LS-DYNA software by using explicit time integration scheme. The development of FE model for impact test simulations in LS-DYNA includes discretization of sample geometry into finite elements, modeling of a composite material including intralaminar failure and delamination failure, modeling of aluminum material with strain-based failure criteria and modeling of a rigid hemispherical striker with appropriate contact algorithm and boundary conditions. Thermal stress prediction and their initialization to impact FE models were performed in the similar fashion as done in the tensile analysis using dynamic relaxation. The material models for carbon fiber/epoxy and aluminum layers were kept same as tensile simulation. The material properties of carbon fiber/epoxy and aluminum layers were kept identical to the tensile simulations. Plastic Kinematic material model was employed for modeling the polyester surfacing veil layers using the material properties mentioned in Table 3.7.

7.2.1 Discretization of Impact FML Specimen

In the low-velocity impact simulations, the aluminum layers of the specimen were modeled using two-dimensional selective reduced (S/R) integrated continuum linear shell elements with four nodes (ELFORM 2). The CFRP plies were also modeled with two-dimensional selective reduced (S/R) integrated linear shell elements considering one layer of shell elements for each lamina with three integration points with respect to ply thickness. The total number elements in FE model for each aluminum and CFRP layer are 15606. Finite element mesh was generated with an element size of 1.0 mm for both aluminum and CFRP layers having 152.4 mm x 101.6 mm geometric dimensions. The finite element model of CARALL FML with a detailed view of tiebreak interface contacts between adjacent layers is shown in Figure 7.7.

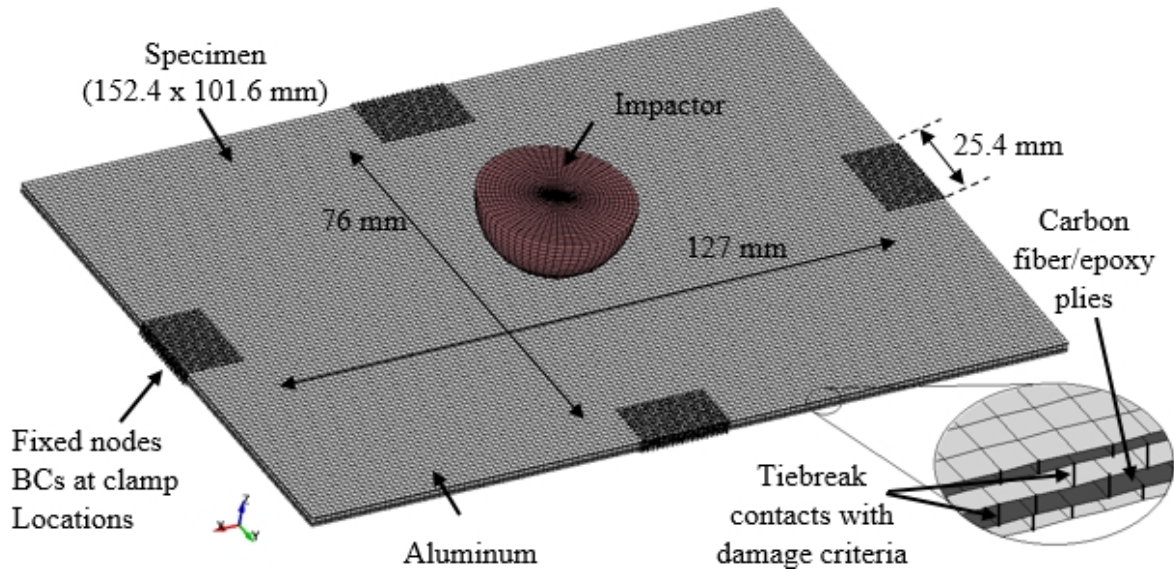


Figure 7.7: Details of finite element model for impact simulation as in actual experiments.

A (IHQ=4) stiffness based hourglass control was used for the aluminum layers, and (IHQ=8) hourglass control which have full-projection warping stiffness control was utilized for the carbon fiber/epoxy layers to get more accurate results. Hourglass control is viscosity or stiffness that is added to selective reduced integrated quadrilateral shell elements or hexahedral solid elements to prevent zero-energy modes of deformation that produce zero strain and no stress. Without hourglass control, these elements will have nonphysical hourglass modes which could grow large and destroy the solution. Two different types of hourglass formulations were chosen considering the material models used to model aluminum and CFRP layers. A stiffness based hourglass formulation (IHQ=8) have an algorithm to activate warping stiffness also, due to which it gives more accurate results for orthotropic materials than hourglass formulation (IHQ=4). The value of hourglass coefficient (QH=0.05) was kept similar in both hourglass formulations

7.2.2 Delamination Modeling

Delamination is the one of the main sources of damage of damage in the laminated fiber metal laminates, separation of plies in low resistance interface between adjacent layers under compressive loading or impacts. The linear fracture mechanics techniques (LEFM) like virtual crack extension [108], the J-integral[109] , the virtual crack closure (VCC) [110, 111] and the stiffness derivative [112] based on Griffith criteria [113] can be used to predict delamination in laminated composites in the absence of any nonlinearities. These methods are restricted to problems where the initial crack is known, therefore, these methods cannot be used to predict the initiation of delamination [114]. Damage mechanics and/or softening plasticity combined with the indirect introduction of fracture mechanics based methodologies have been developed to model the mechanical response of interface [115-121]. Cohesive zone model is one of these methodologies which may be considered to be developed from the work of Hillerborg et al.[115].

7.2.2.1 Cohesive Zone Model

A detailed view of the crack tip can be used to explain the cohesive zone approach. A transition region commonly known as process zone is present in crack ahead of traction free region and before the intact region. The position of different regions available in a crack is illustrated in Figure 7.8. In Figure 7.8, the existence of cohesive forces in the process zone is illustrated by springs. These cohesive forces give birth to a unique traction profile at the crack edge. The dominance of cohesive effect in the *cohesive zone* only is illustrated by drawing the edge of the crack like sharp tip of a water drop. The cohesive zone method relates the tractions to displacement at an interface developing a crack. Bilinear model is the most frequently and successfully used model for traction-separation response of crack in cohesive zone method. Accurate results are provided by the bilinear model for composite materials.

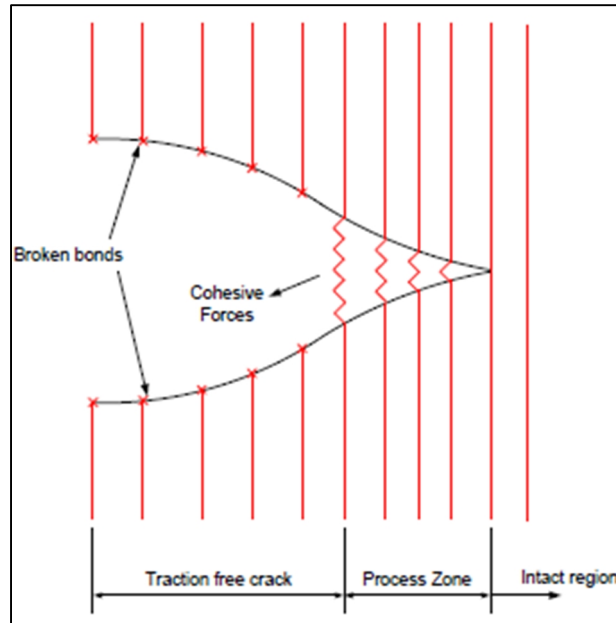


Fig 7.8: Different regions of a crack. [122]

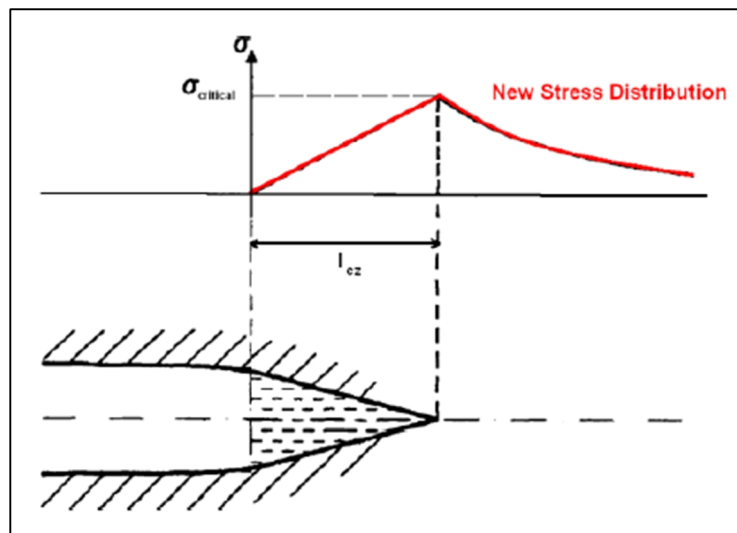


Figure 7.9: Cohesive zone stress distribution.[120]

Intralaminar delamination between the carbon fiber/epoxy (CFRP) and aluminum layers in this research work was modeled by employing tiebreak contact algorithms with cohesive zone method available in LS-DYNA[99]. The transmission of both compressive and tensile forces are allowed in these penalty-based contact algorithms which are used to model connection between surfaces. The tie-break contact algorithms prevent the separation of the slave node from the

master segment before failure of a connection and after the failure, the contact behaves like surface to surface contact with thickness offsets due to the removal of tensile coupling. Depending upon the nature of the connection, an optional failure criterion can be defined in all tie-break contacts.

7.2.2.2 Mixed-Mode Cohesive Zone Model Derivation

In this study, an extended form of Dycoss discrete crack model failure [50, 105, 123-125] criteria that are based on the fracture model defined in a cohesive material which includes a bilinear traction separation law with quadratic mixed-mode delamination criterion and a Benzeggagh–Kenane [126] proposed damage propagation formulation was used. The distance between two points initially in contact in the normal and tangential directions correspond to complete material failure referred as ultimate displacements in the interface cohesive model. A linear stiffness provided by the bilinear traction separation law for loading followed by the linear softening for damage portion is based on the equation (30) that relate the energy release rates, the peak tractions, and the ultimate displacements.

$$G_{IC} = \frac{T \cdot UND}{2} \quad G_{IIC} = \frac{S \cdot UTD}{2} \quad (30)$$

Where UND is the ultimate displacement in the normal direction; UTD is the ultimate displacement in the tangential direction, G_{IC} the Mode I energy release; G_{IIC} the Mode II energy release; T is the peak traction in normal direction and S is the peak traction in the tangential direction.

In the cohesive material model, the total mixed mode relative displacement δ_m is defined as $\delta_m = (\delta_I^2 + \delta_{II}^2)^{1/2}$ (31)

Where $\delta_I = \delta_3$ (Fig: 7.10) is the separation in the normal direction (Mode I) and $\delta_{II} = (\delta_1^2 + \delta_2^2)^{1/2}$ is the separation in the tangential direction (Mode II) and the damage initiation displacement δ_0 for the mixed mode delamination (onset of softening) is given by equation 32.

$$\delta_0 = \delta_I^0 \delta_{II}^0 \sqrt{\frac{1 + \xi^2}{(\delta_{II}^0)^2 + (\xi \delta_I^0)^2}} \quad (32)$$

Where $\delta_I^0 = T/EN$ and $\delta_{II}^0 = S/ET$ are the single mode damage initiation separations, $\xi = \delta_{II}/\delta_I$ is the ‘‘mode mixity’’ (Figure 7.10); EN the stiffness normal to the interface plane; ET the stiffness into the interface plane. The ultimate mixed mode displacement δ^F (total failure) was used according to the Benzeggagh–Kenane law given in equation 33.

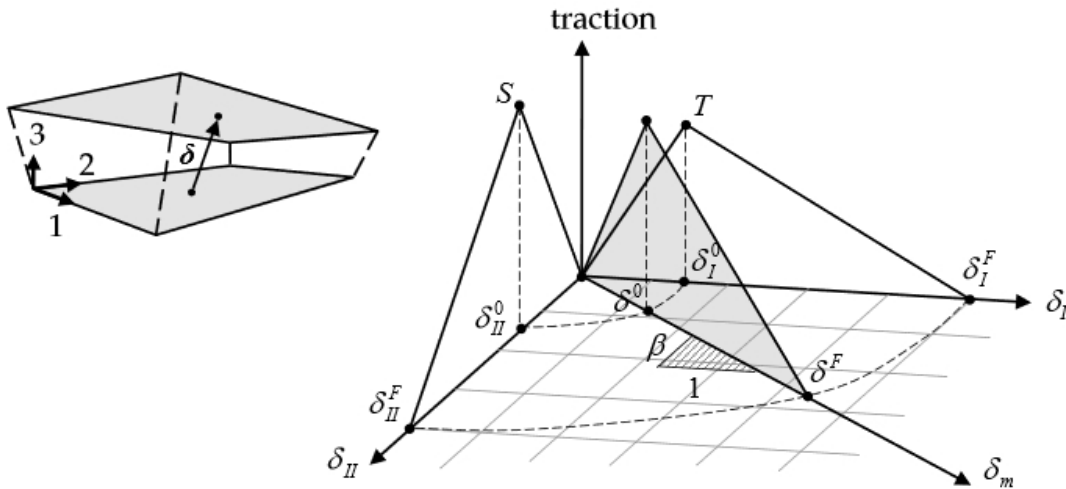


Figure 7.10: Mixed-mode traction-separation law [105]

$$\delta^F = \frac{2}{\delta^0 \left(\frac{1}{1 + \xi^2} EN^\gamma + \frac{\xi^2}{1 + \xi^2} ET^\gamma \right)^{1/\gamma}} G_{IC} + (G_{IIC} - G_{IC}) \frac{\xi^2 ET}{EN + \xi^2 ET}^{XMU} \quad (33)$$

Where XMU is the exponent of mixed mode criteria. Although the computational cost was increased by modeling each layer with separate shell elements but the ability to predict the delamination damage with greater accuracy was offered by this approach. The adhesion properties of aluminum and CFRP layers bond used as input to tiebreak contact in the simulation

are given in Table 7.3. The values of peak tractions in normal and tangential directions were determined experimentally through T-peel and double notch shear strength tests. Mode I energy release rate was calculated from T-peel test data using area method given by equation 34 whereas Mode II energy release rate and mixed mode damage criteria exponent (XMU) values were assumed after referring to the work of Shin and Kim [127]. The values of the rest of the parameters were kept to their defaults settings as described in Table 7.3.

$$G = \frac{1}{b} \frac{E}{a} \quad (34)$$

where b is the width of the sample, ΔE is the area under the load-displacement curve and Δa is the crack extension.

Table 7.3: Cohesive zone delamination model input data

Sample Type	T (MPa)	S (MPa)	G_{IC} (MPa*mm)	G_{IIC} (MPa*mm)	EN	ET2EN	γ	XMU
No Veil	20	15	0.18	0.23	default	1	1	-1.4
With Veil	40	50	0.26	0.52	default	1	1	-1.4

A negative sign of XMU parameter invokes the B-K damage propagation model. The normal stiffness (EN) was not provided explicitly to the damage model. Penalty stiffness (default) was used by the model as the normal stiffness. The parameter ET2EN in Table 7.3 is the ratio of the tangential stiffness to the normal stiffness. The impactor was meshed with 8-node linear brick, reduced-integration solid elements and modeled as hemispherical rigid body using rigid material model (Mat_020) with steel material properties as given in Table 7.4. The impactor was constrained to move only in z-direction through the material model card and a prescribed initial velocity was assigned to it to get desired impact energy. The penalty formulation based surface to surface contact was applied for the interaction of impactor with

impacted plate and each contacted ply of the laminate by setting SOFT option of contact card to equal to 2. The specimen nodes were constrained in all directions located at the toggle clamp locations so as to match the experimental boundary conditions as described in Figure 7.7. A friction coefficient, $\mu=0.3$ was applied for the contact between impactor and the laminate.

Table 7.4: Steel impactor properties

Material	$\rho(\text{kg/m}^3)$	E (GPa)	ν	G(GPa)
Steel	7800	210	0.33	78.9

7.3 Low-Velocity Experimental Impact Test and FEA Results Comparison

In this section, a comparison between finite element predictions and experimental results is made on the basis of force-displacement history curves, impacted and nonimpacted side damage morphologies, cross section images, delaminated area, absorbed energy and energy restitution coefficient for CARALL FMLs. These low-velocity impact characteristics of both CARALL FMLs will be discussed in this section.

7.3.1 Force-Displacement Characteristics

The typical force-displacement (F-D) response of CARALL-A FMLs made with and without using polyester (veil) cloth layers is compared with finite element predictions at different impact energies and shown in figures 7.11 and 7.12. The predictions made through FEM analysis are shown in dashed lines and the experimental results are plotted in solid lines.

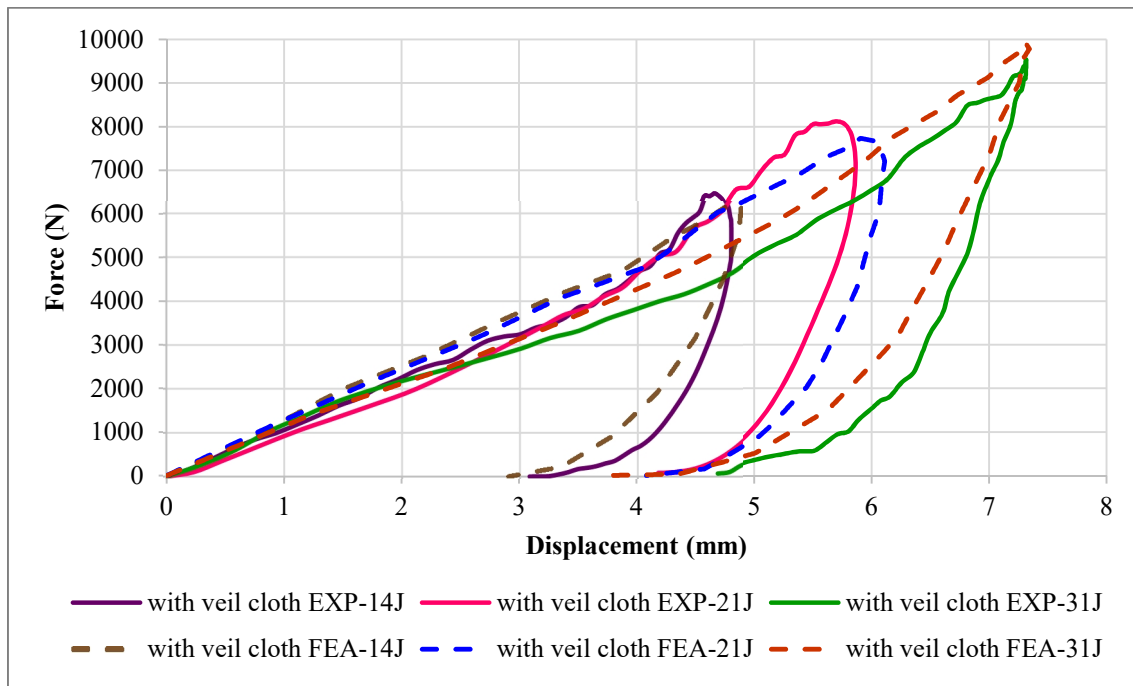


Figure 7.11: Experimental and FEA force-displacement plots for CARALL-A FMLs made with veil cloth

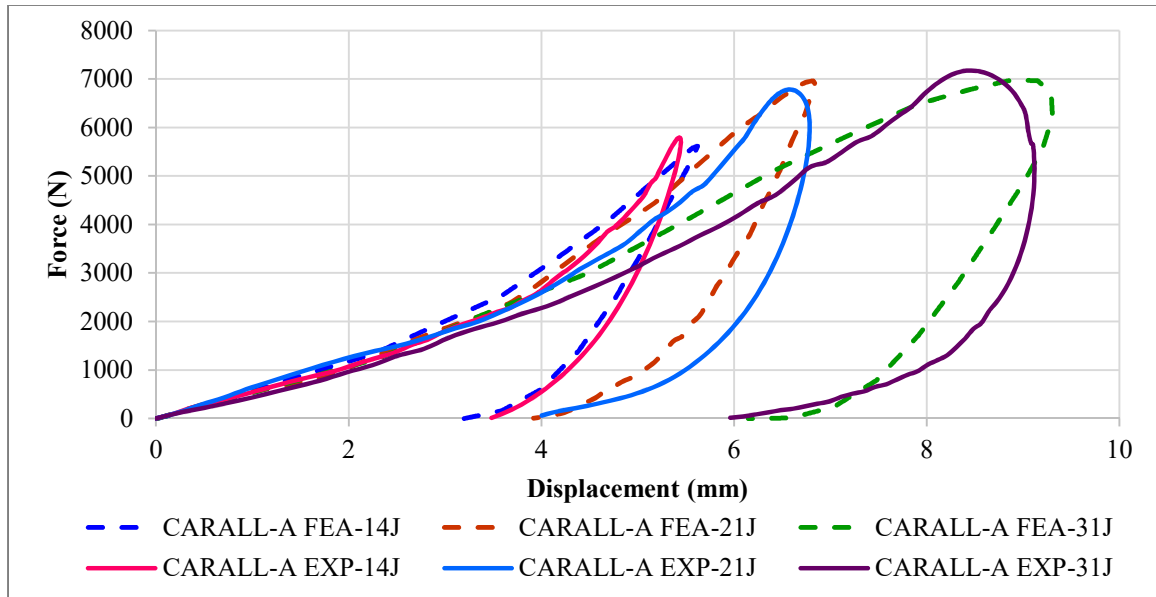


Figure 7.12: Experimental and FEA force-displacement plots for CARALL-A FMLs made without using veil cloth layers.

Each F-D curve has an ascending portion of loading known as bending stiffness due to the resistance of the composite to impact loading, the peak load value and descending section of unloading. The closed type F-D curves of CARALL FMLs for all impact energies implies that complete penetration and perforation was not observed in this study. The peak force increases with the increase in the impact energy for both types of FMLs. However, more damage was induced around the peak force with the increase in the impact energy resulting in a different unloading portion of each F-D curve. The typical force-displacement (F-D) response of CARALL-B FMLs made with and without using polyester, (veil) cloth layers is compared with finite element predictions at different impact energies and shown in figures 7.13 and 7.14. The finite element predictions showed acceptable agreement with the experimental results for the ascending portion of the F-D curves but demonstrated some discrepancies in the unloading section which may be due to the failure of present finite element material model to capture the behavior of FMLs in unloading portion due to complex damage modes of FMLs. The

experimental peak load values of all CARALL FMLs specimens attained at different impact energy levels are tabulated in Table 7.5. The low increase in peak load value from 21J to 31J in CARALL-B specimens may be due to more delamination and excessive crack in metallic layers.

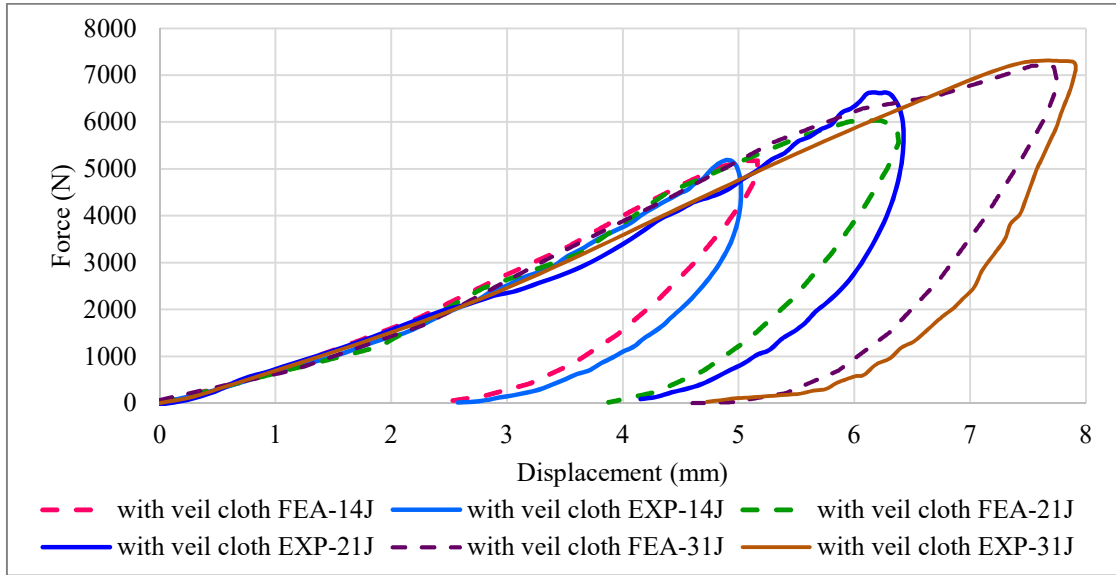


Figure 7.13: Experimental and FEA force-displacement plots for CARALL-B FMLs made with veil cloth layers.

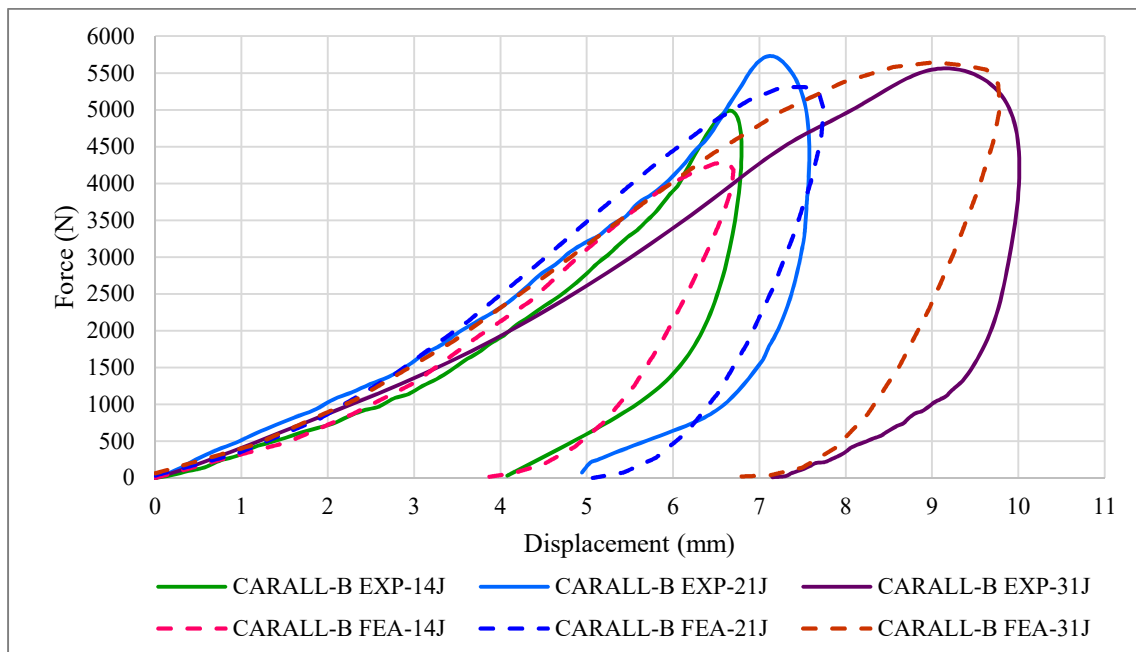


Figure 7.14: Experimental and FEA F-D curves for CARALL-B FMLs made without using veil cloth layers.

Table 7.5: Peak load levels of different CARALL FMLs

Impact energy (J)	CARALL-A (N)	CARALL-A having polyester veil cloth layers (N)	CARALL-B (N)	CARALL-B having polyester veil cloth layers (N)
14	5487	6407	4987	5138
21	6962	8115	5730	6617
31	7132	9440	5640	7286

7.3.2 Damage Morphologies

The damage morphologies of CARALL-A specimens made without and with using polyester veil cloth layers are evaluated at impacted and non-impacted side for the all the impact energies and compared with FEA views as shown in Figures 7.15 and 7.16. The CARALL specimens were cut carefully with a diamond cutter along the main crack direction to observe the inner damage behavior.

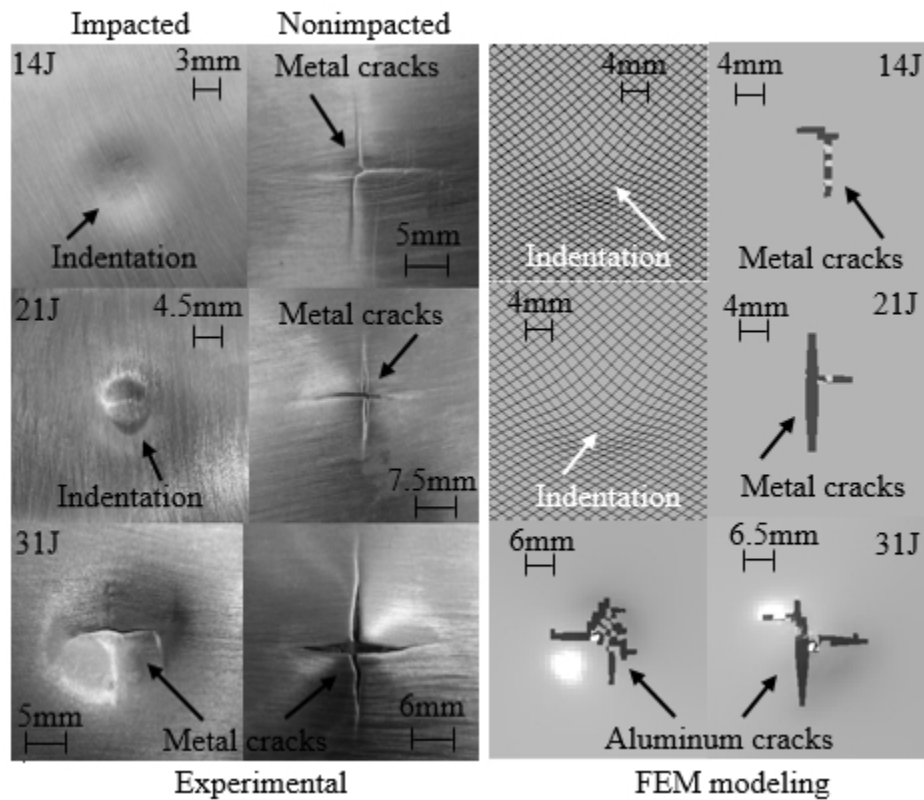


Figure 7.15: Damage morphologies of CARALL-A specimen made without veil cloth layers

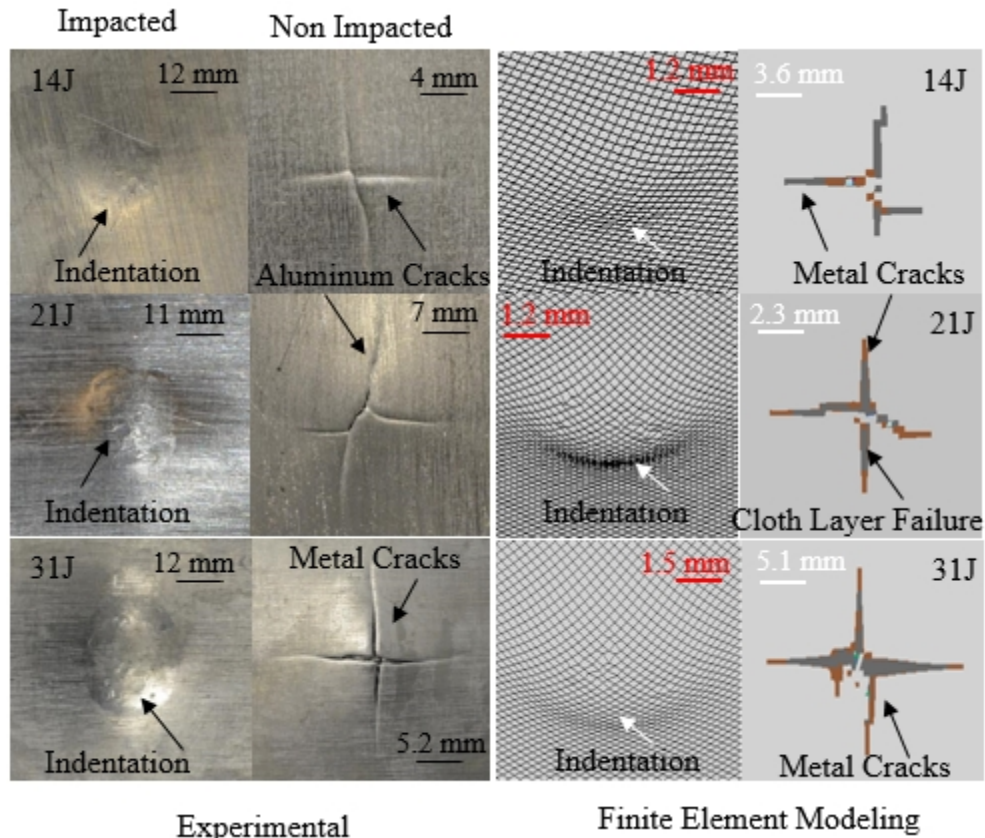


Figure 7.16: Damage morphologies of CARALL-A specimen made with veil cloth layers

The cross-section images of CARALL-A FMLs damaged specimens are examined and compared with FEA model shown in Figures 7.17 and 7.18. The damage morphologies of CARALL-B specimens made without and with using polyester veil cloth layers evaluated at impacted and non-impacted sides for the all the impact energies are compared with FEA views as shown in Figures 7.19 and 7.20. For the lowest impact energy, minor cracks were observed on the non-impacted side aluminum and carbon fiber/epoxy layers in CARALL-A and CARALL-B FMLs specimens respectively. However, the primary damage modes are indentation-induced, fiber fracture and adhesive delamination at the aluminum carbon fiber/epoxy interfaces as shown by the cross-section images in Figures 7.17 and 7.21.

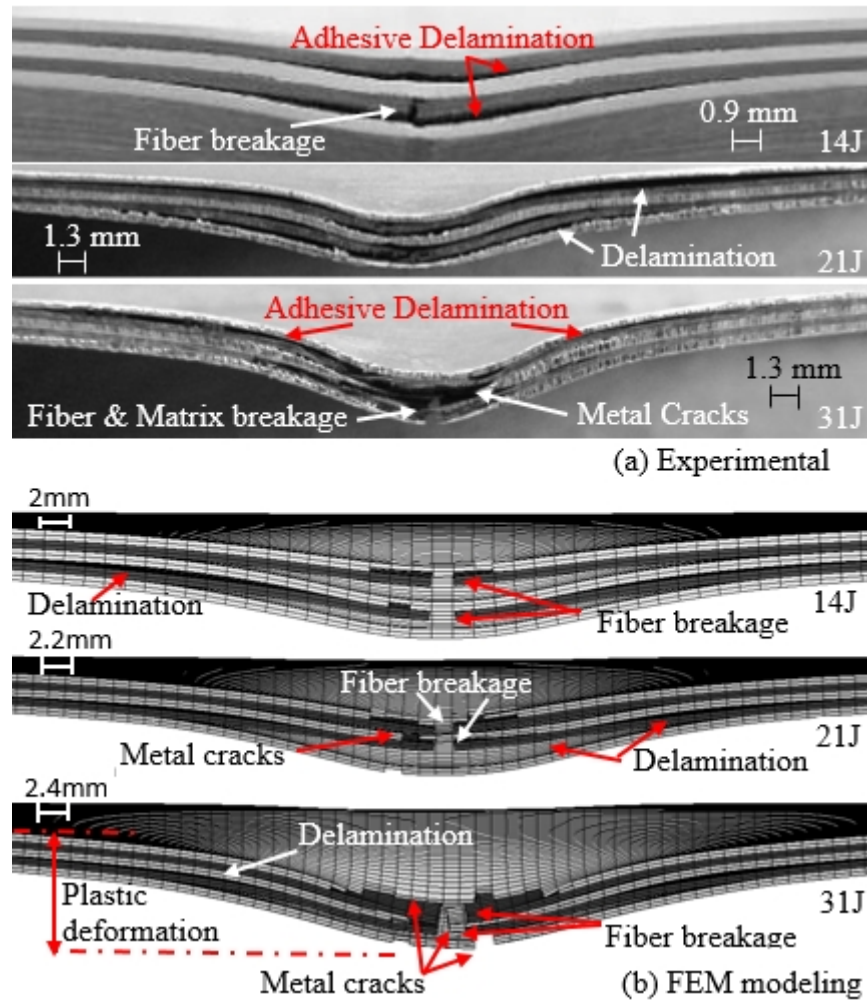


Figure 7.17: Cross-section images of CARALL-A specimens made without using polyester synthetic surfacing veil cloth layers under different impact energies.

The fiber fracture was also observed in both cases along with the adhesive delamination in the cross section images. The finite element model also captures the cracks on the outer aluminum and carbon fiber/epoxy layers through the deletion of elements by using the specified effective plastic failure strain and maximum allowable stress values for aluminum and carbon fiber/epoxy layers, respectively. The predicted crack lengths were found comparable to the measured impact induced crack length. The cross section images of CARALL-A FMLs made with polyester veil cloth layers shown in Figure 7.18 does not show any major adhesive delamination that can be captured by naked eye at 14J and 21J impact energy level. However the

CARALL-B specimens made with veil cloth layer does show delamination in cross section images shown in Figure 7.22 at 14J and 21J impact energy level.

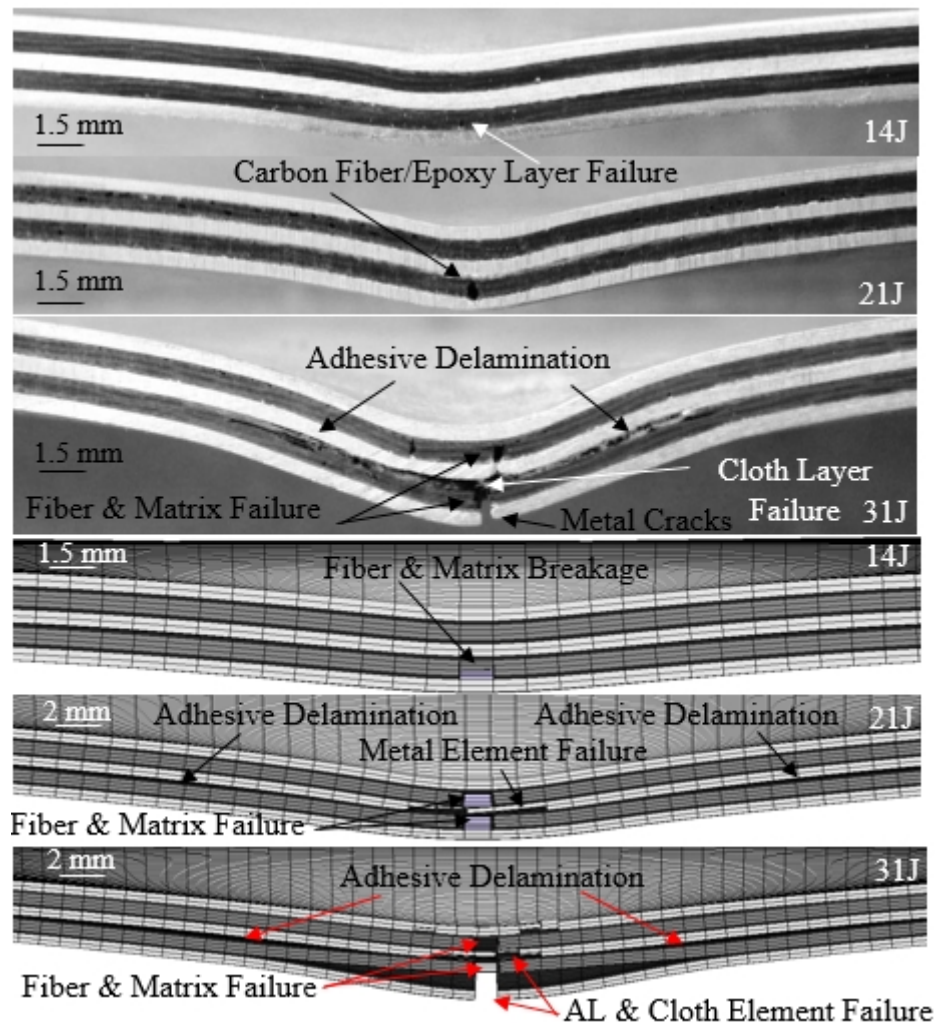


Figure 7.18: Cross-section images of CARALL-A specimens made with polyester synthetic surfacing veil cloth layers under different impact energies.

As the impact energy increases to 21J, the crack lengths on the non-impacted side for CARALL specimens increases, along with indentation depth. Comparatively, to previous impact energy, larger adhesive delamination, fiber, and matrix fracture was observed in the CARALL specimens made without using veil cloth layers shown by cross-section images in figures 7.17 and 7.21.

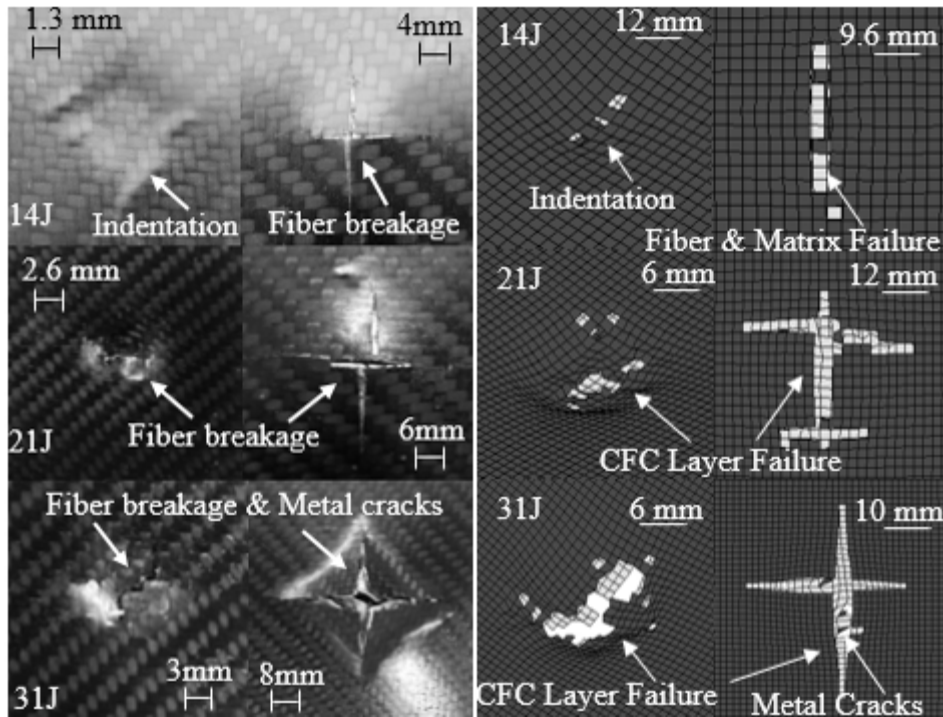


Figure 7.19: Damage morphologies of CARALL-B specimen made without veil cloth layers

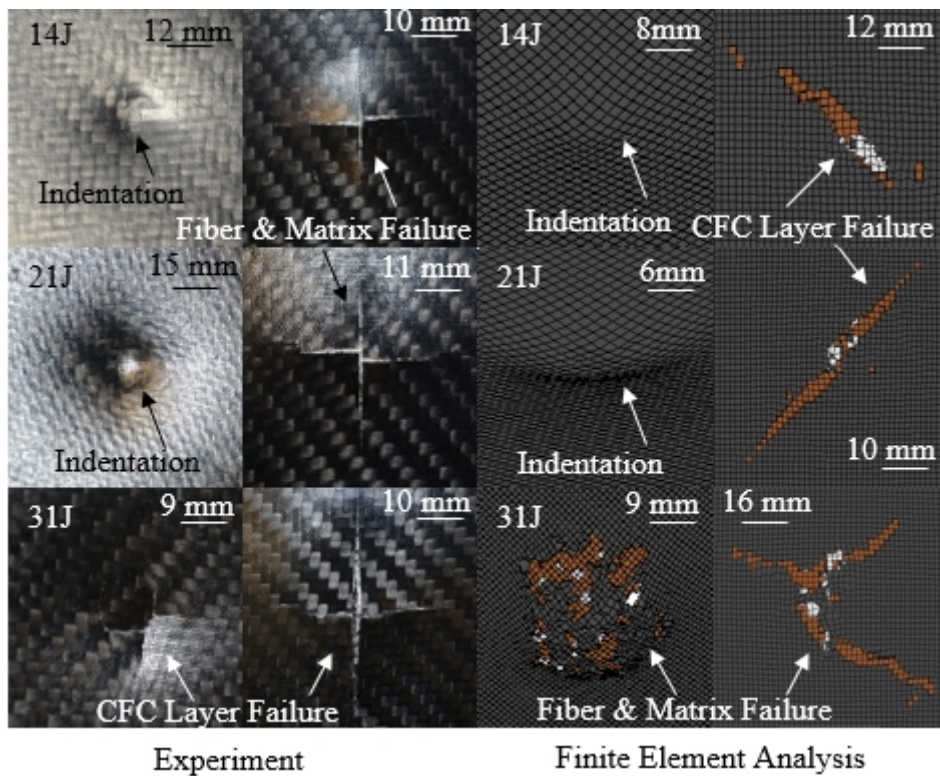


Figure 7.20: Damage morphologies of CARALL-B specimen made with veil cloth layers

The failure of the aluminum layer located adjacent to non-impacted carbon fiber/epoxy along with a minor cohesive delamination between the middle carbon fiber/epoxy layers in CARALL-B specimens not having polyester veil cloth layers was also observed. Further increasing the impact energy to 31J, resulted in a much larger increase in crack lengths on the non-impacted sides of CARALL specimens. The failure of interior metallic aluminum layers and carbon fiber/epoxy layers to a much larger extent at 31J impact energy can be observed in cross section images all CARALL FMLs.

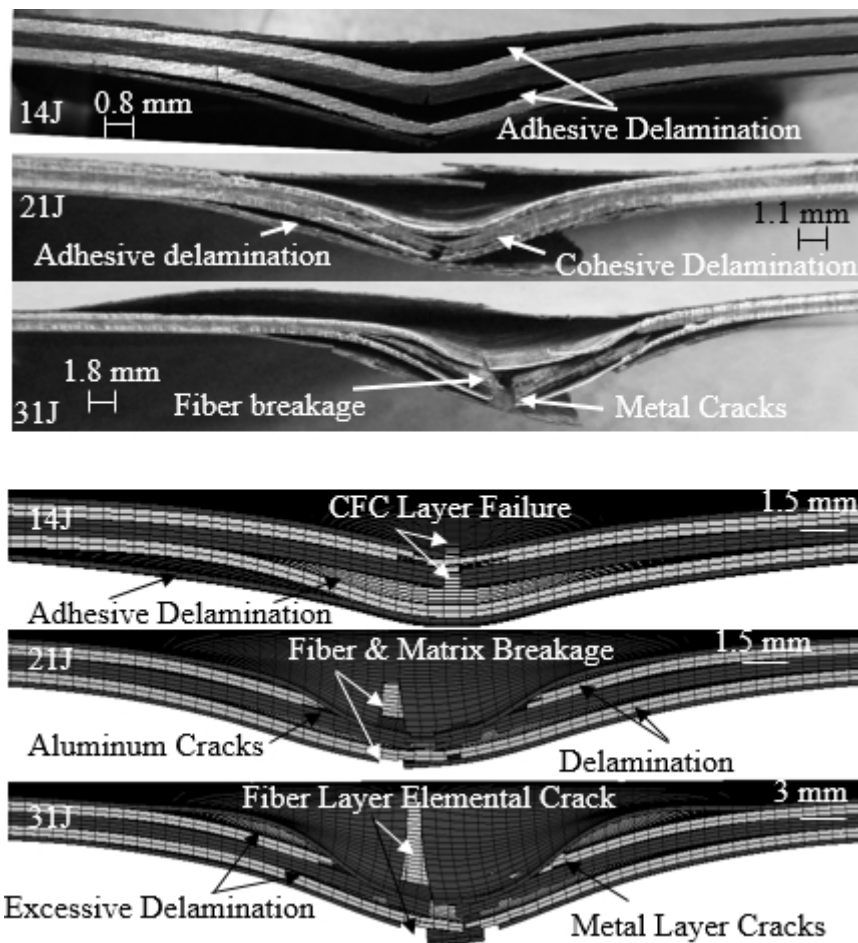


Figure 7.21: Cross-section images of CARALL-B specimens made without using polyester synthetic surfacing veil cloth layers under different impact energies.

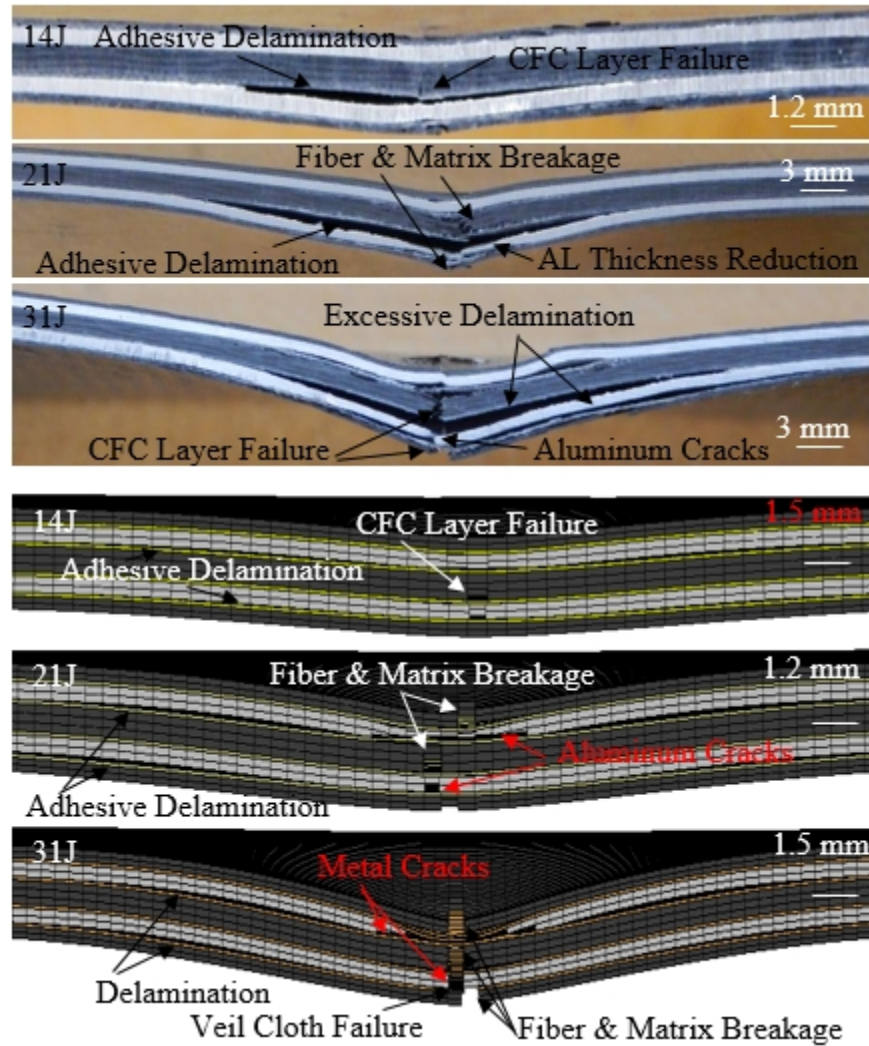


Figure 7.22: Cross-section images of CARALL-B specimens made with polyester synthetic surfacing veil cloth layers under different impact energies.

Indentation-induced damage with no cracks in an aluminum layer on impacted side of CARALL-A specimens having no veil cloth layers was found for 14 J and 21J impact energy, whereas an 18 mm long crack was found in an aluminum layer along with indentation on impacted side for 31J impact energy. Excessive adhesive delamination was observed at all interfaces for this energy level in CARALL-B FMLs specimens.

7.3.3 C-scan and FEA Predicted Delamination Area Comparison

A plan-type view of the damage location and size in test specimen is provided by the C-scan presentation. The transducer scan pattern runs parallel to the plane of the image. An automated data acquisition system, such as a computer controlled immersion scanning system is employed to develop C-scan presentations. Typically, the amplitude or the time-of-flight of the signal is recorded at regular intervals after establishing a data collection gate on the A-scan and moving the transducer over the test piece for scanning the damage size and location. A gray color shade or a standard color for each of the position at which the data is recorded is used to display the relative signal amplitude or the time-of-flight. An image of the test specimen features is provided by the C-scan presentations describing the reflection and scattering pattern of the sound within and on the surfaces. A schematic illustration of C-scan equipment working principle is shown in figure 7.23

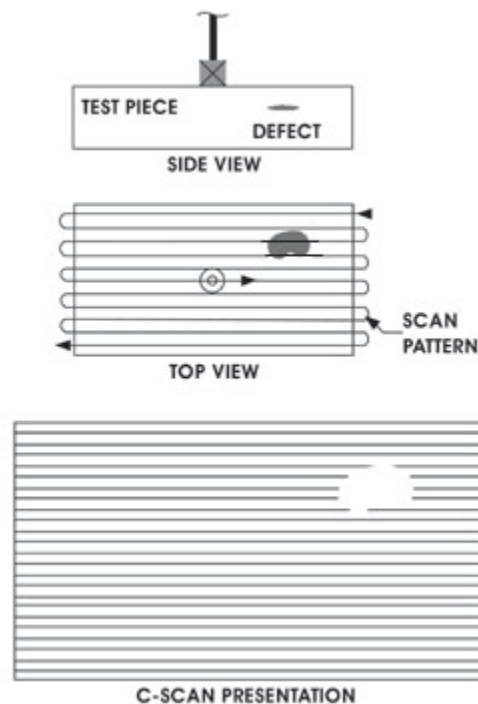


Figure 7.23: Ultrasonic C-scan method schematic illustration [128].

The FFT & A-scan frequencies used during the setup of C-scan equipment for damage assessment of CARALL FMLs are shown in figures 7.24 and 7.25.

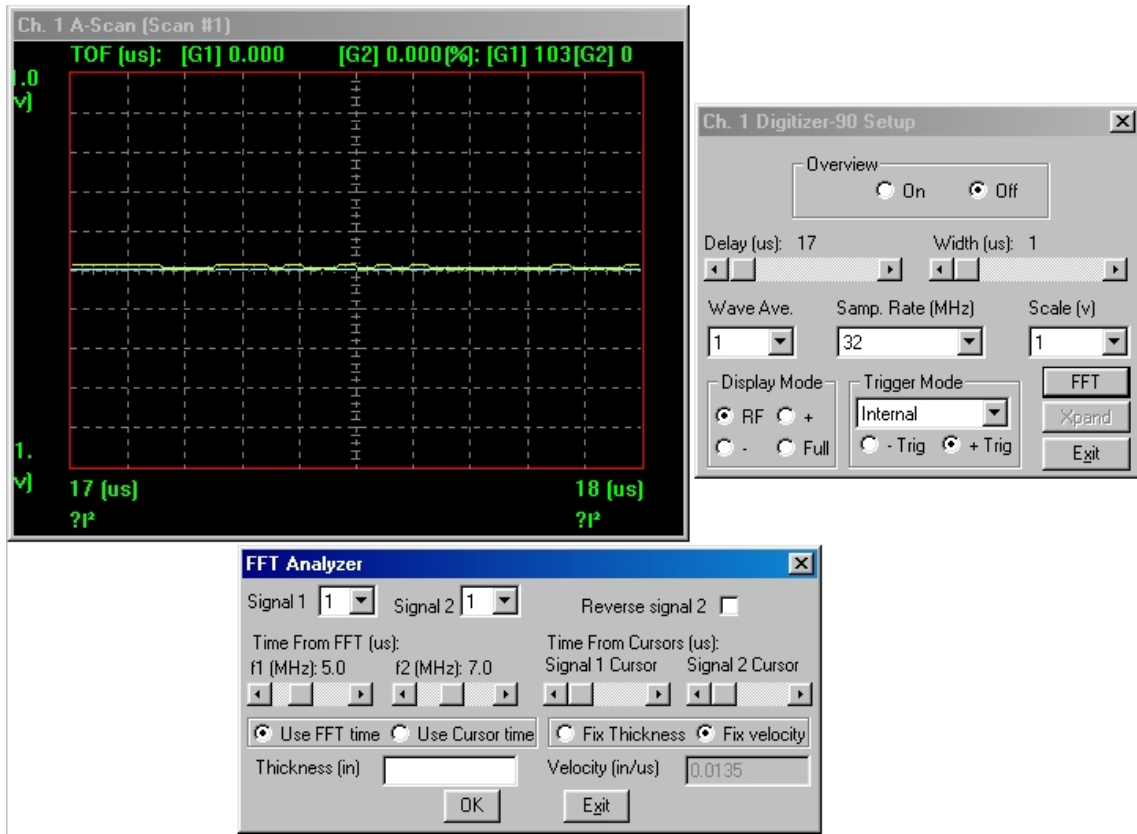


Figure 7.24: FFT Frequency setup

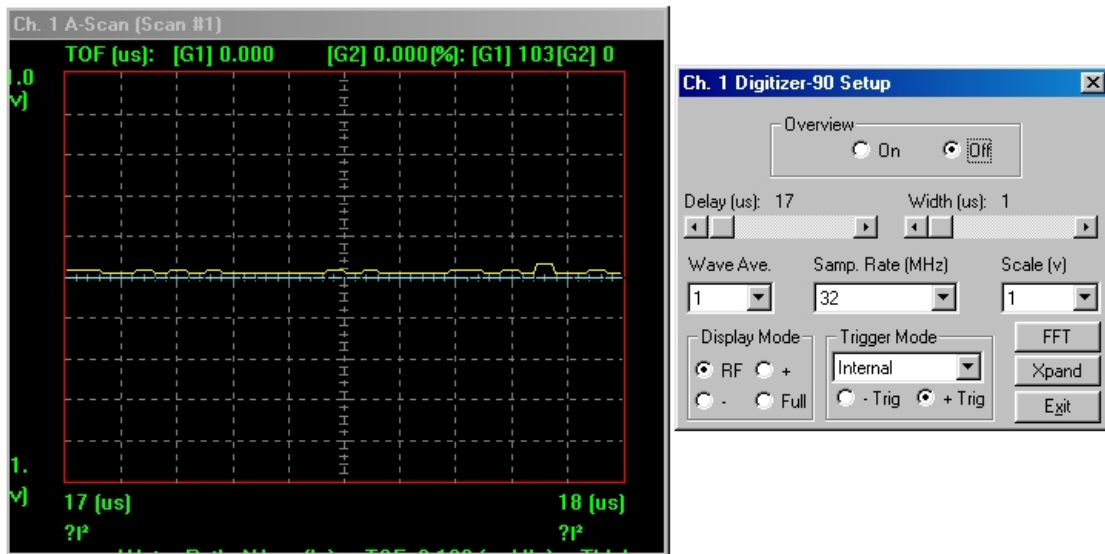


Figure: 7.25: A-scan frequency setting

The delamination damage size was characterized by using C-scan equipment and compared with the finite element simulation results for CARALL specimens as shown by Figures 7.26 and 7.27. Image J image processing and analysis software was used to measure the delamination area from the C-scan pictures. In FEM predictions shown in Figures 7.26 & 7.27, the solid blue color represent that damage is critical (value nearly 0.0) and the red color represent that the damage has not occurred (value nearly 1.0), and others represent different damage states. Similarly, the fully delaminated and no delamination regions in the C-scan results are described by the 100 % and 0% values of the legend, respectively.

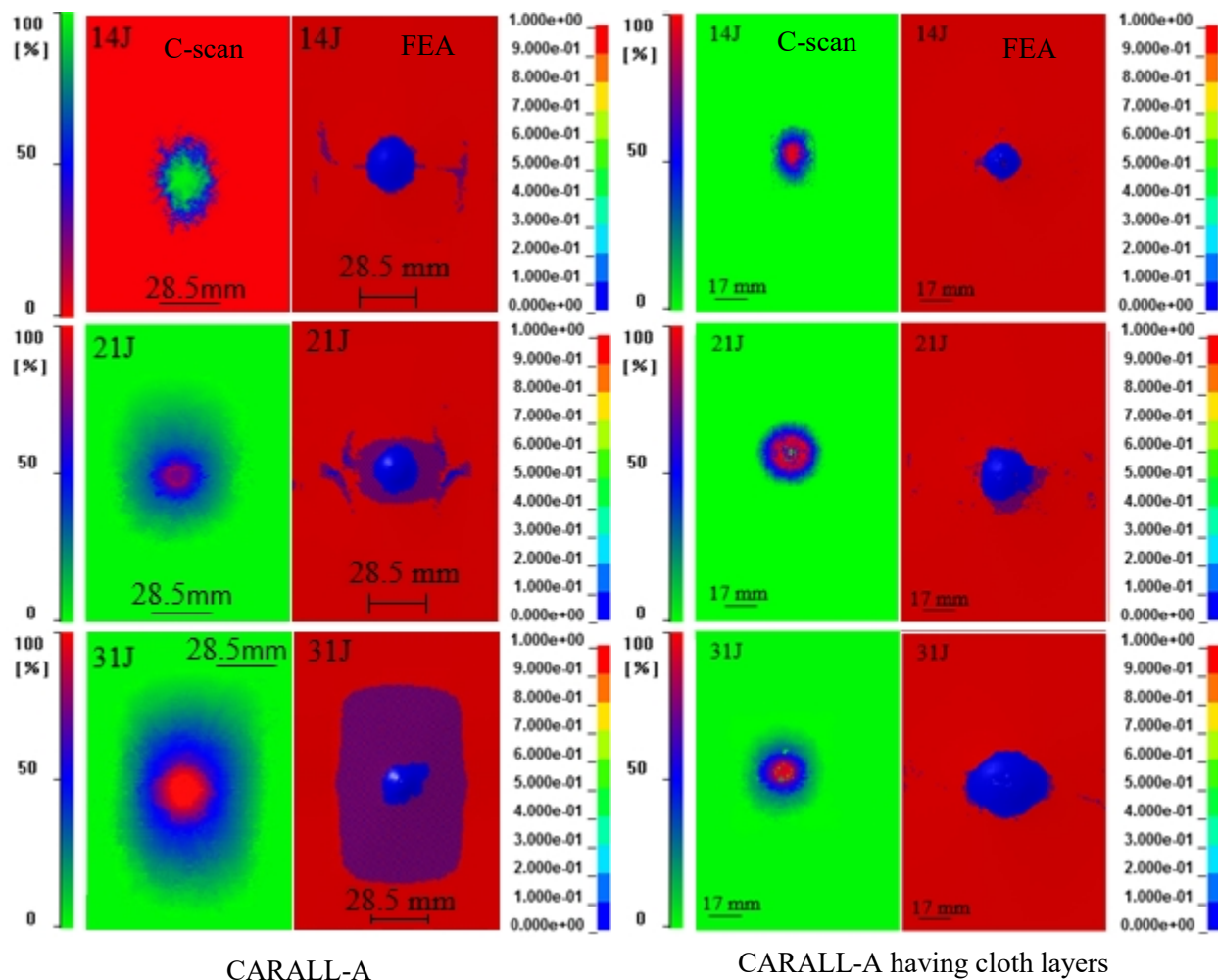


Figure 7.26: Comparison between C-scan and FEA predictions for delamination in CARALL-A specimens under different impact energies

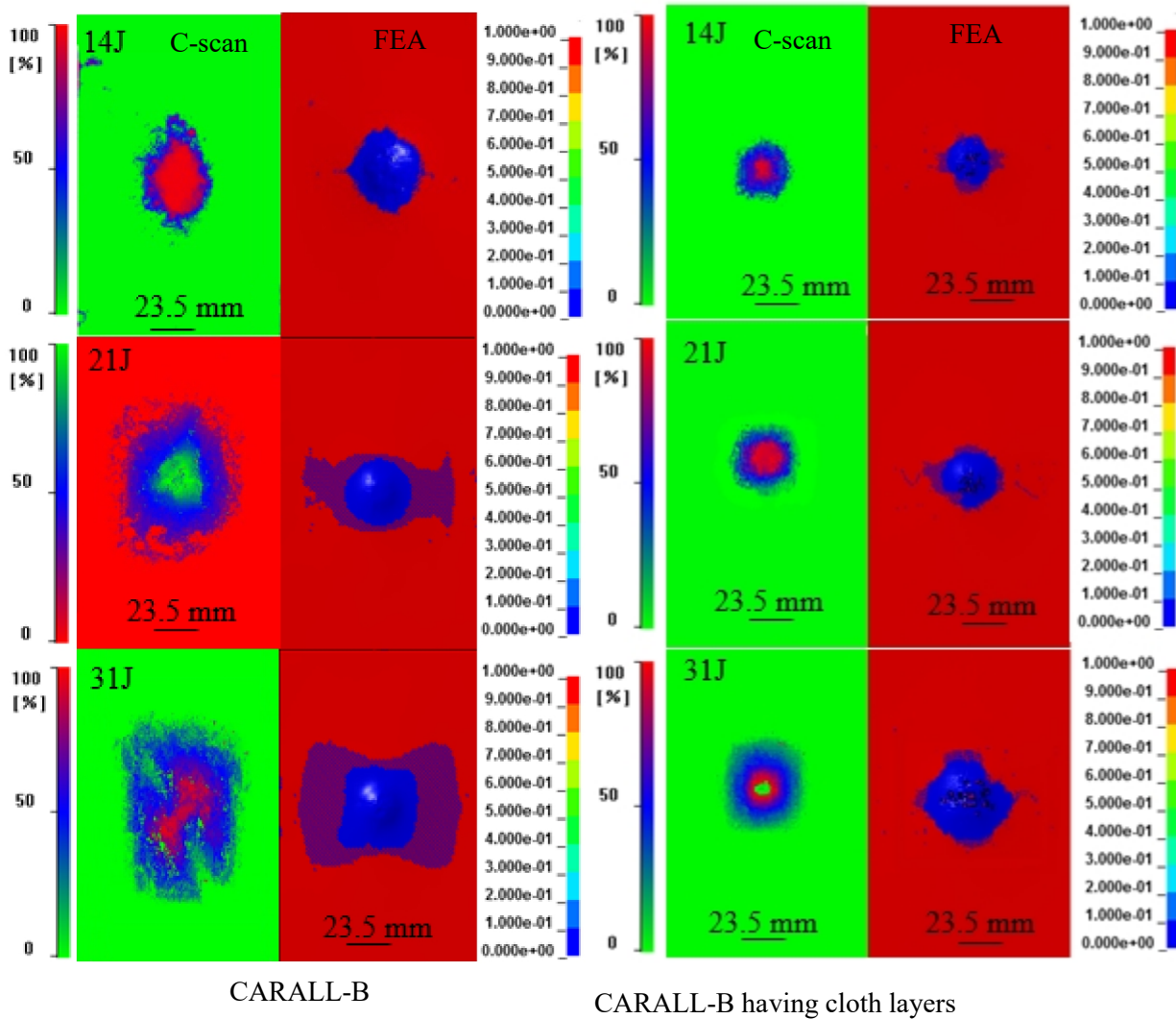


Figure 7.27: Comparison between C-scan and FEA predictions for delamination in CARALL-B specimens under different impact energies

Bilinear traction separation law with quadratic mixed-mode delamination initiation criterion used in this study was found to successfully capture the delamination area giving a good match with the C-scan experimental results. The damaged area is initially small and gradually gets larger with increasing impact energy. A comparison in the form of histograms between experimental results and numerical predictions for the delaminated area of CARALL specimens is shown by figures 7.28 and 7.29. FEA delamination model predicted delaminated area results

similar to experimental results at 14 & 21J impact energies but showed discrepancies in results at 31J impact energy.

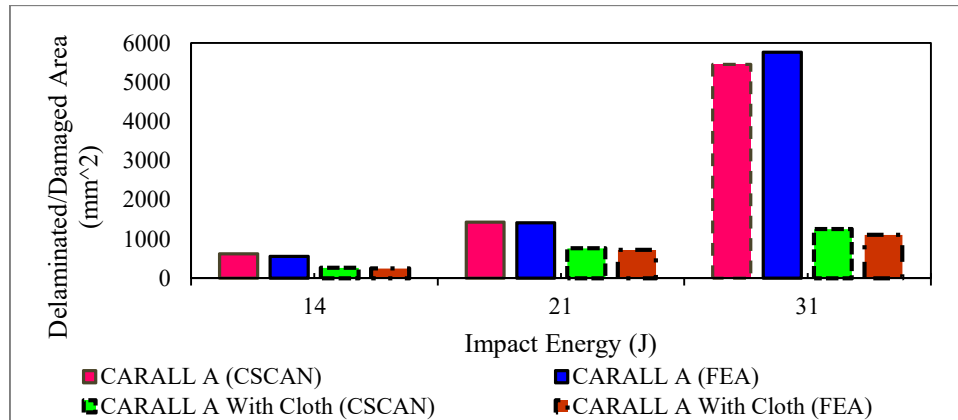


Figure 7.28: Delamination area results for CARALL-A specimens at different impact energies

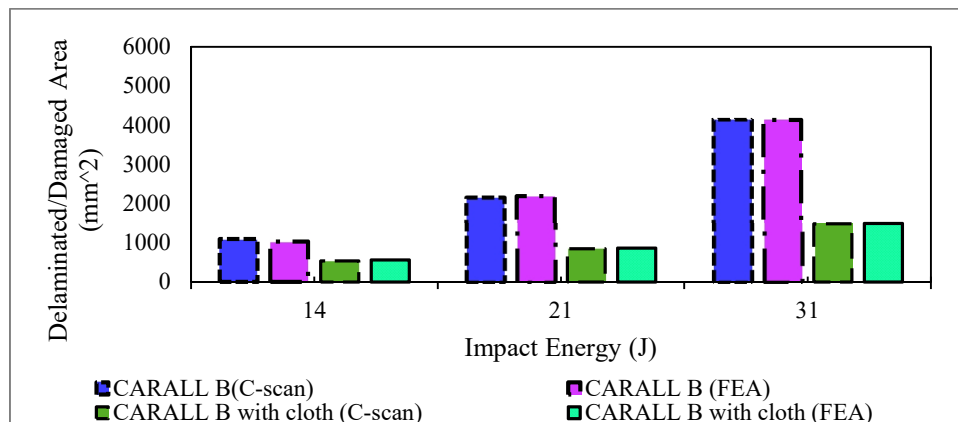


Figure 7.29: Delamination area results for CARALL-B specimens at different impact energies

7.3.4 Carbon fiber/epoxy layers Tensile Failures Numerical Predictions

Numerical prediction results of tensile failures with woven composite layers near the impacted and non-impacted sides are obtained for CARALL-A FMLs in Figs. 7.30 and 7.31, whereas for CARALL-B FMLs in Figures 7.32 and 7.33. The colors represent the damage degree of the composite. While the blue represent that the damage is serious (value nearly 0.0), red represent that the damage does not occur (value nearly 1.0), and others represent different damage degree. As expected, damage in carbon fiber/epoxy layers increased with the increase in

the impact energy. Numerical simulation elucidated the extent of tensile damage in carbon fiber/epoxy layers.

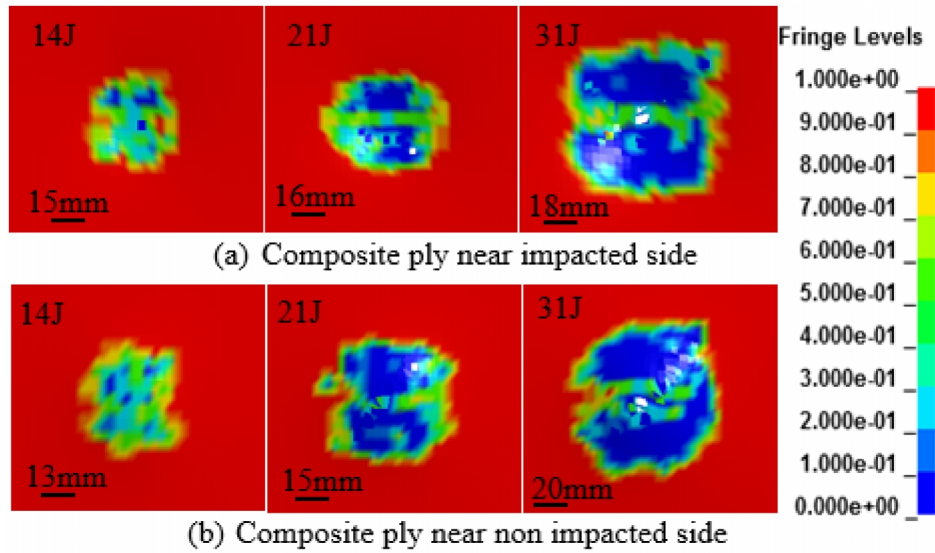


Figure 7.30: Numerical prediction of tensile failures of CFRP layers in CARALL-A FMLs made without using polyester synthetic surfacing veil cloth layers.

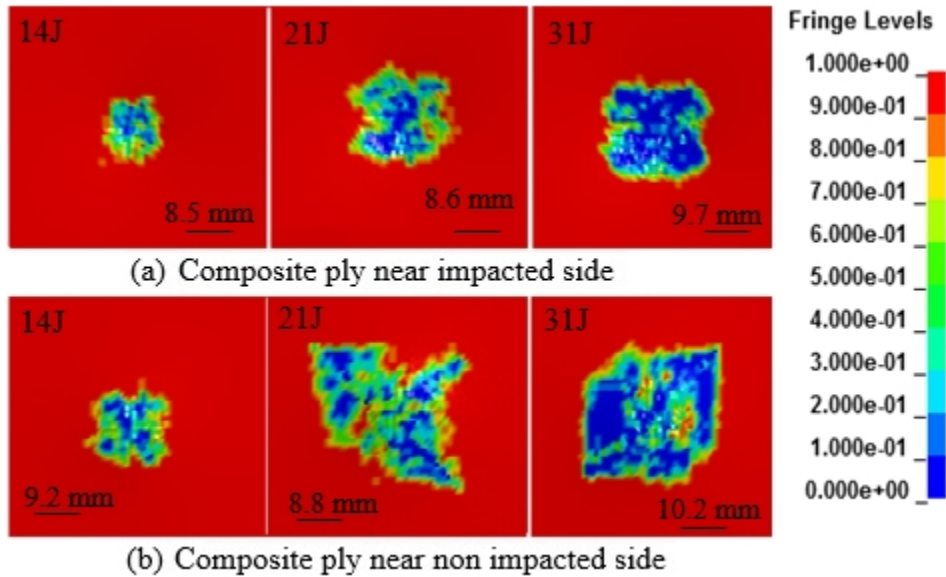


Figure 7.31: Numerical prediction of tensile failures of CFRP layers in CARALL-A FMLs made with polyester synthetic surfacing veil cloth layers.

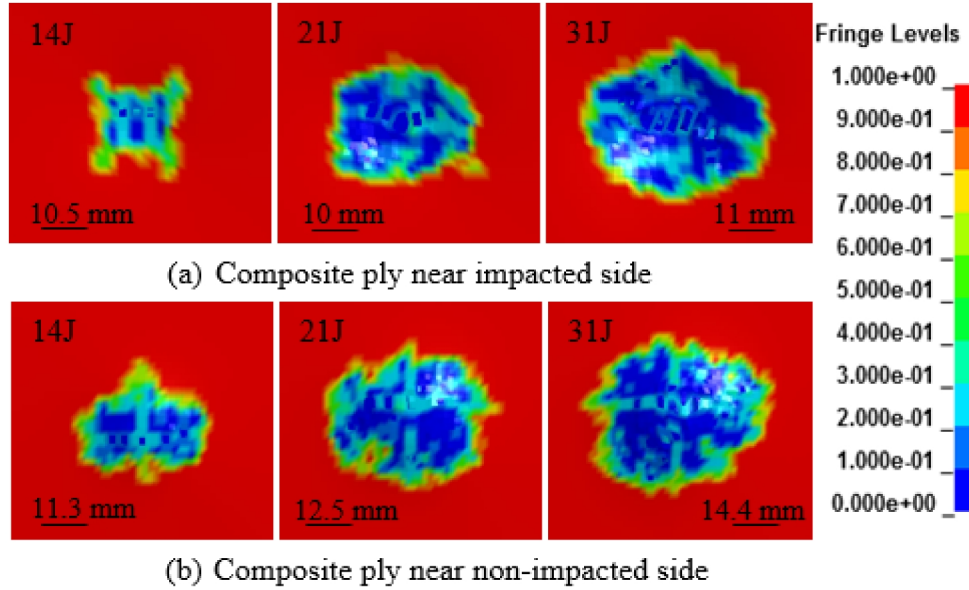


Figure 7.32: Numerical prediction of tensile failures of CFRP layers in CARALL-B FMLs made without using polyester synthetic surfacing veil cloth layers.

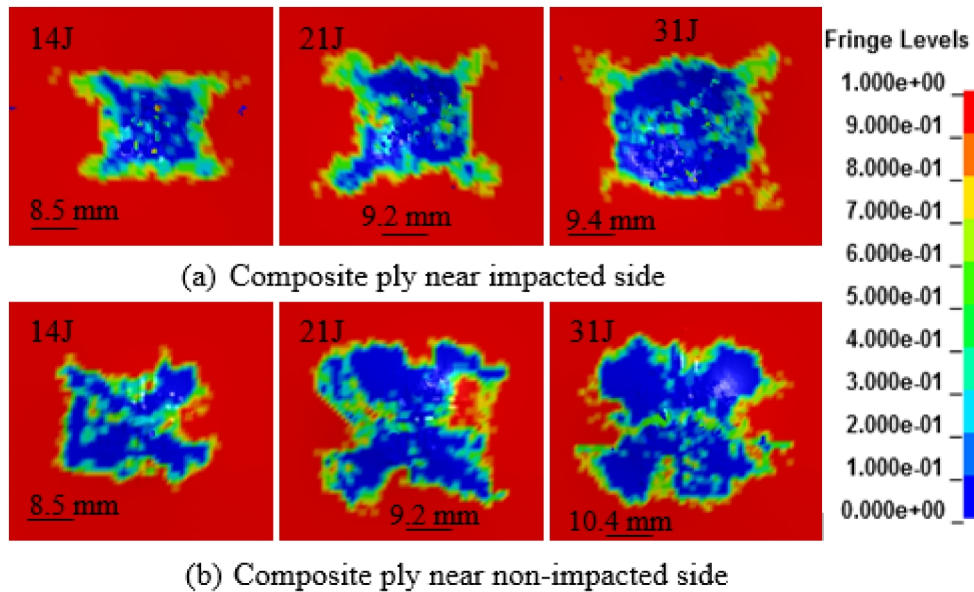


Figure 7.33: Numerical prediction of tensile failures of CFRP layers in CARALL-B FMLs made with polyester synthetic surfacing veil cloth layers.

A correlation between experimental results and numerical prediction results was not achieved for the tensile failure of carbon fiber/epoxy layers due to the difficulty of removing aluminum layers and characterize the damage in experimental samples. Since in CARALL-B

FMLs we are impacting it from the carbon fiber/epoxy side, the addition of cloth layers does not show the effect on the numerical prediction of tensile failures of composite layers. However in CARALL-A laminates it reduced the damage of carbon fiber/ epoxy layers located near the impacted and non-impacted sides.

7.3.5 Absorbed Energy and Energy Restitution Coefficient

A comparison between experimental results and numerical predictions in terms of absorbed energy and energy restitution coefficient for CARALL-A FMLs made with and without using polyester (veil) cloth layers is shown in the form of histogram graph in figures 7.34 and 7.35. Similarly, the comparative histogram plots of absorbed energy and energy restitution coefficient for CARALL-B FMLs is shown in Figures 7.36 and 7.37.

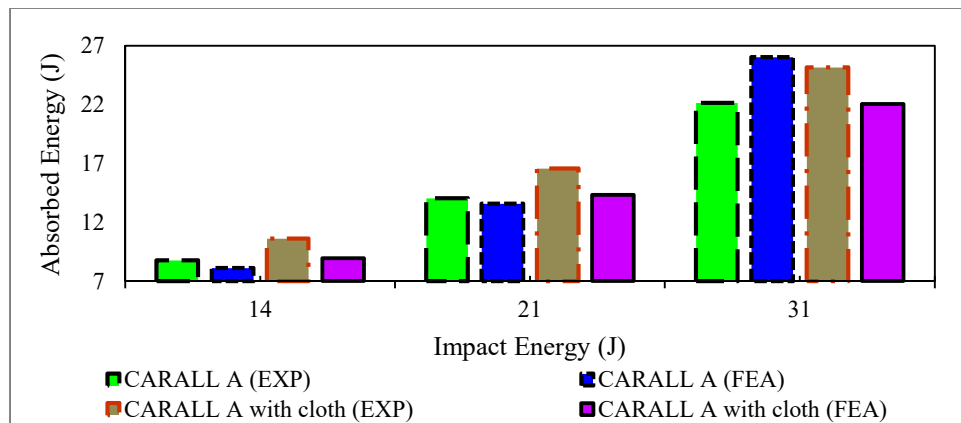


Figure 7.34: Energy absorbed by CARALL-A FMLs during an impact event.

Energy restitution coefficient was calculated for numerical and experimental results for each impact energy using the formula described by equation 35.

$$\text{Energy restitution coefficient (ERC)} = 1 - \frac{\text{Absorbed energy}}{\text{Total Impact energy}} \quad (35)$$

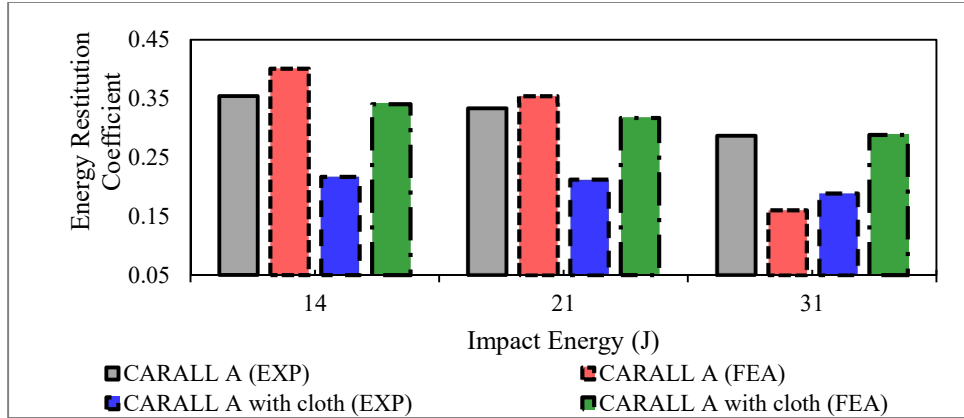


Figure 7.35: Energy Restitution Coefficient results for CARALL-A FMLs

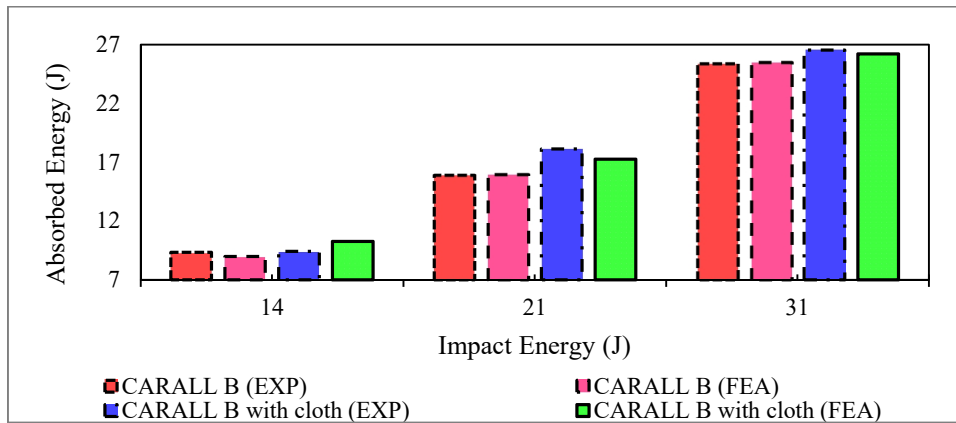


Figure 7.36: Energy absorbed by CARALL-B FMLs during an impact event.

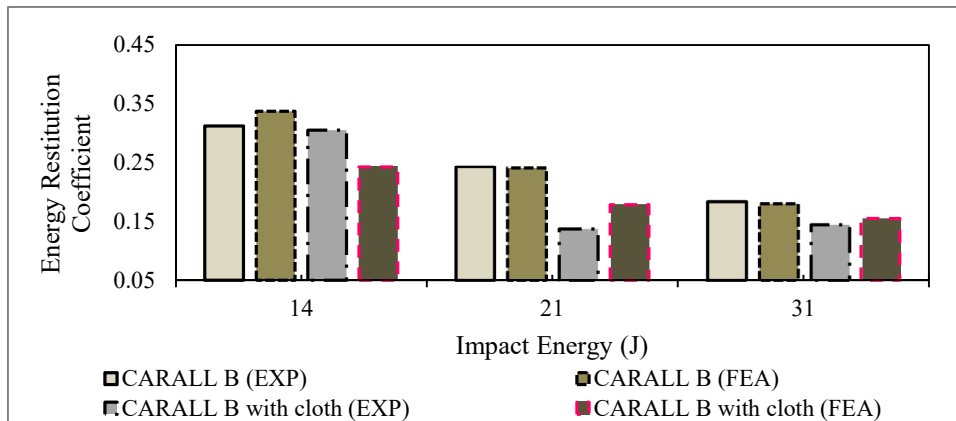


Figure 7.37: Energy Restitution Coefficient results for CARALL-B FMLs

A good correlation was found between numerical and experiment results of CARALL-B FMLs for absorbed energy and energy restitution coefficients at all impact energies but the slight difference was observed in CARALL-A FMLs results.

7.4 CARALL-A and CARALL-B FMLs Impact Behavior Comparison

A comparison of experimental force-displacement results for both CARALL-A and CARALL-B FMLs curved with and without using polyester veil cloth layers are plotted in figures 7.38 and 7.39. CARALL-A FMLs showed higher peak forces and lower contact duration as compared to CARALL-B FMLs at all impact energies. With the increase in impact energy, more fiber, and matrix damage was observed in CARALL-B FMLs resulting in larger permanent central deflection as compared to CARALL-A FMLs at all impact energies.

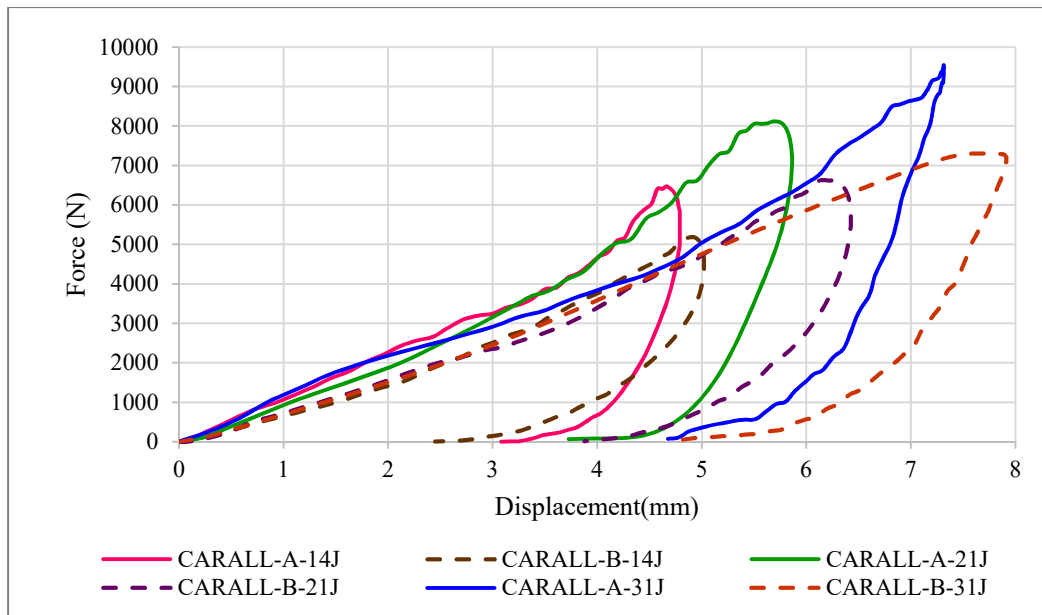


Figure 7.38: Force-displacement plot for CARALL-A & -B FMLs having veil cloth layers.

The outer impacted and non-impacted carbon epoxy layers in CARALL-B FMLs suffered significant damage due to the high stiffness and brittle nature of carbon fibers. As a result, the delaminated/damaged area was more in CARALL-B specimens than CARALL-A.

Thus, it can be implied from the energy restitution coefficient and absorbed energy curves that the impact resistance of CARALL-A specimens is more than CARALL B FMLs due to less damage area and slightly high metal volume fraction.

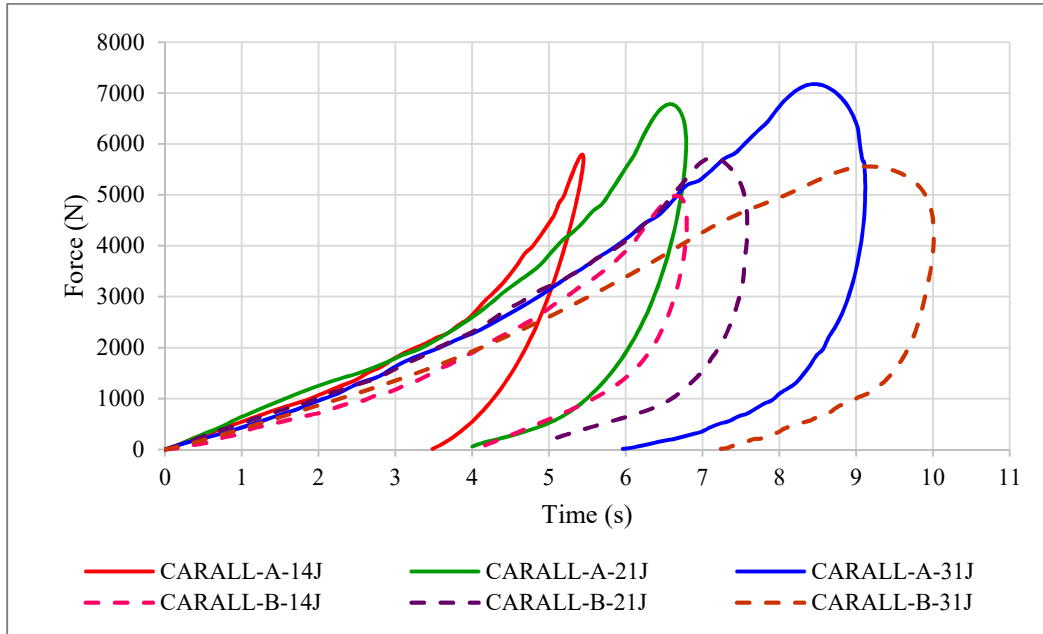


Figure 7.39: Force-displacement plot for CARALL-A & -B FMLs cured without using polyester synthetic surfacing veil cloth layers.

CARALL-A showed lower delaminated area at 14 & 21J impact energies but higher at 31J impact energy than the CARALL-B. This is due to the factor that the primary failure mode in CARALL-B specimens at impact energy 31J shifted from interface delamination to metallic cracks and carbon fiber fracture approximately in all layers of FML leading to incomplete perforation.

CHAPTER 8 COMPRESSION AFTER IMPACT TEST & DATA ANALYSIS

8.1 Compression After Impact Test Experimental Aspects

The compression after impact (CAI) test is commonly used test method to quantify the damage tolerance of composite materials. A standardized method as per ASTM standard D7137 [129] was adopted to characterize the residual strength and stiffness properties of impacted carbon fiber reinforced aluminum laminate specimens. The CAI tests were done at room temperature using Instron MTS machine having a loading cell of 220 KN. The compression after impact fixture along with mounted sample is shown in Figure 8.1. Compression after impact fixture consists of top and bottom halves containing slide plates that constrain the sample on the four edges. The edges of side plates are knife shaped, whereas the top and bottom slide plates have flat edges.

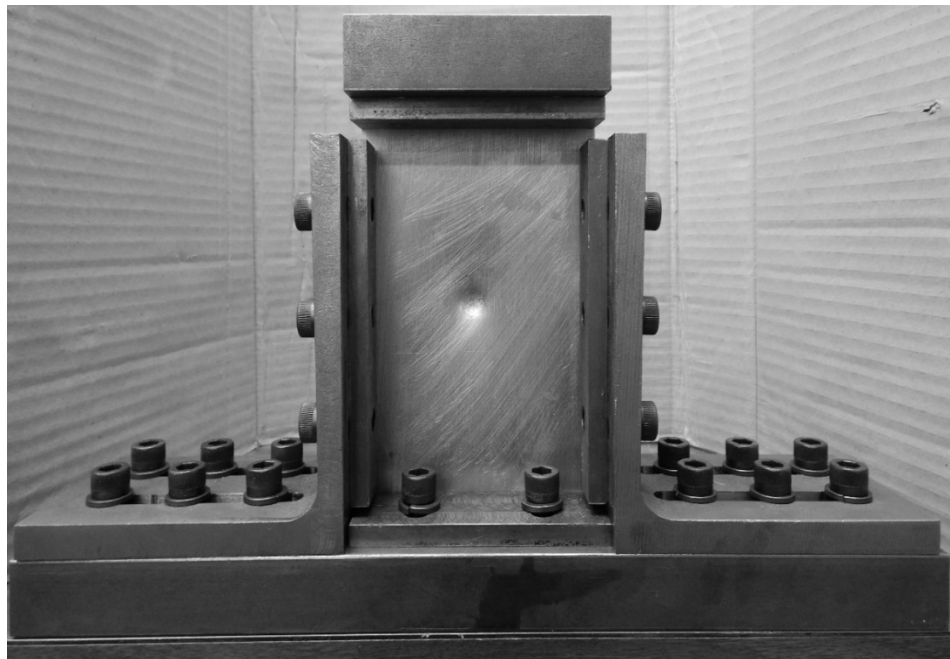


Figure 8.1: Compression after impact along with damaged FML sample

A rotational constraint is placed at the top and bottom edges of the sample due to the geometry of the slide plates. The sample is considered clamped at these locations since the slide plates were fastened by Allen key. The impacted CARALL FMLs specimens which were subjected to three different energy levels (14J, 21J, 31J) were compressed along the length direction at a constant displacement rate of 1 mm/min as specified ASTM standard. The sample must be placed under pure compression for the experiment to be successful, and so the force-displacement curve should be monitored to find the indication of sample bending or buckling in the form of nonlinearity. Eight samples of each FML category was compressed to a displacement value below failure approximately equal to 5mm before stopping the test.

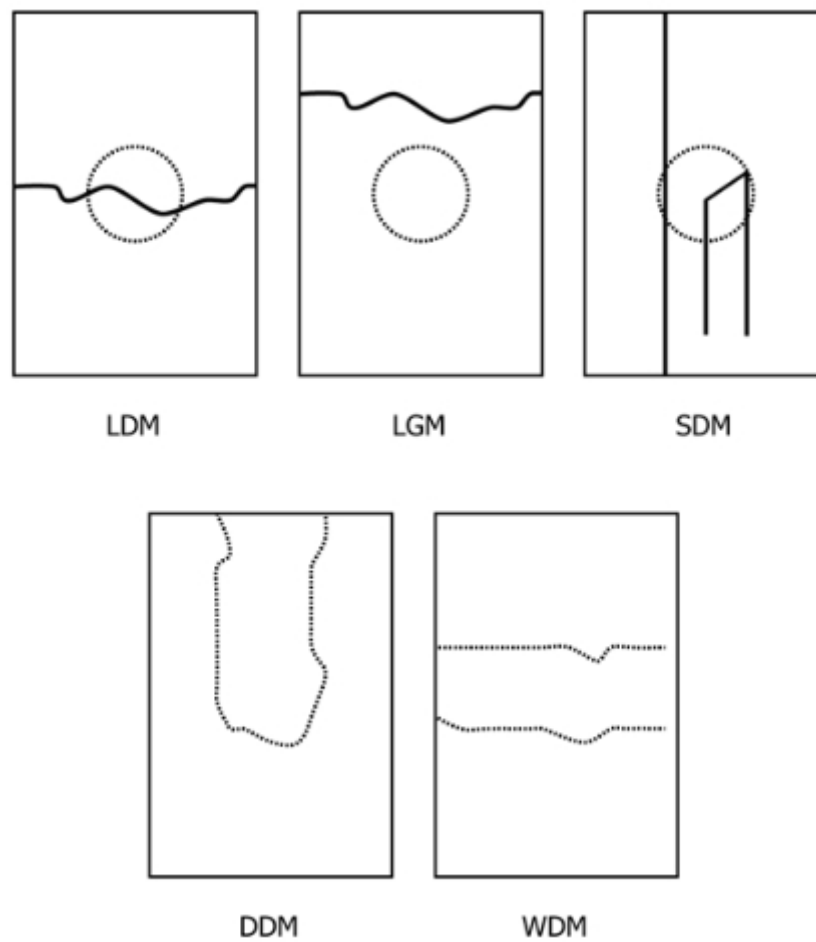


Figure 8.2: Acceptable failure modes as per ASTM standard.[129]

Table 8.1: Failure mode codes as per ASTM D7137 [129]

First Character		Second Character		Third Character	
Failure Type	Code	Failure Area	Code	Failure Location	Code
Lateral	L	At/through Damage	D	Middle	M
Long Splitting	S	Gage, away from damage	G		
Delamination lengthwise	D				
Delamination widthwise	W				

Commonly observed acceptable compressive residual strength failure modes as per ASTM Standard D-7137 is shown in figure 8.2 and the three place failure mode codes are tabulated in Table 8.1. Virgin specimens were also tested and compared with the compressed damaged specimens to obtain the loss of residual strength caused by the impact damage.

8.1.1 Effect of Polyester Synthetic Surfacing Veil Cloth Layers on CAI Behavior

Typical CAI load-displacement curves for CARALL-A FML cured with and without using polyester surfacing veil cloth layers are shown in figures 8.3 and 8.4. The residual strength as a function of impact energy for the CARALL-A FMLs cured with and without using polyester surfacing veil cloth layers which were impacted by 25.4 mm impactor diameter is presented in Figure 8.5. The errors bars in this figure shows the variation in the data at each impact energy level. By comparing CARALL-A FMLs systems cured with and without using polyester surfacing veil cloth layers in terms of residual strength at the same impact energy, it is found that the CARALL-A FMLs having cloth layers provides higher residual strength than the regular CARALL-A FMLs cured without cloth layers composite system due to higher interlaminar bond strength of composite system. Failure load of the damaged specimen should be compared with the failure load of the undamaged one to determine the residual strength of the FML composites.

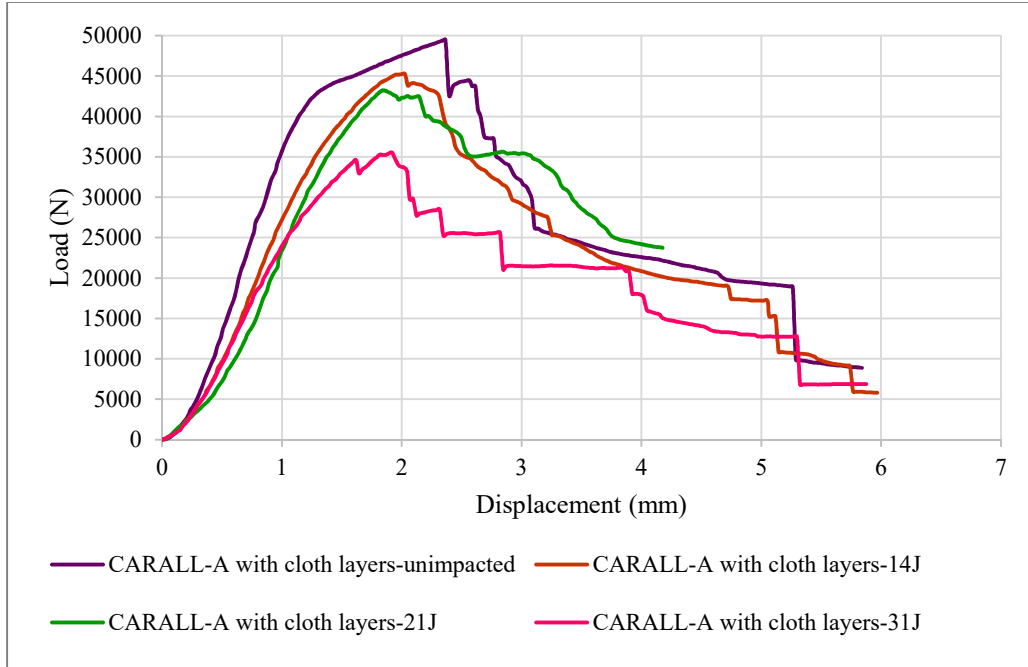


Figure 8.3: Compression After Impact (CAI) load-displacement curves for CARALL-A cured with polyester cloth layers impacted at different impact energies

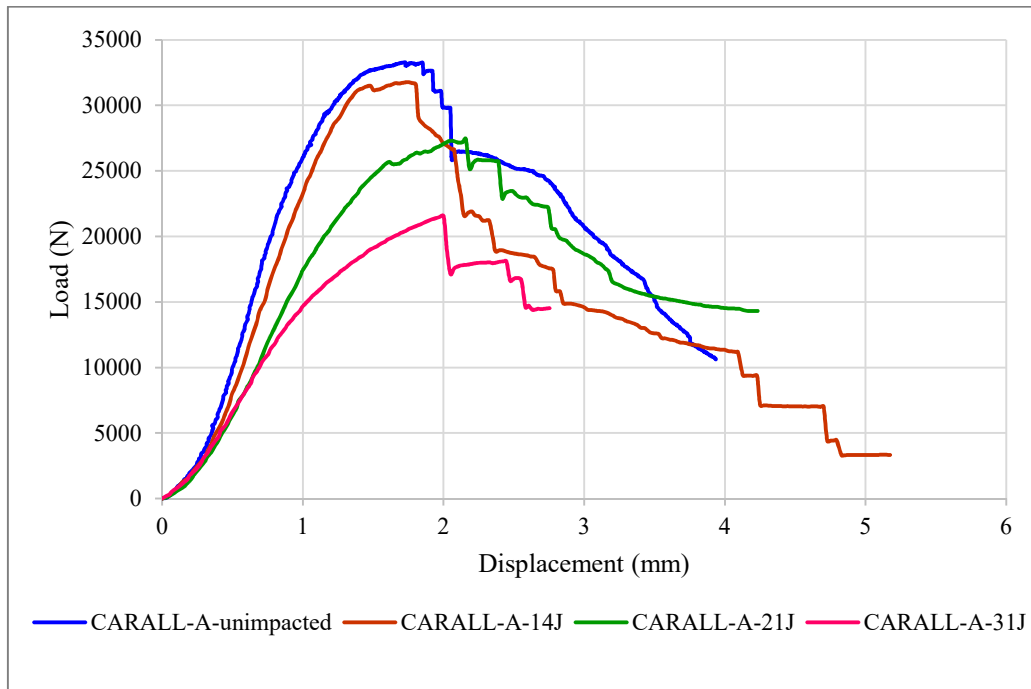


Figure 8.4: Compression After Impact (CAI) load-displacement curves for CARALL-A cured without using polyester cloth layers impacted at different impact energies

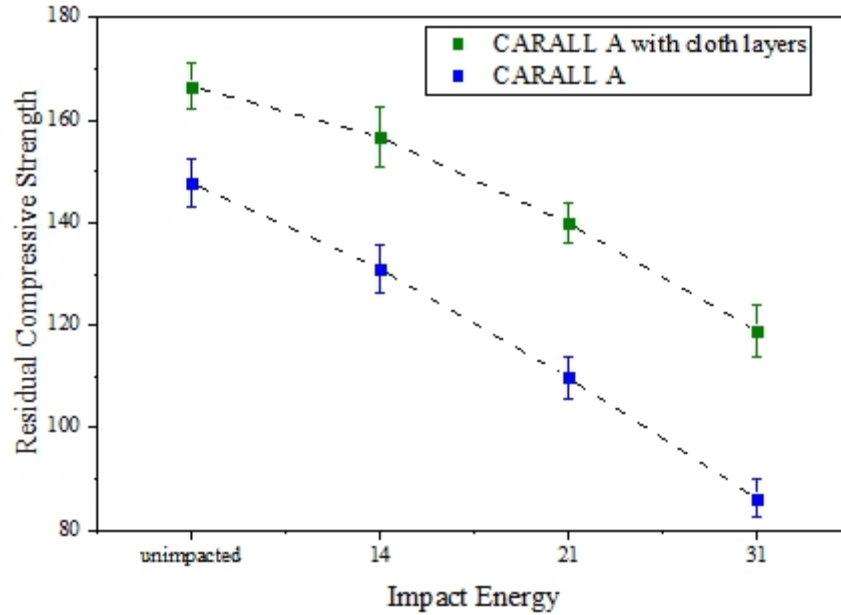


Figure 8.5: Residual strength versus impact energy for CARALL-A FMLs.

From the figures 8.3 and 8.4, it can be seen that as impact energy increases, the failure load decreases due to large damage that was introduced during impact. The reduction in residual strength of CARALL-A specimens cured without cloth layers was more as compared to specimens cured with polyester cloth layers which may be due to larger delaminated area. Similarly, typical CAI load-displacement curves for CARALL-B FML cured with and without using polyester surfacing veil cloth layers are shown in figures 8.6 and 8.7, respectively. The residual strength as a function of impact energy for the CARALL-A FMLs cured with and without using polyester surfacing veil cloth layers is shown in Figure 8.8. CARALL-B FMLs cured with polyester surfacing veil cloth layers also exhibits higher compressive residual strength similar to CARALL-A specimens when compared to specimens cured without cloth layers. Failure load decreases in CARALL-B specimens also as the impact increases as shown by figures 8.6 and 8.7.

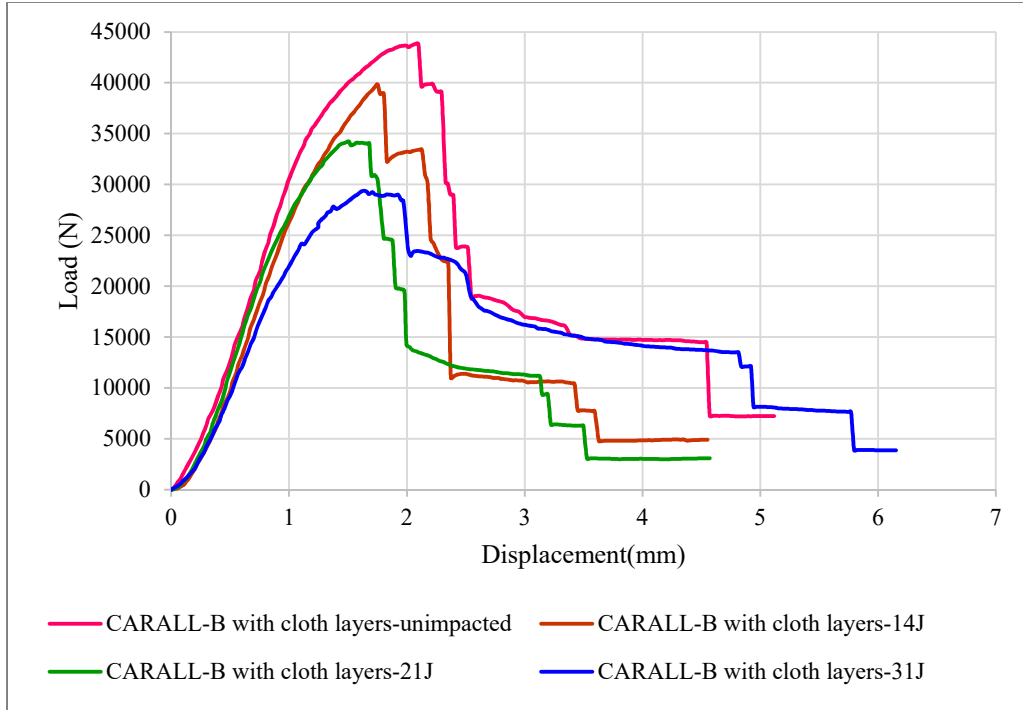


Figure 8.6: Compression After Impact (CAI) load-displacement curves for CARALL-B cured with polyester cloth layers impacted at different impact energies

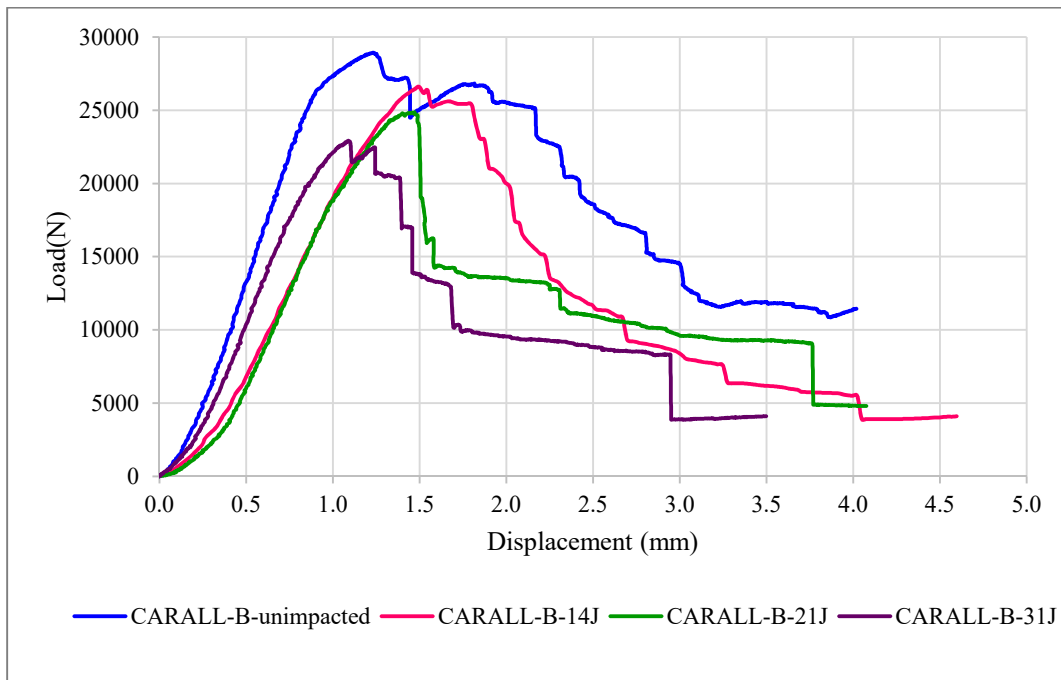


Figure 8.7: Compression After Impact (CAI) load-displacement curves for CARALL-B cured without using polyester cloth layers impacted at different impact energies

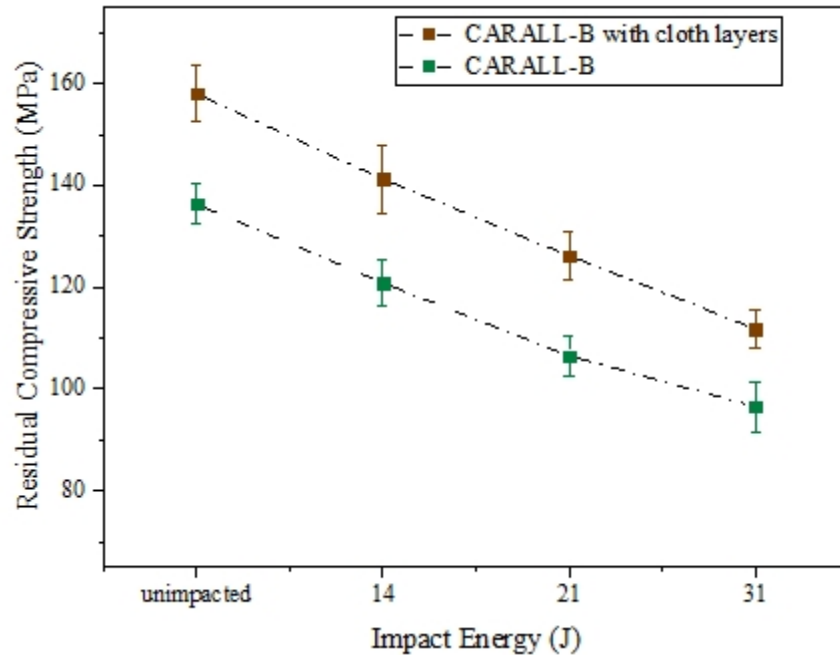


Figure 8.8: Residual strength versus impact energy for CARALL-B FMLs.

The reduction in residual strength of CARALL-B specimens was found to be similar in both types of specimens i.e. specimens cured with and without cloth layers. The compressive strength of CARALL specimens attained during CAI test along with percentage reduction in residual strength as compared to virgin specimens is tabulated in Table 8.2. Thin specimens have a much lower buckling load. This lower load allows global buckling of specimens before the damaged regions have a chance to initiate the specimen failure [130]. The CAI fixture is designed to force the failure to occur in the damaged zone of the impacted specimen. The specimen will fail at a stress concentration such as constrained ends or in a non-compression mode such as buckling if the damaged zone does not initiate failure. The failure modes CARALL-A and CARALL-B specimens impacted at different energies are shown in figures 8.9 and 8.10, respectively. CARALL specimens impacted at 14J does initiate failure in impacted zone but failed in bottom half far from impacted zone. However as the impact energy is increased, the specimens initiate the failure in the damaged zone as can be seen in figure 8.9 and

8.10 for 31J impact energy. The specimens cured with and without polyester surfacing veil cloth layers exhibits similar failure modes in both types of CARALL FMLs.

Table 8.2: CAI test results for CARALL specimens.

Impact energy (J)	CARALL-A		CARALL-A with Polyester Veil Cloth Layers		CARALL-B		CARALL-B with Polyester Veil Cloth Layers	
	CAI strength (MPa)	Decrease W.r.t virgin sample (%)	CAI strength (MPa)	Decrease W.r.t virgin sample (%)	CAI strength (MPa)	Decrease W.r.t virgin sample (%)	CAI strength (MPa)	Decrease W.r.t virgin sample (%)
Virgin	147.71	---	166.58	---	136.30	---	157.96	---
14	130.94	11.34	156.66	5.95	120.82	11.35	141.22	10.59
21	109.71	25.72	139.86	16.04	106.49	21.86	126.15	20.13
31	86.15	41.67	118.89	28.63	96.51	29.19	111.78	29.23

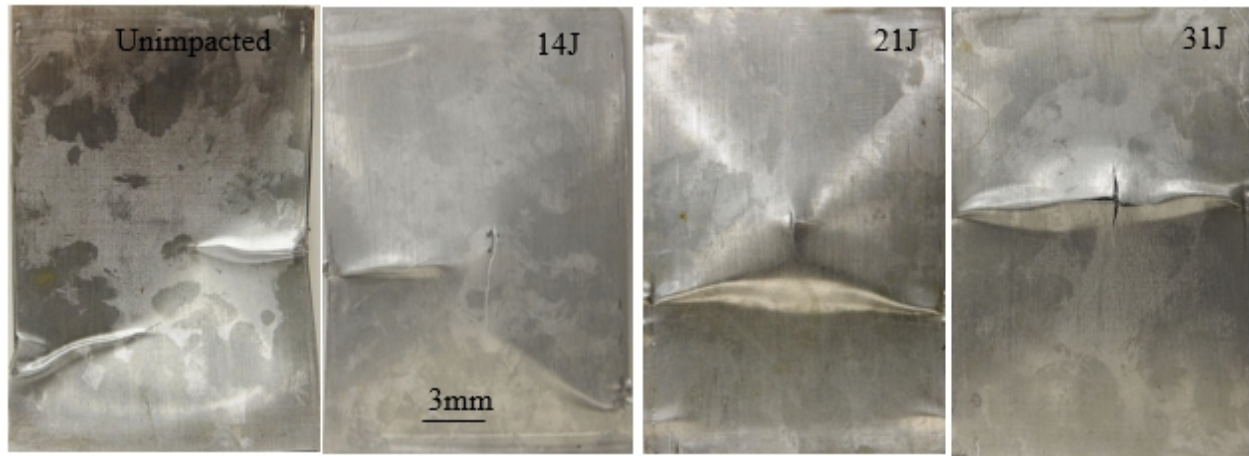


Figure 8.9: Failure mode of CARALL-A specimens.

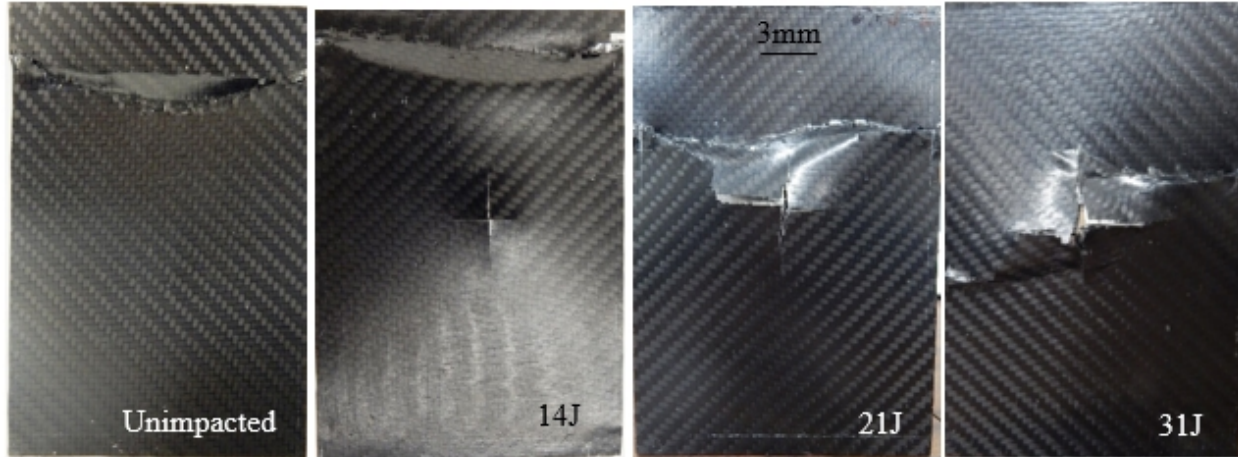


Figure 8.10: Failure mode of CARALL-B specimens.

8.1.2 CARALL-A and CARALL-B FMLs CAI Behavior Comparison

A comparison is made between the CAI behavior of CARALL-A and CARALL-B FMLs by plotting the typical load displacement curves simultaneously on same scatter plot. The curves for specimens cured with and without using polyester veil cloth layers are shown in figures 8.11 and 8.12, respectively. To clearly point the different between the responses of two CARALL systems, the load-displacement curves for specimens impacted at only two energies are plotted.

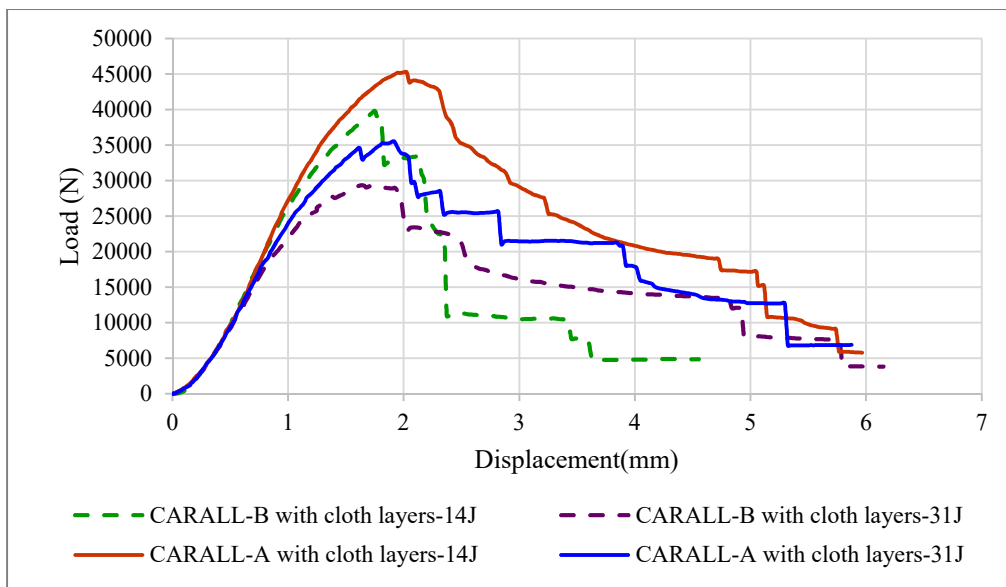


Figure 8.11: Compression After Impact (CAI) load-displacement curves for CARALL-A and CARALL-B cured with polyester cloth layers impacted at 14J and 31J impact energies

Upon comparing the responses, it can be inferred that the CARALL-A specimens carry a higher load than the CARALL-B specimens at same impact energy level. A comparison of residual strength as a function of impact energy for the CARALL-A and CARALL-B FMLs cured with and without using polyester surfacing veil cloth layers are presented in Figures 8.13 and 8.14, respectively.

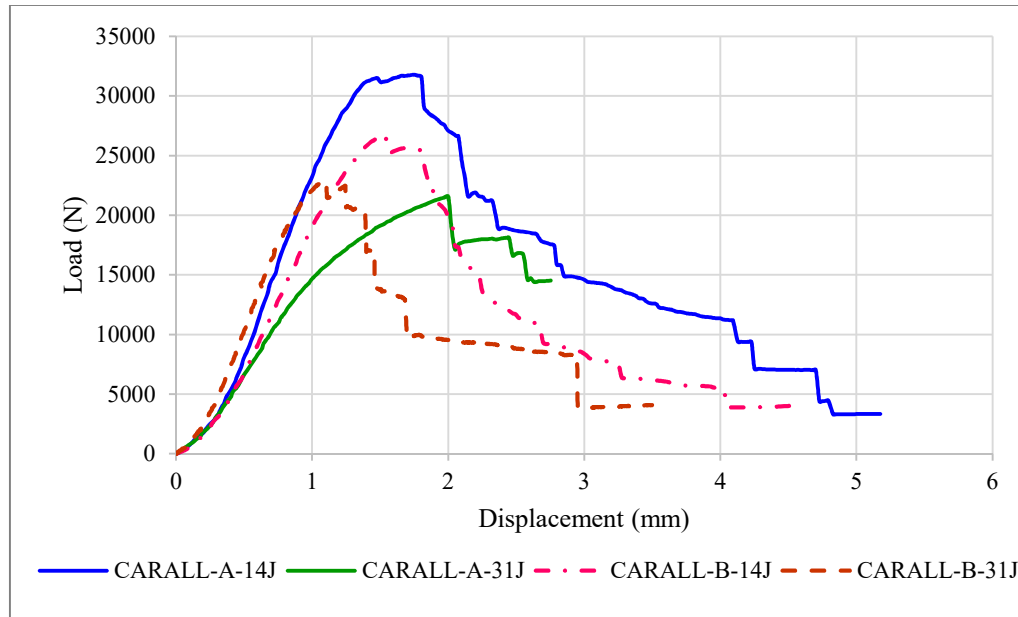


Figure 8.12: Compression After Impact (CAI) load-displacement curves for CARALL-A and CARALL-B cured without using polyester cloth layers impacted at 14J and 31J impact energies

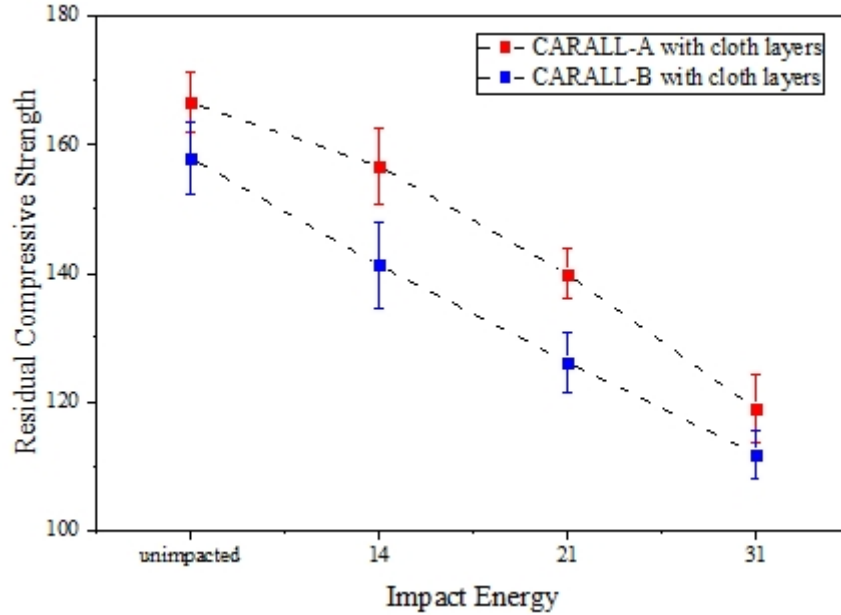


Figure 8.13: Residual strength versus impact energy for CARALL-A and CARALL-B FMLs cured with polyester surfacing veil cloth layers

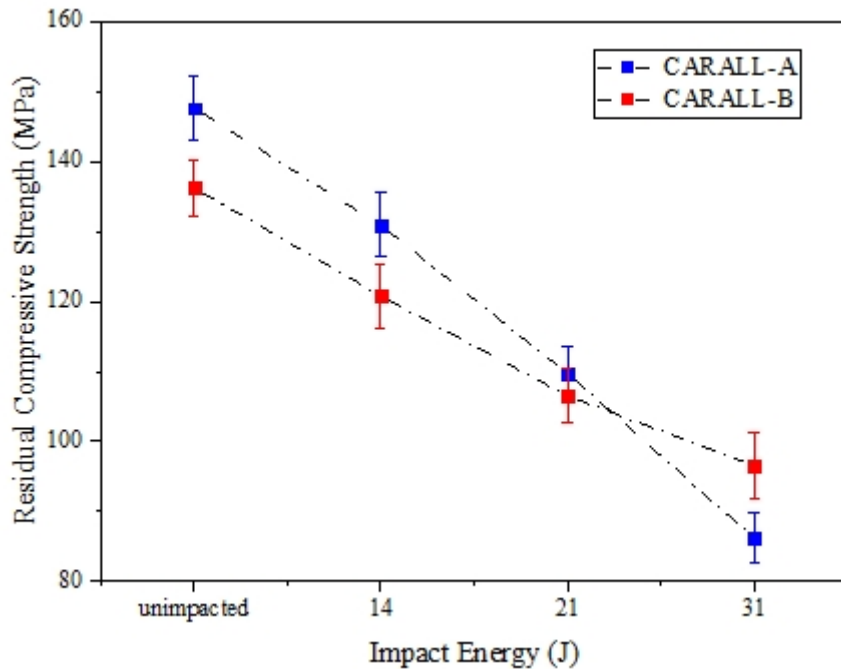


Figure 8.14: Residual strength versus impact energy for CARALL-A and CARALL-B FMLs cured without using cloth layers

It can be inferred from residual strength comparison figures of CARALL specimens, that CARALL-A specimens cured with polyester veil cloth layers have higher residual strength as

compared to CARALL-B specimens having cloth layers at all impact energy levels. However, the CARALL-A specimens cured without using cloth layers exhibit higher residual strength at 14J and 21J impact energies but showed lower residual strength at 31J energy as compared to CARALL-B specimens cured without cloth layers. This is due to more delamination damage in CARALL-A than CARALL-B at 31J impact energy. The effect of delaminated area on the residual strength of CARALL-A and CARALL-B specimens cured with and without polyester cloth layers is shown in figures 8.15 and 8.16 respectively. It can be seen that CARALL-A specimens cured with cloth layers perform better than CARALL-B specimens cured with cloth layers. However, CARALL-B specimens cured without cloth layers perform better than CARALL-A specimens cured without cloth layers.

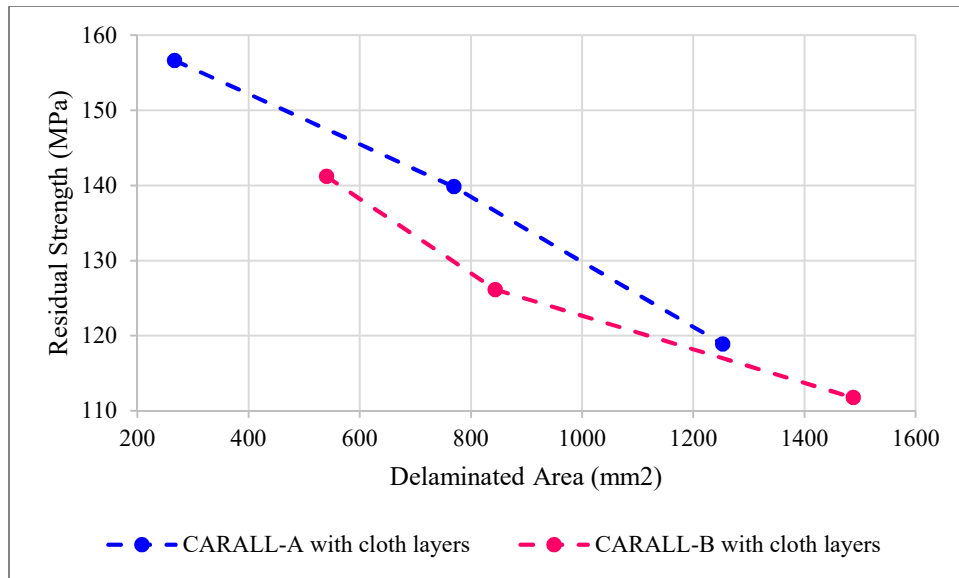


Figure 8.15: Delaminated area versus residual strength of CARALL specimens cured with polyester surfacing cloth layers

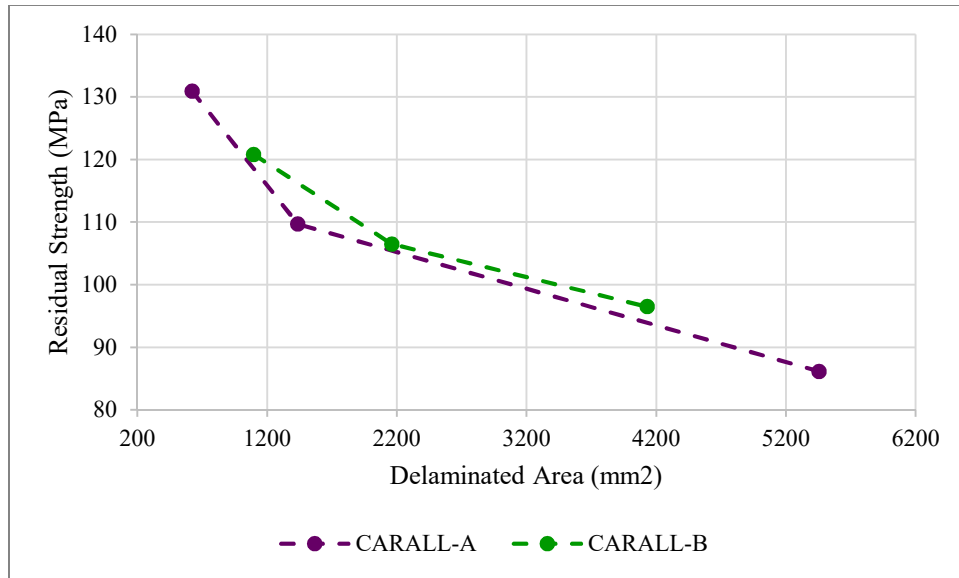


Figure 8.16: Delaminated area versus residual strength of CARALL specimens cured without using polyester surfacing cloth layers

8.2 Compression After Impact :Numerical Simulation

The impact and CAI tests analyzes are performed as a multistep analysis. The CAI test simulation is carried out subsequently after the completion of the impact test analysis using the birth and death time functionality of LS-DYNA available in boundary and contact cards. The translational degrees of freedom in the y, z-direction and the rotational degrees of freedom in the three directions of the upper and clamping plate were constrained, and compressive displacement was applied in the x direction, as shown in Figure 8.17. The compressive loading of the specimen mimics the loading in the experimental investigations.

Although the CAI test is essentially quasi-static, it was simulated by means of the explicit dynamic FE code LS-DYNA. The reason for this choice is due to the fact that high material and geometrical non-linearities occur, resulting in severe convergence difficulties if an implicit FE code is used. Accordingly, a displacement loading was applied with sufficiently slowness and smoothness, so that the kinetic energy is kept low when compared with the internal energy of the

system. Automatic surface to surface contact was used to model the interaction of specimen with the knife-edged side and base plates of CAI fixture. The knife edged side plates are meant to induce a local buckling behavior of the impacted area avoiding a global buckling behavior of the specimens. The CAI fixture including side and base plates were constrained in all degrees of freedom. The birth time of contacts and boundary conditions used in CAI simulation was kept such that they come into the picture after the completion of impact simulation.

The interactions, constraints and impact loading that were applied in impact simulation were removed from CAI analysis by providing death time in their keyword cards. The compression after impact test setup along with loading direction and impacted laminate considered in the numerical investigations are illustrated in Fig. 8.17. The interaction of specimen with the upper surface and clamping plate was modeled by defining a segment based automatic surface to surface contact between them. The coefficient of friction equal to 0.3 was considered in the interactions of the specimen with the components of CAI fixture.

The CAI test can also be modeled separately from impact simulation by writing a “dynain” file at the end of an impact analysis which contains information about deformation, shell element history variables (stress, plastic strain, material-model-dependent extra history variables), and tensorial strains [98] using INTERFACE SPRINGBACK LS-DYNA keyword command. The damaged laminate information can then be imported to LS-PrePost through “dynain” file and the new boundary conditions which reproduce the CAI test can be defined.

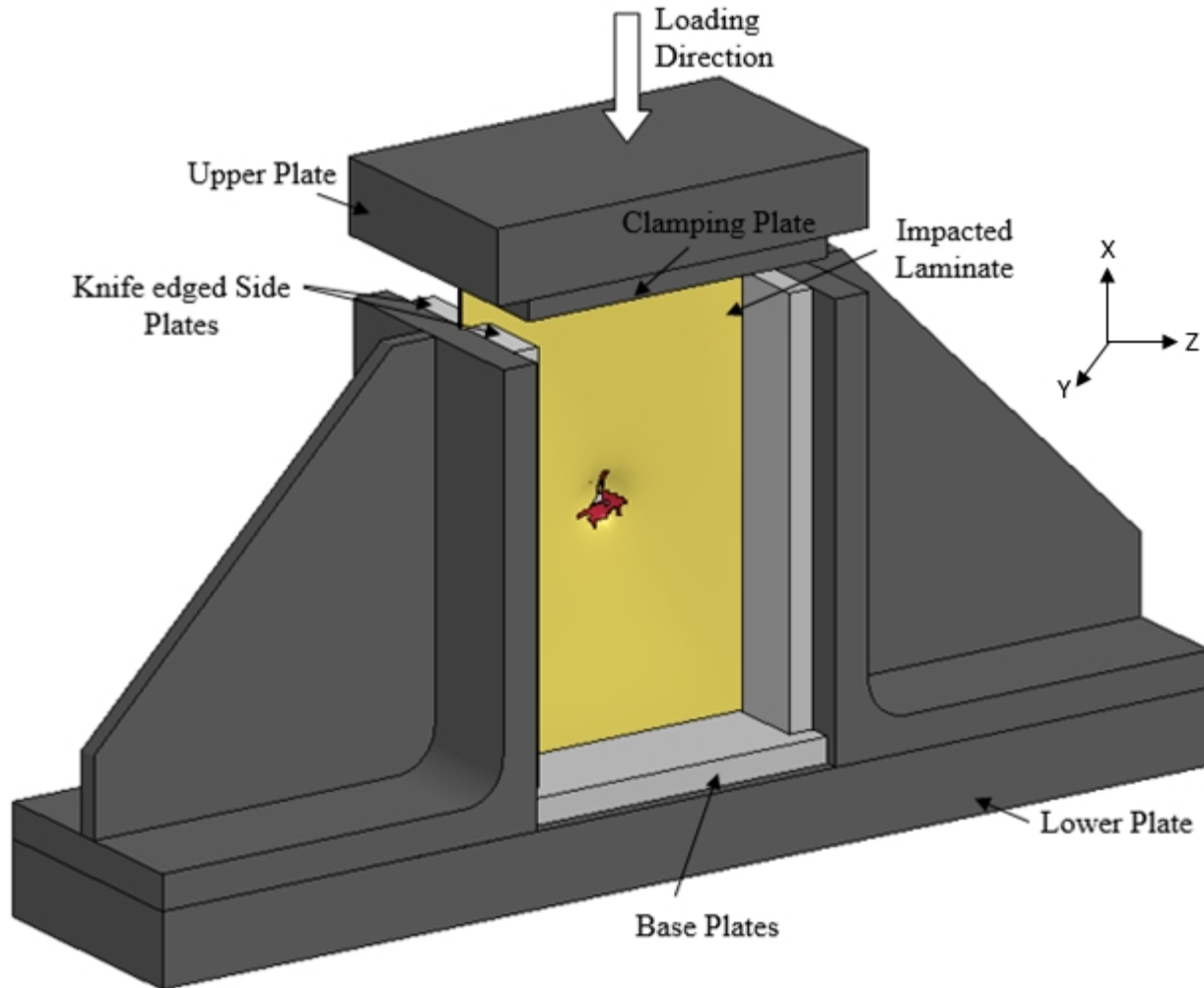


Figure 8.17: CAI test setup adopted in numerical simulation

However, in this research work, CAI test is modeled after the completion of impact test analysis in a combined multistep simulation.

8.2.1 CAI Test Numerical Predictions

The load-displacement curves predicted by the finite element analysis for CARALL-A specimens cured with and without using cloth layers are shown in figures 8.18 & 8.19. It can be observed from the curves the peak load level decreases with the increase in the impact energy. A comparison between experimental and FEA predictions for the residual compressive strength of CARALL-A is shown in Figure 8.20.

It can be seen that FEA model predicts the compressive strength of CARALL-A FMLs cured with cloth layers with less error as compared to specimens made without using cloth layers. Table 8.3 illustrates the percentage error between the experimental and FEA predictions results for CARALL-A specimens. Failure modes of CARALL-A specimens predicted by FEA analysis are shown in Figure 8.21. CARALL-A specimens showed approximately similar pattern of deformation in failure modes for unimpacted and specimens impacted at 21J and 31J.

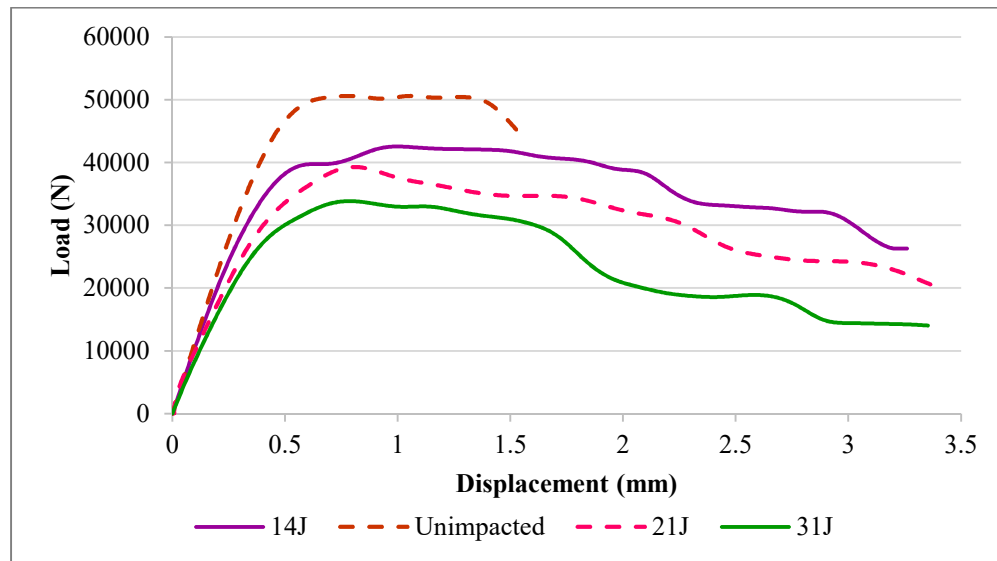


Figure 8.18: Numerical Predictions of CAI test load displacement curves of CARALL-A cured with polyester cloth layers.

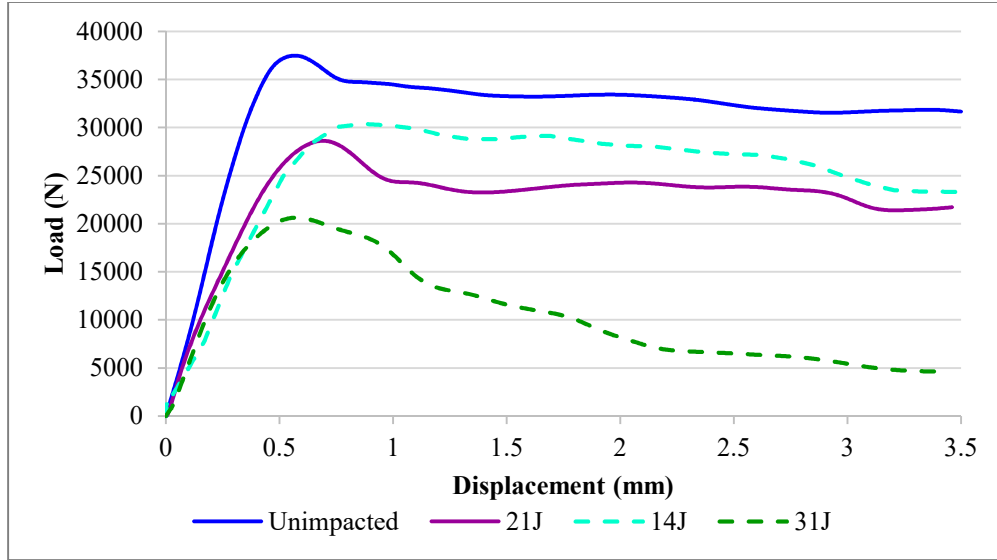


Figure 8.19: Numerical Predictions of CAI test load displacement curves of CARALL-A cured without using polyester cloth layers

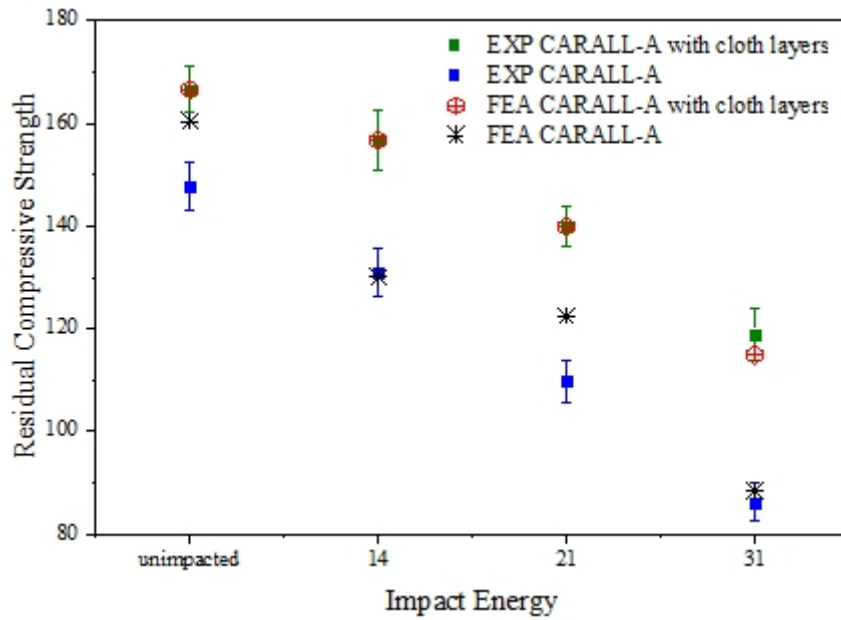


Figure 8.20: Comparison between residual strength experimental results and FEA predictions for CARALL-A FMLs.

Table 8.3: Comparison between experimental and FEA predictions for the residual strength of CARALL-A specimens.

Impact energy (J)	CARALL-A			CARALL-A with Cloth		
	Experimental CAI strength	FEA strength	Error (%)	Experimental CAI strength	FEA strength	Error (%)
Unimpacted	147.71	160.38	-8.57	166.58	171.75	-3.10
14	130.94	130.00	0.72	156.66	144.38	7.84
21	109.71	122.45	-11.61	139.86	133.42	4.60
31	86.15	88.26	-2.45	118.89	114.87	3.38

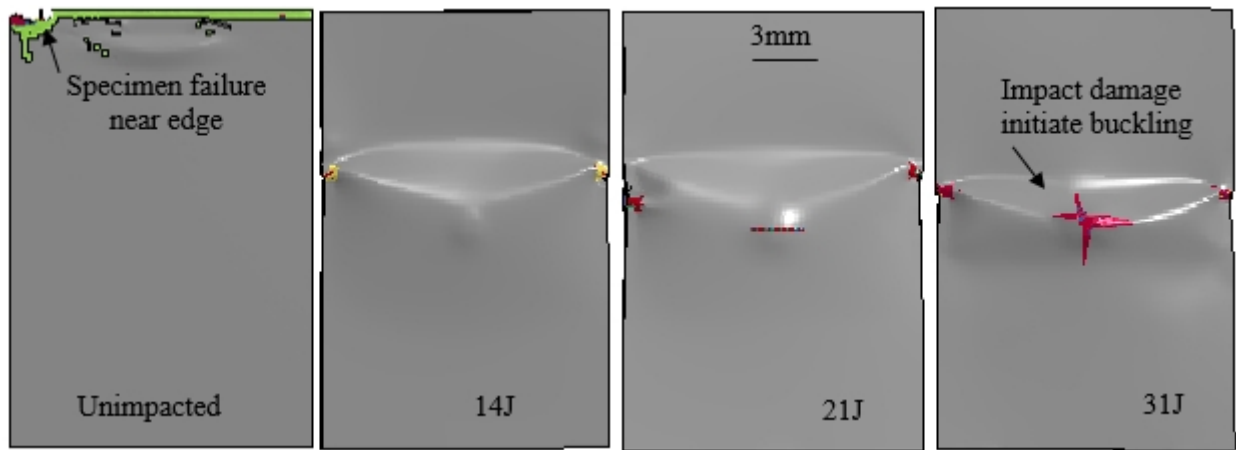


Figure 8.21: Numerical failure mode predictions of CARALL-A specimens.

However, specimens impacted at 14J tends to slightly differ from experimental results. In FEA predictions of these specimens, the impact damage zone slightly participate in the initiation of compressive buckling, whereas this is not the case in the experimental samples. The specimens impacted at 31J initiates the buckling in the damage zone similar to the experimental results. The width wide delamination spread due to compressive loading of CARALL-A specimens are shown in Figure 8.22. Delamination spread across the width makes it clearer that specimens impacted at 31J have a significant amount of damage in terms of strength which forces the specimen to buckle in the impact damaged zone. Similarly, the force-displacement

plots predicted by the finite element analysis for CARALL-B specimens cured with and without using cloth layers are shown in Figures 8.23 & 8.24.

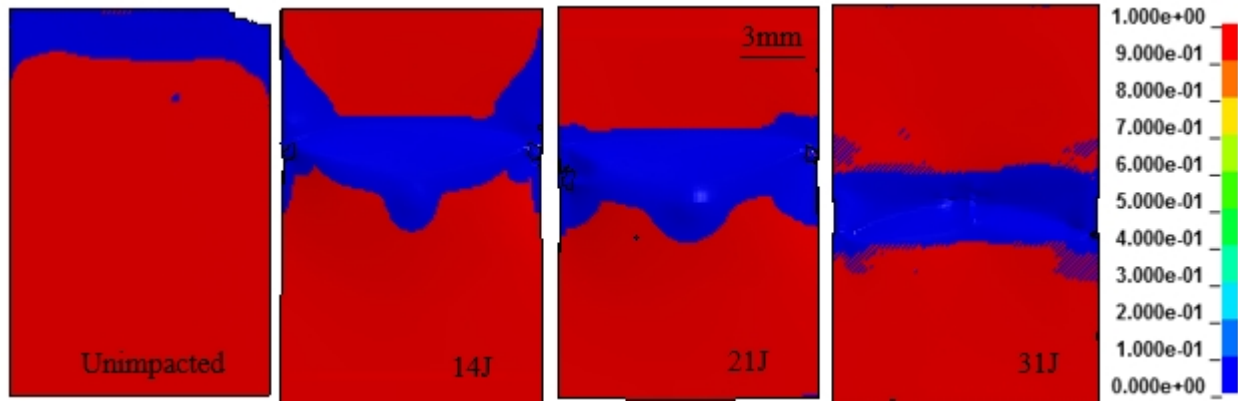


Figure 8.22: FEA predictions for delamination in CARALL-A specimens under compressive loading

CARALL-B laminates also showed a reduction in compressive strength with respect to unimpacted virgin samples similar to CARALL-A specimens. However, the peak load carried by CARALL-B specimens were slightly lower than that of CARALL-A laminates. A comparison between both FMLs in term of peak load and percentage reduction in maximum load w.r.t. virgin specimens are tabulated in Table 8.4.

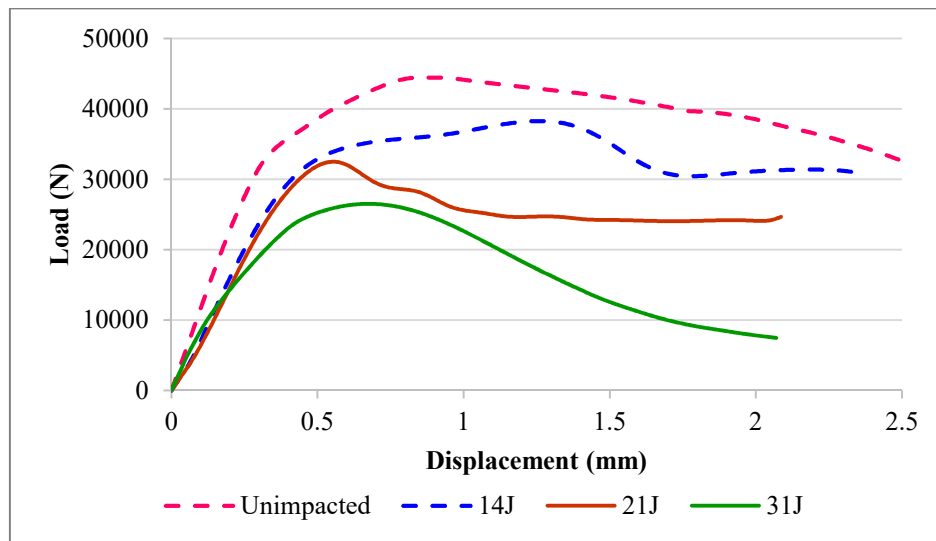


Figure 8.23: Numerical Predictions of CAI test load displacement curves of CARALL-B cured with polyester cloth layers

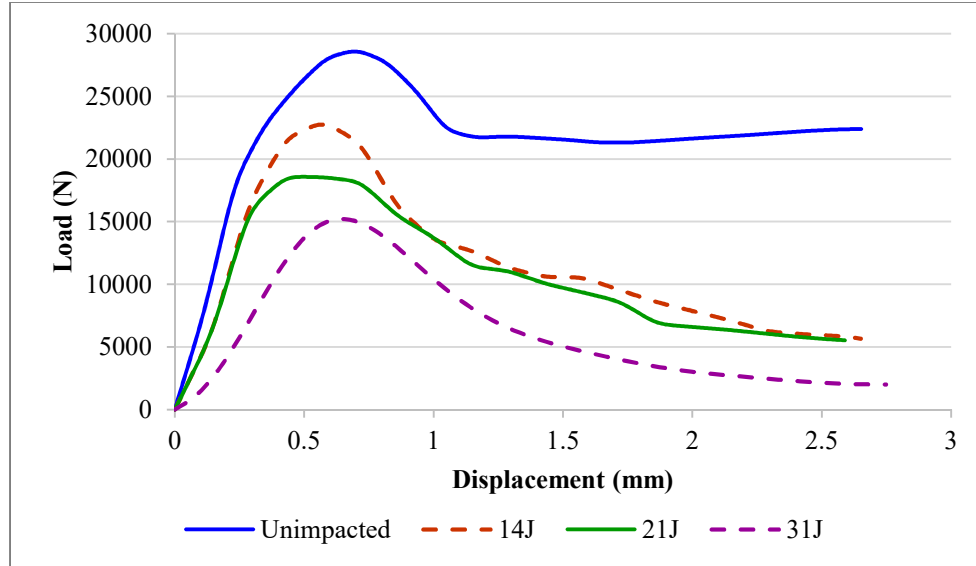


Figure 8.24: Numerical Predictions of CAI test load displacement curves of CARALL-B cured without using polyester cloth layers

Table 8.4: Comparison between all FMLs in terms of peak load.

Impact energy (J)	CARALL-A		CARALL-A with Cloth		CARALL-B		CARALL-B with Cloth	
	Peak load (KN)	Decrease W.r.t virgin sample (%)	Peak load (KN)	Decrease W.r.t virgin sample (%)	Peak load (KN)	Decrease W.r.t virgin sample (%)	Peak load (KN)	Decrease W.r.t virgin sample (%)
Virgin	37.47	----	50.60	----	28.57	----	44.50	----
14	30.38	18.94	42.54	15.93	22.77	20.30	38.29	13.95
21	28.61	23.64	39.31	22.32	18.58	34.99	32.50	26.96
31	20.62	44.96	33.85	33.11	15.21	46.78	26.52	40.41

Figure 8.25 illustrates the comparison between experimental and FEA predictions for the residual compressive strength of CARALL-B specimens. FEA analysis showed greater error in predicted compressive strength values for CARALL-B specimens cured without using the veil cloth layers. Table 8.5 gives the percentage error between the experimental and FEA compressive residual strength values for CARALL-B FMLs. Failure modes of CARALL-B specimens predicted by FEA analysis are shown in Figure 8.26. In CARALL-B FMLs, the unimpacted specimens failed in the region that is clamped between two bases plates similar to what was observed in experimental samples whereas the specimens impacted at 14J and 21J,

showed the buckling failure right above the impact damaged zone indicating that the damage was not significant to buckle the specimens right in the impact damaged area.

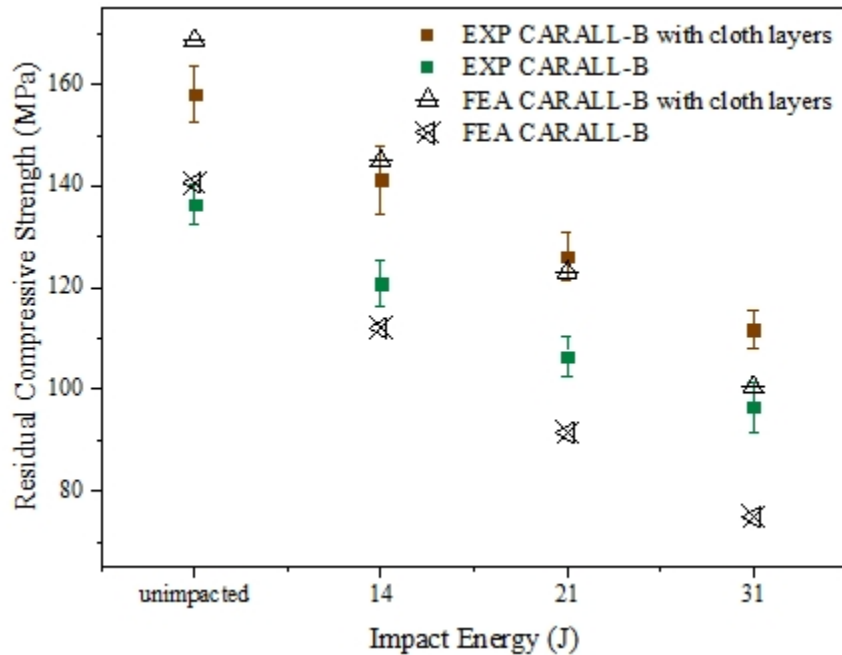


Figure 8.25: Comparison between residual strength experimental results and FEA predictions for CARALL-B FMLs.

Table 8.5: Comparison between experimental and FEA predictions for the residual strength of CARALL-B specimens.

Impact energy (J)	CARALL-B			CARALL-B with Cloth		
	Experimental CAI strength	FEA strength	Error (%)	Experimental CAI strength	FEA strength	Error (%)
Virgin	136.30	140.62	-3.17	157.96	168.47	-6.65
14	120.82	112.06	7.25	141.22	144.96	-2.65
21	106.49	91.42	14.15	126.15	123.04	2.46
31	96.51	74.84	22.45	111.78	100.39	10.19

Similar to CARALL-A FMLs, the specimens impacted at 31J initiates the compressive buckling right in the impact damaged area. The widthwise delamination occurred due to compressive loading of CARALL-B FMLs are shown in Figure 8.27. In FEM predictions shown in Figures 8.22 & 8.27, the solid blue color represent that damage is critical (value nearly 0.0)

and the red color represent that the damage has not occurred (value nearly 1.0), and others represent different damage states.

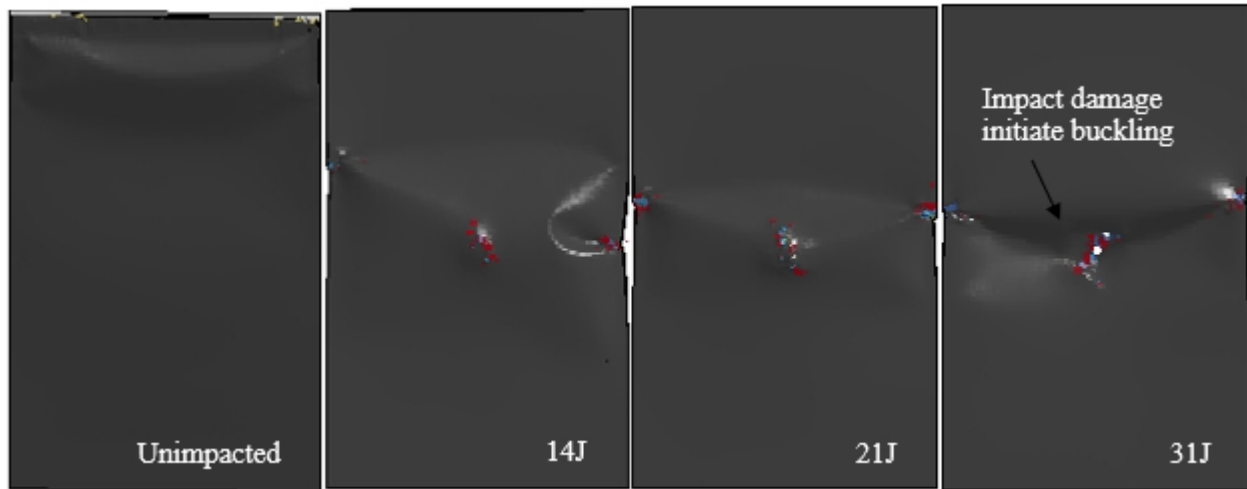


Figure 8.26: Numerical failure mode predictions of CARALL-B specimens.

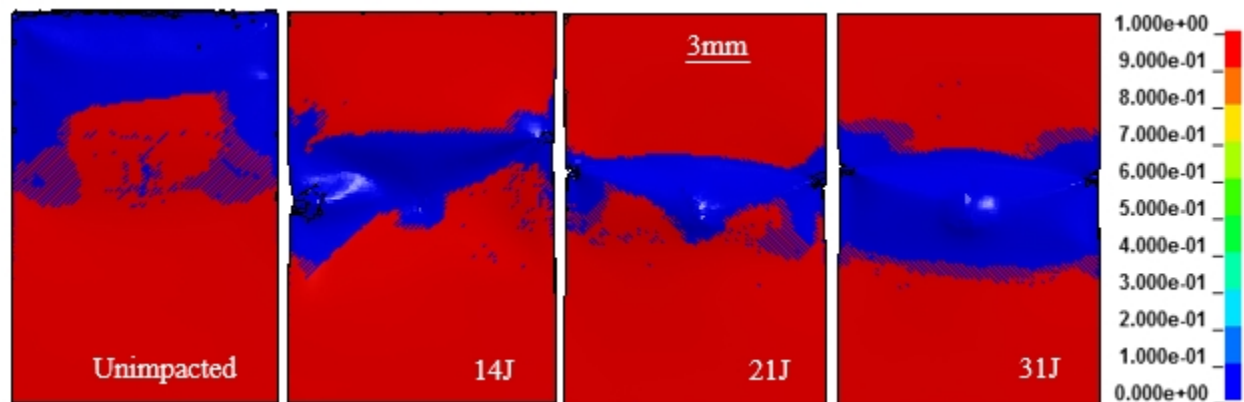


Figure 8.27: FEA predictions for delamination in CARALL-B specimens under compressive loading

CHAPTER 9 CONCLUSIONS & RECOMMENDATIONS

9.1 Conclusions

In this research work, the experimental characterization of damage mechanisms and behavior of the carbon fiber reinforced aluminum laminates cured without using any adhesive film and acid treatment of aluminum layers fiber metal laminates under tensile, flexural, low-velocity impact loading and compression after impact was performed. The effect of the addition of polyester synthetic surface veil cloth layers at the interfaces of carbon fiber aluminum layers on the damage modes and response of these FMLs were also studied. The major contributions for Thesis regarding CARALL FMLs involve thorough characterization of damage mechanisms for both static and impact loading. For static and dynamic loading cases, FEA models were developed for each case which showed excellent correlation. Specific conclusions made from this investigation are listed.

- **Thermal Residual Stresses**

- a) Thermal residual stresses developed during the curing of fiber metal laminates were predicted by utilizing analytical equations and finite element modeling. It was found out that the veil cloth layer does not affect much in reducing the thermal residual stress.
- b) Thermal residual stress developed in aluminum layers of CARALL A (79.2 MPa) was found to be lower than CARALL B (106.2 MPa), however, the residual stresses developed in carbon fiber/epoxy layers was higher in CARALL A (127.7 MPa) laminate than CARALL B (109 MPa).
- c) The correlation between analytical equations and finite element results were very good for the thermal residual stress predictions.

- **Tensile Response Characterization**

- a) The addition of veil cloth layers leads to combined failure of all layers in both CARALL Laminates at the same time, whereas the carbon fiber/ epoxy layers break before the failure of aluminum layers in samples without veil cloth layers.
- b) Bonding between aluminum and carbon fiber/epoxy layers with the addition of resin rich layers does not allow the separation; therefore, the crack has a tendency to propagate through the thickness of the material.
- c) CARALL-B FMLs showed stiffer flexural characteristics having high tangent modulus and small failure strain when the carbon fiber/epoxy layers were stacked exterior to the aluminum layers as compared to CARALL-A specimens having standard 3/2 stacking sequence.
- d) The effect of changing the position of carbon fiber/epoxy layers in carbon fiber reinforced aluminum laminates on the progressive damage failure behavior of CARALL FMLs was investigated experimentally and compared with the finite element predictions.
- e) Predicted progressive damage behavior characteristics of CARALL FMLs under tensile loading matches well with the experimental results.

- **Three Point Flexural Characterization**

- a) The addition of veil cloth increases the flexural strength of both CARALL-A & CARALL-B Laminates by 10-15 %, however, changes the failure mode of CARALL-A leading a simultaneous failure of both aluminum and carbon epoxy layers under tensile stresses.

- b) It was found that the middle carbon fiber/epoxy layer also failed in CARALL B with the addition of veil cloth, whereas no failure of middle carbon fiber layer was found without the addition of resin rich veil cloth.
 - c) Numerical simulation was performed to predict the progressive damage behavior of these FMLs under three point bending. Finite element model was found capable of predicting the complex progressive behavior of FMLs under static flexural loading, capturing all associated flexural failure modes.
 - d) The delamination was found to be reduced to a great extent in both laminate configurations due to the addition of veil cloth layers as they increase the interlaminar strength of laminates.
- **Low-velocity Impact Behavior Characterization**
 - a) Low-velocity impact experimentation showed that CARALL laminates give higher forces and smaller displacement with the addition of polyester veil cloth layers due to reduced delaminated area across all interfaces of aluminum and carbon fiber layers, thus increasing slightly the energy absorption capabilities of these laminates.
 - b) The threshold impact energy, energy at which perforation failure was induced in all metallic and fiber reinforced layers for these laminates was found to be around 31J.
 - c) CARALL-B FMLs was found more susceptible to damage than CARALL A during the impact event at similar energy levels due to more damage in carbon fiber/epoxy layers when placed directly on the impacted side.
 - d) Finite element analysis utilizing LS-DYNA software was performed to predict load-displacement history, delamination area, absorbed energy, damage morphologies on

- impacted and non-impacted sides and tensile failures of CFRP layers for an impact event at three different energy levels.
- e) The numerical material model successfully captured the peak load levels and delaminated area for each impact energy level and compared well with the experimental results.
 - f) The delaminated area was found to be increasing with the impact energy to a level until the primary failure mode is changed from delamination to the failure of carbon fiber/epoxy or metallic layers.
- **Compression After Impact (CAI) Response Characterization**
 - a) Length-wise compression after impact static tests was conducted for impacted and non-impacted samples to determine the residual strength of these fiber metal laminates after the impact event.
 - b) Compressive Buckling was achieved as a failure mode during the experimental procedure adopted as per ASTM norms due to a very small thickness of the FML laminates, however, the buckling load of specimens having veil cloth layers was found to be more as compared to those without veil cloth layers for both CARALL laminates.
 - c) CARALL-A specimens cured with cloth layers perform better than CARALL-B specimens cured with cloth layers.
 - d) It is found that higher impact energy (31J) causes a large reduction in the residual strength for both fiber metal laminate systems in the range of 30-41%.
 - e) Finite element analysis predicts the compressive residual strength of FMLs with an acceptable level of accuracy as compared to experimental results.

9.2 Recommendations

The continued research could be taken to next levels by further developing it in number of ways:

- The influence of the yield strength of aluminum layers on the static and impact performance of these carbon fiber reinforced aluminum laminates cured with polyester cloth layers can be investigated. This is to explore if 2000 series aluminum would be as effective as 5000 or 6000 series.
- The effect of projectile shape on the impact damage mechanism should be investigated as in this study only semi-spherical impactor was used.
- A hybrid system with fewer Al layers can be explored. In this case we expect that the FML density to be closer to 2 g/cc and lighter weight. Whether such FML systems provide good mechanical and impact properties would be of significant interest.
- The influence of veil cloth layers having more plasticity in their properties on the behavior of CARALL laminates can be investigated.

REFERENCES

1. Vogelesang, L.B. and A. Vlot, *Development of fibre metal laminates for advanced aerospace structures*. Journal of Materials Processing Technology, 2000. 103(1): p. 1-5.
2. Lawcock, G., *Novel Fiber Reinforced Metal Laminates for Aerospace Applications-A Review*. SAMPE J., 1995. 31(1): p. 175-183.
3. Sinmazçelik, T., et al., *A review: Fibre metal laminates, background, bonding types and applied test methods*. Materials & Design, 2011. 32(7): p. 3671-3685.
4. Vogelesang, L. and J. Gunnink, *ARALL, a material for the next generation of aircraft. A state of the art*. 1983, Delft University of Technology.
5. Alderliesten, R.C., *Fatigue crack propagation and delamination growth in Glare*. 2005: TU Delft, Delft University of Technology.
6. Verbruggen, M.L.C.E., *Aramid Reinforced Aluminium Laminates: ARALL: Adhesion problems and environmental effects: Vol. A: Adhesion and delamination*. 1986, Delft University of Technology.
7. Vlot, A., L. Vogelesang, and T. De Vries, *Towards application of fibre metal laminates in large aircraft*. Aircraft Engineering and Aerospace Technology, 1999. 71(6): p. 558-570.
8. Asundi, A. and A.Y. Choi, *Fiber metal laminates: an advanced material for future aircraft*. Journal of Materials Processing Technology, 1997. 63(1): p. 384-394.
9. Khan, S., R. Alderliesten, and R. Benedictus, *Post-stretching induced stress redistribution in fibre metal laminates for increased fatigue crack growth resistance*. Composites Science and Technology, 2009. 69(3): p. 396-405.

10. Seo, H., et al., *Numerical simulation of glass-fiber-reinforced aluminum laminates with diverse impact damage*. AIAA journal, 2010. 48(3): p. 676-687.
11. Lawcock, G.D., et al., *Effects of fibre/matrix adhesion on carbon-fibre-reinforced metal laminates—I.: Residual strength*. Composites Science and Technology, 1998. 57(12): p. 1609-1619.
12. Lin, C., P. Kao, and F. Yang, *Fatigue behaviour of carbon fibre-reinforced aluminium laminates*. Composites, 1991. 22(2): p. 135-141.
13. Ng, S.-P., P.-C. Tse, and K.-J. Lau, *Numerical and experimental determination of in-plane elastic properties of 2/2 twill weave fabric composites*. Composites Part B: Engineering, 1998. 29(6): p. 735-744.
14. Rattan, R. and J. Bijwe, *Carbon fabric reinforced polyetherimide composites: Influence of weave of fabric and processing parameters on performance properties and erosive wear*. Materials Science and Engineering: A, 2006. 420(1–2): p. 342-350.
15. Peters, S.T., *Handbook of composites*. 2013: Springer Science & Business Media.
16. [http://www.mtorres.es/sites/default/files/productos/torreslayup_automatic_tape%20_layer_MTorres_09.jpg](http://www.mtorres.es/sites/default/files/productos/torreslayup_automatic_tape%20layer_MTorres_09.jpg).
17. http://www.fokker.com/sites/default/files/media/Files/Brochures/Fokker_Glare.pdf.
18. Hammond, M.W., *Evaluation of the crack initiation and crack growth characteristics in hybrid titanium composite laminates via in situ radiography*. 2005.
19. Vlot, A. and J.W. Gunnink, *Fibre metal laminates: an introduction*. 2011: Springer Science & Business Media.
20. Laliberte, J., et al., *Applications of fiber-metal laminates*. Polymer composites, 2000. 21(4): p. 558-567.

21. Vlot, A., *Glare: history of the development of a new aircraft material*. 2001: Springer Science & Business Media.
22. Krimbalis, P.P., *On the development of a strength prediction methodology for fibre metal laminates in pin bearing*. 2009.
23. Pho, J., *Fracture Mechanics of Glare and Quantitative Prediction of Residual Strength*. Delft University of Technology, The Netherlands, 1992.
24. https://en.wikipedia.org/wiki/Composite_repairs.
25. Abouhamzeh, M., J. Sinke, and R. Benedictus, *On the prediction of cure-process shape deviations in fibre metal laminates*. Journal of Composite Materials, 2015. 49(14): p. 1705-1716.
26. Guo Yajun, Z.R., *The Residual Stresses in Glass Fiber Reinforced Aluminium Laminates(GLARE)*. Journal of Materials Engineering, 1998. 0(1): p. 28-30.
27. Hofslagare, P., *Residual Stress Measurement on Fibre-metal-laminates*. Journal of Neutron Research, 2003. 11(4): p. 215-220.
28. Hofslagare, P. and S. Johansson, *The influence of bonding strength and residual stresses on delamination growth in FML*. 1999.
29. Kawai, M., et al., *Inelastic behavior and strength of fiber-metal hybrid composite: GLARE*. International Journal of mechanical sciences, 1998. 40(2): p. 183-198.
30. Cepeda-Jiménez, C., et al., *Damage tolerance assessment by bend and shear tests of two multilayer composites: glass fibre reinforced metal laminate and aluminium roll-bonded laminate*. Composites Science and Technology, 2009. 69(3): p. 343-348.

31. Khalili, S.M.R., R.K. Mittal, and S.G. Kalibar, *A study of the mechanical properties of steel/aluminium/GRP laminates*. Materials Science and Engineering: A, 2005. 412(1–2): p. 137-140.
32. Park, S.Y., et al., *Effects of surface pre-treatment and void content on GLARE laminate process characteristics*. Journal of Materials Processing Technology, 2010. 210(8): p. 1008-1016.
33. Soltani, P., et al., *Studying the tensile behaviour of GLARE laminates: a finite element modelling approach*. Applied Composite Materials, 2011. 18(4): p. 271-282.
34. Hagenbeek, M., et al., *Static properties of fibre metal laminates*. Applied Composite Materials, 2003. 10(4-5): p. 207-222.
35. Asha, M.V., S. Kumar, and A. Vino, *Comparative study of tensile and Flexural behavior for glass-fiber reinforced Aluminum (glare) laminates and aluminum*. Asian Journal of Computer Science and Technology (AJCST), 2013. 1(1): p. 5-13.
36. Baumert, E.K., et al., *Mechanical evaluation of new fiber metal laminates made by the vartm process*, in *ICCM-17 17th international conference on composite materials*. 2009: Edinburgh, United Kingdom.
37. Wu, G. and J.-M. Yang, *Analytical modelling and numerical simulation of the nonlinear deformation of hybrid fibre–metal laminates*. Modelling and Simulation in Materials Science and Engineering, 2005. 13(3): p. 413.
38. Iaccarino, P., A. Langella, and G. Caprino, *A simplified model to predict the tensile and shear stress–strain behaviour of fibreglass/aluminium laminates*. Composites science and technology, 2007. 67(9): p. 1784-1793.

39. Sadighi, M. and S. Dariushi, *An experimental study of the fibre orientation and laminate sequencing effects on mechanical properties of Glare*. Proceedings of the Institution of Mechanical Engineers, Part G: Journal of Aerospace Engineering, 2008. 222(7): p. 1015-1024.
40. Esfandiari, H., S. Daneshmand, and M. Mondali, *Analysis of Elastic-Plastic Behavior of Fiber Metal Laminates Subjected to In-Plane Tensile Loading*. International Journal of Advanced Design and Manufacturing Technology, 2012. 5(1): p. 61-69.
41. Abouhamzeh, M., et al., *Closed form expression for residual stresses and warpage during cure of composite laminates*. Composite Structures, 2015. 133: p. 902-910.
42. Abouhamzeh, M., J. Sinke, and R. Benedictus, *Investigation of curing effects on distortion of fibre metal laminates*. Composite Structures, 2015. 122: p. 546-552.
43. Botelho, E.C., et al., *A review on the development and properties of continuous fiber/epoxy/aluminum hybrid composites for aircraft structures*. Materials Research, 2006. 9(3): p. 247-256.
44. Caprino, G., G. Spataro, and S. Del Luongo, *Low-velocity impact behaviour of fibreglass-aluminium laminates*. Composites Part A: Applied Science and Manufacturing, 2004. 35(5): p. 605-616.
45. Ardakani, M.A., A.A. Khatibi, and S.A. Ghazavi. *A study on the manufacturing of Glass-Fiber-Reinforced Aluminum Laminates and the effect of interfacial adhesive bonding on the impact behavior*. in *Proceedings of the XI International Congress and Exposition*. 2008.

46. Liu, Y. and B. Liaw. *Drop-weight impact on fiber-metal laminates using various indenters*. in *SEM X International Congress & Exposition on Experimental and Applied Mechanics Costa Mesa, CA*. 2004.
47. Ardakani, M.A., A.A. Khatibi, and H. Parsaiyan. *An experimental study on the impact resistance of glass-fiber-reinforced aluminum (Glare) laminates*. in *Proceedings of the 17th International Conference on Composite Materials*. 2009.
48. Liu, Y. and B. Liaw, *Effects of constituents and lay-up configuration on drop-weight tests of fiber-metal laminates*. *Applied Composite Materials*, 2010. 17(1): p. 43-62.
49. Rajkumar, G., et al., *Experimental investigation of low-velocity repeated impacts on glass fiber metal composites*. *Journal of materials engineering and performance*, 2012. 21(7): p. 1485-1490.
50. Tsartsaris, N., et al., *Low-velocity impact behavior of fiber metal laminates*. *Journal of Composite Materials*, 2011: p. 0021998310376108.
51. Laliberté, J., C. Poon, and P.V. Straznicky, *Low-velocity impact damage in GLARE fibre-metal laminates*. *Proceedings of International Committee on Composite Materials*, 1999. 1001: p. 12.
52. Laliberté, J., C. Poon, and P.V. Straznicky. *Numerical modeling of low-velocity impact damage in fiber-metal laminates*. in *ICAS 2002 Congress (The International Council of the Aeronautical Sciences Congress)*, Toronto, Canada. 2002.
53. Wu, G., J.-M. Yang, and H.T. Hahn, *The impact properties and damage tolerance and of bi-directionally reinforced fiber metal laminates*. *Journal of Materials Science*, 2007. 42(3): p. 948-957.

54. Taheri-Behrooz, F., M.M. Shokrieh, and I. Yahyapour, *Effect of stacking sequence on failure mode of fiber metal laminates under low-velocity impact*. Iranian Polymer Journal, 2014. 23(2): p. 147-152.
55. Jakubczak, P., et al., *The issue of residual strength tests on thin fibre metal laminates*. Composites Theory and Practice, 2014. 14(3): p. 134--138.
56. Starikov, R., *Assessment of impact response of fiber metal laminates*. International Journal of Impact Engineering, 2013. 59: p. 38-45.
57. Caprino, G., V. Lopresto, and P. Iaccarino, *A simple mechanistic model to predict the macroscopic response of fibreglass–aluminium laminates under low-velocity impact*. Composites Part A: Applied Science and Manufacturing, 2007. 38(2): p. 290-300.
58. Morinière, F., et al., *An integrated study on the low-velocity impact response of the GLARE fibre-metal laminate*. Composite Structures, 2013. 100: p. 89-103.
59. Balasingh, C., et al., *Residual stresses in aluminium alloy sheet/aramid fiber laminated composites*. 1988.
60. Wu, H. and L. Wu, *A study of tension test specimens of laminated hybrid composites. 1: Methods of approach*. Composites Part A: Applied Science and Manufacturing, 1996. 27(8): p. 647-654.
61. Hai, Y., et al., *Study on arall failure behaviour under tensile loading*. Scripta materialia, 1996. 35(12): p. 1379-1384.
62. Wu, H., *Temperature dependence of the tensile behaviour of aramid/aluminium laminates*. Journal of materials science, 1993. 28(1): p. 19-34.
63. Chen, J. and C. Sun, *Modeling of orthotropic elastic-plastic properties of ARALL laminates*. Composites science and technology, 1989. 36(4): p. 321-337.

64. Kanakalatha, P., et al., *Preparation and characterization of aluminium alloy sheet Aramid fibre-laminated composites*. Bulletin of Materials Science, 1990. 13(5): p. 305-311.
65. Sun, C., A. Dicken, and H. Wu, *Characterization of impact damage in ARALL laminates*. Composites science and technology, 1993. 49(2): p. 139-144.
66. Vlot, A., *Low-velocity impact loading: on fibre reinforced aluminium laminates (ARALL and GLARE) and other aircraft sheet materials*. 1993, Delft University of Technology.
67. Vlot, A., *Impact tests on fibre metal laminates under a tensile load*. 1993, Delft University of Technology.
68. Hoogsteden, W.P., *Compression-After-Impact Behavior of ARALL (trade name)-I Laminates*. 1992, DTIC Document.
69. Liaw, B., Y. Liu, and E. Villars. *Impact damage mechanisms in fiber-metal laminates*. in *Proceedings of the SEM Annual Conference on Experimental and Applied Mechanics*. 2001.
70. Vlot, A., *Impact loading on fibre metal laminates*. International Journal of Impact Engineering, 1996. 18(3): p. 291-307.
71. Sherman, D., J. Lemaitre, and F.A. Leckie, *The mechanical behavior of an alumina carbon/epoxy laminate*. Acta metallurgica et materialia, 1995. 43(12): p. 4483-4493.
72. Lin, C., P. Kao, and M.-H. Jen, *Thermal residual strains in carbon fibre-reinforced aluminium laminates*. Composites, 1994. 25(4): p. 303-307.
73. Lawcock, G., et al., *The effect of adhesive bonding between aluminum and composite prepreg on the mechanical properties of carbon-fiber-reinforced metal laminates*. Composites Science and Technology, 1997. 57(1): p. 35-45.

74. Ye, L., et al., *Effects of Fibre/Matrix Adhesion on Carbon-fibre-reinforced Metal Laminates. I. Residual Strength*. Composites Science and Technology, 1997. 57(12): p. 1609-1619.
75. Hu, Y., et al., *Preparation and properties of Fibre–Metal Laminates based on carbon fibre reinforced PMR polyimide*. Composites Part B: Engineering, 2015. 69: p. 587-591.
76. Botelho, E., et al., *Evaluation of adhesion of continuous fiber–epoxy composite/aluminum laminates*. Journal of adhesion science and technology, 2004. 18(15-16): p. 1799-1813.
77. Zhao, J., F. Yang, and R. Wang. *Ultrasonic monitoring of asymmetric carbon fibre reinforced aluminum laminates*. in *Fourth International Conference on Smart Materials and Nanotechnology in Engineering*. 2013. International Society for Optics and Photonics.
78. Botelho, E., L. Pardini, and M. Rezende, *Evaluation of hygrothermal effects on the shear properties of Carall composites*. Materials Science and Engineering: A, 2007. 452: p. 292-301.
79. Rajkumar, G., et al., *Investigation of Tensile and Bending Behavior of Aluminum based Hybrid Fiber Metal Laminates*. Procedia Materials Science, 2014. 5: p. 60-68.
80. Kim, J.G., et al., *Tensile behavior of aluminum/carbon fiber reinforced polymer hybrid composites at intermediate strain rates*. Journal of Composite Materials, 2014: p. 0021998314531310.
81. Bieniaś, J. and P. Jakubczak, *Low velocity impact resistance of aluminium/carbon-epoxy fiber metal laminates*. Composites Theory and Practice, 2012. 12(3): p. 193-197.

82. Song, S., et al., *Experimental and numerical investigation on impact performance of carbon reinforced aluminum laminates*. Journal of Materials Science & Technology, 2010. 26(4): p. 327-332.
83. Lawcock, G., et al., *Effects of fibre/matrix adhesion on carbon-fibre-reinforced metal laminates—II. impact behaviour*. Composites science and technology, 1998. 57(12): p. 1621-1628.
84. Kim, H.S., B.C. Kim, and T.S. Lim, *Foreign objects impact damage characteristics of aluminum/composite hybrid drive shaft*. Composite structures, 2004. 66(1): p. 377-389.
85. Yu, G.-C., et al., *Low velocity impact of carbon fiber aluminum laminates*. Composite Structures, 2015. 119: p. 757-766.
86. Rajkumar, G., et al., *Investigation of repeated low velocity impact behaviour of GFRP/Aluminium and CFRP/Aluminium laminates*. Int. J. Soft Comput. Eng, 2012. 1(6): p. 50-58.
87. Jaroslaw, B., S. Barbara, and J. Patryk, *The comparison of low velocity impact resistance of aluminum/carbon and glass fiber metal laminates*. Polymer Composites, 2014.
88. Bieniaś, J., et al., *Low-energy impact behaviour and damage characterization of carbon fibre reinforced polymer and aluminium hybrid laminates*. Archives of Civil and Mechanical Engineering, 2015.
89. <https://www.stainlesssupply.com/order-metal-online/docs/g3c1055s24ss0p0/5052-H32-aluminum-sheet.htm>.
90. <http://asm.matweb.com/search/SpecificMaterial.asp?bassnum=MA5052H32>.
91. *Advanced Composite Materials, Chapter-07, Aviation Maintenance Technician Handbook-Airframe*. Vol. 1. 2012.

92. *ASTM D3846 - 08, Standard Test Method for In-Plane Shear Strength of Reinforced Plastics*. 2015, ASTM International, West Conshohocken, PA.
93. Frantz, M., C. Lauter, and T. Tröster, *Advanced manufacturing technologies for automotive structures in multi-material design consisting of high-strength steels and CFRP*, in *56th International Scientific Colloquium (56th IWK)*. 2011, 12 bis: Ilmenau.
94. *ASTM D1876 - 08, Standard Test Method for Peel Resistance of Adhesives (T-Peel Test)*. 2015, ASTM International, West Conshohocken, PA.
95. *ISO 11339: 2010. Adhesives—T-peel test for flexible-to-flexible bonded assemblies*.
96. Chang, F.-K. and K.-Y. Chang, *A progressive damage model for laminated composites containing stress concentrations*. *Journal of Composite Materials*, 1987. 21(9): p. 834-855.
97. http://www.atlassteels.com.au/documents/Atlas_Aluminium_datasheet_5052_rev_Oct_2013.pdf.
98. *Livermore Software Technology Corporation, LS DYNA Version 971, Theory Manual*.
99. Bala, S., *Tie-break contacts in LS-DYNA*. 2010, Livermore Software Technology Corporation: Livermore, CA, USA.
100. Loikkanen, M., G. Praveen, and D. Powell. *Simulation of ballistic impact on composite panels*. in *10th International LS-DYNA Users Conference*. 2008.
101. Lemmen, P.P.M., G.J. Meijer, and E.A. Rasmussen. *Dynamic behaviour of composite structures (DYCOSS) Failure Prediction Tool*. in *70th Shock and Vibration Symposium*. 1999. Albuquerque, NM, USA.
102. Meijer, G.J., et al. *Dynamic Behavior of Composite Ship Structures (DYCOSS); Tests and Analyses Efforts*. in *70th Shock and Vibration Symposium*. 15-19 November, 1999. Albuquerque, NM, USA.

103. Davila, C.G. and P.P. Camanho. *Decohesion elements using two and three-parameter mixed-mode criteria*. in *American Helicopter Society Conference*. Oct 29 – Nov 1,2001. Williamsburg, VA.
104. Lemmen, P.P.M. and G.J. Meiger, *Failure Prediction Tool Theory and User Manual*. 2001, Center for Maritime Engineering,TNO Building and Construction Research: The Netherlands.
105. *Livermore Software Technology Corporation,LS DYNA Version 971,Keyword User's Manual*.
106. Carrillo, J. and W. Cantwell, *Mechanical properties of a novel fiber–metal laminate based on a polypropylene composite*. *Mechanics of Materials*, 2009. 41(7): p. 828-838.
107. *ASTM D7136 / D7136M-15,Standard Test Method for Measuring the Damage Resistance of a Fiber-Reinforced Polymer Matrix Composite to a Drop-Weight Impact Event*. 2015, ASTM International: West Conshohocken, PA.
108. Hellen, T.K., *On the method of virtual crack extensions*. *International Journal for Numerical Methods in Engineering*, 1975. 9(1): p. 187-207.
109. Rice, J.R., *A path independent integral and the approximate analysis of strain concentration by notches and cracks*. *Journal of applied mechanics*, 1968. 35(2): p. 379-386.
110. Rybicki, E.F. and M. Kanninen, *A finite element calculation of stress intensity factors by a modified crack closure integral*. *Engineering Fracture Mechanics*, 1977. 9(4): p. 931-938.
111. Raju, I., *Calculation of strain-energy release rates with higher order and singular finite elements*. *Engineering Fracture Mechanics*, 1987. 28(3): p. 251-274.

112. Parks, D.M., *A stiffness derivative finite element technique for determination of crack tip stress intensity factors*. International Journal of fracture, 1974. 10(4): p. 487-502.
113. Griffith, A.A., *The phenomena of rupture and flow in solids*. Philosophical transactions of the royal society of london. Series A, containing papers of a mathematical or physical character, 1921: p. 163-198.
114. Gordnian, K., et al., *Determination of fracture energy and tensile cohesive strength in Mode I delamination of angle-ply laminated composites*. Composite Structures, 2008. 82(4): p. 577-586.
115. Hillerborg, A., M. Mod er, and P.-E. Petersson, *Analysis of crack formation and crack growth in concrete by means of fracture mechanics and finite elements*. Cement and concrete research, 1976. 6(6): p. 773-781.
116. Needleman, A., *A continuum model for void nucleation by inclusion debonding*. Journal of applied mechanics, 1987. 54(3): p. 525-531.
117. Tvergaard, V. and J.W. Hutchinson, *The relation between crack growth resistance and fracture process parameters in elastic-plastic solids*. Journal of the Mechanics and Physics of Solids, 1992. 40(6): p. 1377-1397.
118. Tvergaard, V. and J.W. Hutchinson, *The influence of plasticity on mixed mode interface toughness*. Journal of the Mechanics and Physics of Solids, 1993. 41(6): p. 1119-1135.
119. Camacho, G.T. and M. Ortiz, *Computational modelling of impact damage in brittle materials*. International Journal of solids and structures, 1996. 33(20): p. 2899-2938.
120. Mi, Y., et al., *Progressive delamination using interface elements*. Journal of composite materials, 1998. 32(14): p. 1246-1272.

121. Hillerborg, A., *Application of the fictitious crack model to different types of materials*. International Journal of Fracture, 1991. 51(2): p. 95-102.
122. Gözlüklü, B., *Delamination analysis by using cohesive interface elements in laminated composites*. 2009, Middle East Technical University.
123. Lemmen, P., G. Meijer, and E. Rasmussen. *Dynamic behavior of composite ship structures (DYCOSS) failure prediction tool*. in *70th Shock and Vibration Symposium*. 1999.
124. Meijer, G., et al. *Dynamic behavior of composite ship structures (DYCOSS); tests and analyses efforts*. in *70th Shock and Vibration Symposium*. 1999.
125. Lemmen, P. and G. Meijer, *Failure prediction tool theory and user manual*. TNO Report, 2001.
126. Benzeggagh, M. and M. Kenane, *Measurement of mixed-mode delamination fracture toughness of unidirectional glass/epoxy composites with mixed-mode bending apparatus*. Composites science and technology, 1996. 56(4): p. 439-449.
127. Shin, D.K., H.C. Kim, and J.J. Lee, *Numerical analysis of the damage behavior of an aluminum/CFRP hybrid beam under three point bending*. Composites Part B: Engineering, 2014. 56: p. 397-407.
128. <https://www.nde-ed.org/EducationResources/CommunityCollege/Ultrasonics/EquipmentTrans/DataPres.htm>.
129. *ASTM D7137/D7137M-12 Standard Test Method for Compressive Residual Strength Properties of Damaged Polymer Matrix Composite Plates*. 2012, ASTM International: West Conshohocken, PA.
130. Manieri and Harmsworth, *compressive properties of damaged graphite/Epoxy composites*. AFWAL-TM-86-102, 1986.

ABSTRACT**STATIC AND DYNAMIC BEHAVIOUR OF CARBON FIBER REINFORCED ALUMINUM (CARALL) LAMINATES**

by

GURPINDER SINGH DHALIWAL**August 2016****Advisor:** Dr. Golam Newaz**Major:** Mechanical Engineering**Degree:** Doctor of Philosophy

The main aim of this research work was to investigate the static and dynamic properties of carbon fiber reinforced aluminum laminates cured without using any external adhesive and acid treatment of aluminum layers. A comprehensive study was undertaken to study the effect of adding epoxy resin rich polyester synthetic surface veil cloth layers on the failure modes and flexural and tensile response of these fiber metal laminates (FMLs). The main purpose of adding veil cloth layers was to prevent the occurrence of galvanic corrosion by avoiding direct contact between aluminum and carbon fiber layers. The addition of veil cloth layers leads to the combined failure of all layers in carbon fiber reinforced aluminum laminates at the same time, whereas the carbon fiber/ epoxy layers break before the failure of aluminum layers in samples cured without using veil cloth layers under tensile loading.

The delamination was found to be reduced to a great extent in these laminate configurations due to the addition of veil cloth layers. Thermal residual stress developed during the curing of fiber metal laminates were predicted by utilizing analytical equations and finite element modeling. It was found out that the veil cloth layer does not affect much in reducing the

thermal residual stress. Low-velocity impact tests were carried out using a drop-weight impact tower by impacting these fiber metal laminates at the center with three different energy levels to address energy absorption characteristics of these composites. Results showed that these laminates give higher forces and smaller displacement with the addition of polyester veil cloth layers due to reduced delaminated area across all interfaces of aluminum and carbon fiber layers, thus increasing slightly the energy absorption capabilities of these laminates. Primary failure modes observed during impact tests in these FMLs were cracks in the non-impacted aluminum layer, carbon fiber (CFRP) layer breakage and delamination b/w aluminum & CFRP layers. The threshold impact energy, energy at which perforation failure was induced in all metallic and fiber reinforced layers for these laminates was found to be around 31J. Finite element analysis utilizing LS-DYNA software was performed to predict load-displacement history, delamination area, absorbed energy, damage morphologies on impacted and non-impacted sides and tensile failures of CFRP layers for an impact event at three different energy levels.

Delamination at the aluminum and carbon fiber layers interfaces was modeled by using with traction separation law and damage criterion proposed by Benzeggagh–Kenane was used for interface damage evolution. Predicted impact behavior results match well with experimental results. Length-wise compression after impact static tests was conducted for impacted and non-impacted samples to determine the residual strength of these fiber metal laminates after the impact event. By comparing FMLs systems cured with and without using polyester surfacing veil cloth layers in terms of residual strength at the same impact energy, it is found that the FMLs having cloth layers provides higher residual strength than the regular FMLs cured without cloth layers composite system due to the higher interlaminar strength of the composite system. These results provide a clear understanding of the failure modes of these FMLs under different loading

conditions and how they influence the overall composite behavior. A unique contribution of the thesis work is the investigation of the effect of resin rich polyester veil cloth on flexural, tensile, low-velocity impact & compression after impact characteristics of these carbon fiber reinforced aluminum laminates. These results can be used in designing lightweight automotive and aerospace components.

AUTOBIOGRAPHICAL STATEMENT

GURPINDER SINGH DHALIWAL

Gurpinder Singh Dhaliwal is currently a Ph.D. candidate at Wayne State University and expects to graduate in this year 2016. He earned his Bachelor's degree in Mechanical Engineering from Punjab Technical University in 2006. Because of his enthusiasm towards product development and design, he worked at standard electrical company subsidiary of Havells as a tool/die designer before coming abroad for higher education in the year 2008. He earned his Master of Science degree focusing his specialization in solid mechanics area from Wayne State University in 2010. With his passion, he continued his research work in the Ph.D. program in 2011 working in the advanced composite materials lab. His research interests include damage tolerance assessment of both laminates and sandwich composite material both by experiment and numerical simulations. He received Graduate Professional Scholarship during his Master's program and two times Thomas C. Rumble University Graduate Fellowship from Wayne State graduate school during his Ph.D.'s program. Gurpinder Singh Dhaliwal is an active member in a variety of honor and engineering organizations such as Golden Key Honor Society, American Society of Mechanical Engineers (WSU Chapter) etc.

Publications:

- Dhaliwal, G.S. and G.M. Newaz, “**Experimental and numerical investigation of flexural behavior of carbon fiber reinforced aluminum laminates**”. Journal of Reinforced Plastics and Composites, 2016. DOI: 10.1177/0731684416632606.
- Dhaliwal, G.S. and G.M. Newaz, “**Modeling Low Velocity Impact Response of Carbon Fiber Reinforced Aluminum Laminates (CARALL)**”. Journal of Dynamic Behavior of Materials, 2016: p. 1-13.